uOttawa
L'Université canadienne
Canada's university

Assessing Moisture Resilience of Wall Assemblies to Wind-Driven Rain Loads Arising from Climate Change

Submitted By

Zhe Xiao

Thesis Supervisors

Prof. Elena Dragomirescu

Prof. Michael Lacasse

In partial fulfillment of the requirements for the degree of
Doctor of Philosophy in Civil Engineering
Faculty of Engineering, Department of Civil Engineering
University of Ottawa
Ottawa, Canada
November, 2021

Acknowledgements

First of all, with the utmost respect and pleasure, I would like to express my sincere gratitude and appreciation to my supervisors Prof. Elena Dragomirescu and Prof. Michael A. Lacasse for their endless support throughout every phase of my research and for their patience, motivation, and immense knowledge. Without their experience, insight and guidance, I would not have had the opportunity to reach where I am today.

My special thanks also go to my family, who tirelessly encouraged and supported me in many ways on my journey to pursue the Doctoral degree. Their sacrifices, understanding and endless love have motivated me to achieve more than I expected of myself.

I would like to thank Dr. Maurice Defo for helping me performing the hygrothermal simulation. I would also thank Dr. Abhishek Gaur for his assistance on acquiring the climate data.

Finally, my special thanks must be extended to the technical staff members at the department of Civil Engineering and the National Research Council Canada for their continuous and professional assistance and collaboration over the years.

This work is a part of the Climate-Resilient Buildings and Core Public Infrastructure (CRBCPI) project supported by the National Research Council of Canada's Construction Research Centre (CRC) and Infrastructure Canada

Abstract

Moisture loads arising from the deposition of wind-driven rain (WDR) on building façades can induce detrimental effects to wall assembly components and can adversely influence their long-term performance. Wind-driven rain as a climatic phenomenon will inevitably be affected by the evident changing climate in the near future. Wall assemblies subjected to wind-driven rain loads will also perform differently due to a varying moisture environment over the course of time. The performance of the building envelope, including the wall assembly, largely determines the serviceability of a building over its life cycle. Thus, it is essential for practitioners to understand and to be able to assess such performance. In this study, a complete procedure has been developed to permit assessing the moisture resilience of wall assemblies to wind-driven rain loads arising from climate change. The development of this procedure included four phases. In the first phase the historical and projected climate data was analysed to identify the possible wind-driven rain conditions to which a wall assembly may be exposed. The magnitudes of wind-driven rain and driving-rain-wind-pressure for different return periods were also investigated. Based on the results from phase one, a watertightness test protocol was established taking into consideration the possible ranges of wind-driven rain and driving-rain-wind-pressure as they may occur spatially, as well as temporally, across Canada. The range of watertightness test parameters was accommodated in the newly built Dynamic Wind and Wall Testing Facility (DWTF) at the National Research Council Canada. Thereafter in phase two of the research, wall assemblies having different configurations were tested in the DWTF following the test protocol to obtain the moisture load for wall assemblies under different wind-driven rain conditions. Such moisture loads were formulized and used in the third phase, where hygrothermal simulations were conducted to derive the hygrothermal parameters of the wall assemblies subjected to historical and projected climate data. In the final research development phase, different criteria and methods were explored to describe the performance of wall assemblies based on the hygrothermal parameters. During the development of the moisture resilience assessment procedure, a novel wind-driven-rain-pressure-index was devised to describe the extent of the effects arising from the concurrent action of wind-driven rain and driving-rain-wind-pressure loads on a vertical wall assembly; a new two-step approach was established to

formulize the watertightness test results and thereby permit calculating the moisture load using values of hourly wind-driven-rain and hourly driving-rain-wind-pressure of a given location; a novel severity index was proposed to quantitatively describe the damage events arising from such moisture load on the wall assemblies. The moisture performance of tested wall assemblies subjected to historical and projected future climate were compared and discussed. The risks of occurrence of damage events in wall assemblies during different time periods were also demonstrated.
Keywords: Climate change, driving-rain-wind-pressure, hygrothermal simulation, moisture load, risk analysis, watertightness test, wind-driving rain, wood frame wall assembly

Table of Content

List of Figures

List of Tables

Chapter 1 Introduction

1.1 Introduction

The global average precipitation will certainly increase with the rise in temperature of the atmosphere, as reported by the Intergovernmental Panel on Climate Change (IPCC) (Krinner et al., 2013). Extremes climatic conditions, such as heavy precipitations, will also occur more frequently and with higher intensity due to the changing climate. Based on different emission scenarios, the projected extent of changes in precipitation will likely increase by 0.5% to 4% $°C^{-1}$, for a mitigation scenario for which the mean temperature will increase no more than 2°C, and an increase by 1% to 3% $°C^{-1}$ is expected for all the other emission scenarios (Mirle et al., 2013). The projected median increase in surface temperature in Canada under the mitigation scenario is 1.8°C by the mid of 21st century, while by the end of the 21st century the surface temperature is expected to increase by 6°C. As a result, precipitations under these two scenarios will increase by 7 % and 24 %, respectively, which are largely due to the transformation of snow into rain in the spring and autumn seasons. Moreover, the daily extreme precipitation is very likely to occur more frequently during the projected time periods (Bush & Lemmen, 2019; Il Jeong & Sushama, 2018).

Wind-Driven Rain (WDR) is one of the most common phenomena in the atmosphere and represents the co-occurrence of rain and wind. During the process of the downward movement of failing raindrop, except for the transfer of potential energy, wind flow also contributes to the kinetic energy of the raindrop given that it applies horizontal velocity components to raindrops. In theory, all rain events on earth can be considered as WDR due to the constant movement of air in the atmosphere. When a raindrop reaches the façade of the building, it may splash, spread or bounce from the building surface, depending on the façade materials, on the raindrop final velocity, as well as the attack angle of the raindrop to that of the wall (Abuku et al., 2009). After impact, the water from the raindrop will either be drained from the façade, absorbed by the façade material, if porous in nature, or enter the building envelope through any cracks or openings present on the façade surface. The building envelope, by design, is intended to prevent water intrusion induced by WDR loads acting on the building envelope exterior. However, the existence of deficiencies in the building envelope can, over its life cycle, allow the passage of water through openings on the façade surface. This effect is most likely inevitable given the aging and deterioration of materials, the mechanical failure of structural members arising from extreme and cyclic loads, and faulty construction or lack of adequate maintenance of the building façade. All these could cause damage to the exterior building materials and small openings to occur on façade surfaces. Although the infiltrated water can still be drained from a wall assembly after entering the wall, it also has the potential to further penetrate and be retained within the wall assembly which is referred to as the moisture load. Adverse problems arising from the presence of moisture in wall assemblies include, but are not limited to, mould growth, decay of wood components, corrosion of metals, and frost damage to porous materials such as mortar and brick masonry, might also be encountered (Franke et al., 1995; Kumaran et al., 2003; Lacasse & Vanier (Eds.), 1999b, 1999a; Rousseau, 1999; Smegal et al., 2013).

The amount of WDR that reaches the exterior surface of the wall assembly can be calculated given the precipitation intensity and the velocity of the concurrent action of the wind using semi-empirical equations, as described in §1.3. Thus, the imminent changes in precipitation over projected future time periods will inevitably affect WDR loads, which in turn will influence the level of moisture load to the wall assembly, and subsequently will alter the moisture performance of the wall assembly.

1.2 Research objectives

It is of significant importance to understand the resilience of building envelope, that are currently designed based on the historical climate loads and experience gained from existing applications, but given the anticipated changes induced by the changing climate to moisture loads, the long-term performance and the sustainability of building envelope may be compromised. In this research, the main objective is to develop a procedure to properly estimate the moisture resilience of wall assemblies subjected to the effects of climate change. Such a procedure will include the following tasks:

The first task to be investigated is assessing the moisture load in wall assemblies assuming that WDR is the primary source of this moisture load. Given that Canada has the second largest national territorial area in the world, cities across Canada have very diverse geographical conditions, which unavoidably result in different local climate characteristics. Thus, WDR conditions in each major city across Canada will be analyzed. In addition to the climate parameters during the historical time period, the potential future climate conditions will also be investigated.

The next task to be achieved once climatic parameters are determined, is evaluating the WDR load, which is the amount of WDR deposited on the exterior surface of the wall, and thereafter, the corresponding moisture load to wall assemblies when exposed to different WDR conditions. The extent of water infiltration into wall assemblies is affected by the WDR load, concurrent Driving Rain Wind Pressure (DRWP) and the configuration of the wall assembly. These three factors are expected to be formulized on the basis of the results derived from evaluating the moisture load of wall assemblies.

The moisture performance of wall assemblies will be assessed using the moisture load derived from hourly WDR loads and hourly DRWPs, which are obtained from the climate data. Thus, the moisture performance can be directly correlated to the climatic conditions. The mould index and decay models (Ojanen et al., 2010; Viitanen et al., 2010) are usually used as performance indicators when assessing for moisture performance. These criteria allow determining whether a detrimental effect has, or has not, occurred in any of the wall assembly components. However, over a long period of time, such adverse phenomena may occur multiple times. Simply characterising the performance as "good" or "bad" may not be sufficient to adequately describe the fluctuating performance of the wall assembly over long periods of time. Therefore, new indicators will be investigated to quantify the extent of the detrimental effects on the wall assemblies, as may occur from WDR loads acting over continuous periods of time.

The ultimate goal of this research is to assess the resilience in moisture performance of wall assemblies, which can be revealed by comparing the performance over an historical time period to that of a future projected time period. In the research described in this project, the assessment strategies will be applied to two types of wood frame wall assemblies that include a brick masonry clad wall assembly and a vinyl clad wall assembly. The performance of the wall assemblies located in selected Canadian cities will also be discussed. The validated strategies are expected to be applied to other types of wall assemblies and a greater number of locations across Canada in the future.

1.3 Research approach and methodology

The historical climate data used in this study was obtained from meteorological stations operated by Environment and Climate Change Canada during the period 1986 to 2016. The rainfall was measured by standard rain gauges, the wind velocities and directions were measured by anemometers at a height of 10 meters above the ground. In addition, the snowfall precipitations were distinguished from the rainfall precipitations to be excluded from the analysis. The collected historical climate data was not only for the analysis of the performance, but also this was used to generate the projected climate data through climate models. Initially, 15 bias-corrected datasets, which are also called 15 realizations, for the time period 1986-2016, were generated based on the collected historical climate data. Each realization had different initial conditions and the bias-correction methods for different types of climatic parameters were also different (Ashfaq et al., 2010; Berg et al., 2012; Cannon, 2018; Leander & Buishand, 2007; Li et al., 2010; Piani et al., 2010). Thereafter, the 15 realizations of climate data for the historical time period 1986-2016 were utilized as the baseline to generate climate data for projected time periods. Two projected time periods have been considered in this research: 2034-2064 and 2062-2092. Each time period corresponded to a scenario with certain increases in temperature. The average temperature increment during 2034-2064 is expected to be 2°C, whereas over the 2062-2092 time period the temperature increment is predicted to be 3.5°C. The climate data during the projected time periods were generated by a regional climate model CanRCM4 (Scinocca et al., 2016). This model was developed from downscaling the large ensemble simulation CanESM2 (Environment and Climate Change Canada, 2018), which is part of a Global Climate Model (Arora et al., 2011) in which interactions of the atmosphere, ocean, sea ice, land and carbon cycle components were considered, using a 2.8° spatial resolution to a 0.44° grid. Overall, 15 realizations, each with 31-year climate data, were generated for 3 time periods and for 11 Canadian cities (Figure 1.1). Thus, a total number of 495 sets of climate data were implemented for the analysis. The temporal resolution for parameters in each set of climate data is one hour.

Figure 1.1 Location of Canadian cities considered in this study; from left to right: VAN-Vancouver, CAL-Calgary, SAS-Saskatoon, WIN-Winnipeg, TOR-Toronto, OTT-Ottawa, MON-Montreal, MNC-Moncton, CHA-Charlottetown, HAL-Halifax, and STJ-St. John's.

Several different methodologies can be used to assess WDR loads, such as: semi-empirical equation method, in-field tests, laboratory tests and numerical simulations. Each of these methods has its advantages and shortcomings. Semi-empirical functions consider characteristics of the raindrop, building geometry, wind velocity, wind direction and wind angle with the building façade. Once these parameters are determined, the wind-driven rain load can be easily derived from these equations, and thereafter can be used as input for watertightness test. However, according to numerous studies (Blocken & Carmeliet, 2004; Ge et al., 2017, 2018; Kubilay et al., 2014) the wind-driven rain load derived from semi-empirical equations is inconsistent with the results from field measurements. Field measurements of WDR can be conducted by installing rain gauges on building façades. At the same time, other relevant factors such as rain intensity, wind velocity, wind direction, building geometry and surroundings can also be recorded or characterized. As compared with other methods to evaluate the WDR load, this method is the most realistic approach as it involves the entire process of exposing the building to realistic rain events. It is worthwhile noting that, WDR loads derived from field measurements are significantly affected by the temporal resolution of the measurement due to the rapid changes in wind direction, wind velocity and rain intensity, during one rain event (Blocken & Carmeliet, 2005). Moreover, the randomness of the environmental conditions, as is evident from the field measurements, makes it challenging to replicate all these conditions in a laboratory environment. Nevertheless, replicating field test in an experimental facility, within a very short period of time is considered to be feasible (Mayo 1998). Regarding this research, the WDR load deposited onto the wall assembly was calculated by equation (1.1) given in the ASHRAE 160 standard (ASHRAE, 2016).

$$r_{bv} = r_h \mathrm{F_E F_D F_L} U \cos\theta \tag{1.1}$$

Where, r_{bv} is the WDR intensity (kg/m2·h), r_h is the horizontal rainfall intensity (mm/h), F_E, F_D and F_L are the rain exposure factor, rain deposition factor, and an empirical constant of 0.2 kg·s (m^3·mm), respectively. The hourly average wind speed is U (m/s), and θ is the angle between the wind direction and normal to the wall. The rainfall intensity and hourly average wind speed could be obtained from the climate dataset. The rain exposure factor (F_E), the deposition factor (F_D), and the angle (θ) to the wind are determined by configurations of the building and topography surrounding the building. The DRWP is another major factor to be considered; this has been derived using Bernoulli's principle (Eq. 1.2). The air density, ρ, was 1.225 kg/m^3 and V was the hourly average wind velocity in m/s.

$$DRWP = \frac{1}{2}\rho V^2 \tag{1.2}$$

A watertightness laboratory test is commonly used to investigate the resistance to water entry through imperfections and deficiencies in standard size wall assemblies, or to quantify the rate of water entry across the cladding layer of the wall assembly. In such a test, wall assemblies are subjected to different levels of simulated WDR load and simulated DRWP. The ranges of WDR load and DRWP implemented in the watertightness test can be obtained from an analysis of climate data. Test facilities used to perform such test usually impose the pressure to the specimen by the aid of a pressure chamber (Figure 1.2), or an aero engine (Figure 1.3), or both. These experimental facilities are able to mimic the wind effects applied to the building façades during WDR events. In addition, a water spray system is integrated into the facility to implement the driving-rain effects to the test specimens. The simultaneous actions of both systems are considered as replicating WDR in the atmosphere.

Figure 1.2 Norwegian Building Research Institute, Trondheim. RAWI-BOX

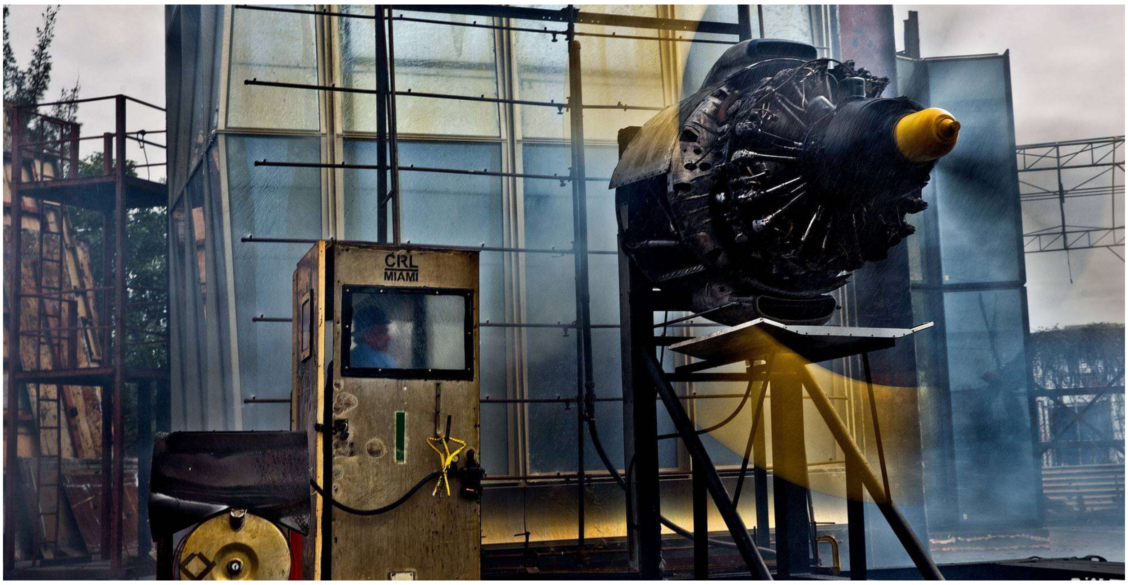

Figure 1.3 Construction Research Laboratory, Miami.

It is common for a WDR laboratory test to comply with a testing protocol, thus permitting experimental conditions in the facility to be repeatable as test conditions are clearly defined and generated by engineered devices employed in the laboratory. As such, different types of specimens can be tested using the predefined set of WDR conditions and test results are comparable between them. However, not all watertightness test protocols have been developed on the basis of climate loads, or for that matter were not derived from water deposition input obtained from semi-empirical equations. Since the results of watertightness tests are typically used to prove the wall assembly design, the relation between test WDR loads on the wall assembly, and the actual climate loads, has not been the focus of testing; rather in a watertightness test procedure, the wall assembly may very well be subjected to WDR loads that exceed the in-filed conditions. Thus, to permit accurately assessing the water entry rate and moisture load to different wall assemblies subjected to different levels of WDR loads, a watertightness test protocol was developed in this study based on the use of a newly built Dynamic Wind and Wall Testing Facility (DWTF) located at the National Research Council Canada (NRC).

The DWTF consists of a steel chamber (Figure 1.4a) that allows the testing of a wall specimen of up to 2.44 m by 2.44 m. The chamber is connected to an industrial blower that is able to generate large air pressures on the exterior surface of the test specimen. A water spray system (Figure 1.4b) is installed within the steel chamber and provides simulated driving-rain effects whereas a flap control system positioned to one side of the steel chamber is used to control the pressure within the chamber and the rate of pressure fluctuations acting of the test specimen. A measuring and control system has been integrated into a computer such that most of the experimental steps can be conducted automatically. The wall assemblies as were analyzed in this research study were tested using the DWTF such that a relation could be established in which considered the WDR, DRWP conditions and the moisture load to the wall assemblies are considered. This relation in which the WDR, DRWP conditions and moisture load were considered was thereafter used to develop water entry equations to calculate the moisture load to the wall based on the hourly WDR load and hourly DRWP as obtained from the climate data.

(a)

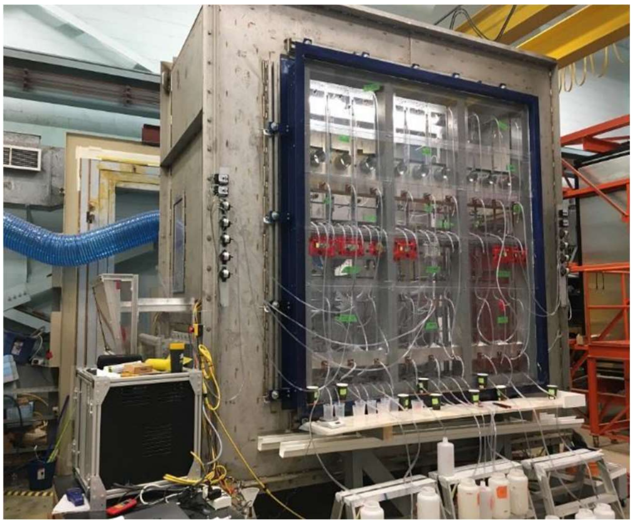

(b)

(c)

Figure 1.4 (a) Dynamic Wind and Wall Testing Facility (DWTF); (b) Water spray system; (c) Flap control system.

The hygrothermal simulations which can simulate the transportation of heat, air and moisture in the models, are often used to estimate the hygrothermal parameters, which are usually considered as the references for the performance assessment of the wall assembly located in different regions, bearing various climate conditions. For this stage of the research program, the moisture performance of wall assemblies would also be evaluated through the outputs of the hygrothermal simulations. Normally, a hygrothermal simulation requires information of climate conditions to which the modelled samples are exposed and numerous types of parameters which are obtained from the climate data can be employed. In this research, the moisture load input for the simulation was derived from water entry equations developed from results of watertightness tests. Subsequently, the mould index and a new proposed severity index have been generated using the output of the hygrothermal simulation. Quality and quantity information of these two indices between historical and projected time periods were compared and discussed. Resilience of different wall assemblies subjected to climate change was concluded from those discussions.

1.4 Research novelty

Overall, this research has established a new performance evaluation framework to properly estimate the effects of a changing climate on the moisture performance of different types of wood frame wall assemblies subjected to WDR conditions corresponding to 11 major cities in Canada. The use of this evaluation framework can help determine the moisture resilience of wall assemblies, assess risks of performance degradation and provide design guidance for projected future climate scenarios. At each phase of the research program, new methodologies and concepts were also proposed to facilitate the development and implementation of this evaluation.

When analyzing the climate data, a new Wind Driven Rain Pressure Index (WDRPI) was proposed to describe the concurrent effects of the WDR and DRWP acting on the exterior surface of a wall assembly, given that the amount of water penetration into a wall assembly is positively correlated with these two parameters. Also, a novel probabilistic study was performed for the WDR and DRWPI derived based on the historical and projected climatic data and the Gumbel distribution was proved to be the best distribution to conduct the extreme value analysis for the WDR and the WDRPI corresponding to the future climate change conditions.

Based on the findings from climate data analysis, a new watertightness test protocol was proposed to be compatible with the NRCC simulator DWTF. Each step of the protocol was designed to obtain parameters that would be considered to further assess the performance of the wall specimens. Experimental input conditions implemented in the test considered values generated from the extreme value analysis for future climate data, such that the wall specimen can be subjected to all possible WDR conditions during the test. In addition, a two-step approach was proposed to correlate the moisture load in the wall assembly with the experimental inputs, water spray rates and applied pressures, which represent the WDR intensity and DRWP in the atmosphere, respectively. Thus, the moisture load can be calculated using the hourly WDR intensity and hourly DRWP. A comparison to the moisture load calculated as the equivalent to 1% of the WDR load, as specified in the ASHRAE 160 standard (ASHRAE, 2016), proved the necessity of deriving moisture load from the watertightness tests.

The moisture loads derived from the watertightness tests were implemented in the subsequent hygrothermal simulations. Hydrothermal parameters obtained from the simulations were thereafter used to derive the performance indicators, mould index and development of decay for the oriented strand boards (OSB) in the wall assembly. The mould index was summarized as different events with exposure durations and high severity. Changes of these events for future projected time periods incorporating different future climate change conditions, were discussed. In terms of the decay, a newly proposed severity index was calculated from normalized values of relative humidity and temperature to represent the extent of decay for wood elements in wall assemblies subjected to moisture loads. The mass loss caused by the decay in different cities for different time periods was assessed by considering the decay intensity and duration of decay separately, given that the inherent uncertainty of projected climate data generated from the climate models. The likelihood of occurrence of a specific decay intensity and the likelihood of annual durations of decay events were generated by fitting selected distributions to the histograms of these two parameters.

1.5 Structure of the thesis

This research consists of 6 chapters. It is worth noting that Chapter 3, Chapter 4 and Chapter 5 contain four (4) technical articles and a conference proceedings paper with added complementary materials. Each article will be presented completely from the abstract to references. Corresponding complementary materials will be added following the review of the article.

Chapter 1 presents the introduction for the proposed research. It firstly states the reason for conducting this research and explains the causes of problems in wall assemblies. Then, methodologies and approaches have been proposed and described to achieve the research proposal.

Chapter 2 is a review of relevant studies relating to the problems and approaches as appear in this study. Detailed topics include climate change, WDR studies, watertightness tests, hygrothermal simulations, and the durability of wood materials in wall assemblies.

Chapter 3 offers information on the WDR conditions during the historical time periods. Also, the distribution used to generate WDR loads for different return periods has been investigated. A preliminary watertightness test for a vinyl wall assembly considering historical WDR conditions and using a dated testing protocol is conducted. The outcomes from this chapter contribute to the investigation as described in the subsequent chapters.

Chapter 4 provides information on the analysis of WDR conditions during future projected time periods. Watertightness tests results, for two wall assemblies in respect to the future projected WDR loads and using a newly established testing protocol are given. These results are then used to establish water entry equations to estimate the moisture loads of wall assemblies located in selected Canadian cities. Details of the new testing protocol and the development of water entry equations are presented as complementary materials in this chapter.

Chapter 5 introduces the setup and implementation of the hygrothermal simulations. Also, the simulation output has been converted to performance-based indices. Discussions are made for indices in different time periods to reveal the resilience of wall assemblies when subjected to WDR loads as occur from climate change.

Chapter 6 concludes all the work that has been completed and key information derived from analysis and discussions. The recommendations for future work are also given.

1.6 References

Abuku, M., Blocken, B., Poesen, J., & Roels, S. (2009). Spreading, splashing and bouncing of wind-driven raindrops on building façades. *11th Americas Conference on Wind Engineering*.

Arora, V. K., Scinocca, J. F., Boer, G. J., Christian, J. R., Denman, K. L., Flato, G. M., Kharin, V. V., Lee, W. G., & Merryfield, W. J. (2011). Carbon emission limits required to satisfy future representative concentration pathways of greenhouse gases.

Geophysical Research Letters, *38*(5), n/a-n/a. https://doi.org/10.1029/2010GL046270

Ashfaq, M., Bowling, L. C., Cherkauer, K., Pal, J. S., & Diffenbaugh, N. S. (2010). Influence of climate model biases and daily-scale temperature and precipitation events on hydrological impacts assessment: A case study of the United States. *Journal of Geophysical Research Atmospheres*. https://doi.org/10.1029/2009JD012965

ASHRAE. (2016). ASHRAE standard 160P-criteria for moisture control design analysis in buildings. In *ASHRAE Transactions*.

Berg, P., Feldmann, H., & Panitz, H. J. (2012). Bias correction of high resolution regional climate model data. *Journal of Hydrology*. https://doi.org/10.1016/j.jhydrol.2012.04.026

Blocken, B., & Carmeliet, J. (2004). A review of wind-driven rain research in building science. *Journal of Wind Engineering and Industrial Aerodynamics*, *92*(13), 1079–1130. https://doi.org/10.1016/j.jweia.2004.06.003

Blocken, B., & Carmeliet, J. (2005). High-resolution wind-driven rain measurements on a low-rise building—experimental data for model development and model validation. *Journal of Wind Engineering and Industrial Aerodynamics*, *93*(12), 905–928. https://doi.org/10.1016/j.jweia.2005.09.004

Bush, E., & Lemmen, D. S. (2019). *Canada's Changing Climate Report*. http://www.changingclimate.ca/CCCR2019

Cannon, A. J. (2018). Multivariate quantile mapping bias correction: an N-dimensional probability density function transform for climate model simulations of multiple variables. *Climate Dynamics*. https://doi.org/10.1007/s00382-017-3580-6

Environment and Climate Change Canada. (2018). *Memorandum ofUnderstanding between National Research Council and Environment and Climate Change Canada on Climate Resilient Buildings and Core Public Infrastructure: Future Projections ofClimate Design Values. Tier 1 Climate Projections* (p. 48). Government of Canada.

Franke, L., Schumann, I., Hees, R., Klugt, L. V. D., Naldini, S., Balen, K., & Mateus, J. M. (1995). Damage Atlas, Classification and Analysis of Damage Patterns found in Brick Masonry. In *Research Report No. 8*.

Ge, H., Chiu, V., Stathopoulos, T., & Souri, F. (2018). Improved assessment of wind-driven rain on building façade based on ISO standard with high-resolution on-site weather data. *Journal of Wind Engineering and Industrial Aerodynamics*, *176*, 183–196. https://doi.org/10.1016/j.jweia.2018.03.013

Ge, H., Deb Nath, U. K., & Chiu, V. (2017). Field measurements of wind-driven rain on mid-and high-rise buildings in three Canadian regions. *Building and Environment*, *116*, 228–245. https://doi.org/10.1016/j.buildenv.2017.02.016

Il Jeong, D., & Sushama, L. (2018). Rain-on-snow events over North America based on two Canadian regional climate models. *Climate Dynamics*, *50*(1–2), 303–316. https://doi.org/10.1007/s00382-017-3609-x

Krinner, G., Germany, F., Shongwe, M., Africa, S., France, S. B., Uk, B. B. B. B., Germany, V. B., Uk, O. B., France, C. B., Uk, R. C., Canada, M. E., Erich, M., Uk, R. W. L., Uk, S. L., & Lucas, C. (2013). Long-term Climate Change: Projections, Commitments and Irreversibility Pages 1029 to 1076. In Intergovernmental Panel on Climate Change (Ed.), *Climate Change 2013 - The Physical Science Basis* (Vol.

9781107057, pp. 1029–1136). Cambridge University Press. https://doi.org/10.1017/CBO9781107415324.024
Kubilay, A., Derome, D., Blocken, B., & Carmeliet, J. (2014). High-resolution field measurements of wind-driven rain on an array of low-rise cubic buildings. *Building and Environment*, *78*, 1–13. https://doi.org/10.1016/j.buildenv.2014.04.004
Kumaran, M. K., Mukhopadhyaya, P., Cornick, S. M., Lacasse, M. A., Rousseau, M. Z., Maref, W., Nofal, M., Quirt, J. D., & Dalgliesh, W. A. (2003). An Integrated methodology to develop moisture management strategies for exterior wall systems. *Proceedings of the 9th Canadian Conference on Building Science and Technology*.
Lacasse, M. A., & Vanier (Eds.), D. J. (1999a). *Durability of building materials and components 8: service life and asset management, Durability of Building Assemblies and Methods of Service Life Prediction, vol. 2*. NRC Research Press.
Lacasse, M. A., & Vanier (Eds.), D. J. (1999b). *Durability of building materials and components 8: service life and asset management, Service Life and Durability of Materials and Components, vol. 1*. NRC Research Press.
Leander, R., & Buishand, T. A. (2007). Resampling of regional climate model output for the simulation of extreme river flows. *Journal of Hydrology*. https://doi.org/10.1016/j.jhydrol.2006.08.006
Li, H., Sheffield, J., & Wood, E. F. (2010). Bias correction of monthly precipitation and temperature fields from Intergovernmental Panel on Climate Change AR4 models using equidistant quantile matching. *Journal of Geophysical Research Atmospheres*. https://doi.org/10.1029/2009JD012882
Mirle, K., Uk, M. R. A., Canada, N. G., Gutzler, D., Uk, J. G., Quintana, J. I., Republic, S. M., Uk, D. M., Germany, T. M., Uk, D. P., & France, A. R. (2013). Detection and attribution of climate change: From global to regional. In *Climate Change 2013 the Physical Science Basis: Working Group I Contribution to the Fifth Assessment Report of the Intergovernmental Panel on Climate Change* (Vol. 9781107057). https://doi.org/10.1017/CBO9781107415324.022
Ojanen, T., Viitanen, H., Peuhkuri, R., Lähdesmäki, K., Vinha, J., & Salminen, K. (2010). Mould growth modeling of building structures using sensitivity classes of materials. *Thermal Performance of the Exterior Envelopes of Whole Buildings - 11th International Conference*.
Piani, C., Weedon, G. P., Best, M., Gomes, S. M., Viterbo, P., Hagemann, S., & Haerter, J. O. (2010). Statistical bias correction of global simulated daily precipitation and temperature for the application of hydrological models. *Journal of Hydrology*. https://doi.org/10.1016/j.jhydrol.2010.10.024
Rousseau, M. (1999). Overview of the survey of building envelope failures in the coastal climate of British Columbia, performed by Morrisson-Hershfield Limited for CMHC (1996). *Journal of Thermal Envelope and Building Science*. https://doi.org/10.1177/109719639902200411
Scinocca, J. F., Kharin, V. V., Jiao, Y., Qian, M. W., Lazare, M., Solheim, L., Flato, G. M., Biner, S., Desgagne, M., & Dugas, B. (2016). Coordinated global and regional climate modeling. *Journal of Climate*. https://doi.org/10.1175/JCLI-D-15-0161.1
Smegal, J., Lstiburek, J., Straube, J., & Grin, A. (2013). Moisture-related durability of walls with exterior insulation in the pacific northwest. *Thermal Performance of the Exterior Envelopes of Whole Buildings - 12th International Conference*.

Viitanen, H., Toratti, T., Makkonen, L., Peuhkuri, R., Ojanen, T., Ruokolainen, L., & Räisänen, J. (2010). Towards modelling of decay risk of wooden materials. *European Journal of Wood and Wood Products*, *68*(3), 303–313. https://doi.org/10.1007/s00107-010-0450-x

Chapter 2 Literature Review

The current research project focuses on assessing the moisture performance resilience of wall assemblies subjected to future projected climate loads induced by changing climate. The state-of-the-art for the projection of future climate as well as studies relating to moisture effects to the building envelope when subjected to climate loads occurring for the future projected time periods, were firstly reviewed. Since the WDR load is the primary source of the moisture load in wall assemblies, studies undertaken with the intent of estimating the WDR load deposited on the building façade are also of interest. Water penetrating into cladding layers of wall assemblies is usually quantified by conducting experimental tests using designated test facilities. It is essential to review and understand the advantages and disadvantages of these types of facilities to permit developing testing procedures that support the current research objectives. Hygrothermal simulations are used as a numerical tool to simulate the transfer of air, heat and moisture in wall assemblies and can be performed using many different numerical models. In addition, the setup of the hydrothermal simulation requires extensive knowledge regarding the properties of materials, as well as understanding the boundary conditions to which wall assemblies may be exposed. Therefore, discussing and reviewing studies employing these numerical tools are of importance to enhance the accuracy and reliability of the numerical simulations in this study. The moisture performance of wall assemblies as were analyzed in this study were evaluated using different criteria, thus, reviews of the development and implementation of such performance criteria have also been provided.

2.1 Future climate, precipitation and moisture load

In Chapter 12 of the Fifth Assessment Report of the Intergovernmental Panel on Climate Changes (Intergovernmental Panel on Climate Change, 2013b) it is stated that "*Global mean temperatures will continue to rise over the 21st century if greenhouse gas (GHG) emissions continue unabated*". The increase in surface temperature is predicted to vary from 0.3°C to 1.7°C under a low GHG emission scenario, and from 2.6°C to 4.8°C under a high GHG emission for the period 2081-2100 comparing to 1986-2005. As a consequence, it is almost certain that global precipitation will increase by 0.5% °C^{-1} to

4% °C^{-1} for the low GHG emission scenario and by 1 to 3% °C^{-1} for all other scenarios. The future changes in precipitation will differ significantly for different regions in Canada. Overall, the discrepancies in precipitation values between wet and dry regions, as well as those between wet and dry seasons, will increasingly become important. According to the projection data generated from CMIP5 models, under the high GHG emission scenario, the precipitation in almost all the regions of Canada will increase. The extent of increases in precipitation will progressively increase from the southwest to the northeast of Canada (Figure 2.1). In addition, in the future, extreme precipitation will also increase with increases in temperature (Intergovernmental Panel on Climate Change, 2013a).

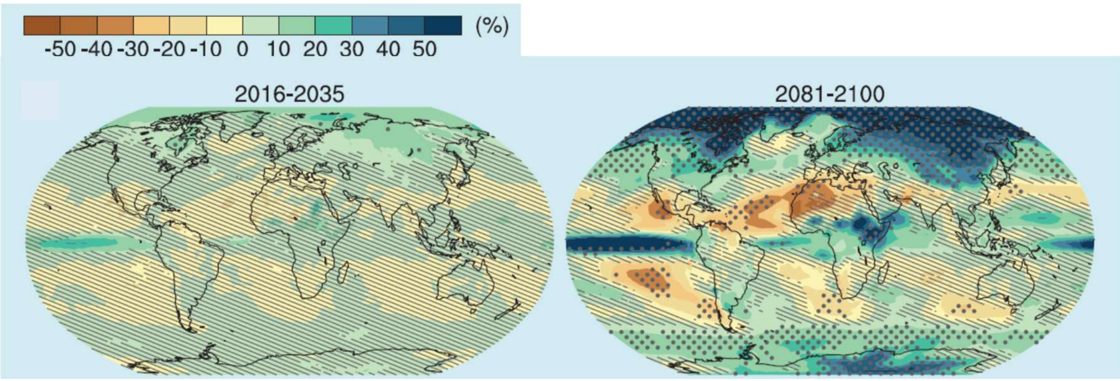

Figure 2.1 Projected change in precipitation for time periods 2016-2035 and 2081-2100, comparing to 1986-2005 derived from CMIP5 models (Intergovernmental Panel on Climate Change, 2013b).

In Canada's Changing Climate Report (Bush & Lemmen, 2019), possible changes of the key climatic parameters in Canada have been described, such as temperature and precipitation, snow and ice, freshwater availability, amongst other environmental factors. The generation of the future climate data, as well as the considerations that have been given during the generating process are also introduced in the report. The annual precipitation and the amount of precipitation during the winter season is expected to increase in all regions of Canada over 21st Century, as compared to the current historical period. A greater increase in precipitation is projected to occur in northern Canada, whereas the precipitation for southern Canada will decrease during summer under a high GHG emission scenario. With a low GHG emission scenario, the changes in precipitation will be very limited. The daily extreme precipitations are also predicted to increase for the projected climate scenarios.

The shift from snow to rain in spring and autumn is the primary reason for the increase in precipitations in Canada, as concluded by Jeong & Sushama (2018). Six simulations performed for two Canadian regional climate models (RCMs) considering median and high GHG emission scenarios have been used to characterize the rain-on-snow (ROS) events during future projected climate scenarios as well as its spatial patterns. The analysis suggests that the frequency of rainfall precipitations will increase in the future due to a warmer air temperature in northern Canada whereas rainfall will decrease to the south of the freezing line, due to a decrease in snow water equivalent (SWE). The rain-on-snow (ROS) runoff is also expected to increase for most regions of Canada, as the snowmelt process will be accelerated.

Several studies have investigated the impact of the changes in climate on the moisture performance of the building envelope. Nik et al. (2015) studied the changes in WDR load during future projected climate scenarios and the hygrothermal performance of building façades subjected to WDR load of such scenarios in Sweden. The future projected climate data were generated for 2021-2050 and 2071-2100 and the benchmark climate data were for 1961-1991. The WDR loads during the analyzed time periods were derived from the method given in the ASHRAE model (ASHRAE, 2016) and the driving rain coefficients. These coefficients were thereafter implemented to the hygrothermal simulation model to obtain water contents in the wall assembly. Moreover, the uncertainties as occurred in the process of generating the future projected climate data caused by global climate models, GHG emissions scenarios, and spatial resolutions were also investigated. It was concluded that the 30-year averaged water content would increase up to 13% in the future projected climate scenario with a 28% standard deviation. This study also concluded that for the climatic conditions considered, the potential changes in wind load would not affect significantly the WDR load. Other studies, considering the current experimental program, have found otherwise, and fluctuating wind load effects were taken into consideration when investigating the WDR load on wall assemblies.

Another study treating the WDR loads increase as a cause of future risks to heritage buildings in the UK was conducted by Orr et al. (2018). This work had used the UKCP09 Weather Generator to produce the future climate data for 2070-2099, under a high GHG emission scenario in UK. The WDR load deposited on the building façade was estimated using the semi-empirical model recommended by the ISO standard (ISO 15927-3, 2009). It was projected that the rain spell would have a higher volume of water at eight (8) analyzed cites for the future time period, although the occurrence of rain spells would remain constant. However, the duration of future rain spells would be shorter and the time period between adjacent rain spells would be longer. This work had concluded that the failure of building elements exposed to future climate would occur more frequently and would become more severe. Furthermore, the near-surface cycling and the deep-seated wetting for porous cladding materials would become more serious and frequent for all locations analyzed in this study.

For the future projected scenarios over Canada, Jeong & Cannon (2020) investigated the changes in moisture index which is usually considered in the design and management of the moisture performance of the building envelope (NRCC, 2015). For this study, an ensemble of 15 future projected climate data with different initial conditions was generated from the CanRCM4 (Canadian Regional Climate Model), a regional climate model of 50-km spatial resolution. The generated climate data were adjusted by a simple linear bias method, as the CanRCM4 model tended to overestimate wetting potential and to underestimate drying potential, the potentials being a measure of the durations of wet and dry weather conditions, respectively. The comparison was made for 1986-2016 and 2034-2064 under different emission scenarios. The results from the evaluation suggested that the moisture load over western and eastern coastal regions of Canada was projected to increase for the future climate scenario, whereas that over south-central and northern Canada would decrease

Many other studies focused on assessing the impact of climate change to the building envelope have been conducted (Gaur et al., 2019; Lankester & Brimblecombe, 2012; Nik, 2017; Sanderson et al., 2017) with evident conclusions that the changes in climate will affect the moisture load of the building envelope and thereafter have an impact on its long-term performance. From these aforementioned studies, it has also been determined that the precipitation over different regions of Canada will necessarily change for future projected climate scenarios but such changes will differ in relation to the region being considered. However, to permit understanding the extent of impact of climate change loads on the building envelope, further and more comprehensive studies are nonetheless still necessary

2.2 WDR load on the building façades

The WDR load is the amount of rain that is deposited onto the vertical surface of wall assemblies during a rain event. Assessing the WDR load can be completed through several methods, including the use of: semi-empirical equations, field measurements, and Computational Fluid Dynamic (CFD) numerical simulations. Each of these methods has its advantages and limitations.

The most recognized semi-empirical equation (Eq. 2.1) for which all the necessary factors for estimating the WDR load are considered, was established by Lacy (1977):

$$WDR = \alpha \times v(\mathrm{z}) \times i_h^{0.88} \times \cos(\theta) \tag{2.1}$$

Where, α is the WDR coefficient (s/m), $v(z)$ is the wind velocity at height z, i_h is the horizontal rainfall intensity and θ is the attack angle between the wind and the wall surface. In 2000, Straube & Burnett (2000) modified the equation (Eq. 2.1) by taking the effects of building geometry into consideration:

$$WDR = RAF \times DRF \times \cos(\theta) \times V(h) \times r_h \tag{2.2}$$

Where RAF represents the rain admittance factor, values of which range from 0.3 to 1.0 depending on the building geometry. The *DRF* is the driving rain factor calculated as $1/Vt$, and Vt is the raindrop terminal velocity. The angle of the incoming wind speed to the wall surface is θ, where $V(h)$ is the wind velocity at a height h and r_h is the horizontal rainfall intensity. Moreover, as given in ISO standard (ISO 15927-3, 2009) the wind-driven rain load is estimated as following:

$$I_A = \frac{2}{9} \times \sum v \times R_h^{8/9} \times \cos(D - \theta) \tag{2.3}$$

And

$$I_{AW} = I_A \times C_R \times C_T \times O \times W \tag{2.4}$$

Where v is the hourly mean wind speed at the given height, R_h is the hourly rainfall intensity, D is the angle between hourly wind speed directions to the north, and θ is the wall orientation in regards to the north direction. To assess the wind-driven rain load on the building façade, a few more factors must be considered based on the wind-driven rain load in the airfield; these include: terrain roughness coefficient C_R, topography coefficient C_T, obstruction factor O and wall factor W. These factors are individually determined for each case being investigated. Comparing Eq. (2.1) to Eq. (2.2), it can be noticed that the ISO standard additionally considers the effect of terrain roughness, topography, nearby obstructions and the wall assembly on the wind-driven rain load.

As evident, the characteristics of the raindrop, building geometry, wind velocity, wind direction and wind angle with the building façade are considered in the formulation of these semi-empirical functions. Once these parameters are determined, the wind-driven rain load can be derived from these equations, and thereafter this can be used as input to the watertightness experimental test. However, according to numerous studies (Blocken & Carmeliet, 2004; Ge et al., 2017, 2018; Kubilay et al., 2014), the wind-driven rain load derived from semi-empirical Eqs. (2.2) and (2.3), are inconsistent with the results derived from field measurements. The WDR load determined from the field measurements is achieved by installing rain gauges on a building façade, or a number of façades. Together with other measured parameters, such as temperature, relative humidity probes and wind anemometers, the WDR load can be determined whilst considering recorded rain intensity, wind velocity, wind direction, building geometry and the surroundings. As compared with other methods used to measure the WDR, this method is the most realistic approach because it involves the entire process of exposing the building to realistic rain events. On the other hand, the results derived from field measurements of WDR are significantly impacted by the temporal resolution due to the rapid changes in wind direction, wind velocity and rain intensity, during a rain event (Blocken & Carmeliet, 2005). Moreover, the randomness of environmental conditions occurring in the field makes it challenging to replicate all these conditions in a test environment, such as in a laboratory.

Computational approaches are now widely used to solve building envelope problems. For example, in respect to WDR loads acting on buildings, a steady-state numerical simulation model for WDR was developed by Choi (1993). The wind action in this model was governed by the Reynolds-Averaged Navier-Stocks (RANS) equation and the raindrops were simulated by a Lagrangian particle tracking (LPT) model. The implementation of this technique requires an iteration process to identify the location used to input the raindrops to ensure that the simulated building façades are fully covered by the simulated WDR load, given that the movement of raindrops is affected by the wind flow during the simulation.

Thereafter, Blocken & Carmeliet (2002) improved Choi's approach by adding the temporal component to this model for investigating the variations of WDR load as a function of time. Huang & Li (2012) proposed using the Eulerian Multiphase (EM) model for WDR simulations as the EM model provided more accurate WDR results on the windward façade of a building. This technique considers wind and rain as different phases that can be set up at the beginning of a simulation regardless of the coverage area of the wind-driven rain. Therefore, comparing results obtained from the LPT model to that of the EM model needs much less time given that the iterative process has been omitted

A series of field WDR measurements were conducted by Ge et al. (2017) at three different regions in Canada, namely: Fredericton, on the east coast, Montreal, in Eastern Canada, and Vancouver, on the west coast. The range of building heights which were part of these studies was from 19.8 m (Vancouver) to 45.6m (Montreal). Instrumentation to acquire the field measurements were installed on the roofs and vertical façades of the test buildings; typically, these included a wind anemometer, temperature and relative humidity probes, horizontal rain gauge and numerous customized driving rain gauges.

The locations of the driving rain gauges were selected by considering the prevailing wind direction, building geometry and building surroundings. Values from the field measurements obtained for the catch ratio (ratio of the amount of water collected from the measurements to the theoretical amount of water deposited on the building) matched well with the classic wetting pattern on the building façades. A higher catch ratio was obtained at the top of the façade as compared to the lower part of a building, where smaller catch ratio values were found. As expected, the catch ratios were different for each of the buildings investigated; one of the reasons for such differences was the different geometries of the respective buildings, which had different aspect ratios, and as such, these buildings generated "wind blocking effects", unique to each building geometry and its surroundings. In addition, the catch ratios also varied with the wind speed, wind incidence angle and rain fall intensity. The wind speed in particular, was positively correlated with the catch ratio, whilst the wind incidence angle and rainfall intensity were negatively correlated with the catch ratio. The wall factor, as a function of wind speed, incidence angle, and rainfall intensity was also investigated. In general, the WDR load predicted using the ISO standard semi-empirical model (Eq. 2.3) was found to be greater than the WDR load measured in the field. This was due to the significant discrepancies between the values for wall factors as prescribed in the ISO standard (ISO 15927-3, 2009) and the values for wall factors as measured in the field.

Blocken & Carmeliet (2005) performed field WDR measurements on a full-scale building (VLIET) at the Katholieke Universiteit Leuven located in Belgium. The building was initially designed for investigating energy efficiency, hygrothermal behavior and the durability of building components. Through this study, it was determined that WDR was one of the most critical boundary conditions affecting the building. Wind-driven rain gauges (Figure 2.2) were installed on protruding and recessed façade parts of the test building. The gauges were fabricated using PMMA (polymethyl-methacrylate) and each gauge had a 0.2 x 0.2m^2 collection area that gathered precipitation into reservoirs through tubes that connected these gauge elements. To acquire the high-resolution spatial information, a high number of WDR gauges were installed across the façade. In addition, to generate the wind profile information a meteorological mast equipped with 3 cup anemometers, as well as an ultrasonic anemometer, were located 20 m away from the south-west façade of the test building. A rain gauge tube surrounded by a circular turf wall was used to record the rain intensity. The turf wall was used to avoid the "wind error" caused by the sudden increase in vertical wind speed at the windward roof edge of the gauge body. Six rain events were found to be suitable for the WDR load assessments; these occurred over a 7-month period during which the experiments were completed. Initial data was selected for mitigating the errors caused by the adhesion-water-evaporation phenomena, evaporation of water from reservoirs, raindrop slashing and wind direction. Moreover, the fluctuations of wind speed, wind direction and rain intensity in cumuliform and stratiform rain events were also reviewed. It was found that stratiform rain events had more stabilized WDR conditions than that of cumuliform rain events. The processed results for WDR load measured in this study were compared to those obtained from the semi-empirical equation (Eq. 2.1) established by Lacy (1977), however only rough matches were observed from this comparison.

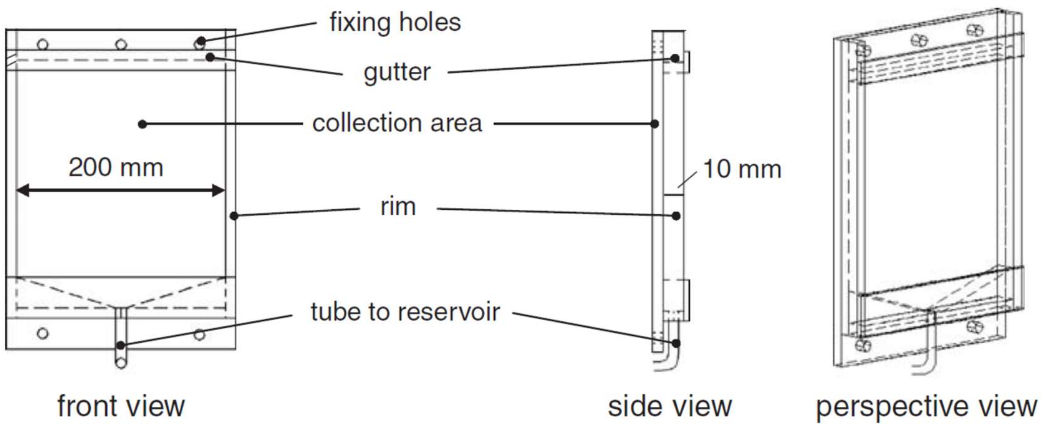

Figure 2.2 Wind-driven rain gauges designed, manufactured and installed at the Laboratory of Building Physics, Katholieke Universiteit Leuven (Blocken & Carmeliet, 2005).

As previously mentioned, the results derived from CFD simulations can also provide WDR information using either a Lagrangian particle tracking (LPT) model or an Eulerian Multiphase model.

Khalilzadeh et al. (2019) performed a CFD simulation for determining WDR on a mid-rise building using the LPT model and they investigated the differences in the results obtained from the CFD simulations that applied different turbulence models for the wind modeling. Turbulence models used in this study included: (i) Realizable k-ε; (ii) standard k-ω, and (iii) k-ω SST in conjunction with log-law and power-law inlet wind velocity profile information.

The k-ε model was useful for predicting the WDR far from the simulation boundaries (i.e. wall) whereas the k-ω model provided better WDR prediction in close proximity to the boundary of the wall, even though this is dependent on the dimension Y+. The k-ω SST model is a combination of both, k-ε and k-ω models. The wind flow pattern in the k-ω SST CFD modeling was validated by wind tunnel tests and WDR results were determined as the catch ratio compared with the field measurement results. To maintain the wind velocity profile, the Y+ value should approach the roughness height value Ks given a two-equation turbulence model. The surroundings had a small impact on the object of study. As a mean of saving computational costs the simulation was implemented using a stand-alone building model given that the upper portion of the façade of the building was the primary concern. The discrepancies between the flow velocity, caused by different turbulence models, and the inlet velocity profiles were less than 5%. Subsequently, the differences in catch ratio values, derived from flow velocities, were negligible. For the WDR simulation, the CFD model was only reliable at the upper and edge portions of the windward façade, as compared with the WDR measurement results obtained in the field; large discrepancies in catch ratio values were found at the center and the lower regions of the façade. For a stand-alone mid-rise building located in a suburban terrain, the standard k-ω model with a log law inlet velocity profile could better mimic the WDR. For a surrounded structure in the same terrain, no significant difference between the results was noticed when using different CFD models. Two-equation turbulence models together with the inlet velocity profile, could simulate the top half portion of the mid-rise building situated in a suburban area within a 20% error for wind speed and 25% error for WDR, as compared to the wind velocity and WDR values obtained from field measurements.

Another study conducted by Blocken & Carmeliet (2005) compared the WDR results obtained from a field measurement and the corresponding CFD simulation to validate techniques used in the simulation. In this instance, however, the Lagrangian particle tracking (LPT) model was used to simulate the WDR load on building façade. The wind flow pattern was solved using a k-ε turbulence model together with the RANS equations. For this WDR modeling exercise, the authors followed the rain-drop distribution proposed by Best (1950) and they neglected the turbulent dispersion of raindrops in the air. For comparison, three rain events were selected from the field measurement database. Rain events 1 and 2 were cumuliform rain events, and rain event 3 was a long stratiform rain event. The wind direction of these rain events was approximately perpendicular to the façade of the test building. In addition, measurement errors of these events, due to the adhesion-water-evaporation phenomenon and water evaporation in the collection reservoirs were corrected, whereas the deviation in the results arising from the raindrop splashing was negligible owing to the low wind-speed in all rain events. Good agreement was observed between the simulation and the field measurement results, with the exception of the overestimation on that area of the building in the proximity to the sloped roof. The reason for such a discrepancy was determined as an air flow retarding effect resulting from a row of trees at the upstream region of the simulation. For future CFD validation studies, it was proposed that the WDR be investigated on different building configurations, WDR on groups of buildings, and WDR mapping over different topographic conditions.

2.3 Assessing moisture load in wall assemblies

The ASHRAE standard 160 (ASHRAE, 2016) suggests that the moisture load on the water-resistive barrier in a wall assembly be considered as 1% of the WDR load deposited onto the exterior surface of the wall assembly if no reliable full-scale tests results are available. At the same time, the watertightness test is an evident approach to estimating the degree of water entry through, and into the wall assemblies, based on replicating, the WDR conditions in a laboratory test facility with good approximation. At the National Research Council of Canada an extensive number of studies have been carried out, including, but not limited to, evaluating the water penetration for several different types of wall assemblies and wall components (Lacasse et al., 2003; Moore & Nicholls, 2014; Saber et al., 2014; N Sahal & Lacasse, 2004; Nil Sahal & Lacasse, 2005).

One of the tasks of the Moisture Management for Exterior Wall Systems (MEWS) project (Lacasse et al., 2003) was to test 17 different wall assemblies, representative of a broad class of residential wall assemblies as could then be found in practice across Canada. Thus, the residential wall assemblies were grouped based on their cladding type that included: stucco, EIFS (Exterior Insulated Finish System), brick masonry veneer and vinyl siding. A "generic" wall assembly consisting of three layers of acrylic sheathing representing the exterior cladding, exterior sheathing panel and interior sheathing panel, was also tested as the "base case" wall. Each test in this study was carried out using a standard procedure that involved the following steps: (i) characterization of the air leakage and pressure equalization of the wall assembly; (ii)) applying 1.7L/min-m^2 and 3.4L/min-m^2 water deposition rates, coupled with static and dynamic conditions to the test specimens; (iii) applying 16 hours of water spray at 0.4 L/min-m^2 at 20 Pa, to mimic long term rain events; (iv) characterizing the effects of different wall assembly deficiencies at corresponding static and dynamic pressure conditions and varying water deposition rates. The static pressure steps used in the test were: 50 Pa, 75 Pa, 150 Pa, 300 Pa, 500 Pa, 1000 Pa and the dynamic pressure steps were: 75 Pa+40 sin(2πft) Pa; 150 Pa+60 sin(2πft) Pa; 300 Pa+125 sin(2πft) Pa and; 700 Pa+300 sin(2πft) Pa, where f represents the frequency and t represents the time in seconds. The dwell time for each step was 20 minutes.

Different types of wall deficiencies were intentionally built within the wall assemblies and were representative of deficiencies typically found on actual in-service wall assemblies. The types of wall components incorporated in the wall assemblies tested in this study, and those normally found in many of residential walls, included: ventilation ducts, electrical outlets and windows. Moreover, some deficiencies were also incorporated in the water resistance barrier to represent the inevitable imprecisions encountered in the real wall assembly construction. The water entry results were grouped based on the wall category and were analyzed for different pressure conditions and water deposition rates. These tests results can be analyzed to develop water entry functions unique to each type of wall assembly. For example, a water entry function was proposed based on the results obtained from a set of water entry test on a hardboard siding-clad wood stud wall (Sahal & Lacasse, 2005). Deficiencies of the wall assembly specimens were located at the ventilation duct, electrical outlet and the wall-window interface. Water collection troughs and pressure taps were distributed across the wall assembly for the collection of water entering the assembly and for measuring pressure variations across the wall, respectively. Five water deposition rates and six pressure steps were applied during the test and each pressure step lasted 10 minutes. Three air leakage conditions were characterized based on the area of the air leakage opening and the pressure difference. The water entry function was established as:

$$Q = m_p \times R_p \tag{2.5}$$

Where Q is the water entry rate (L/min), m_p is the water entry potential (L min^{-1}/ L min^{-1} m^{-2}) and R_p is the applied water deposition rate (L/min.m^2). The value of m_p was expressed as a function of static pressure difference acting across the wall. From these results the water entry potential of the hardboard siding-clad wall at the ventilation duct was defined as:

$$m_p = 3\,E^{-11}\,(\Delta P)^3 - \,8\,E^{-7}\,(\Delta P)^2 + 5\,E^{-5}\,(\Delta P) + 0.0123 \tag{2.6}$$

Where ΔP is the pressure difference and E represents the powers of 10. Besides the characterization of the water entry rate to wall assemblies, test specimens can also be subjected to watertightness tests that might be used to investigate the causes of the water infiltration into the wall.

Bossche et al. (2015) performed a test to assess the watertightness of curtain wall systems (Figure 2.3). The complexity of the curtain wall systems, arising from thermal and mechanical design requirements, makes it effectively impossible to prevent water ingress over time in all circumstances. In this work, a full-scale curtain wall system was subjected to a range of static and dynamic pressure differences. The testing protocol that was used was prescribed in EN12155 (2000) standard for static pressure steps and EN12865 (2001) for cyclic dynamic pressure steps. The testing specimen was an aluminium stick curtain wall system incorporating with a turn-and-tilt window, a tilted transom and different types of T-connections. Overall dimension of the sample was 3m x 4m. The specimen was classified as very airtight and the airtightness was measured before and immediately after the test. The water infiltrations were recorded at the following pressures and locations for static pressure steps: 450 Pa at the junction of the mullion and lower transom, 705 Pa at the junction of the mullion and lower transom and 900 Pa at lower right corner turn and tilt window. For the cyclic dynamic pressure steps, the water infiltrations were found at: 0-300 Pa at junction mullion and lower transom, 0-450 Pa at lower right corner turn-and-tilt window, 0-750 Pa at lower left corner turn-and-tilt window. The results indicated that this curtain wall system appeared to be sensitive to water infiltration. The results did not provide a clear correlation between the water entry rate and the pressure difference, which indicated that the hydrostatic pressure exerted by the runoff film caused the water ingress for the curtain wall system. However, under the cyclic pressure test conditions, more water infiltration was observed in these tests.

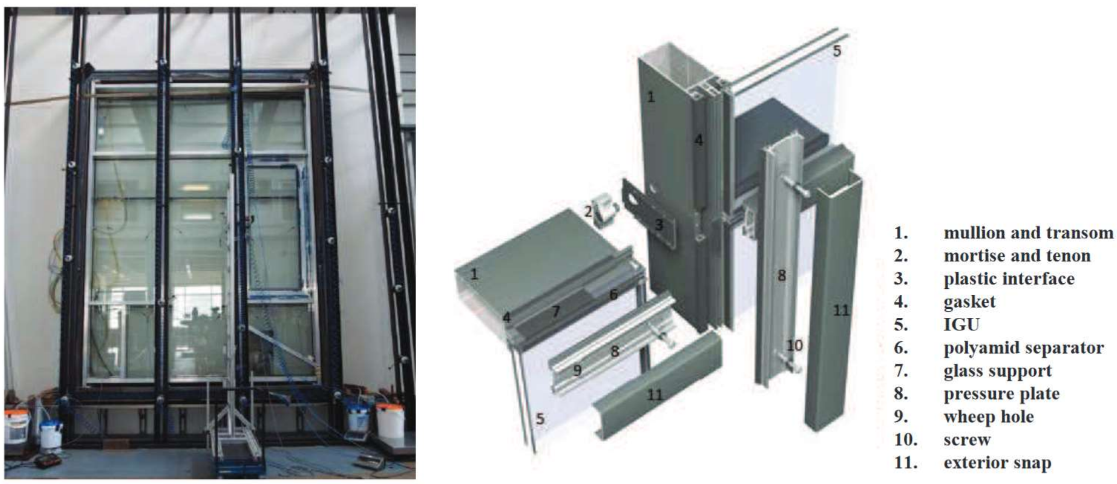

Figure 2.3 Compositions of curtain wall system (Bossche et al., 2015).

The WDR effects are simulated using different apparatus in the laboratory. A review is provided that includes a brief description of some of the existing dynamic watertightness test facilities as could be found in research laboratories worldwide. The Construction Research Laboratory (Figure 1.3), in Miami, uses an airplane engine to generate the wind and turbulence which is applied to the test specimen and a water spray rack provides water up to a spray rate of 3.4 L/min.m^2. The standard dynamic test protocol AAMA 501-83 (AAMA 501-83, 1983) was adopted by this laboratory. The test protocol AAMA 501-83 was subsequently modified by the Centre for Windows and

Cladding Technology in Bath, UK where the protocol requires 25% of pressure applied as negative pressure and 75% applied as positive pressure.

Taywood Engineering Limited, UK has also used an airplane engine to generate high wind speeds and likewise has used the AAMA 501-83 dynamic test protocol for its facility. The amount of deflection of the test frame was used to determine the pressure applied to the specimens.

The Building Research Establishment located in the UK has a cladding watertightness testing facility located in Bedfordshire. In this facility, the air pressure applied to the test specimen (maximum size 4m x4m) is generated by a three-phase axial air blower with a 600mm diameter rotor, capable of delivering $5m^3/s$ of air to the test chamber. The interior surface of the test specimen is installed inside the test chamber that can generate ± 3,500 Pa static pressure, and 50 – 1,000 Pa cyclic dynamic pressure. The flow velocity at the center of the duct can reach 22m/s and no less than 10m/s for the entire area of the specimen. The runoff film can be redirected and interrupted by the airflow at 8m/s. When the airflow reaches 14m/s, the water is distributed to all the directions (including upwards). The water deposition rates range from 1.2 to 4.0 L/min. m^2.

The Norwegian Building Research Institute in Trondheim (RAWI-BOX) employs the water spray method based on the EN86 (1980) standard, which requires an overall water spray rate of 2.1L/ min-m^2 and that consists of 1.7L/min-m^2 runoff water, located at the top of the test specimen, and 1.7L/min-m^2 water spray. Airflow generated from air jets affront of which water droplets are released into the jet of air permits simulating WDR effects. The pressure chamber is capable of generating up to 1,100 Pa of dynamic pressure, while the maximum specimen size is 2.45m x 2.45m.

The commercial enterprise Permasteelisa SpA located in Italy can test specimens of up to 8.3m height and 8m width. The airflow is created by an airplane engine, which can be moved from 2m to 5m above the ground; the maximum airflow velocity generated by the engine is 55m/s. A pressure chamber encloses the interior surface of the specimens where 5,900 Pa positive and negative pressures can be attained. The dynamic pressure range is ± 2,000 Pa. The water deposition rates range from 2.0 L/min.m^2 to 5.4 L/min.m^2. The testing procedure used at Permasteelisa follows the protocol given in AAMA 501-83.

The SIROWET test, as developed in Australia (Sankaran et al., 1996), uses a watertightness test protocol that requires not less than 3 L/min.m^2 for the rate of the water deposition to the test specimen. The applied pressure includes the following stages: Stage 1: 150 to 300 Pa; Stage 2: 300-600 Pa; Stage 3: 0.3 Wp to 0.6 Wp (Wp: serviceability design wind pressure). Dwell time for each tests stage is not less than 5 minutes.

Some common requirements to which a dynamic test should comply, can be summarized as follows: (i) curtain wall deflects and recovers under wind gust strikes; (ii) rain on the façade is driven by the air flow; (iii) both wind and rain actions have a dynamic behavior, applied to the façade randomly or with certain frequencies; (iv) the wind gust has to envelope the entire specimen to simulate realistic boundary conditions.

As setup, in which all these requirements are met is, however, both energy and cost – demanding. Also, air flow and turbulence induced by the airplane engine is not reproducible in different other test facilities. Moreover, the flow conditions on the façade are not uniform. Thus, it is difficult to quantify the effects of these different factors using these facilities and a comparison of results from different facilities is problematic and represents a significant challenge.

There are several factors to consider in the preparation of a test protocol for dynamic watertightness testing. The European standard dynamic watertightness test for curtain walling was established by Mayo (1998) for which, initially, the WDR conditions were characterized by identifying the range of combined wind speed and rainfall intensity in Europe. Short term data on simultaneous wind velocity and rainfall intensity was collected to predict the conditions that curtain walls can encounter during their life span. The pressure value of the protocol was derived from the corresponding wind speed. The collected wind speed was categorized into 3 ranges:

- low wind speed: 4.2-4.3m/s equivalent to 11-11 Pa;
- high wind speed: 12 – 25.9m/s equivalent to 324-412 Pa; and
- moderate wind speed: 13.7-15 m/s equivalent to 115-138 Pa.

The subsequent pressure steps used for the tests were: 50 Pa, 100 Pa, 200 Pa, 300 Pa and 400 Pa. The water deposition rate was obtained from collecting 1 minute averaged and 5 minutes averaged rainfall data for 10-year and 30-year return periods. Lacy's (1977) equation (Eq. 2.1) was used to calculate the rainfall on the wall surface and horizontal surfaces. Most tests for rainfall on vertical surfaces were performed from moderate rainfall events, whereas the highest rainfall rate was 204mm/h and the equivalent deposition rate to the test specimen was 3.4L/min.m^2.

2.4 Hygrothermal simulations

To permit understanding the moisture performance and the response of materials forming part of a wall assembly to in-situ environmental conditions, different environmental parameters must be assessed, at different locations within the wall assembly including: the relative humidity, temperature and moisture content. These parameters can be directly measured in a real wall assembly using different apparatus (Hamid & Wallentén, 2017; Jensen et al., 2020; Kordziel et al., 2020; Soulios et al., 2021; R. Wang et al., 2020). However, such measurements are not practical for long-term and multi-location assessments, nor for walls as may be subjected to projected future climate loads. Another universal method to assess the hygrothermal performance of wall assemblies is to undertake hygrothermal simulations using Heat-Air-Moisture (HAM) simulation tools, which are capable of replicating the transport of heat, air and moisture within the modelled wall assemblies whilst considering the effects from climate and interior environmental loads acting on the wall.

By 1996 (Hens, 1996), at least 37 different numerical tools for hygrothermal simulations had been developed by researchers worldwide. Later, Straube & Burnett (2001) provided a detailed review of the most commonly used HAM models at that time and summarized the needs for conducting hygrothermal analysis as follows: investigating the response of the enclosure (building envelope) to the environment, identifying the performance of materials, and quantifying the energy flow through the enclosure. In the model developed by Cunningham (1990), vapour diffusion and convection were consided the only mechasim for moisture transport. This extensively simplied model was validate from laboratorey tests (Cunningham, 1990b); however, this model could not be applied to porous materials, given that the model did not consider the capillary action in such materials. The WALLDRY model (Schuyler et al., 1989) was developed to simulate the drying of wall assemblies by considering vapour diffusion as the only moisture transport mechanism. The TRATMO model developed by Kohonen (1984) was one of the first relatively complete models that used both the vapour pressure and temperature as the driving potentials for moisture tansport. A one dimentional model, MATCH (Pedersen, 1992), used sorption and suction curves to determine the mositure storage in materials. For hygroscopic regions, the sorption isotherm was used and moisture transport was driven by vapour pressure only. The MOIST model (Burch et al., 1989) was very similar to the MATCH model in many aspects. The moisture transport was driven by the vapour pressure and capillary transport by capillary pressure. Also, the moisture content was determined by both the vapour permeability and hydraulic conductivity. No moisture storage capacity was considered for fibrous materials and no air-leakage could be modelled in this model. The TCCD2 model developed by Ojanen and Kohonen (1989) was a two-dimentional model focused on anlyzing wall frames. As compared to an earlier version, the diffusivity in this model was depenent on the moisture conent. The TCCD2 model is able to reveal the influence of convection ariflow in resepct to hygrothermal performance (Kohonen, 1985). FSEC was a comprehensive model (Kerestecioglu et al., 1989) which was capable of modelling all moisture trasnport mechanisms. The vapour pressure and capillary suction in this model were used as the driving potential for vapour and liquid water. However, this program requires extensive knowledge of hygrothermal properties to operate. A Windows-based software WUFI developed by Künzel & Kiessl (1996) was a realiable and robust model validated by long-term field tests which was able to incorporate the effects from driving rain deposition as a boundary condition. Also, different liquid diffusivities were implemented for the wetting and drying processes respectively. However, this version of the model does not deal with air-leakage. The LATENITE model (Karagiozis & Solonvaara, 1994) was considered as one of the most sophisticated models when it was first dveloped in the ealry 1990s which was capable of completing one, two and three dimentional simulations. This model was not validated by field tests but proved to be reliable for results of relevent projects. More recently, Delgado et al. (2010, 2013) collected and reviewed 57 HAM models. Although, many HAM models have been developed, only a few commercial HAM models are accessible to the public. These include WUFI, DELPHIN and COMSOL Multiphysics software packages are considered the most commonly used commercial HAM models that are widely used by practitioners across the world (Defo et al., 2021).

Hygrothermal simulations were used to investigate the effects of air-leakage on the moisture performance of wood frame wall assemblies by Wang and Ge (2017). The air-leakage was modelled using the air convection and air infiltration methods and was applied to three types of wall assemblies having different insulation details. The simulations were validated by the field measurements and the results suggested a good applicability of two air-leakage modelling methods with appropriate setups. In this study the risks of mould growth for wall assemblies having different types of insulation were also investigated. Specifically, wall assemblies having cellulose fiber we shown to have a lower risk to mould growth than those using fiberglass and the exterior insulated wall assembly was demonstrated to be free from condensation and mould growth.

Jensen et al. (2020) assessed the hygrothermal performance of four insulation systems used for the retrofitting solid masonry walls from the interior; the building was located in Lyngby, Denmark. The numerical simulations for the four insulation systems were calibrated by 2-4 years of field measurements and was further used to evaluate several more design variations such as assemblies incorporating different mortars and types of brick masonry, having different thickness of masonry and insulation products, and as well, assemblies for which the indoor moisture levels varied. Such benchmarking results permit assessing the impact of the future projected climate on the moisture response of such wall assembly types. The simulation results suggested that reducing the indoor moisture level could be beneficial to the hygrothermal performance of the interface between wall and insulation. The increase in thickness of the masonry wall would worsen the hygrothermal performance for the interface as a result of a longer drying time for existing moisture, whereas a greater thickness of masonry wall would improve the hygrothermal performance if the initial moisture load was low. A greater relative humidity was observed for mortar of high cement content and the brick type had no significant effect to the relative humidity level. Only two insulation systems were found to be robust to future climate loads with exterior hydrophobisation.

Attics of buildings located in extreme cold climate regions might be subjected to moisture related issues due to moisture built-up from indoor air and fully-sealed construction. To provide design recommendations for reducing moisture risks in attics, Wang et al. (2020) investigated the impact of the attic ventilation rate, ceiling air-leakage rate, and un-intentional air infiltration rate on the moisture performance of attics using hygrothermal simulations. The hygrothermal models were firstly validated by field measurements and parametric studies thereafter followed. The performance was determined by determining the values of mould growth index on the sheathing. No risk to mould growth was found in the attic with ventilation, whereas for an un-ventilated attic, the mould growth index was positively correlated to the ceiling air-leakage rates and negatively correlated to the un-intentional air infiltration rates. The conclusions from this study suggested that ventilation was a favourable choice, as compared to lack of ventilation in the attic.

2.5 Moisture in wall assemblies

It is evident that the moisture load is the cause of many problems in building envelope enclosures. Considering the high number of applications, the total impact of those problems is both unfortunate and costly (Desjarlais et al., 2001). The building envelope is designed to prevent changes in the exterior environment, including moisture, from affecting the indoor environment of the building. Unintended moisture-related problems can accelerate the deterioration of building envelope performance, as more moisture could infiltrate the envelope, given a building envelope of already diminished performance. A survey of building envelope failures in British Columbia conducted by Rousseau (1999) found that almost all the reported problems occurred at windows, decks and penetrations in the walls, where water could not be drained or could not dry sufficiently fast. In this survey 46 low-rise wood-frame residential buildings were investigated and it was found that 37 had experienced moisture related problems. The surveyed buildings were at least 8 years old and the reported problems required over 10,000$ to repair for each building.

For different types of wall assemblies and different materials that constitute the building envelope, moisture-related damages are correspondingly different. Regarding masonry walls, the interior surface can be exposed to mould growth due to excessive moisture caused by capillary action (Abuku et al., 2009; Teasdale-St-Hilaire & Derome, 2007). The glassy phase of bricks dissolves when subjected to acid rain and the calcareous components of mortar also react to acid (Charola & Lazzarini, 1986). The soluble salts obtained from these reactions are transported into the porous space of the masonry from the presence of rain water or condensed moisture. After the water evaporates, these salts accumulate in the masonry and result in mechanical disruption of the material. Other problematic phenomena arising from water in porous materials includes, but is not limited to: frost damage on wall surfaces (Van Balen, 1996); erosion of building surfaces caused by WDR (Tang et al., 2004); and, efflorescence of surface materials (Franke et al., 1998).

For wood-frame wall assemblies, both mould and decay can occur when wood components are continuously exposed to a humid environment (Chouinard & Lawton, 2001; Nofal & Kumaran, 2011). Mould growth is a sign of excessive moisture loads and its presence affects the appearance of the surface of materials. If mould is directly exposed to indoor air, it can also adversely affect the indoor air quality. To permit describing the development of mould growth, Hukka and Viitanen (1999) developed a mathematical model based on experimental data (Hannu Viitanen, 1996; Hannu Viitanen & Ritschkoff, 1991). The severity of mould growth was expressed as the mould index calculated from the mathematical model and its value ranged from 0 (no mould growth) to 6 (heavy mould growth with 100% coverage). The most recent version of the mould growth model (Ojanen et al., 2010) had been included in the ASHRAE standard 160 (ASHRAE, 2016) as a moisture performance criteria. It is suggested in the ASHRAE standard 160 that for the materials being analyzed, the mould index must be lower than 3 to have an acceptable moisture performance given that one can visually detect mould growth above this threshold value.

The mould index is calculated from equation 2.6 (ASHRAE, 2016):

$$\mathrm{M}_t = M_{t-1} + \Delta M \tag{2.6}$$

Where, Mt is the mould index for the current hour and M_{t-1} is the mould index for the previous hour. The change of mould index, ΔM, for each hour is determined based on the values of temperature and relative humidity of the component. When a wood component is exposed to both favourable temperature and relative humidity conditions, the ΔM is a positive value. Otherwise, the mould index declines. The calculation of the mould index is also affected by the sensitivity class of the material component. The required relative humidity for mould growth in sensitive materials is lower than that for less sensitive materials.

Compared to the mould growth of which only causes damage to the surface of materials, wood decay fungi on the other hand are able to deteriorate the mechanical properties of wood materials. The strength loss of wood structural members due to the fungal attack could bring important consequences to the structural integrity of the member (Hansen et al., 2020). The decay of wood building materials has been widely observed in both European and North American cities (Nofal & Kumaran, 2011). Viitanen (1997) and Viitanen & Bjurman (1995) investigated the damage of fungi species prevalent in European cities of both Norway spruce and Scots pine wood elements. Duncan & Lombard (1965) have identified different fungus located in the USA, which are able to cause decay damage to building materials including: Antrodia serialis, Antrodia vaillantii, Coniophora puteana, Gloeophyllum trabeum, Meruliporia incrassata, Postia placenta, Sepula lacrymans, and Tapinella panuoides. However, no comprehensive studies have been conducted to determine the range of wood-decay fungi species prevalent in Canada although Morris (1998) has suggested that those fungi species found in the USA may also commonly exist in Canada.

When investigating the nature and extent of wood decay through experimental studies, the weight loss of wood materials is typically used as an assessment criterion; for the fungus to survive and grow it consumes and thus induces weight loss in the wood material. At the early stage of decay, however, the weight loss cannot be detected (Nofal & Kumaran, 2011). Nonetheless, most researchers still use weight loss as an indicator to develop mathematical models for the advance of damage due to wood decay (Saito, 2017; Saito et al., 2012; Schmidt et al., 1983; H. Viitanen et al., 2010; Hannu Viitanen & Bjurman, 1995). The Japanese decay model (Saito, 2017; Saito et al., 2012) was developed based on the mass loss rate of wood samples under brown rot fungus. The decay process was initiated when the relative humidity was above a critical value of 98%; the mass loss rate was then calculated based on the temperature.

As compared to the Japanese wood decay model, the decay process used the VTT model (H. Viitanen et al., 2010) considers two process stages. The first stage is the activation process. The wood material is exposed to concurrent levels of relative humidity and temperature that are above threshold values for a critical period of time prior to the onset of mass loss. The critical time is a function of relative humidity and temperature. If any dry conditions occur over the activation process, the required exposure time is extended. During the mass loss process, which is also the second stage of the decay process, the temperature and relative humidity on the material should also be above threshold values; these are 0°C and 95% respectively. After being exposed to dry condition for prolonged period of time, the mass loss process stops; however, this loss in mass is considered irrecoverable.

2.6 Research knowledge gap

Based on this review of pertinent literature, it is evident that precipitations will very likely increase for the future projected time periods in most regions of Canada under a changing climate. The moisture performance of wall assemblies subjected to the environment conditions imposed by the changing climate will not be the same as for those exposed to previous climate conditions, as have occurred over the past years. Several studies have investigated the changes in WDR, as well as their potential effects on the moisture performance of wall assemblies. However, a part of those studies has been based on indices that describe the ambient environment to which wall assemblies are subjected to. The performance of wall assemblies using such indices cannot be accurately assessed. Although, in other studies the changes in the hygrothermal parameters in wall assemblies were investigated for future projected time periods, the moisture load as was implemented to the simulation models, was based on assumptions and characteristics of the regional climate of another country and thus, was different from the climate as occurs in Canada. Therefore, there is a need to address this research gap.

Experimental inputs for existing watertightness tests did not consider the distribution in magnitude of WDR in the atmosphere, nor WDR conditions as they occur in Canadian climate. Consequently, results obtained from existing watertightness tests were not sufficiently accurate to establish a relationship between the WDR conditions and the moisture load applicable for wall assemblies in Canada. Also, existing water entry functions can only estimate the moisture load of wall assemblies when subjected to certain WDR intensities (water spray rates). This is not applicable to a changing and random climate dataset. Moisture loads used in hygrothermal simulations are usually estimated as 1% of the WDR load (ASHRAE, 2016). However, according to observations from watertightness test, such an assumption is not accurate and could significantly affect results of a moisture performance assessment; different methods of estimating the moisture load need to be addressed.

2.7 References

AAMA 501-83. (1983). *Methods of Test for Metal Curtain Walls*.

Abdul Hamid, A., & Wallentén, P. (2017). Hygrothermal assessment of internally added thermal insulation on external brick walls in Swedish multifamily buildings. *Building and Environment*, *123*, 351–362. https://doi.org/10.1016/j.buildenv.2017.05.019

Abuku, M., Janssen, H., & Roels, S. (2009). Impact of wind-driven rain on historic brick wall buildings in a moderately cold and humid climate: Numerical analyses of mould growth risk, indoor climate and energy consumption. *Energy and Buildings*, *41*(1), 101–110. https://doi.org/10.1016/j.enbuild.2008.07.011

ASHRAE. (2016). ASHRAE standard 160P-criteria for moisture control design analysis in buildings. In *ASHRAE Transactions*.

Best, A. C. (1950). The size distribution of raindrops. *Quarterly Journal of the Royal Meteorological Society*, *76*(327), 16–36. https://doi.org/10.1002/qj.49707632704

Blocken, B., & Carmeliet, J. (2002). Spatial and temporal distribution of driving rain on a low-rise building. *Wind and Structures, An International Journal*, *5*(5). https://doi.org/10.12989/was.2002.5.5.441

Blocken, B., & Carmeliet, J. (2004). A review of wind-driven rain research in building science. *Journal of Wind Engineering and Industrial Aerodynamics*, *92*(13), 1079–1130. https://doi.org/10.1016/j.jweia.2004.06.003

Blocken, B., & Carmeliet, J. (2005). High-resolution wind-driven rain measurements on a low-rise building—experimental data for model development and model validation. *Journal of Wind Engineering and Industrial Aerodynamics*, *93*(12), 905–928. https://doi.org/10.1016/j.jweia.2005.09.004

Bossche, N. Van Den, Goethem, S. Van, Scharlaken, S., Sulmon, S., & Janssens, A. (2015). Watertightness and water management of curtain walls. *Watertightness and Water Management of Curtain Walls*, 431–438.

Burch, D. M., Thomas, W. C., Mathena, L. R., Licitra, B. A., & Ward, D. B. (1989). Transient Heat and Moisture Transfer in Multi- Layer, Non-Isothermal Walls—Comparison of Predicted and Measured Results. *Proceedings of Thermal Performance of the Exterior Envelopes of Buildings IV*, 513–531.

Bush, E., & Lemmen, D. S. (2019). *Canada's Changing Climate Report*. Government of Canada. http://www.changingclimate.ca/CCCR2019

Charola, A. E., & Lazzarini, L. (1986). Deterioration of Brick Masonry Caused By Acid Rain. In *ACS Symposium Series* (pp. 250–258). https://doi.org/10.1021/bk-1986-

0318.ch017
Choi, E. C. . (1993). Simulation of wind-driven-rain around a building. *Journal of Wind Engineering and Industrial Aerodynamics*, *46–47*(C), 721–729. https://doi.org/10.1016/0167-6105(93)90342-L
Chouinard, K. L., & Lawton, M. D. (2001). Rotting wood framed apartments-Not just a Vancouver problem. *Proc of the 8th Canadian Conference on Building Science and Technology*, 304–318.
Cunningham, M. J. (1990a). Modelling of moisture transfer in structures—I. A description of a finite-difference nodal model. *Building and Environment*, *25*(1), 55–61. https://doi.org/10.1016/0360-1323(90)90041-O
Cunningham, M. J. (1990b). Modelling of moisture transfer in structures—II. A comparison of a numerical model, an analytical model and some experimental results. *Building and Environment*, *25*(2), 85–94. https://doi.org/10.1016/0360-1323(90)90019-N
Defo, M., Lacasse, M., & Laouadi, A. (2021). A comparison of hygrothermal simulation results derived from four simulation tools. *Journal of Building Physics*, 174425912098876. https://doi.org/10.1177/1744259120988760
Delgado, J. M. P. Q., Barreira, E., Ramos, N. M. M., & de Freitas, V. P. (2013). *Hygrothermal Numerical Simulation Tools Applied to Building Physics*. Springer Berlin Heidelberg. https://doi.org/10.1007/978-3-642-35003-0
Delgado, J. M. P. Q., Ramos, N. M. M., Barreira, E., & de Freitas, V. P. (2010). A CRITICAL REVIEW OF HYGROTHERMAL MODELS USED IN POROUS BUILDING MATERIALS. *Journal of Porous Media*, *13*(3), 221–234. https://doi.org/10.1615/JPorMedia.v13.i3.30
Desjarlais, A. O., Karagiozis, A. N., & Aoki-Kramer, M. (2001). Wall moisture problems in Seattle. *Buildings VIII Proceedings, ASHRAE, 8p*, *July*.
Duncan, C. G., & Lombard, F. K. F. (1965). *Fungi associated with principal decays in wood products in the United States*. Dept. of Agriculture,. https://doi.org/10.5962/bhl.title.87851
EN12155. (2000). *Curtain walling. Watertightness. Laboratory test under static pressure*. CEN.
EN12865. (2001). *Hygrothermal performance of building components and building elements - Determination of the resistance of external wall systems to driving rain under pulsating air pressure*. CEN.
EN86. (1980). *Methods of testing – Windows – Part 2 Watertightness test under static pressure*. CEN.
Franke, L., Schumann, I., van Hees, R. P. J., van der Klugt, L., Naldini, S., Binda, L., Baronio, G., Van Balen, K., & Mateus, J. (1998). Damage Atlas: Classification and Analyses of Damage Patterns Found in Brick Masonry. In *Protection and Conservation of European Cultural Heritage, Research Report No. 8, Volume 2*. Fraunhofer IRB Verlag.
Gaur, A., Lacasse, M., & Armstrong, M. (2019). Climate Data to Undertake Hygrothermal and Whole Building Simulations Under Projected Climate Change Influences for 11 Canadian Cities. *Data*, *4*(2), 72. https://doi.org/10.3390/data4020072
Ge, H., Chiu, V., Stathopoulos, T., & Souri, F. (2018). Improved assessment of wind-

driven rain on building façade based on ISO standard with high-resolution on-site weather data. *Journal of Wind Engineering and Industrial Aerodynamics*, *176*, 183–196. https://doi.org/10.1016/j.jweia.2018.03.013

Ge, H., Deb Nath, U. K., & Chiu, V. (2017). Field measurements of wind-driven rain on mid-and high-rise buildings in three Canadian regions. *Building and Environment*, *116*, 228–245. https://doi.org/10.1016/j.buildenv.2017.02.016

Hens, H. (1996). *Final report task 1: Modelling common exercises. Summary reports. Annex 24, heat and moisture transfer in insulated envelope parts*. International Energy Agency.

Huang, S. H., & Li, Q. S. (2012). Large Eddy Simulations of Wind-Driven Rain on Tall Building Façades. *Journal of Structural Engineering*, *138*(8), 967–983. https://doi.org/10.1061/(ASCE)ST.1943-541X.0000516

Hukka, A., & Viitanen, H. A. (1999). A mathematical model of mould growth on wooden material. *Wood Science and Technology*, *33*(6), 475–485. https://doi.org/10.1007/s002260050131

Il Jeong, D., & Sushama, L. (2018). Rain-on-snow events over North America based on two Canadian regional climate models. *Climate Dynamics*, *50*(1–2), 303–316. https://doi.org/10.1007/s00382-017-3609-x

Intergovernmental Panel on Climate Change (Ed.). (2013a). Detection and Attribution of Climate Change: from Global to Regional. In *Climate Change 2013 - The Physical Science Basis* (pp. 867–952). Cambridge University Press. https://doi.org/10.1017/CBO9781107415324.022

Intergovernmental Panel on Climate Change (Ed.). (2013b). Long-term Climate Change: Projections, Commitments and Irreversibility Pages 1029 to 1076. In *Climate Change 2013 - The Physical Science Basis* (pp. 1029–1136). Cambridge University Press. https://doi.org/10.1017/CBO9781107415324.024

ISO 15927-3. (2009). *ISO 15927-3, Hygrothermal performance of buildings Calculation and presentation of climatic data Part 3: Calculation of a driving rain index for vertical surfaces from hourly wind and rain data*.

Jensen, N. F., Bjarløv, S. P., Rode, C., & Møller, E. B. (2020). Hygrothermal assessment of four insulation systems for interior retrofitting of solid masonry walls through calibrated numerical simulations. *Building and Environment*, *180*, 107031. https://doi.org/10.1016/j.buildenv.2020.107031

Jeong, D. Il, & Cannon, A. J. (2020). Projected changes to moisture loads for design and management of building exteriors over Canada. *Building and Environment*, *170*, 106609. https://doi.org/10.1016/j.buildenv.2019.106609

Karagiozis, A., & Solonvaara, M. (1994). Moisture Transport in Building Envelopes Using an Approximate Factorization Solution Method. *CFD Society of Canada Meeting*.

Kerestecioglu, A., Swami, M., Fairey, P., Gu, L., & Chandra, S. (1989). Modelling Heat Moisture and Contaminant Transport in Buildings: Toward a New Generation Software. *Professional Paper FSEC-PF-165-89, Florida Solar Energy Center*.

Khalilzadeh, A., Ge, H., & Ng, H. D. (2019). Effect of turbulence modeling schemes on wind-driven rain deposition on a mid-rise building: CFD modeling and validation. *Journal of Wind Engineering and Industrial Aerodynamics*, *184*(April 2018), 362–377. https://doi.org/10.1016/j.jweia.2018.11.012

Kohonen, R. (1984). Transient analysis of the thermal and moisture physical behaviour of building constructions. *Building and Environment*, *19*(1), 1–11. https://doi.org/10.1016/0360-1323(84)90008-8

Kohonen, R. (1985). Thermal Effects of Airflows and Moisture on Exterior Wall Structures. *Proceedings of Thermal Performance of the Exterior Envelopes of Buildings III*, 583–605.

Kordziel, S., Glass, S. V., Boardman, C. R., Munson, R. A., Zelinka, S. L., Pei, S., & Tabares-Velasco, P. C. (2020). Hygrothermal characterization and modeling of cross-laminated timber in the building envelope. *Building and Environment*, *177*, 106866. https://doi.org/10.1016/j.buildenv.2020.106866

Kubilay, A., Derome, D., Blocken, B., & Carmeliet, J. (2014). High-resolution field measurements of wind-driven rain on an array of low-rise cubic buildings. *Building and Environment*, *78*, 1–13. https://doi.org/10.1016/j.buildenv.2014.04.004

KÜNZEL, H. M., & KIESSL, K. (1996). Calculation of heat and moisture transfer in exposed building components. *International Journal of Heat and Mass Transfer*, *40*(1), 159–167. https://doi.org/10.1016/S0017-9310(96)00084-1

Kvist Hansen, T., Feldt Jensen, N., Møller, E., Jan de Place Hansen, E., & Peuhkuri, R. (2020). Monitored conditions in wooden wall plates in relation to mould and wood decaying fungi. *E3S Web of Conferences*, *172*, 20004. https://doi.org/10.1051/e3sconf/202017220004

Lacasse, M. A., O'Connor, T., Nunes, S. C., & Beaulieu, P. (2003). Report from Task 6 of MEWS Project: Experimental Assessment of Water Penetration and Entry into Wood-Frame Wall Specimens - Final Report. In *Research Report (National Research Council of Canada. Institute for Research in Construction); no. RR-133*. National Research Council of Canada. https://doi.org/10.4224/20386351

Lacy, R. E. (1977). Climate and building in Britain. London: In *Her Majesty's Stationery Office*. John Wiley & Sons, Ltd. https://doi.org/10.1002/qj.49710544325

Lankester, P., & Brimblecombe, P. (2012). The impact of future climate on historic interiors. *Science of The Total Environment*, *417–418*, 248–254. https://doi.org/10.1016/j.scitotenv.2011.12.026

Mayo, A. P. (1998). Task 3 Define the conditions to be reproduced in the standard test – To develop a European standard dynamic water tightness test for curtain walling. In *Building Research Establishment*.

Moore, T., & Nicholls, M. (2014). Performance evaluation of proprietary drainage components and sheathing membranes when subjected to climate loads, task 5: characterization of water entry, retention and drainage of components. In *Client Report (National Research Council of Canada. Construction); no. A1-000030.06*. National Research Council of Canada. Construction. https://doi.org/10.4224/23002855

Morris, P. I. (1998). *Understanding biodeterioration of wood in structures*.

Nik, V. M. (2017). Application of typical and extreme weather data sets in the hygrothermal simulation of building components for future climate – A case study for a wooden frame wall. *Energy and Buildings*, *154*, 30–45. https://doi.org/10.1016/j.enbuild.2017.08.042

Nik, V. M., Mundt-Petersen, S. O., Kalagasidis, A. S., & De Wilde, P. (2015). Future moisture loads for building façades in Sweden: Climate change and wind-driven rain.

Building and Environment, *93*(P2), 362–375. https://doi.org/10.1016/j.buildenv.2015.07.012

Nofal, M., & Kumaran, K. (2011). Biological damage function models for durability assessments of wood and wood-based products in building envelopes. *European Journal of Wood and Wood Products*, *69*(4), 619–631. https://doi.org/10.1007/s00107-010-0508-9

NRCC. (2015). National Building Code of Canada. *Institute for Research in Construction*.

Ojanen, T., & Kohonen, R. (1989). Hygrothermal Influence of Air Convection in Wall Structures. *Proceedings of Thermal Performance of the Exterior Envelopes of Buildings IV*, 234–242.

Ojanen, Tuomo, Viitanen, H., Peuhkuri, R., Lähdesmäki, K., Vinha, J., & Salminen, K. (2010). Mould growth modeling of building structures using sensitivity classes of materials. *Thermal Performance of the Exterior Envelopes of Whole Buildings - 11th International Conference*.

Orr, S. A., Young, M., Stelfox, D., Curran, J., & Viles, H. (2018). Wind-driven rain and future risk to built heritage in the United Kingdom: Novel metrics for characterising rain spells. *Science of The Total Environment*, *640–641*, 1098–1111. https://doi.org/10.1016/j.scitotenv.2018.05.354

Pedersen, C. R. (1992). Prediction of moisture transfer in building constructions. *Building and Environment*, *27*(3), 387–397. https://doi.org/10.1016/0360-1323(92)90038-Q

Rousseau, M. (1999). An Overview of the Survey of Building Envelope Failures in the Coastal Climate of British Columbia, Performed by Morrisson-Hershfield Limited for CMHC (1996). *Journal of Thermal Envelope and Building Science*, *22*(4), 364–367. https://doi.org/10.1177/109719639902200411

Saber, H. H., Lacasse, M. A., Moore, T. V, & Nicholls, M. (2014). Mid-rise wood constructions: investigation of water penetration through cladding and deficiencies: report to Research Consortium for Wood and Wood-Hybrid Mid-Rise Buildings. In *Client Report (National Research Council of Canada. Construction); no. A1-100035-03.3*. National Research Council of Canada. https://doi.org/10.4224/21274581

Sahal, N, & Lacasse, M. A. (2004). Experimental assessment of water penetration and entry into siding-clad wall specimen. In *Internal Report (National Research Council of Canada. Institute for Research in Construction); no. IRC-IR-862*. National Research Council of Canada. https://doi.org/10.4224/20377802

Sahal, Nil, & Lacasse, M. A. (2005). Water entry function of a hardboard siding-clad wood stud wall. *Building and Environment*, *40*(11), 1479–1491. https://doi.org/10.1016/j.buildenv.2004.11.019

Saito, H. (2017). Application of the Wood Degradation Model to an Actual Roof Assembly subjected to Rain Penetration. *Energy Procedia*, *132*, 399–404. https://doi.org/10.1016/j.egypro.2017.09.644

Saito, H., Fukuda, K., & Sawachi, T. (2012). Integration model of hygrothermal analysis with decay process for durability assessment of building envelopes. *Building Simulation*, *5*(4), 315–324. https://doi.org/10.1007/s12273-012-0081-8

Sanderson, M., Arbuthnott, K., Kovats, S., Hajat, S., & Falloon, P. (2017). The use of climate information to estimate future mortality from high ambient temperature: A systematic literature review. *PLOS ONE*, *12*(7), e0180369.

https://doi.org/10.1371/journal.pone.0180369
Sankaran, R., Roberts, G. F., & Mayo, A. (1996). SIROWET II : an advanced technique for weather testing façades. *Applications of the Performance Concept in Building, 3rd International Symposium : Proceedings*, 349–358.
Schmidt, E. L., Hall, H. J., Gertjejansen, R. O., Carll, C. G., & DeGroot, R. C. (1983). Biodeterioration and strength reductions in preservative treated aspen waferboard. *Aspen Bibliography*, *Paper 4103*.
Schuyler, G. D., Swinton, M., & Lankin, J. (1989). Walldry—A Computer Model that Simulates Moisture Migration ThroughWood Frame Walls—Comparison to Field Data. *Proceedings of Thermal Performance of the Exterior Envelopes of Buildings IV*, 492–505.
Soulios, V., Jan de Place Hansen, E., & Peuhkuri, R. (2021). Hygrothermal performance of hydrophobized and internally insulated masonry walls - Simulating the impact of hydrophobization based on experimental results. *Building and Environment*, *187*, 107410. https://doi.org/10.1016/j.buildenv.2020.107410
Straube, J., & Burnett, E. F. P. (2001). Overview of hygrothermal (HAM) analysis methods. *ASTM Moisture Control Manual*, 81–89.
Straube, J. F., & Burnett, E. F. P. (2000). Simplified prediction of driving rain on buildings. *Proceedings of the International Building Physics Conference*, *January 2000*, 375–382.
Tang, W., Davidson, C. I., Finger, S., & Vance, K. (2004). Erosion of limestone building surfaces caused by wind-driven rain: 1. Field measurements. *Atmospheric Environment*, *38*(33), 5589–5599. https://doi.org/10.1016/j.atmosenv.2004.06.030
Teasdale-St-Hilaire, A., & Derome, D. (2007). Comparison of experimental and numerical results of wood-frame wall assemblies wetted by simulated wind-driven rain infiltration. *Energy and Buildings*, *39*(11), 1131–1139. https://doi.org/10.1016/j.enbuild.2006.12.004
Van Balen, K. (1996). Expert system for evaluation of deterioration of ancient brick masonry structures. *Science of The Total Environment*, *189–190*, 247–254. https://doi.org/10.1016/0048-9697(96)05215-1
Viitanen, H., Toratti, T., Makkonen, L., Peuhkuri, R., Ojanen, T., Ruokolainen, L., & Räisänen, J. (2010). Towards modelling of decay risk of wooden materials. *European Journal of Wood and Wood Products*, *68*(3), 303–313. https://doi.org/10.1007/s00107-010-0450-x
Viitanen, Hannu. (1996). *Factors affecting the development of mould and brown rot decay in wooden material and wooden structures. Effect of humidity, temperature and exposure time*.
Viitanen, Hannu. (1997). Modelling the time factor in the development of mould fungi: The effect of critical humidity and temperature conditions on pine and spruce sapwood. *Holzforschung*, *51*(1), 6–14. https://doi.org/10.1515/hfsg.1997.51.1.6
Viitanen, Hannu, & Bjurman, J. (1995). Mould growth on wood under fluctuating humidity conditions. *Material Und Organismen*, *29*(1), 27–46.
Viitanen, Hannu, & Ritschkoff, A.-C. (1991). *Mould growth in pine and spruce sapwood in relation to air humidity and temperature*.
Wang, L., & Ge, H. (2017). Effect of air leakage on the hygrothermal performance of highly insulated wood frame walls: Comparison of air leakage modelling methods.

Building and Environment, *123*, 363–377. https://doi.org/10.1016/j.buildenv.2017.07.012

Wang, R., Ge, H., & Baril, D. (2020). Moisture-safe attic design in extremely cold climate: Hygrothermal simulations. *Building and Environment*, *182*, 107166. https://doi.org/10.1016/j.buildenv.2020.107166

Chapter 3 Historical climate data analysis and a preliminary watertightness test

3.1 An Analysis of Historical Wind-driven Rain Loads for selected Canadian Cities

Zhe Xiao, Michael A. Lacasse and Elena Dragomirescu

Journal of Wind Engineering & Industrial Aerodynamics 213 (2021) 104611

3.1.1 Abstract

The performance and durability of wall assemblies are greatly affected by the moisture load to which they may be subjected in particular those arising from Wind-Driven Rain (WDR). Standard approaches for estimating such moisture loads assume 1% of the WDR load, whereas these loads have also been assessed from watertightness tests, although these assumed loads have been determined based on limited climate information. To more accurately estimate the moisture loads to which wall assemblies may be subjected over their service life, an analysis of historical WDR loads was completed for 11 cities across Canada. The magnitude, probability of occurrence of WDR loads in different cities, and correlations between WDR related climate parameters, are discussed in this paper. Also, a novel WDR severity index is introduced, referred to as the Wind-Driven Rain Pressure Index, to permit quantifying the real-time and simultaneously occurring effects of WDR intensity and Driving Rain Wind Pressure (DRWP). To estimate the WDR intensity and DRWP with a specific probability of occurrence, an Extreme Value Analysis (EVA) was completed for a climate dataset of 31 years (1986 to 2016) using the Generalized Extreme Value and Gumbel distributions.

Keywords: wind-driven rain; climate loads; extreme value analysis; goodness of fit test

3.1.2 Introduction

The long-term performance and durability of building façades, for which the façade maintains the function and integrity of a structure by impeding most of the detrimental effects of the surrounding environment from entering the building envelope, are adversely affected by moisture loads to which they may be subjected over time

(Desjarlais et al., 2001; Rousseau, 1999; Smegal et al., 2013). For example, in respect to masonry walls, mould growth problems may arise at the interior layers of the wall assembly due to excessive moisture load (Abuku et al., 2009b). For wood-framed wall assemblies, the wood materials can decay when exposed to a humid environment for prolonged periods of time (Chouinard and Lawton, 2001). Other undesirable problems arising from the presence of moisture in masonry and cementitious wall clad assemblies include, but are not limited to, frost damage of, and salt migration in porous materials, the erosion of building materials and efflorescence at the surface of the façades (Charola and Lazzarini, 1986; Franke et al., 1998; Tang et al., 2004; Van Balen, 1996).

Wind-driven rain (WDR), as the primary source of the moisture load for wall assemblies, is the co-occurrence of wind and rain (Lacy, 1977). The horizontal velocity component of raindrops, as part of WDR, can be attributed to the action of wind and its direction usually in accordance with the wind velocity vector. The amount of water that is deposited on a vertical surface of a building façade is identified as the WDR load, which can be assessed by semi-empirical equations provided the rainfall intensity, wind velocity and direction, and the surrounding conditions are known (ASHRAE, 2016; ISO, 2009; Lacy, 1977; Straube and Burnett, 2000). A more accurate assessment for WDR load at specific locations may require the information of building geometry (Blocken et al., 2009; Blocken and Carmeliet, 2006; Karagiozis et al., 1997; Kubilay et al., 2015). In addition, the WDR load on a building façade can also be determined from field measurements by installing collection troughs at exterior surfaces of the façade (Blocken and Carmeliet, 2005; Ge et al., 2018, 2017; Kubilay et al., 2014; Wang et al., 2020).

When a raindrop reaches the façade of a building, it may splash, spread, or bounce from the building surface, depending on the façade materials, on the raindrop final velocity, as well as on the attack angle between the raindrop and the wall assembly (Abuku et al., 2009a). After the impact, the raindrop would either be drained from the façade, absorbed by façade materials, provided theses are porous in nature, or enter the building envelope through any deficiencies, such as cracks or openings present on the façade surface. However, the existence of deficiencies in the building envelope also allows the passage of water through these openings, over its life cycle, and this is most likely inevitable given the effect of aging and deterioration of materials, mechanical failure of structural members arising from extreme and cyclic loads and faulty construction and maintenance practice. Currently, there are two typical approaches to quantify the amount of water, namely the moisture load, that could penetrate the exterior cladding of the wall assembly during WDR events. One approach is to simply consider that the moisture load is 1% of the WDR load to which the exterior wall surface is subjected during a rain event, as specified in the ASHRAE standard 160 (ASHRAE, 2016). Another approach is to conduct a watertightness test in which water spray onto the wall assembly and pressure difference across the wall are applied simultaneously to simulate the action of WDR on the wall test specimen. Such tests are able to quantify the rate of water entry across the exterior wall cladding and the portion of water that enters the wall assembly (Boardman and Glass, 2013; Bossche et al., 2012; Sahal and Lacasse, 2005, 2004).

The National Research Council Canada has launched a series of research studies the results of which have permitted establishing a watertightness test protocol to properly manage risks of damage to wall assemblies over the long-term due to moisture loads arising from WDR. As such, the entire assessment encompasses the following steps: (i) Understanding the WDR conditions based on climatic data collected at meteorological stations and from which to derive the WDR load; (ii) Measuring the level of water entry in and water retention of wall assemblies exposed to the corresponding WDR loads through watertightness tests using the new test protocol; (iii) Relating the climate data with the rate of water entry to wall assemblies; (iv) Correlating the degree of water retention with the moisture response of wall assemblies.

In this paper, the historical WDR conditions from 1986 to 2016 are analyzed for 11 cities located across Canada and the results are discussed at different temporal scales. Outputs from the analysis were used to determine boundary conditions for the new watertightness test protocol to be established using the information described in this paper.

3.1.3 Methodologies

3.1.3.1 Observational Dataset

Hourly rainfall intensity and wind velocity for different cities were obtained from the climate dataset for 1986 to 2016, as recorded at meteorological stations operated by

Environment and Climate Change Canada. Rainfall is usually measured using a standard rain gauge consisting of a 40 cm high and 11.3 cm diameter cylindrical metal container, where the volume of collected rain water is funneled into a graduated cylinder for the measurement. Based on the hourly rate, the rainfall intensity is classified as “Very light”, i.e., rain does not completely wet a surface; “Light” i.e., greater than a trace and up to 2.5 mm an hour; “Moderate”, i.e., rate of rainfall is between 2.6 mm to 7.5 mm per hour, and; "Heavy", i.e., 7 mm per hour or more. Wind velocities and directions are measured from an anemometer at a height of 10 metres. Precipitation events during hours of snowfall were also recorded and differentiated from those of rainfall; these data were excluded from the analysis in this study

3.1.3.2 WDR and DRWP

The amount of water that is deposited on a vertical exterior wall surface during a rain event is defined as the WDR load to the wall. The semi-empirical equation used to calculate this load based on the rainfall intensity and the wind speed, was firstly proposed by Hoppestad (1955) and subsequently further developed and improved by Lacy (1977), and thereafter, Straube and Burnett (2000). The applicability and limitations of these equations have been discussed in detail by Blocken and Carmeliet (2004). Subsequent versions of equations to calculate the WDR load, which were also put in practice for practical applications, were specified in ISO 15927 standard (ISO, 2009) and ASHRAE standard 160 (ASHRAE, 2016). Eqs. (3.1) and (3.2) are the semi-empirical expressions used to calculate the WDR load as given in the ISO15927 standard (ISO, 2009):

$$I_A = \frac{2}{9}\sum\left(vR_h^{\frac{8}{9}}\cos(D-\theta)\right) \tag{3.1}$$

$$I_{AW} = I_A C_R\, C_T O W \tag{3.2}$$

In which I_A is the airfield WDR index, v is the hourly mean wind speed (m/s) at the given height, R_h is the hourly rainfall intensity (mm/h), D is the angle between hourly wind speed directions to the north, and θ is the wall orientation in regard to the north direction.

To assess the WDR load (I_{WA}) on a building façade, a few more factors were considered in addition to the airfield WDR index, specifically the: terrain roughness coefficient C_R, topography coefficient C_T, obstruction factor O and wall factor W. These factors are individually determined for each case of interest.

Eq. (3.3) is the semi-empirical equation specified in the ASHRAE standard 160 (ASHRAE, 2016) to calculate the WDR load:

$$r_{bv} = r_h \mathrm{F_E F_D F_L} U \cos\theta \quad (3.3)$$

Where r_{bv} is the rain deposition rate on a vertical wall (kg/m^2·h), r_h is the rainfall intensity on a horizontal surface (mm/h), F_E is the rain exposure factor, F_D is the rain deposition factor, F_L is an empirical constant, 0.2 kg·s (m^3·mm), U is the hourly average wind speed (m/s) and θ is the angle between the wind direction and normal to the wall. Amongst these factors, the rain exposure factor (F_E), the deposition factor (F_D), and the wind direction angle (θ) are determined considering the configurations of the building and the topography surrounding the building.

Both sets of equations consider the effect of wind direction, exposure of the wall, and surrounding topography for estimating the WDR load on a wall surface. The ISO 15927 standard considers the effect of a possible obstruction near the wall, which is ignored in the ASHRAE standard. The wall factor W of the ISO 15927 standard describes the distributions of WDR load on wall assemblies for different types of building configurations without taking water runoff into account. Runoff on the wall surface is, however, considered in the ASHRAE standard through the use of a rain deposition factor but this factor lacks accounting for the distribution of the WDR load in the horizontal direction.

The WDR load in this study was calculated using the semi-empirical equation provided in the ASHRAE standard given that when undertaking a hygrothermal simulation, the WDR load is usually coupled with other criteria in the ASHRAE standard pertinent to this use. To normalize the WDR analysis undertaken in this study, which is intended for the characterisation of WDR loads on buildings, the values of the rain exposure factor (F_E) and the deposition factor (F_D) were set to 1. The hourly horizontal rainfall intensity and hourly averaged wind velocity were the two primary climate variables considered, which could readily be obtained from the available climate data.

To permit simulating WDR effects on wall assemblies from a watertightness test, water deposition onto the wall assembly and pressure differential across the assembly must be applied to a test specimen simultaneously, in controlled magnitudes, given that these parameters, represent, respectively, the WDR load and Driving Rain Wind Pressure (DRWP) as might be acting on a wall for a specified amount of time during a rain event. Regarding the applied pressure during testing, Mayo (1998) suggested that the most extreme wind pressure be used based on the longest period of time as recorded for the DRWP load. However, the most extreme wind pressure for all hours might not be representative of the level of wind pressure present during rain events. Sacré et al (Sacré, 1984) and Surry et al. (1997) indicated that the peak wind velocities during rain events were 5% to 30% lower when compare to those for all hours of wind and the corresponding peak wind pressure should be reduced by 10% to 51%. Hourly wind velocities from the historical dataset for Canadian cities for all hours during rain events will be discussed in the subsequent section of this paper.

According to the results of multiple watertightness tests (Bossche et al., 2012; Sahal and Lacasse, 2005, 2004), water ingress to a wall assembly can be affected by both the water spray rate and concurrently applied pressure differential. Choi (1994) characterized the relationship between the wind and rain to permit calculating the driving rain from a driving-rain index. Cornick and Lacasse (2010) reported a poor correlation between the rainfall intensity and wind during rain events and a weak positive correlation between the WDR and DRWP, which was attributed likely to the WDR equation that included the DRWP as a factor. Van Den Bossche et al. (2013) developed a spectrum for the WDR and DRWP using a Pareto Front Analysis which provided boundary conditions of these two parameters for different return periods. Pérez-Bella et al. (2013) addressed a Risk Index for Water Penetration, as given in Eq. (3.4), that permits integrating both the WDR and DRWP parameters:

$$RIWP = \sqrt{\alpha \cdot (WDR)^2 + \beta \cdot (DRWP)^2} \quad (3.4)$$

In which, α and β were two weighting factors and the WDR and DRWP were normalised by the minimum and maximum values for 30 years of sample climate data. Although, from these studies it was possible to summarize the correlation and to quantify the two simultaneous factors over a long period of time, it was not possible to reflect the real-time WDR and DRWP conditions. Consequently, these relations could not be used to establish the relationship between the co-occurrence of WDR, DRWP and the water entry rate, which would be used in the subsequent hygrothermal simulations.

As a means of representing real-time WDR conditions to which a wall assembly may be exposed during rain events, a new Wind-Driven-Rain Pressure ($WDRP$) index, is proposed; this is the product of the $WDR\ intensity$ (mm/h) and the simultaneous action of $DRWP$ (Pa). The WDR intensity describes the amount of water that is deposited onto the exterior surface of the wall assembly and the pressure differences across the wall assembly derived from the DRWP, which induces the force that drives the water into the wall assembly when deficiencies are present. Although the response of the wall assemblies to WDR and DRWP are not the same due to many factors, such as the selection of wall components and materials, wall cavity depths, and the size of deficiencies, it is supposed that the value of the WDRP index may be determined as given in Eq. (3.5). The coefficients α and β would be applied to different configurations of wall assemblies according to the performance of the wall when subjected to watertightness tests.

$$WDRP = WDR^{\alpha} \cdot DRWP^{\beta} \tag{3.5}$$

Correlations between the WDRP index and the water entry rate obtained from the MEWS project (Lacasse et al., 2003) are shown in Figure 1. The vertical axis of each plot is the water entry rate in L/min during a watertightness test and the horizontal axis is the corresponding WDRP index calculated from the experimental inputs of that test, i.e., the spray rate representing the WDR intensity and applied pressure as represented by the DRWP in Eq. (5). The blue '+' mark is the water entry rate (L/min) at a WDRP index that considers α and β equal to 1 and the green '**x**' mark represents the water entry rate (L/min) at a WDRP index calculated from flexible adjustment. The blue solid line and the green dotted line are the trendlines for each set of relations. It is evident that the correlations between the water entry rate and the WDRP index have increased by adjusting the two coefficients, α and β, for WDR intensity and DRWP respectively. The water entry rates at the deficiency above the electrical outlet for a stucco wall assembly, as shown in Figure 1 (a), are more sensitive to the variation of WDR intensity than the variation of DRWP given α, the adjustment coefficient for WDR intensity, is larger than β, the adjustment coefficient for the DRWP. In contrast, the variation of water entry rates at the vertical joint for an EIFS wall assembly, as shown in Figure 1 (b), is more greatly affected by the variation of the DRWP, as the value of β is larger than that of α. Figure 1 (c) and Figure 1(d) show the water entry rates for two different deficiencies in the same type of wall assembly. The water entry rates at the ventilation duct are not as greatly affected by the DRWP and more so by the WDR intensity, as compared to that for the water entry rates at the window given a smaller value of α and a larger value of β. When analyzing the WDRP index from the climate data, both coefficients are considered as having a value of 1.

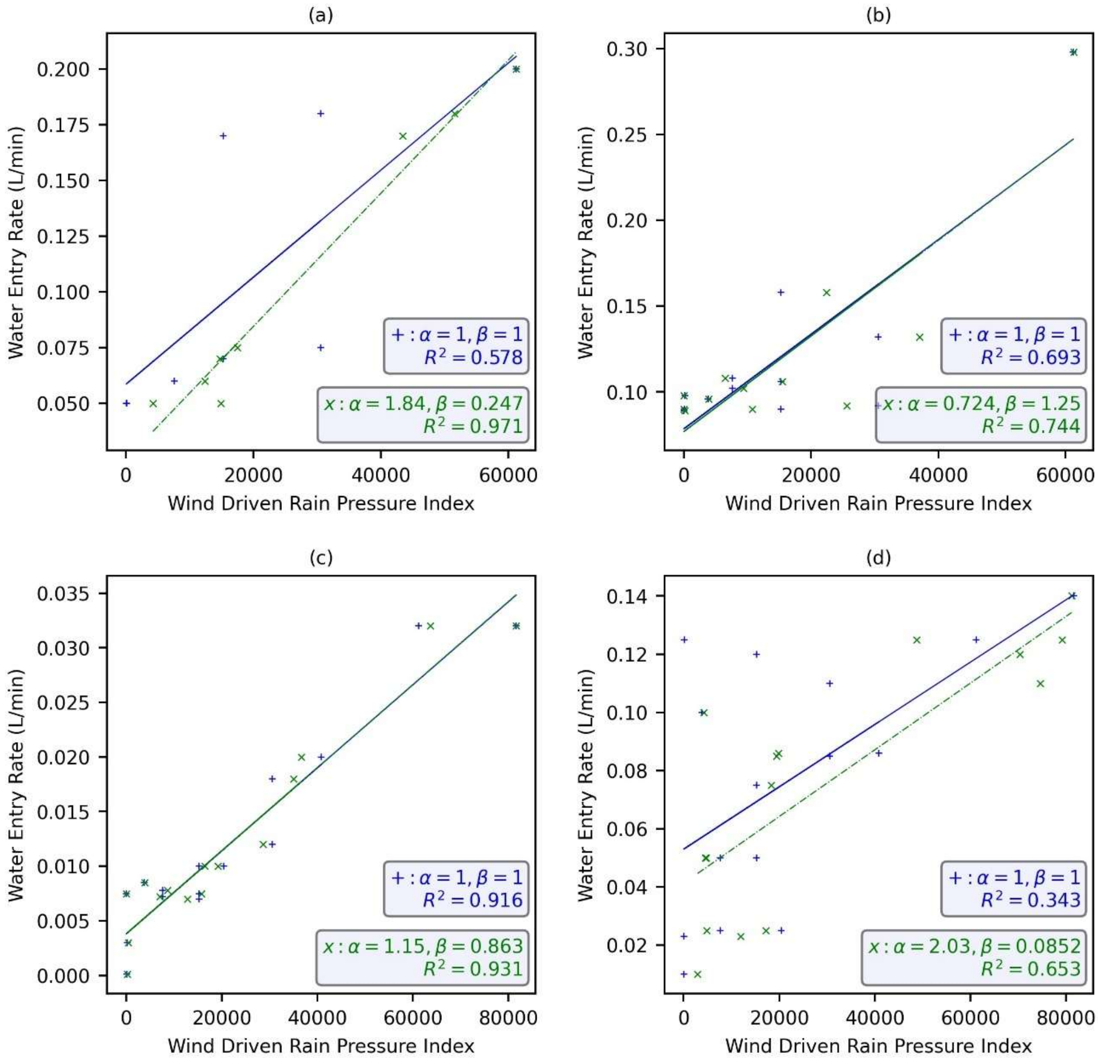

Figure 3.1 (a) Stucco wall assembly (WA-4)* - Water entry rate at deficiency above electrical outlet; (b) EIFS wall assembly (WA-7)* - Water entry rate at vertical joint; (c) Hardboard siding wall assembly (WA-16)* - Water entry rate at the ventilation duct; (d) Hardboard siding wall assembly (WA-16)* - Water entry rate at the window.

*** Designations of wall assemblies from the MEWS project** (Lacasse et al., 2003).

3.1.3.3 Distributions for EVA

Extreme value distributions are usually applied to extreme events such as annual maximum rainfall and in hydrology, to river discharges rates to estimate the severity of these events at different return periods. The life span of wall assemblies is usually greater than 31 years, which is the length of collected historical climate data for this study. To evaluate the extreme WDR conditions for a longer period of time, Intensity-Duration-Frequency (IDF) curves were generated for different hourly values of WDR intensity and WDRP index. Empirical approaches (Chow, 1962; Sherman, 1931) were mostly implemented to generate IDF curves for the rainfall intensity with respect to hydraulic engineering applications. Within these approaches the values of parameters usually varied with location and the duration of rain events. In this study, the Gumbel distribution (Eq. (3.6)), Fréchet distribution (Eq. (3.7)), Weibull distribution (Eq. (3.8)), and Generalized Extreme Value (GEV) distribution (Eq. (3.9)) were selected to analyze the extreme values of WDR intensities and hourly WDRP index. The annual maximum values of WDR intensity and hourly WDRP index over different durations for 31 years have been selected to fit with these distributions. The value of the parameters of these distributions obtained from the fitting process would thereafter be used to calculate the WDR intensities and hourly WDRP indices at different return periods. Goodness of fit tests were also carried out to examine the effectiveness of the four distributions.

$$G_{(\mu,\sigma)}(x) = EXP\left(-(EXP)^{\frac{-(x-\mu)}{\sigma}}\right) \quad (3.6)$$

$$G_{(\xi,\mu,\sigma)}(x) = EXP\left(-(\frac{x-\mu}{\sigma})^{-1/\xi}\right) \quad (3.7)$$

$$G_{(\xi,\sigma)}(x) = 1 - EXP\left(-(\frac{x}{\sigma})^{\xi}\right) \quad (3.8)$$

$$G_{(\xi,\mu,\sigma)}(x) = EXP\left(-\left(1+\xi\left(\frac{x-\mu}{\sigma}\right)\right)^{-\frac{1}{\xi}}\right) \quad (3.9)$$

3.1.4 WDR Conditions for Selected Cities

Parameters in the climate dataset that may affect the WDR load on a wall assembly include frequency of rain events, wind velocity during rain events, rainfall intensity, and direction of rain events. The frequency of rain events is representative of how often a wall assembly may be subjected to WDR and can be quantified by the number of rain hours in the climate dataset. This is an important factor to be considered when characterizing performance of wall assemblies used in different regions having different climatic conditions given that increases in the frequency of rain events assuredly have an adverse effect on the long-term performance of wall assemblies. The wind velocity and rainfall intensity are the two primary parameters from which the WDR load is derived. Knowledge of the probability of occurrence and distribution of the magnitude of both these parameters permit understanding the differences of WDR conditions in distinct cities, as well as providing specific conditions to which a watertightness test could be conducted. The proposed WDRP index could reveal the relative severity amongst wind-driven rain events given the rainfall intensity and DRWP of an event. Since the product of the rainfall intensity and DRWP cannot be larger than the maximum value for the WDRP index, this then represents the extent of influence in respect to the risk of water entry of these climate load parameters when acting together. Knowing the prevailing wind direction in different cities will be helpful in determining the most problematic direction, in regards to the risk to water entry to which a wall assembly is exposed during a WDR event.

3.1.4.1 Rainfall and Wind

Frequencies of rain events are depicted as the Rain Frequency (%) in Table 3-1. It is the ratio between the number of hours with rainfall to the total number of hours over a period of 31 years. For each city, the annual maximum hourly wind velocities during rain events were selected and compared with the annual maximum hourly wind velocities. In Table 3-1, the Wind Velocity (%) is the ratio of the annual maximum hourly wind velocity during rain to that of all events averaged over 31 years. In addition, the ratios between the annual maximum wind pressures during rain events and annual maximum wind pressure are denoted as Wind Pressure (%). The wind pressure was calculated using the Bernoulli's principle (Eq. (3.10)), where P is the calculated wind pressure, ρ is the air density, and v is the wind velocity; the value for air density was assumed to be 1.225kg/m^3.

$$P = \frac{1}{2}\rho v^2 \tag{3.10}$$

Table 3-1 Frequency of rain events and ratio of averaged annual maximum wind velocity and wind pressure during rain events to that for all hours.

City	Rain Frequency %	Wind Velocity %	Wind Pressure %
Calgary	3.15	76.1	59.4
Charlottetown	6.3	81.9	68.4
Halifax	7.74	91.2	83.9
Moncton	6.2	82.1	68.8
Montreal	9.69	83.3	70.3
Ottawa	6.01	81.5	67.7
Saskatoon	3.92	87.3	77.7
St. John's	7.63	82.2	68.9
Toronto	7.49	84.2	72.1
Vancouver	19.8	91.1	83.8
Winnipeg	4.1	85.2	73.8

Vancouver had a much higher frequency of rain hours than all other major cities in Canada as were analyzed during the period, 1986-2016. Rain events occurred almost 20% of time in this city. Conversely, Calgary had the fewest hours of rain over the same period of time where rain fall only occurred 3.15% of time. The annual maximum hourly wind velocities during rain events were 8.8% to 23.9% less than that for all hours. Based on this information, the corresponding hourly wind pressures during rain events were then determined to range between 16.1% and 40.6% from all hours. Halifax had the highest Wind Velocity % and, rain occurred 7.74% over this time period, which was the top 3 amongst these 11 cities. However, Saskatoon received the second least amount of rain for the 31 years whilst having a higher Wind Velocity % than the other 8 cities. From these observations, no clear correlation could be concluded between the frequency of rain hours and the ratio of wind velocities for rain events and all hours. The rank of the Wind Pressure % followed the rank of the Wind Velocity % as they were positively correlated through Bernoulli's principle. Theoretically speaking, a higher frequency of rain hours would increase the probability of occurrence of large values for wind velocity during rain events. However, this conjecture was not reflected in this analysis of annual maximum hourly wind velocities.

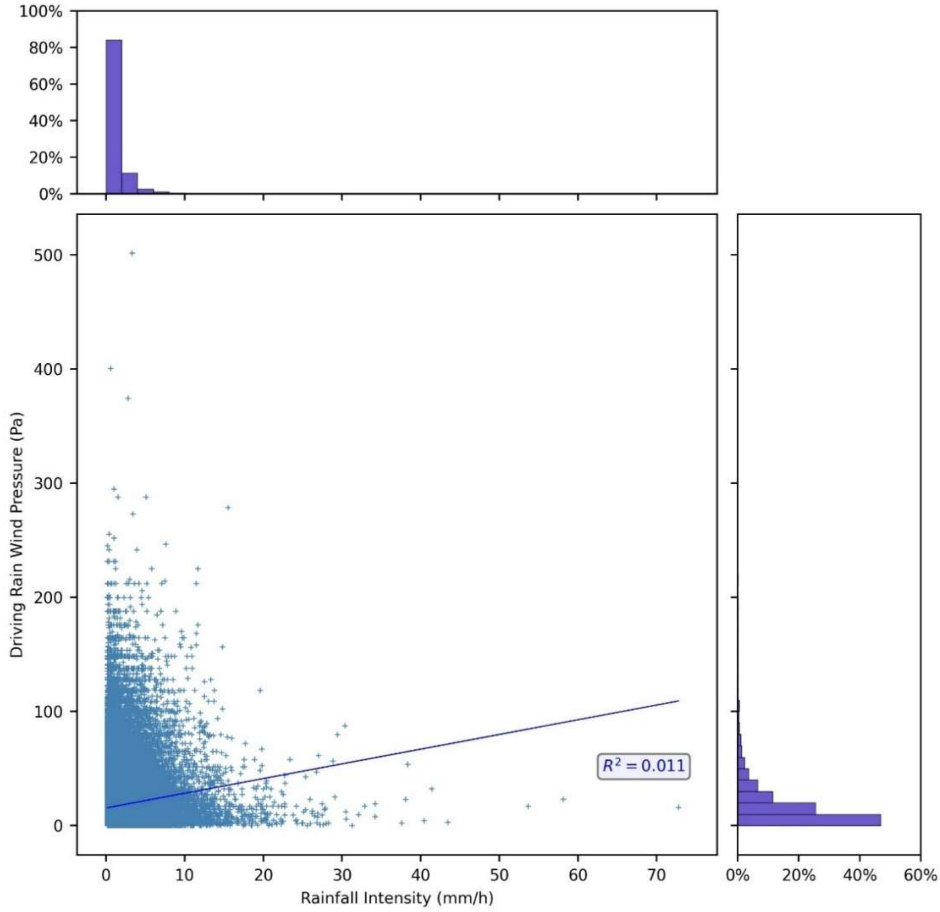

Figure 3.2 Correlations and histograms between DRWP and concurrent rainfall intensities for all cities.

Hourly DRWPs during rain events and that had a rainfall intensity of more than 0.2mm/h, defined (by ECCC) as a 'trace' amount of rain which cannot completely wet a surface, were plotted with concurrent rainfall intensities, as shown in Figure 3.2. In general, most of the hourly DRWPs during WDR events in all selected cities were less than 100Pa. Over 45% of the hourly DRWPs were less than 10Pa whereas only 3 events had hourly DRWPs that were over 300Pa. Existing watertightness test protocols are required to apply different levels of pressure to test specimens. However, most of these lack consideration for wind pressure acting at relatively low levels. For example, in AAMA 501-05 (AAMA 501-05, 2005), the minimum test air pressure is 300Pa. The lowest dynamic pressure step in the European Code EN12865 (EN 12865, 2001) is 0-150Pa and this directly goes to 0-300Pa. Lacasse et al. (2003), used a testing protocol as described in the MEWS project that considered pressure levels under 250Pa, respectively, at 50Pa, 75Pa, and 150Pa. To obtain accurate relationships between real-time WDR conditions and water ingress, more steps at lower pressure levels ought to be considered given that over 50% of wind pressure occurring during rain events are less than 20Pa. The R-squared values for the hourly rainfall intensity and hourly DRWPs were less than 0.1; this indicates that there is no meaningful association that can be established between these two parameters.

3.1.4.2 WDR intensity and WDRP index

WDR intensities were calculated by using Eq. (1), assuming that the rain exposure factor, the deposition factor, and the cosine of wind direction equaled 1. The value of the WDRP index was then calculated on the basis of the WDR intensity and concurrent DRWP using Eq. (3), with values of α and β equal to 1. WDR intensities and the corresponding values for hourly WDRP index for each city are shown in Figure 3.3.

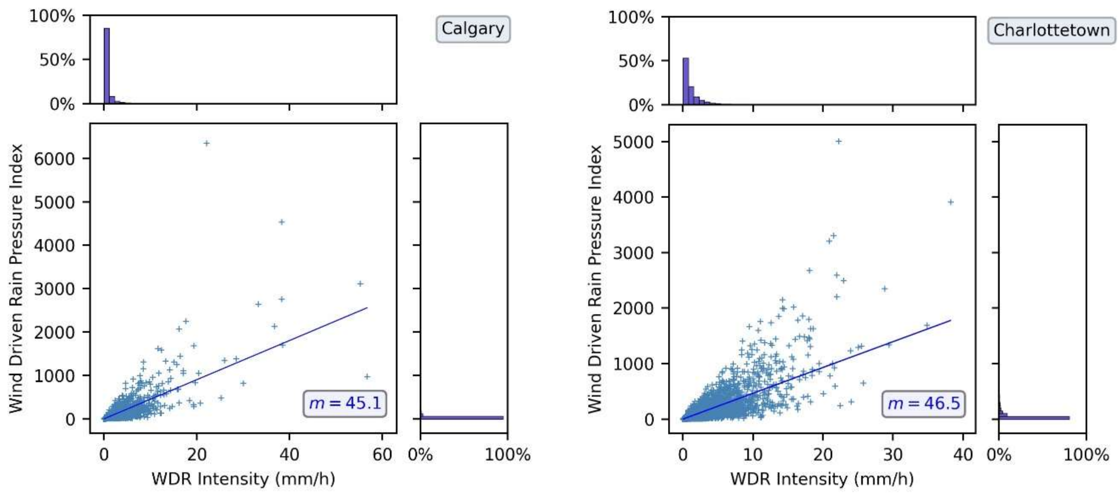

(a) Calgary (b) Charlottetown

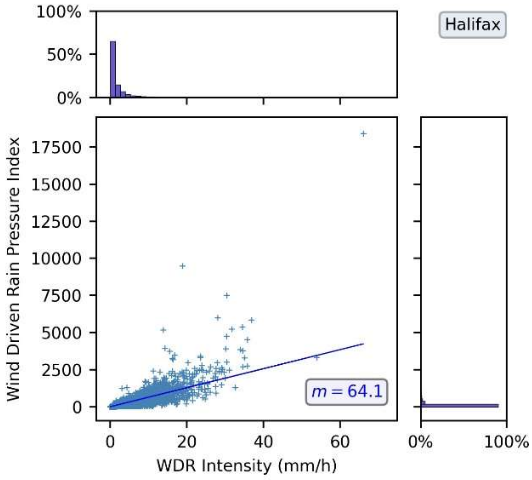

(c) Halifax

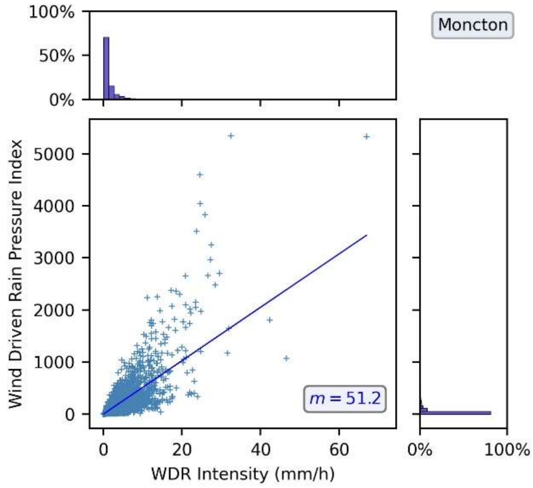

(d) Moncton

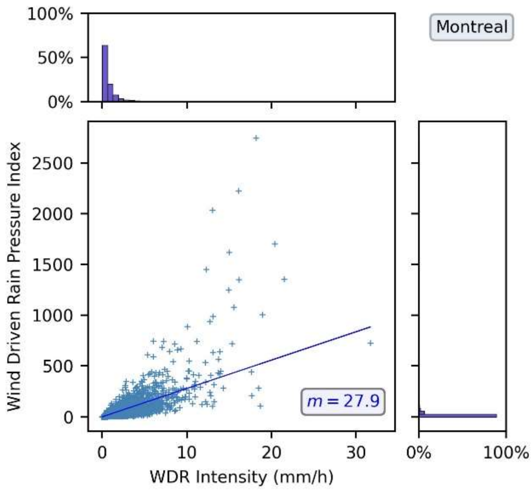

(e) Montreal

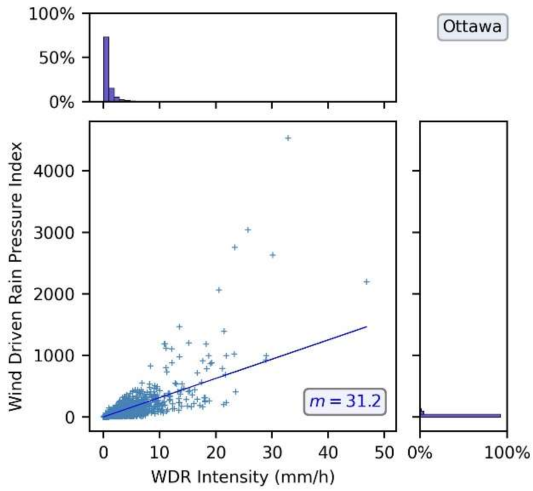

(f) Ottawa

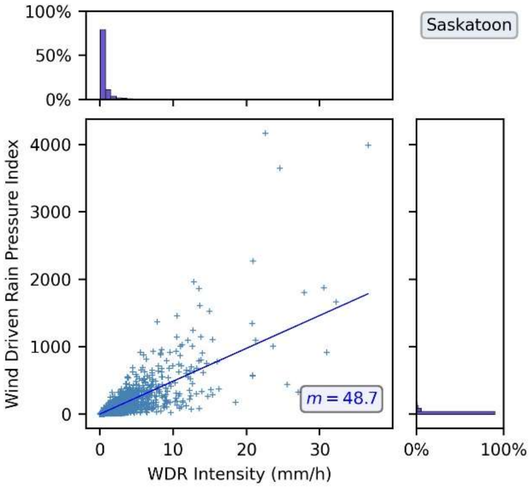

(g) Saskatoon

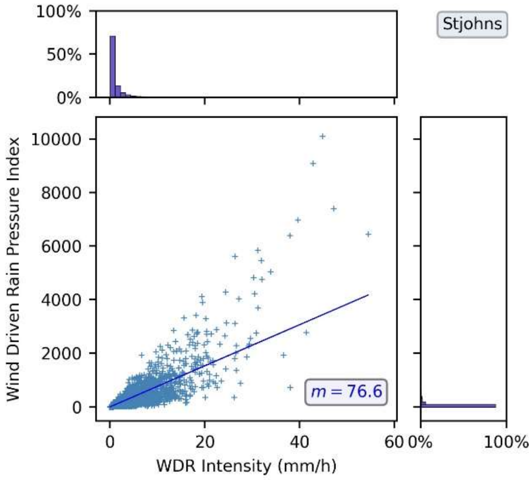

(h) St. John's

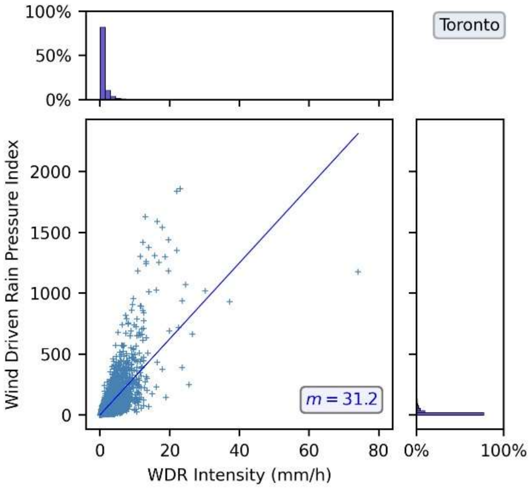

(i) Toronto

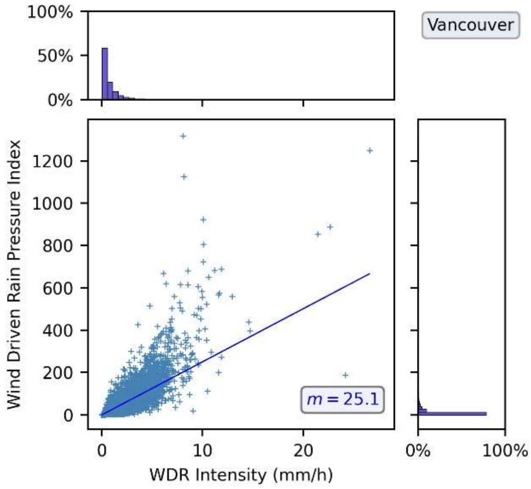

(j) Vancouver

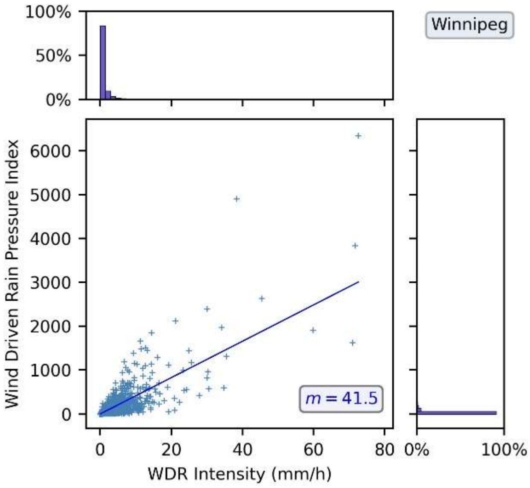

(k) Winnipeg

Figure 3.3 The WDR intensity and WDRP index in different cities

During the 31 years, only Halifax, Moncton, Toronto, and Winnipeg experienced WDR intensities over 60mm/h. The maximum WDR intensity of 74mm/h, was observed in Toronto. Winnipeg reported 3 events with this level of extreme WDR intensity, whereas the other 3 cities, respectively, only experienced WDR of this magnitude once. Frequencies of WDR intensities between 20mm/h and 60mm/h in Halifax, St. John's, and Moncton were, respectively, 95, 58 and 38. However, such levels of WDR intensity only occurred 4 times in Vancouver and 3 times in Montreal although these two cities had the most, and second most, rain hours over the 31 years investigated. In the remaining cities, such frequencies ranged from 11 to 21.

Over 99% of WDR intensities in all cities were less than 20mm/h, which is equivalent to a water spray rate of 0.7L/m^2-min for a 10-minute period according to that proposed by Linsley et al. (1975) in Eq. (3.11):

$$\frac{i(t)}{i_h} = (\frac{3600}{t})^{\gamma} \tag{3.11}$$

Where $i(t)$ is the rainfall intensity (mm/h) for a particular time interval (s), i_h is the hourly rainfall intensity and the Linsley exponent γ, which is set to 0.42. In these watertightness test standards (ASTM E331-00, 2016; EN 12865, 2001; Lacasse et al., 2003), the minimum specified spray rates were 1.5L/m^2-min plus 1.2L/m-min runoff, 1.0L/m^2-min, and 3.4L/m^2-min respectively; these were all much larger than the 0.7L/m^2-

min spray rate derived from a WDR intensity of 20mm/h. In a watertightness test protocol, spray rates at lower levels should be given more consideration when attempting to more accurately correlate the WDR and DRWP to a consequent moisture load. The large hourly values of WDRP index for Calgary, Charlottetown, Halifax, Moncton, Ottawa, and Saskatoon were primarily caused by large values of DRWP during rain events. Moreover, in St. John’s and Winnipeg, the WDR intensity was the major factor that increased the value of the hourly WDRP index. In Montreal, Toronto, and Vancouver, the respective values of hourly WDRP index were lower than other cities. Thus, risks of water ingress for wall assemblies in these locations would also be relatively minor. The trend line in each plot expresses the relative contribution of DRWP and WDR intensity to that of the WDRP index. A steeper trend line, as expressed by slope ratio, implies higher DRWP at the same cumulative probability of occurrence as depicted in Table 3-2. For instance, St. John’s, Halifax, and Moncton had the highest 3 slope ratios and the DRWPs in these 3 cities were overall, larger than that in other cities, at the same cumulative probability level. Similar conclusions could also be drawn when comparing DRWPs in cities having slope ratios in the 40s to cities having lower values for slope ratio.

Table 3-2 Cumulative probability of WDR and DRWP in different cities

Cumulative Probability		0.5	0.9	0.95	0.99	0.995	1
Calgary	*WDR (mm/h)*	0.587	2.74	4.2	9.36	12.4	56.7
	DRWP (Pa)	10.7	37.1	51.5	91.5	109	288
Charlottetown	*WDR (mm/h)*	0.75	3.45	5.22	11	14	38.2
	DRWP (Pa)	17.1	46.9	64.7	100	118	225
Halifax	*WDR (mm/h)*	0.799	4.94	8.01	16	20.1	66.1
	DRWP (Pa)	13.1	53.9	72.8	109	124	501
Moncton	*WDR (mm/h)*	0.639	3.6	5.34	11.7	14.7	77
	DRWP (Pa)	13.6	48.4	64.7	109	128	231
Montreal	*WDR (mm/h)*	0.435	1.8	2.78	5.98	7.7	31.7
	DRWP (Pa)	6.23	22.9	29.5	50.4	60.2	156
Ottawa	*WDR (mm/h)*	0.54	2.3	3.54	7.94	10.9	46.8
	DRWP (Pa)	9.27	27.2	37.1	57.9	70	176
Saskatoon	*WDR (mm/h)*	0.542	2.42	3.73	8.96	12.2	36.6
	DRWP (Pa)	18.9	51.5	64.7	100	118	194
St. John's	*WDR (mm/h)*	0.467	3.23	5.33	12.3	16.4	54.4
	DRWP (Pa)	7.98	51.5	73.2	128	148	288
Toronto	*WDR (mm/h)*	0.529	2.57	4	8.61	11.1	74.1
	DRWP (Pa)	11.1	35.3	47.4	76.8	88.8	202
Vancouver	*WDR (mm/h)*	0.44	1.93	2.78	5.06	6.04	26.6
	DRWP (Pa)	7.98	23.4	31.3	49.9	59.6	165
Winnipeg	*WDR (mm/h)*	0.5	2.38	3.83	9.74	13.1	72.6
	DRWP (Pa)	13.6	42.5	57.9	95.7	109	358

3.1.4.3 Wind Directions during Rain Events

The averaged wind direction, measured at the same location as the averaged wind speed, is the direction from which the wind blows. The minimum scale of the measured direction is 10 °. Prevailing wind directions of each city during rain events are shown in Figure 4. A wind blowing from the north is denoted as 0-degree, and the 90-degree represents the easterly direction. In Calgary, the prevailing wind direction during rain events was between 0 and 320 ° and it was found that over 30% of the time the wind was blowing from this range of directions. In Charlottetown, over 40% of the time the wind during rain events were recorded from the south-southeast direction. Most of the wind in Halifax was blowing from the Atlantic Ocean, which is southeast to city. The top 2 prevailing wind directions for Moncton were north and southeast by south. In Montreal, over 50% of the time the wind was blowing from the direction between southeast and southwest, whereas over 10% of that wind was from north-easterly direction. Wind during rain events in Ottawa was recorded mainly from the east-northeast and south by west. In Saskatoon, the north direction alone had over 27% of wind during rain events, whereas 8.5% and 9.5% of the time the wind was blowing, respectively, from the northwest and north-northwest directions. The wind in all other directions occurred less than 5% of the time. The prevailing wind direction during rain events in St. John's did not blow from the Atlantic Ocean as is the case for Halifax; over 50% of the time the wind was blowing from a direction between southeast and southwest, whereas the ocean is situated directly east of the city. The wind direction in Toronto came from two notable directions: east by north and south-southeast whereas in Vancouver east by north was the only prevailing wind direction. In Winnipeg, wind directions were irregularly distributed over all directions; the wind from the south direction was slightly more frequent than other directions.

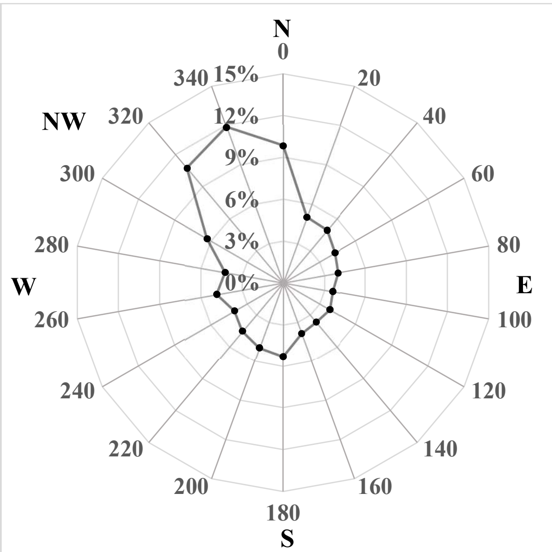

(a) Calgary

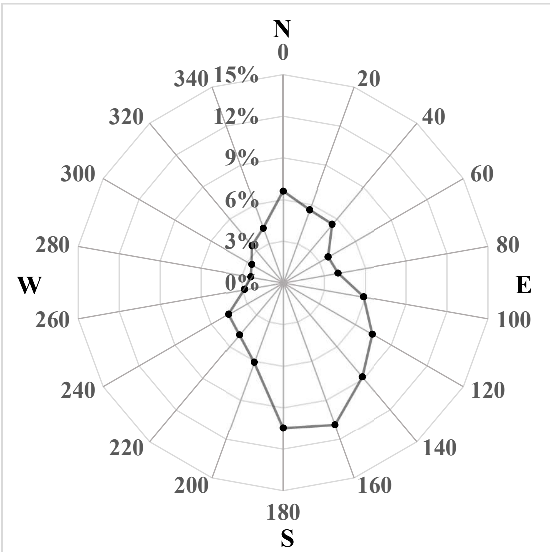

(b) Charlottetown

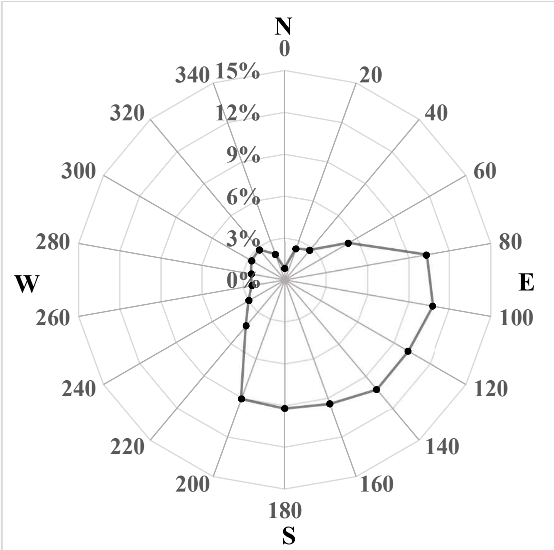

(c) Halifax

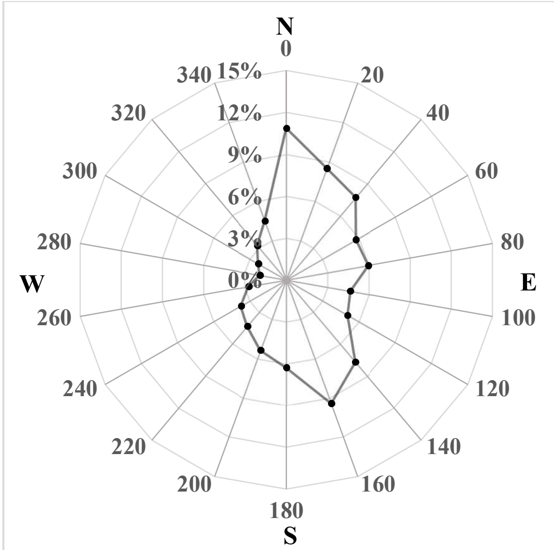

(d) Moncton

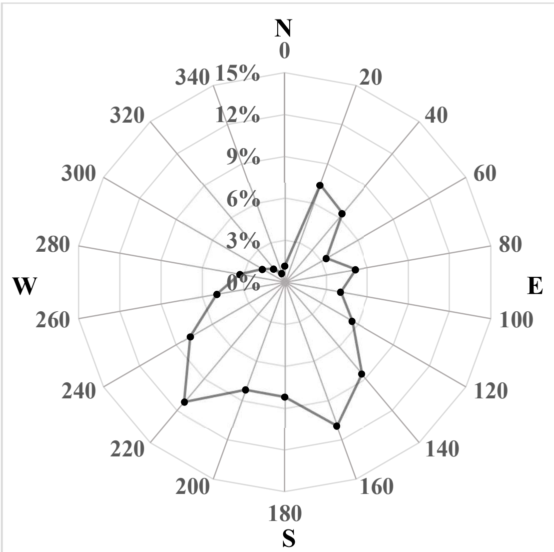

(e) Montreal

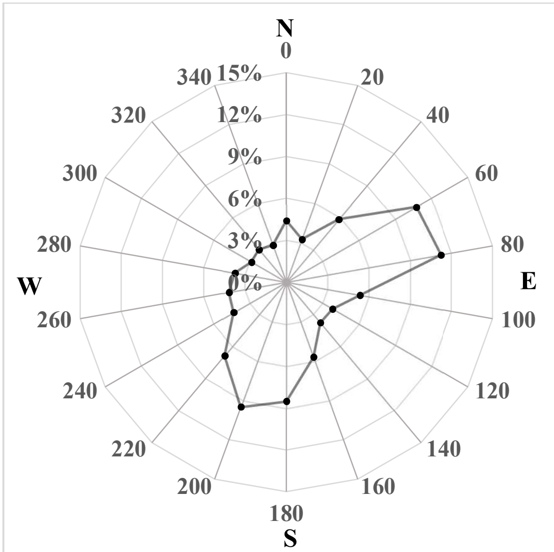

(f) Ottawa

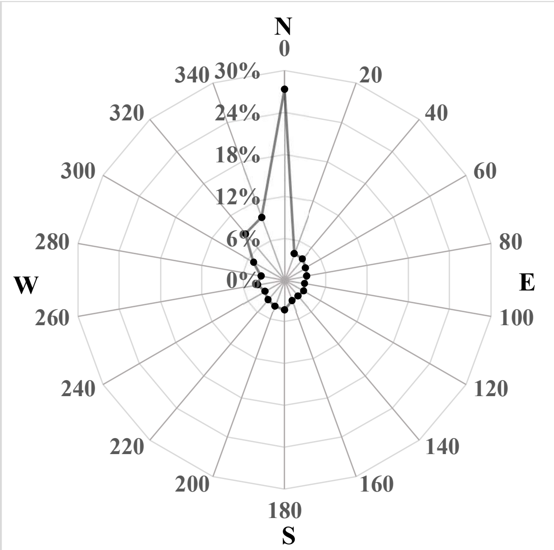

(g) Saskatoon

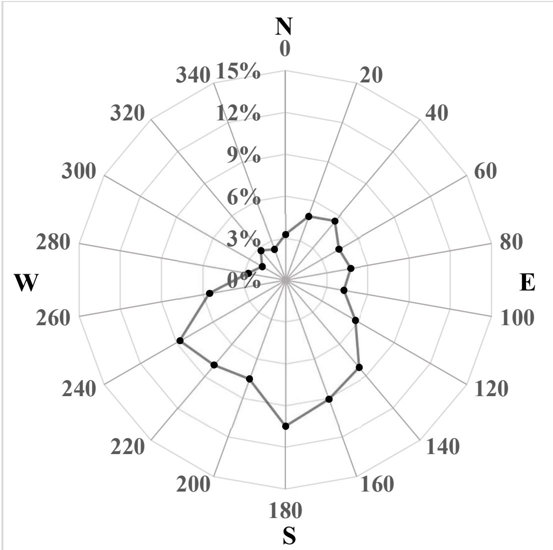

(h) St. John's

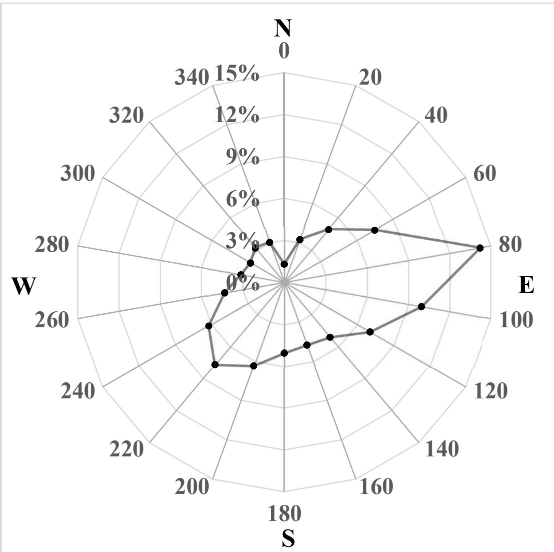

(i) Toronto

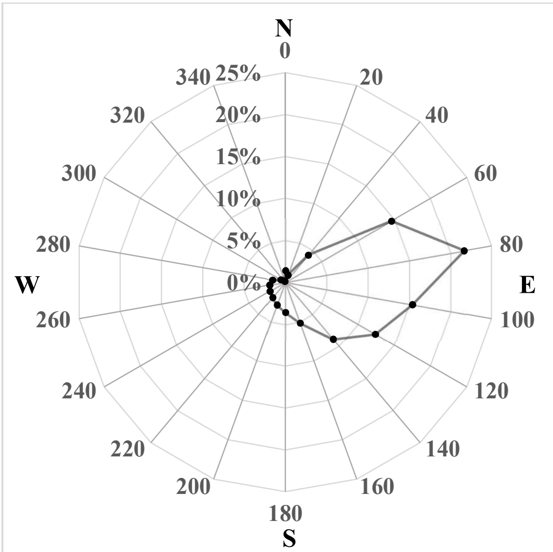

(j) Vancouver

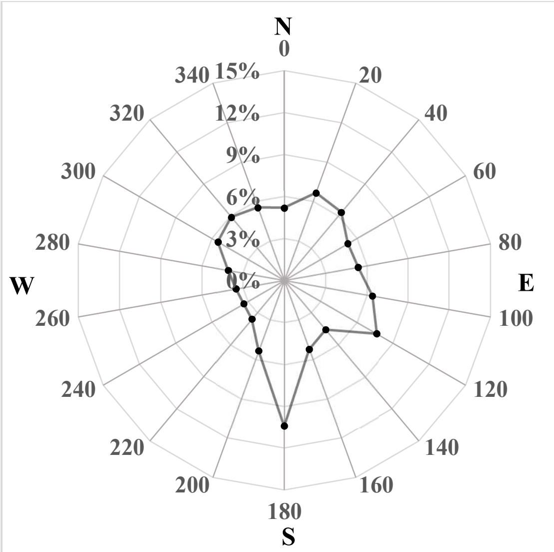

(k) Winnipeg

Figure 3.4 Distributions of wind directions during rain events

3.1.5 Extreme Value Analysis

A watertightness protocol permits determining the risk and thereafter, the acceptable range of risk of water entry to a wall assembly when subjecting the wall to all possible WDR conditions for a given climate zone or location. Such boundary conditions considering both the magnitude and the probability of occurrence could be derived from the EVA of historical climate data. Semi-empirical and theoretical models have been used to analyze the precipitation and have been validated by hydraulic applications, whereas few efforts have been made to analyze WDR loads and thus no models could be referenced. As such, goodness of fit tests has been added to this analysis to examine the quality of the models being implemented. In addition, an approach is discussed to derive the magnitude of DRWP at a required probability of occurrence, by studying the magnitude and probability of occurrence of concurrent WDR.

The first step of this analysis was to fit the observed datasets with selected distributions for which parameters were obtained through the fitting process. Thereafter, values of events could be calculated by inserting probabilities of occurrence for different return periods into the inverse distribution function using the parameters generated. Annual maximum averaged WDR intensity and hourly WDRP index values for any 1, 2, 4 ,8 ,12 and 24 consecutive hours, from the 31-year historical data were used to fit with the Fréchet, Weibull, Gumbel, and Generalized Extreme Value distributions. Their values at 2, 5, 10, 20, 50, and 100-year return periods were then calculated to generate the IDF curves. The averaged WDR intensity for a consecutive hourly event equals the total WDR load collected during these hours divided by the number of hours; the hourly values of WDRP index were also calculated in the same way. The annual maximum values for each type of data were selected from the observed datasets. Thus, for a 31 year period, each dataset would have 31 annual maxima, whereas Cook (1985) has suggested having at least 20 annual maxima when implementing an EVA.

3.1.5.1 Goodness of fit tests

The Chi-square test (Pearson, 1900) and Bayesian Information Criterion (BIC) (Schwarz, 1978) were used to exam the goodness of fit for all tested distributions. From the expression of the Chi-square test, a smaller value for χ^2 means a relatively small gap between the observed and expected data generated by a given distribution. Compared to the Chi-square test, the BIC applies a penalty term for the number of parameters in the distribution as it may lead to overfitting of data, for which overfitting is the output of a curve fitting process that comes closely to a portion of the data but may fail thereafter to fit the remainder of the data. Thus, smaller values of BIC represent a greater likelihood of fit.

To select the best distributions to fit the WDR intensity and WDRP index data, the test results for all distributions have been listed together and scores were applied based on their likelihood of occurrence. As shown in Table A.1 and Table A.2 in the Appendix, the distribution with the greatest likelihood for a fitting of one set of data was marked with a green color and given 2 points. The second greatest likelihood for the same set of data was marked with a yellow color and given 1 point. Thus, a greater value for the sum of the scores of a distribution represents the preferred choice to be used to fit the data. A summary of the scores for each distribution type is given in Table 3-3.

The GEV distribution obtained the highest scores for both goodness of fit test criteria; this means that for most of the cases, the GEV distribution generated a greater likelihood for a good fit than other distributions. In comparison, the Gumbel distribution would be considered the second choice to be used to fit the WDR intensity and WDRPI data, as it received the 2nd highest score amongst these four distributions. It was noted that the

Gumbel distribution obtained a higher score under the BIC test than under the Chi-square test, which was attributed to a penalty term applied by the BIC method to the number of parameters in the distributions, given that there are only two parameters in the Gumbel distribution and three parameters in the GEV distribution.

Table 3-3 Goodness of fit test scores

	Chi-square test			**BIC**		
Distributions	WDR Scores	WDRPI Scores	Total Scores	WDR Scores	WDRPI Scores	Total Scores
Fréchet	20	24	44	19	24	43
Weibull	12	22	34	11	18	29
Gumbel	36	23	59	60	39	99
GEV	130	129	259	108	117	225

Other than estimating the likelihood of the distributions, the hypothesis test has also been conducted to determine if the sample data are consistent with the hypothesized distributions. The null hypothesis states that the data are consistent with a specified distribution and the alternative hypothesis states that the data are not consistent with a specified distribution. A 0.05 significance level, which is the probability of the test rejecting the null hypothesis, was the criteria for the current test. If the generated value of Chi-square goodness of fit test χ^2_1 is greater than the table value χ^2_2 (Table A.3), the null hypothesis would be rejected. The Chi-square table value was determined based on the significance level and the degree of freedom (DOF). In this study, the DOF for a two-parameter distribution is 28 and for a three-parameter distribution is 27; their corresponding values for χ^2_2 are 41.3 and 40.1 respectively. The maximum Chi-square test value χ^2_1 from Table A.1 is 3.77 which is much lower than values given in Table A.3. As such, the null hypothesis was accepted. No significant difference could be found between the observed data and the data generated from the distribution.

3.1.5.2 IDF and extreme values

The Gumbel and GEV distributions, which obtained higher scores than the other two distributions, have been used to generate IDF curves to provided information of WDR intensities and WDRPI for each consecutive hourly event. WDR intensities for 1-hour and 24-consecutive hourly events, respectively representing the upper and lower limits of rain events, varied markedly in different cities, as shown in Figure 3.5. For 1-hour events, and for all return periods, the cities of St. John's and Winnipeg, both distributions generated higher WDR intensities than any of the other cities. Between these two cities, WDR intensities for 2-year, 5-year and 10-year return periods in St. John's were greater than those obtained for Winnipeg and conversely smaller for 20-year, 50-year and 100-year return periods. The maximum WDR intensities observed in Winnipeg for the 100-year return period were 56.1 mm/h from the Gumbel distribution and 312.6 mm/h from the GEV distribution; the significant difference between the values obtained from the respective distributions is discussed in more detail in the subsequent section. Additionally, for WDR intensities during 24-consecutive hourly events, the largest values were observed in St. John's; 11mm/h from the Gumbel distribution and 17.3mm/h from the GEV distribution. The WDR load within 24 hours in St. John's was 264mm and 451.2mm derived from the Gumbel and GEV distributions, respectively. A larger value of 18.7mm/h from the GEV distribution was also noted for Saskatoon. However, such a value was generated by a poor fitting which will next be discussed.

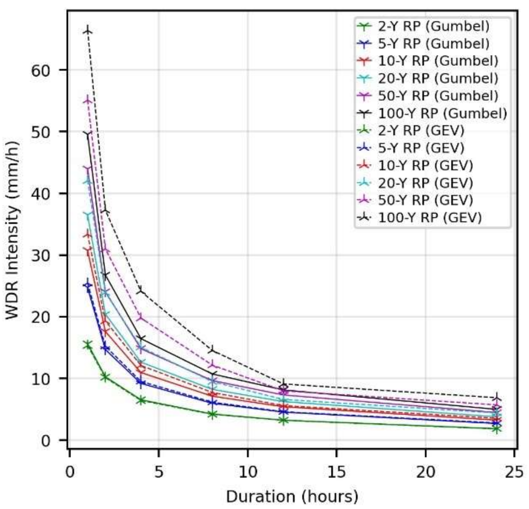

(a) Calgary

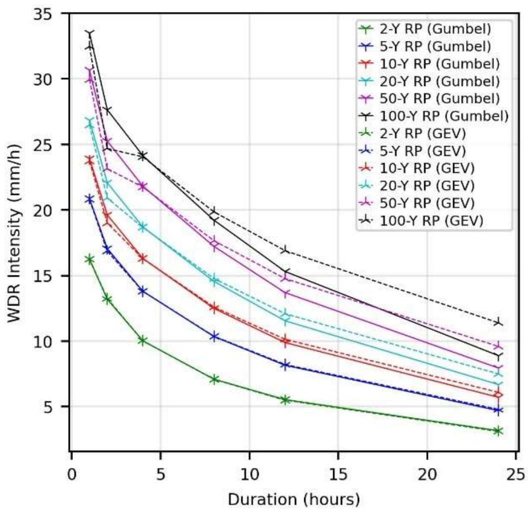

(b) Charlottetown

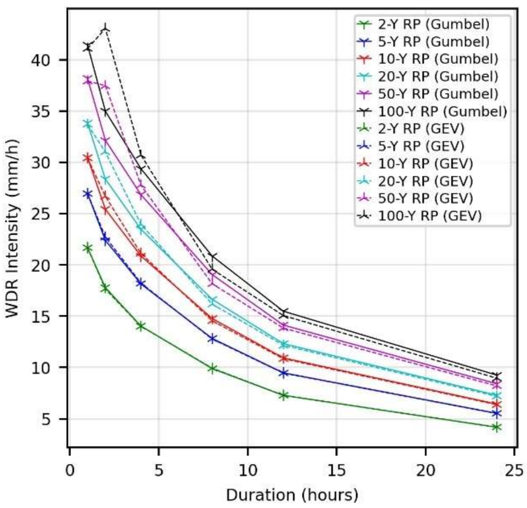

(c) Halifax

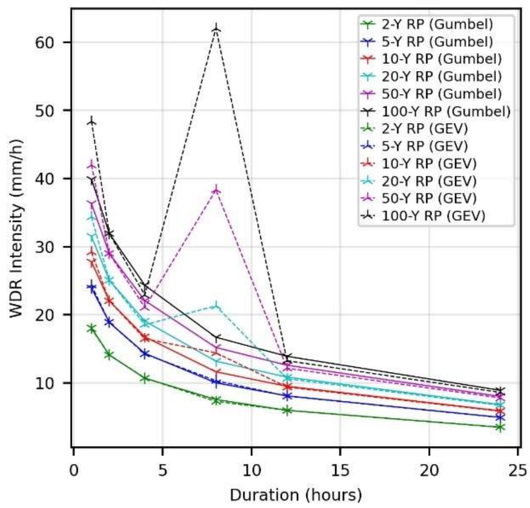

(d) Moncton

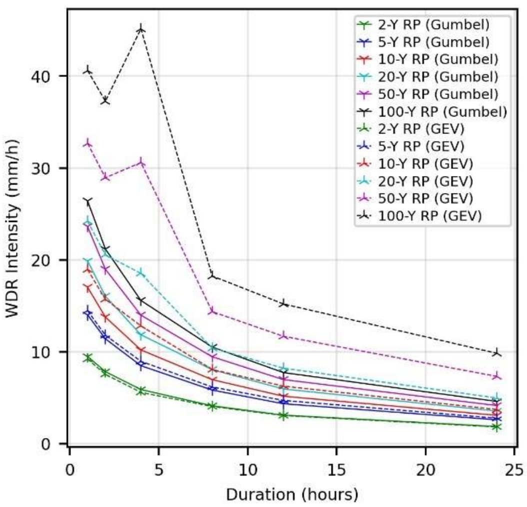

(e) Montreal

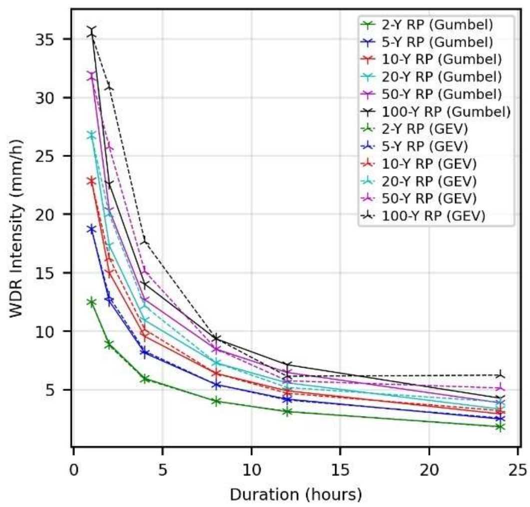

(f) Ottawa

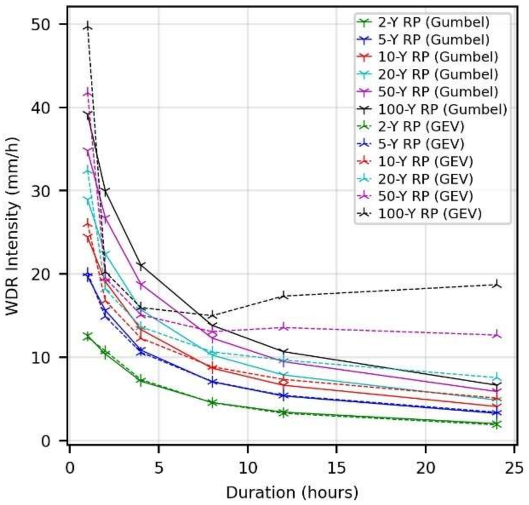

(g) Saskatoon

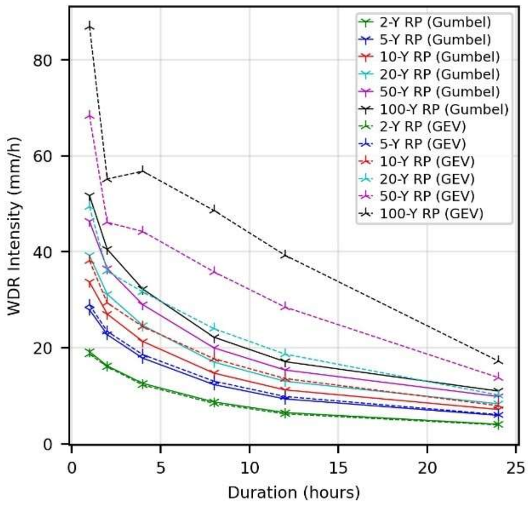

(h) St. John's

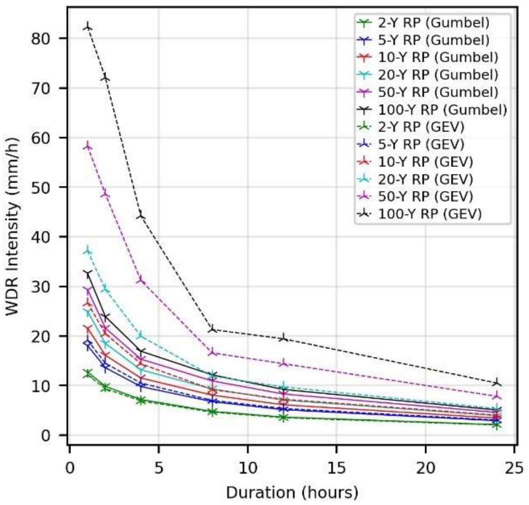

(i) Toronto

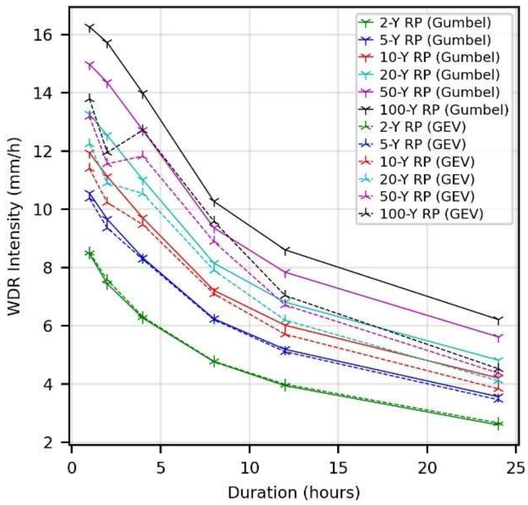

(j) Vancouver

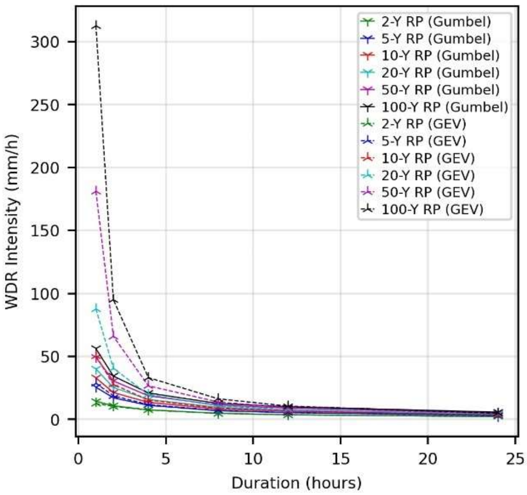

(k) Winnipeg

Figure 3.5 IDF curves for WDR in each city investigated

In all the above extreme WDR values, the GEV distribution generated a much more conservative value than that of the Gumbel distribution in Calgary, Montreal, Saskatoon, St. John's, Toronto, and Winnipeg. Some 'spikes' in the curves generated by the GEV distribution were also noted in: Halifax, Moncton, Montreal, and Vancouver for 50-year and 100-year return periods where WDR intensities at a given duration were larger than that for an adjacent and smaller duration; this is not possible from the observational data, as the averaged value from a longer duration event is always smaller than the average value from a shorter duration event. The reason for such phenomena was mainly attributed to the lack of limitation of the heaviness of distribution tails estimated through the shape factor in the GEV distribution equation. For example, the WDR intensities generated by the GEV distribution in Moncton for the 8-consecutive hourly events at 20-year, 50-year and 100-year return periods were larger than the WDR intensities generated by the same distribution for 4-consecutive hourly events, as well as larger than the WDR intensities generated by the Gumbel distribution for 8-consecutive hourly events, as shown in Figure 3.5 (d).

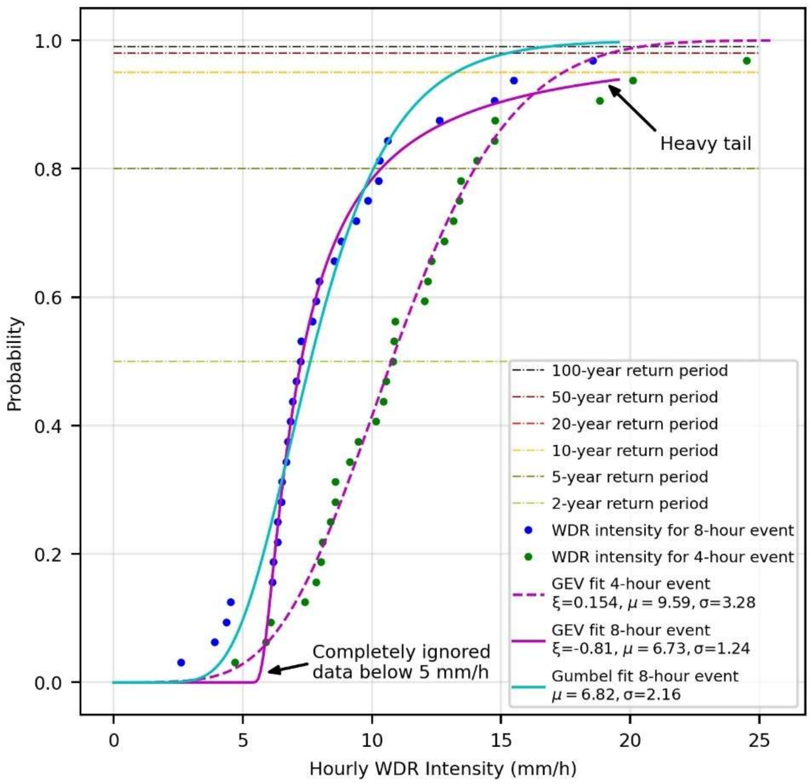

Figure 3.6 Fitting plots of WDR intensities for 8-consecutive hourly events in Moncton

Fitting plots of the three, previously mentioned, cases are presented in Figure 3.6. The probabilities of occurrence for each return period, are also marked in the plot. It is evident that the tail of the GEV distribution for 8-consecutive hourly events is "heavier" than that of the Gumbel distribution for the same event, as well as, the tail of the GEV distribution for 4-consecutive hourly events. Consequently, the value for WDR intensity generated by the GEV distribution, as fitted to the 8-hourly events were much higher than that generated by the GEV distribution fitted to the 4-hourly events and as well, the Gumbel distribution fitted to the 8-hourly events at a 100-year return period (probability of occurrence 0.99). The shape factor ζ of the Gumbel distribution has a constant value of 0, which resulted in changing the tail of the Gumbel distribution to be monotonic; this is a prerequisite for the monotonicity of WDR intensities in the IDF curves. Overfitting is another issue observed in the GEV distribution plots. The GEV distribution fitted values extremely well for hourly WDR intensity larger than 5mm/h, whereas it completely failed to fit values for WDR intensity of less than 5mm/h. For the same case, the Gumbel distribution balanced the fitting for each portion of the data thereby providing a smoother and indeed, monotonical change of WDR intensities in the IDF curves. Given these observations, the Gumbel distribution was considered a better choice than the GEV distribution to fit with WDR data to be used for generating the IDF curves.

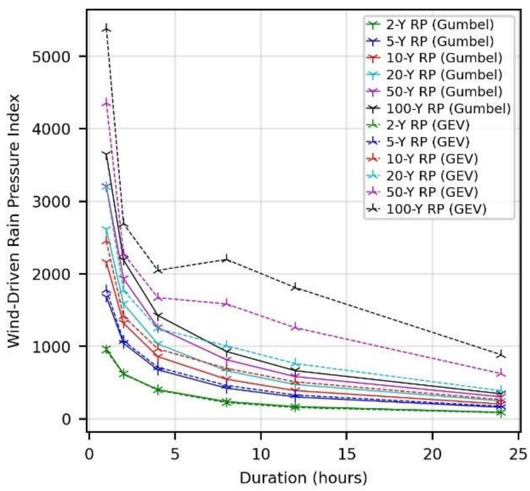

(a) Calgary

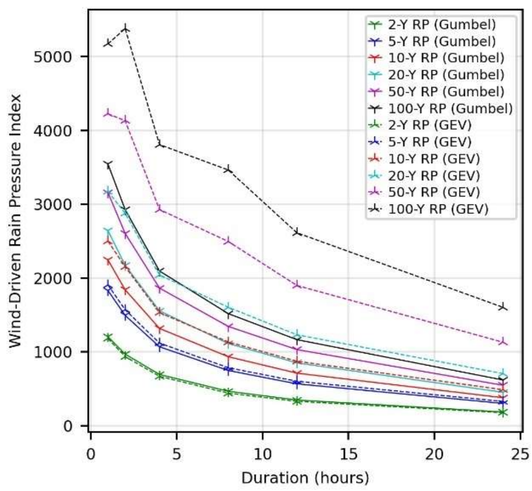

(b) Charlottetown

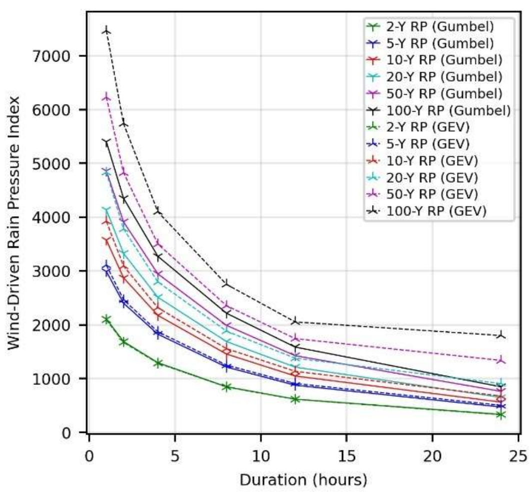

(c) Halifax

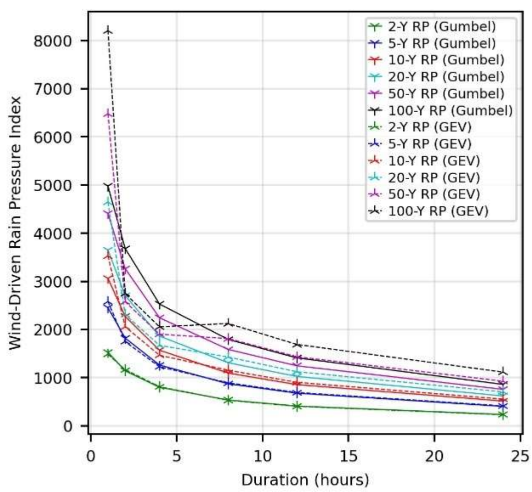

(d) Moncton

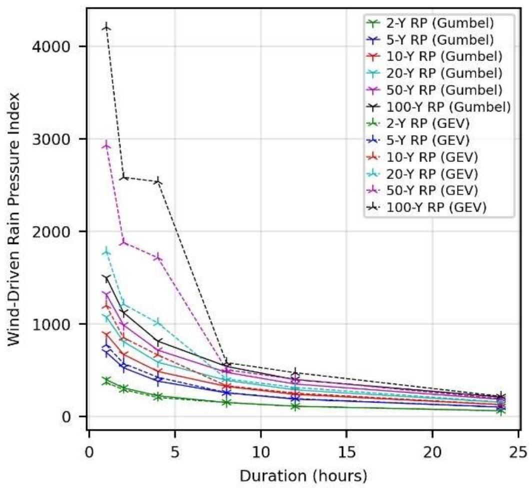

(e) Montreal

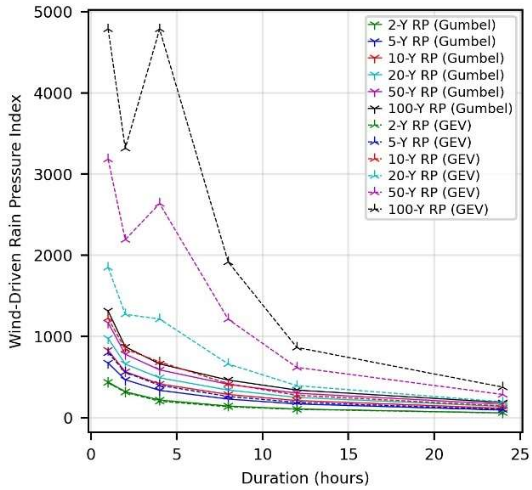

(f) Ottawa

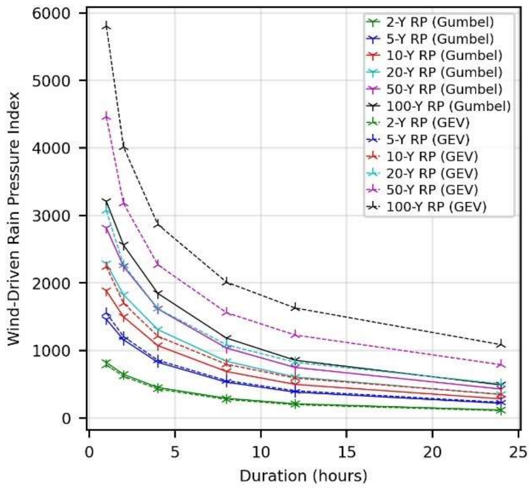

(g) Saskatoon

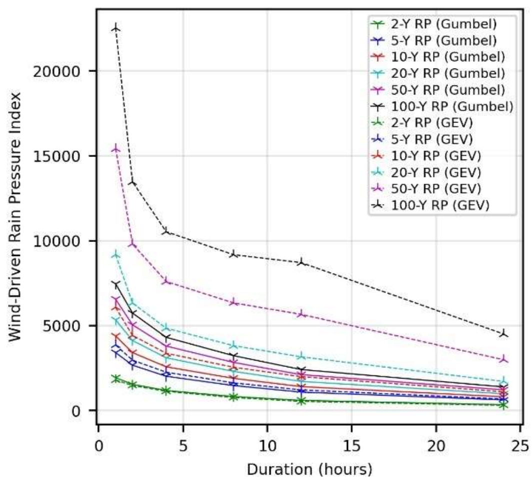

(h) St. John’s

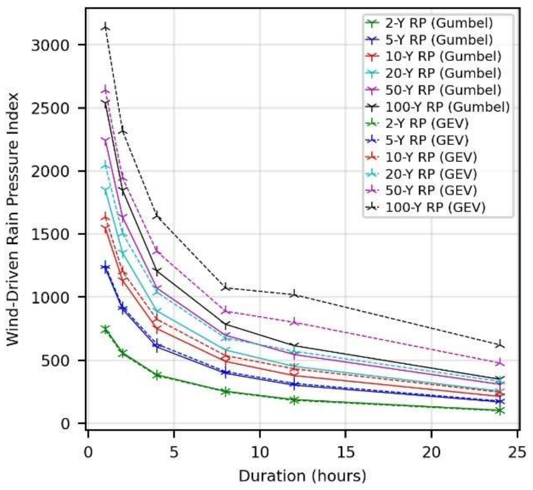

(i) Toronto

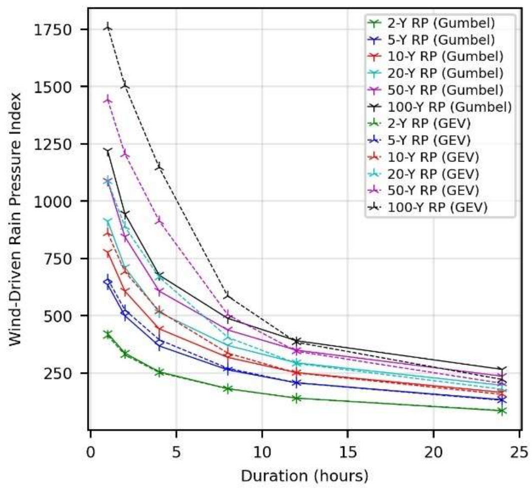

(j) Vancouver

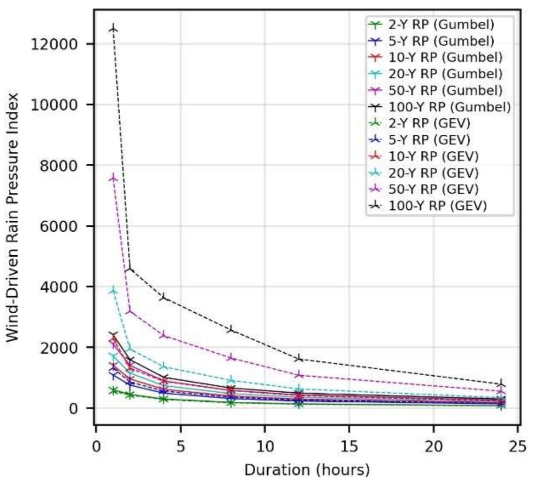

(k) Winnipeg

Figure 3.7 IDF curves for WDRP index in each city investigated

In Figure 3.7, the IDF curves are shown for the hourly WDRP index for the different cities; fittings of values for hourly WDRP index as a function of rain duration (h) are plotted for both the GEV and Gumbel distributions. In most of the scenarios, the GEV distribution generated greater hourly values of WDRP index, as compared to that generated using the Gumbel distribution; this could be determined from controlling tails of the distributions and overfitting, as previously discussed. The highest value for hourly WDRP index occurred in St. John's for all return periods, all hourly duration events, and for both distributions. The values for WDRP indices with a 100-year return period generated by the GEV and Gumbel distributions respectively were, for 1-hour events 22529 and 7470, respectively, and for 24-consecutive hourly events these were 4510 and 1393, respectively.

Table 3-4 WDR and WDRP index for 50 and 100-year return period at different durations

Parameters		WDR		WDRP index	
Cities	Duration	1-hr (mm/h)	24-hr total* (mm)	1-hr	24-hr total*
Calgary	*50-Year*	44	108	3206	7312
	100-Year	49.6	120	3648	8304
Charlottetown	*50-Year*	30.7	191	3157	13112
	100-Year	33.5	213	3543	14828
Halifax	*50-Year*	38.2	202	3665	17723
	100-Year	41.4	222	4092	19655
Moncton	*50-Year*	36.3	192	4410	18170
	100-Year	39.9	213	4979	20640
Montreal	*50-Year*	23.6	99.8	779	4335
	100-Year	26.4	111	883	4901
Ottawa	*50-Year*	32	93	1169	3963
	100-Year	35.9	102	1313	4466
Saskatoon	*50-Year*	34.8	141	2813	10288
	100-Year	39.2	160	3207	11757
St. John’s	*50-Year*	46.4	237	6558	29304
	100-Year	51.7	264	8471	33447
Toronto	*50-Year*	29.3	110	2243	7394
	100-Year	32.6	121	2537	8364
Vancouver	*50-Year*	15	135	1088	5674
	100-Year	16.3	149	1219	6389
Winnipeg	*50-Year*	49.2	123	2116	6401
	100-Year	56.1	137	2414	7277

* Product of 24-hour intensity and 24 hours

Overall, the Gumbel distribution is considered a better option for EVA, as it had a higher score than the Fréchet and Weibull distributions from the goodness of fit test. Also, Gumbel distribution supresses overfitting during the fitting process; this is an essential element to permit generating monotonic and smooth curves to be used for IDF plots.

Extreme values generated by the Gumbel distribution in each city obtained from the analysis are depicted in Table 3-4. For the 50-year and 100-year return periods, the highest WDR intensities for 1-hour events were, respectively, 49.2mm/h and 56.1mm/h, both of which occurred in Winnipeg. Whereas St. John's had the greatest WDR load of 237mm and 264mm, respectively, for the 50-year and 100-year return periods, within 24 hours and the second highest WDR intensities. Additionally, the most extreme WDR conditions, represented by the WDRP index, were also observed in St. John's. Overall, St. John's had a greater chance to experience more severe WDR conditions than most cities in Canada that were studied using the EVA. The extreme WDR intensity obtained for Vancouver was much lower than any other cities whereas the total WDR load over 24 hours ranked 5th amongst the 11 cities studied, this being attributed to the higher frequency of rain events in this location. Wall assemblies in Montreal were exposed to the least severe WDR conditions over the studied period of 31 years, given that the value of the hourly WDRP index was the smallest of all cities examined, whereas Ottawa had the least cumulative value for WDRP index over 24-hour rain events.

3.1.5.3 Extreme DRWP

As discussed in the previous sections, no meaningful correlations could be established between the rainfall intensity and DRWP. In other words, the magnitude and the occurrence of DRWP were independent of the magnitude and occurrence of WDR intensity. Thus, the output of the EVA for the DRWP could not be associated with the output of the EVA for the WDR intensity. The moisture load to which wall assemblies are subjected is the result of the simultaneous action of both WDR and DRWP. The 'co-occurrence' of these actions ought to be taken into account when deriving the magnitude of these two parameters. The WDRP index represents the joint action of WDR concurrent with the DRWP and were used to balance the relative magnitudes of these two parameters. The maximum value of the WDRP index permits determining the extent of influence of the two concurrent climate load parameters in respect to the risk of water entry, and such a limit was not necessarily the upper limit for the uncorrelated parameters. For instance, the maximum value for the WDRP index in St. John's was 10096, as shown in Figure 3.3(h). The WDR intensity and concurrent DRWP for this event were 44.8mm/h and 225Pa respectively, whereas, as shown in Table 3-2, the maximum value of WDR intensity and maximum value of DRWP were 54.4mm/h and 288Pa respectively. The events with the maximum WDR intensity and the maximum DRWP may not render the worst WDR conditions, which is reflected by the value of the WDRP index. Thus, a reasonable DRWP magnitude should be derived from the relevant values of WDR intensity and the WDRP index.

As given in Eq. (5), the DRWP could be calculated from the WDRP index, by knowing the magnitude of the WDR intensity. However, once the EVA is applied, the probabilities of occurrence of these 3 parameters also need to be considered. A 100-year return period represents a 1% probability of occurrence of an event within a year. If the event was derived from two uncorrelated events, then the product of probabilities of occurrence of the two events also has to be 1%. Thus, to obtain the DRWP for a 50-year return period (2% probability of occurrence), the corresponding WDR intensity and the WDRP index used in the calculation should be for a 2-year return period (50% probability of occurrence) and 100-year return period respectively (1% probability of occurrence). The DRWP calculated based on the values of WDRP index at a 100-year return period and 2-year return period of WDR, as listed in Table 3-5. The highest hourly DRWP during 1-hour events for a 50-year return period was observed in St. John's, the value of which was 324 Pa. The second highest DRWP was obtained in another coastal city, Halifax, whereas Ottawa had the smallest value of DRWP amongst the 11 cities evaluated in this paper.

Table 3-5 Hourly averaged DRWP for 50-year return period

Cities	Calgary	Charlottetown	Halifax	Moncton	Montreal	Ottawa
DRWP (Pa)	189	196	235	225	124	94.5
Cities	Saskatoon	St. John's	Toronto	Vancouver	Winnipeg	
DRWP (Pa)	201	324	156	118	159	

3.1.6 Conclusion

Detailed WDR conditions, as occurred between 1986 and 2016, for 11 major cities located in Canada were described and discussed in this paper. The magnitude of rainfall intensity, DRWP, and WDR intensity, as well as the corresponding frequencies and probabilities of occurrence of rain events, varied considerably amongst the different cities, given their differences in geographic location and hence differences in regional climate.

Vancouver had more rain hours than all the other cities, while having the smallest WDR intensity at the same probability of occurrence. The wind velocity determined during rain events was established not to be relevant in respect to the frequency of rain events, although, in general, the cities with more rain hours should have a higher probability to encounter greater wind velocities. The histograms of rainfall intensity and wind velocity during rain events revealed that the most frequent wind velocity during rain events was less than 5m/s in all cities, whereas no meaningful correlation could be established between these two parameters. Over 90% of rain events in all cities had a WDR intensity of less than 5mm/h. The distribution of values for WDRP index indicated that St. John's had a higher probability to experience more severe WDR conditions than all the other locations studied. The magnitude of parameters obtained from the analysis suggest that greater consideration should be given to more temperate WDR conditions when undertaking a watertightness test.

The Fréchet, Weibull, Gumbel and GEV distributions were used to fit the historical WDR and WDRP index data for the cities, as analyzed in this study. The performance of each distribution was assessed by the goodness of fit test using the Chi-square test and Bayesian information criterion. The Gumbel and GEV distributions were both selected to be used in the EVA to generate the IDF curves for the WDR and WDRP index, as these distributions provided a better fit to the relationships than the Fréchet and Weibull distributions. Although, the hypothesis test suggested no significant difference could be found between the observed data and the data generated by all four distributions. After comparing the data generated by the Gumbel and GEV distributions, it was found that for the GEV distribution overfittings and regularly occurring "heavy tails" were evident from the fitting process. This led to obtaining non-monotonic curves for the IDF plots. Thus, only values generated by the Gumbel distribution were subsequently used for the analysis. As such, St. John's had a greater probability to experience larger values for hourly WDRP index, DRWP, WDR load and 24-hour WDRP index, than all other cities examined in this study, whereas the most severe WDR intensities for 50-year and 100-year return periods were observed for Winnipeg.

Boundary conditions of WDR related parameters obtained in these studies will contribute to the development a watertightness test protocol that will permit establishing relationships between the climate loads acting on buildings and moisture loads in wall assemblies.

3.1.7 References

AAMA 501-05, 2005. Methods of Tests for Exterior Walls. American Architectural Manufacturers Association, Schaumburg, IL.

Abuku, M., Blocken, B., Poesen, J., Roels, S., 2009a. Spreading, splashing and bouncing of wind-driven raindrops on building façades. 11th Am. Conf. Wind Eng.

Abuku, M., Janssen, H., Roels, S., 2009b. Impact of wind-driven rain on historic brick wall buildings in a moderately cold and humid climate: Numerical analyses of mould growth risk, indoor climate and energy consumption. Energy Build. 41, 101–110. https://doi.org/10.1016/j.enbuild.2008.07.011

ASHRAE, 2016. ASHRAE standard 160P-criteria for moisture control design analysis in buildings, ASHRAE Transactions.

ASTM E331-00, 2016. Standard Test Method for Structural Performance of Exterior Windows , Curtain Walls , and Doors by Uniform Static Air Pressure Difference. ASTM International, West Conshohocken, PA. https://doi.org/10.1520/E0331-00R16

Blocken, B., Carmeliet, J., 2006. The influence of the wind-blocking effect by a building on its wind-driven rain exposure. J. Wind Eng. Ind. Aerodyn. 94, 101–127. https://doi.org/10.1016/j.jweia.2005.11.001

Blocken, B., Carmeliet, J., 2005. High-resolution wind-driven rain measurements on a low-rise building—experimental data for model development and model validation. J. Wind Eng. Ind. Aerodyn. 93, 905–928. https://doi.org/10.1016/j.jweia.2005.09.004

Blocken, B., Carmeliet, J., 2004. A review of wind-driven rain research in building science. J. Wind Eng. Ind. Aerodyn. 92, 1079–1130. https://doi.org/10.1016/j.jweia.2004.06.003

Blocken, B., Dezsö, G., van Beeck, J., Carmeliet, J., 2009. The mutual influence of two buildings on their wind-driven rain exposure and comments on the obstruction factor. J. Wind Eng. Ind. Aerodyn. 97, 180–196. https://doi.org/10.1016/j.jweia.2009.06.003

Boardman, C.R., Glass, S. V., 2013. Investigating wind-driven rain intrusion in walls with the CARWASh, in: Thermal Performance of the Exterior Envelopes of Whole Buildings - 12th International Conference.

Bossche, N. Van Den, Lacasse, M., Moore, T., Janssens, A., 2012. Water infiltration through openings in a vertical plane under static boundary conditions, in: Proceedings of the 5th IBPC. Kyoto, Japan.

Charola, A.E., Lazzarini, L., 1986. Deterioration of Brick Masonry Caused by Acid Rain, in: ACS Symposium Series. pp. 250–258. https://doi.org/10.1021/bk-1986-

0318.ch017
Choi, E.C.C., 1994. Characteristics of the co-occurrence of wind and rain and the driving-rain index. J. Wind Eng. Ind. Aerodyn. 53, 49–62. https://doi.org/10.1016/0167-6105(94)90018-3
Chouinard, K.L., Lawton, M.D., 2001. Rotting wood framed apartments-Not just a Vancouver problem. Proc 8th Can. Conf. Build. Sci. Technol. 304–318.
Chow, V. Te, 1962. Hydrologic determination of waterway areas for the design of drainage structures in small drainage basins. Eng. Exp. Stn. Bull. 462, 104.
Cook, N.J., 1985. The designer's guide to wind loading of building structures. Part 1: background, damage survey, wind data and structural classification.
Cornick, S.M., Lacasse, M.A., 2010. An Investigation of Climate Loads on Building Façades for Selected Locations in the United States, in: Symposium on "Up Against the Wall": An Examination of Building Envelope Interface. ASTM International, 100 Barr Harbor Drive, PO Box C700, West Conshohocken, PA 19428-2959, pp. 12-12–36. https://doi.org/10.1520/STP48941S
Desjarlais, A.O., Karagiozis, A.N., Aoki-Kramer, M., 2001. Wall moisture problems in Seattle. Build. VIII proceedings, ASHRAE, 8p.
EN 12865, 2001. BS EN 12865:2001 Hygrothermal performance of building components and building elements. Determination of the resistance of external wall systems to driving rain under pulsating air pressure. Br. Stand. Inst.
Franke, L., Schumann, I., Hees, R. van, Klugt, L. van der, Naldini, S., Binda, L., Balen, K. van, Baronio, G., Mateus, J., 1998. Damage Atlas: Classification and Analyses of Damage Patterns Found in Brick Masonry, Protection and Conservation of European Cultural Heritage, Research Report No. 8, Volume 2. Fraunhofer IRB Verlag.
Ge, H., Chiu, V., Stathopoulos, T., Souri, F., 2018. Improved assessment of wind-driven rain on building façade based on ISO standard with high-resolution on-site weather data. J. Wind Eng. Ind. Aerodyn. 176, 183–196. https://doi.org/10.1016/j.jweia.2018.03.013
Ge, H., Deb Nath, U.K., Chiu, V., 2017. Field measurements of wind-driven rain on mid- and high-rise buildings in three Canadian regions. Build. Environ. 116, 228–245. https://doi.org/10.1016/j.buildenv.2017.02.016
Hoppestad, S., 1955. Slagregn i Norge. Norwegian Building Research Institute, Oslo.
ISO, 2009. ISO 15927-3, Hygrothermal performance of buildings Calculation and presentation of climatic data Part 3: Calculation of a driving rain index for vertical surfaces from hourly wind and rain data.
Karagiozis, A., Hadjisophocleous, G., Cao, S., 1997. Wind-driven rain distributions on two buildings. J. Wind Eng. Ind. Aerodyn. 67–68, 559–572. https://doi.org/10.1016/S0167-6105(97)00100-1
Kubilay, A., Derome, D., Blocken, B., Carmeliet, J., 2015. Wind-driven rain on two parallel wide buildings: Field measurements and CFD simulations. J. Wind Eng. Ind. Aerodyn. 146, 11–28. https://doi.org/10.1016/j.jweia.2015.07.006
Kubilay, A., Derome, D., Blocken, B., Carmeliet, J., 2014. High-resolution field measurements of wind-driven rain on an array of low-rise cubic buildings. Build. Environ. 78, 1D., Blocken, B., Carmeliet, J., 2014. High-resoluti
Lacasse, M.A., O'Connor, T., Nunes, S.C., Beaulieu, P., 2003. Report from Task 6 of MEWS Project: Experimental Assessment of Water Penetration and Entry into

Wood-Frame Wall Specimens - Final Report, Research Report (National Research Council of Canada. Institute for Research in Construction); no. RR-133.
Lacy, R.E., 1977. Climate and building in Britain. London:, Her Majesty's Stationery Office. John Wiley & Sons, Ltd. https://doi.org/10.1002/qj.49710544325
Linsley, R., Kohler, M., JLH, P., 1975. Applied hydrology. McGraw-Hill, New York, US.
Mayo, A.P., 1998. Task 3 Define the conditions to be reproduced in the standard test –To develop a European standard dynamic water tightness test for curtain walling, Building Research Establishment.
Pearson, K., 1900. X. On the criterion that a given system of deviations from the probable in the case of a correlated system of variables is such that it can be reasonably supposed to have arisen from random sampling. London, Edinburgh, Dublin Philos. Mag. J. Sci. 50, 157–175. https://doi.org/10.1080/14786440009463897
Pérez-Bella, J.M., Domínguez-Hernández, J., Rodríguez-Soria, B., del Coz-Díaz, J.J., Cano-Suñén, E., 2013. Combined use of wind-driven rain and wind pressure to define water penetration risk into building façades: The Spanish case. Build. Environ. 64, 46–56. https://doi.org/10.1016/j.buildenv.2013.03.004
Rousseau, M., 1999. Overview of the survey of building envelope failures in the coastal climate of British Columbia, performed by Morrisson-Hershfield Limited for CMHC (1996). J. Therm. Envel. Build. Sci. 22, 364–367. https://doi.org/10.1177/109719639902200411
Sacré, C., 1984. Concomitance de la plui et du vent en France: approche statistique., in: Colloque de Centre Scientifique et Technique Du B Envel. Build. Sci. à l'eau Des Couvertures et Petits Éléments Sous l'effet de La Concomitance Vent-Plui. pp. 18–21.
Sahal, N., Lacasse, M.A., 2005. Water entry function of a hardboard siding-clad wood stud wall. Build. Environ. 40, 1479a hardboard siding-clad wood stud wallenv.2004.11.019
Sahal, N., Lacasse, M.A., 2004. Experimental Assessment of Water Penetration and Entry into Siding-Clad Wall Specimen. NRC Publications Archive. https://doi.org/10.4224/20377802
Schwarz, G., 1978. Estimating the Dimension of a Model. Ann. Stat. 6, 461–464. https://doi.org/10.1214/aos/1176344136
Sherman, C.W., 1931. Frequency and Intensity of Excessive Rainfalls at Boston, Massachusetts. Trans. Am. Soc. Civ. Eng. 95, 951–960. https://doi.org/10.1061/TACEAT.0004286
Smegal, J., Lstiburek, J., Straube, J., Grin, A., 2013. Moisture-related durability of walls with exterior insulation in the pacific northwest, in: Thermal Performance of the Exterior Envelopes of Whole Buildings - 12th International Conference. American Society of Heating, Refrigeration, and Air-Conditioning Engineers (ASHRAE).
Straube, J.F., Burnett, E.F.P., 2000. Simplified prediction of driving rain on buildings, in: Proceedings of the International Building Physics Conference. pp. 375–382.
Surry, D., Skerlj, P., Mikitiuk, M., 1997. An Exploratory Study of the Climatic Relationships between Rain and Wind. J. Therm. Insul. Build. Envel. 21, 121–124. https://doi.org/10.1177/109719639702100202
Tang, W., Davidson, C.I., Finger, S., Vance, K., 2004. Erosion of limestone building surfaces caused by wind-driven rain: 1. Field measurements. Atmos. Environ. 38,

5589–5599. https://doi.org/10.1016/j.atmosenv.2004.06.030
Van Balen, K., 1996. Expert system for evaluation of deterioration of ancient brick masonry structures. Sci. Total Environ. 189–190, 247–254. https://doi.org/10.1016/0048-9697(96)05215-1
Van Den Bossche, N., Lacasse, M.A., Janssens, A., 2013. A uniform methodology to establish test parameters for watertightness testing part II: Pareto front analysis on co-occurring rain and wind. Build. Environ. 63, 157o establish test parameters for watertightness testi
Wang, X.J., Li, Q.S., Li, J.C., 2020. Field measurements and numerical simulations of wind-driven rain on a low-rise building during typhoons. J. Wind Eng. Ind. Aerodyn. 204, 104274. https://doi.org/10.1016/j.jweia.2020.104274

3.1.8 Appendix A

Table A.1 Chi-Square test results

Chi-Square Test		WDR						WDRP					
Cities	Durations	1H	2H	4H	8H	12H	24H	1H	2H	4H	8H	12H	24H
CAL	**Fréchet**	0.077	0.075	0.267	0.503	0.133	0.742	0.112	0.179	1.753	0.317	0.141	0.112
	Weibull	0.194	0.286	0.152	0.159	0.137	0.265	0.107	0.134	0.133	0.250	0.248	0.218
	GBL	0.126	0.104	0.086	0.087	0.102	0.171	0.146	0.165	0.150	0.236	0.244	0.253
	GEV	0.051	0.067	0.081	0.087	0.102	0.163	0.106	0.141	0.109	0.056	0.022	0.034
CHAR	**Fréchet**	0.282	0.389	0.112	0.428	0.137	0.876	0.760	0.081	0.291	0.168	0.069	0.063
	Weibull	0.083	0.071	0.187	0.239	0.241	0.523	0.197	0.197	0.373	0.364	0.311	0.326
	GBL	0.107	0.113	0.109	0.163	0.166	0.217	0.094	0.146	0.231	0.238	0.208	0.161
	GEV	0.073	0.070	0.097	0.147	0.125	0.172	0.046	0.076	0.173	0.130	0.061	0.052
HALI	**Fréchet**	0.246	0.211	0.868	0.327	0.854	0.366	0.582	0.716	1.331	1.835	0.249	0.313
	Weibull	0.101	0.382	0.259	0.218	0.134	0.115	0.287	0.186	0.180	0.129	0.155	0.217
	GBL	0.049	0.044	0.107	0.090	0.066	0.025	0.156	0.134	0.158	0.148	0.210	0.224
	GEV	0.042	0.036	0.107	0.089	0.064	0.023	0.156	0.132	0.149	0.125	0.139	0.201
MONC	**Fréchet**	0.252	0.241	0.112	0.328	0.238	0.391	0.407	0.115	0.590	0.613	0.090	3.605
	Weibull	0.146	0.202	0.083	0.292	0.112	0.053	0.142	0.100	0.092	0.075	0.056	0.066
	GBL	0.066	0.173	0.076	0.316	0.186	0.079	0.097	0.107	0.102	0.088	0.079	0.097
	GEV	0.066	0.152	0.060	0.327	0.103	0.049	0.059	0.104	0.099	0.069	0.049	0.058
MONT	**Fréchet**	1.041	0.563	0.109	0.082	0.168	0.180	0.405	0.398	0.187	0.433	0.415	0.323
	Weibull	0.907	0.783	0.826	0.302	0.263	0.524	0.379	0.292	0.299	0.405	0.472	0.263
	GBL	0.467	0.562	0.328	0.082	0.185	0.243	0.428	0.270	0.397	0.396	0.458	0.254
	GEV	0.213	0.172	0.107	0.053	0.140	0.148	0.128	0.112	0.089	0.259	0.337	0.214
OTT	**Fréchet**	0.074	0.485	1.778	1.506	3.768	0.060	0.244	0.206	0.128	0.138	0.088	0.287
	Weibull	0.075	0.256	0.576	0.316	0.082	0.290	0.373	0.204	0.554	0.401	0.305	0.205
	GBL	0.055	0.072	0.229	0.123	0.052	0.090	0.203	0.171	0.304	0.302	0.195	0.197
	GEV	0.055	0.051	0.102	0.092	0.050	0.060	0.155	0.164	0.112	0.129	0.060	0.099
SASK	**Fréchet**	1.084	0.370	0.115	0.423	0.388	0.174	0.741	1.236	1.753	0.860	0.578	0.388
	Weibull	0.168	0.103	0.083	0.113	0.285	0.447	0.087	0.080	0.135	0.095	0.110	0.143
	GBL	0.095	0.151	0.076	0.087	0.216	0.321	0.222	0.228	0.243	0.206	0.197	0.320

	GEV	0.064	0.108	0.068	0.086	0.203	0.153	0.061	0.068	0.100	0.084	0.067	0.046
ST.J	**Fréchet**	0.108	0.247	0.093	0.086	0.072	0.370	0.186	0.046	0.207	0.187	0.206	0.380
	Weibull	0.370	0.307	0.388	0.580	0.939	0.421	0.334	0.129	0.288	0.291	0.527	0.669
	GBL	0.173	0.116	0.161	0.261	0.261	0.218	0.282	0.208	0.187	0.354	0.425	0.616
	GEV	0.062	0.109	0.083	0.085	0.069	0.096	0.062	0.045	0.094	0.055	0.076	0.115
TOR	**Fréchet**	0.077	0.184	0.082	0.112	0.104	0.109	0.081	0.563	1.553	1.059	0.077	0.267
	Weibull	0.740	1.190	0.904	0.439	0.519	0.531	0.104	0.146	0.109	0.082	0.109	0.229
	GBL	0.276	0.615	0.285	0.187	0.150	0.235	0.126	0.133	0.080	0.059	0.096	0.174
	GEV	0.073	0.134	0.074	0.103	0.091	0.095	0.078	0.126	0.063	0.058	0.064	0.072
VAN	**Fréchet**	0.295	0.179	1.066	0.174	0.177	0.261	0.164	0.421	0.208	0.245	0.145	0.115
	Weibull	0.098	0.272	0.356	0.105	0.069	0.080	0.374	0.315	0.215	0.241	0.128	0.121
	GBL	0.154	0.169	0.140	0.118	0.159	0.165	0.216	0.168	0.119	0.227	0.128	0.114
	GEV	0.075	0.169	0.118	0.072	0.066	0.079	0.107	0.093	0.102	0.226	0.122	0.106
WINNI	**Fréchet**	0.241	0.133	0.168	0.518	1.712	0.802	0.113	0.073	0.061	0.067	0.075	0.107
	Weibull	0.464	0.220	0.277	0.140	0.169	0.071	0.210	0.146	0.215	0.489	0.267	0.243
	GBL	0.571	0.137	0.148	0.060	0.127	0.078	0.358	0.145	0.199	0.318	0.287	0.254
	GEV	0.181	0.085	0.142	0.058	0.126	0.067	0.079	0.038	0.051	0.065	0.061	0.051

Table A.2 BIC test results

BIC		**WDR**						**WDRP**					
Cities	Durations	1H	2H	4H	8H	12H	24H	1H	2H	4H	8H	12H	24H
CAL	**Fréchet**	-175	-176	-137	-117	-159	-105	-164	-149	-79	-132	-157	-164
	Weibull	-147	-135	-155	-153	-158	-137	-165	-158	-159	-139	-139	-143
	GBL	-164	-170	-175	-175	-170	-154	-159	-155	-158	-144	-143	-142
	GEV	-188	-180	-174	-172	-167	-152	-166	-157	-165	-186	-214	-201
CHAR	**Fréchet**	-135	-125	-164	-122	-158	-100	-105	-174	-134	-151	-179	-182
	Weibull	-173	-178	-148	-141	-140	-116	-147	-147	-127	-127	-132	-131
	GBL	-169	-167	-168	-156	-155	-147	-173	-159	-145	-144	-148	-156
	GEV	-177	-179	-169	-156	-161	-151	-192	-176	-151	-159	-183	-188
HALI	**Fréchet**	-140	-144	-101	-131	-101	-127	-113	-106	-87	-77	-139	-132
	Weibull	-167	-126	-138	-143	-158	-163	-135	-148	-149	-160	-154	-144
	GBL	-193	-197	-169	-174	-184	-214	-157	-162	-157	-159	-148	-146
	GEV	-194	-199	-165	-171	-182	-213	-154	-159	-155	-161	-157	-146
MONC	**Fréchet**	-139	-140	-164	-131	-141	-125	-124	-163	-113	-111	-171	-56
	Weibull	-156	-146	-173	-134	-164	-187	-157	-168	-170	-176	-185	-180
	GBL	-184	-154	-179	-135	-152	-178	-172	-169	-170	-175	-178	-172
	GEV	-181	-155	-183	-131	-167	-190	-184	-166	-168	-179	-190	-184
MONT	**Fréchet**	-95	-114	-165	-174	-151	-149	-124	-125	-148	-122	-123	-131
	Weibull	-99	-104	-102	-133	-138	-116	-126	-134	-134	-124	-119	-137
	GBL	-123	-117	-134	-177	-152	-143	-126	-140	-128	-128	-124	-142
	GEV	-144	-151	-165	-187	-157	-155	-160	-164	-171	-138	-130	-144
OTT	**Fréchet**	-177	-119	-78	-83	-55	-183	-140	-145	-160	-158	-172	-135
	Weibull	-176	-138	-113	-132	-174	-134	-127	-145	-114	-125	-133	-145
	GBL	-190	-181	-145	-165	-191	-174	-149	-154	-136	-137	-150	-150
	GEV	-186	-188	-167	-170	-189	-183	-154	-152	-164	-160	-184	-168

SASK	**Fréchet**	-94	-127	-163	-123	-126	-150	-105	-90	-79	-101	-113	-125
	Weibull	-151	-167	-173	-164	-135	-121	-172	-174	-158	-169	-165	-156
	GBL	-172	-158	-180	-175	-147	-135	-146	-145	-143	-149	-150	-135
	GEV	-181	-165	-179	-172	-146	-154	-183	-179	-167	-173	-180	-192
ST.J	**Fréchet**	-165	-140	-170	-172	-178	-127	-148	-191	-145	-148	-145	-126
	Weibull	-127	-133	-126	-113	-98	-123	-130	-160	-135	-134	-116	-109
	GBL	-154	-166	-156	-141	-141	-147	-139	-148	-152	-132	-126	-115
	GEV	-182	-165	-173	-173	-179	-169	-182	-193	-170	-186	-176	-163
TOR	**Fréchet**	-176	-149	-174	-164	-166	-165	-174	-114	-83	-94	-176	-137
	Weibull	-105	-91	-99	-122	-116	-116	-166	-156	-165	-174	-165	-142
	GBL	-140	-115	-138	-152	-158	-144	-164	-162	-178	-187	-172	-154
	GEV	-177	-158	-177	-167	-170	-169	-175	-160	-182	-185	-181	-178
VAN	**Fréchet**	-134	-149	-94	-150	-150	-138	-152	-123	-145	-140	-156	-163
	Weibull	-168	-136	-128	-166	-179	-175	-127	-132	-144	-140	-160	-162
	GBL	-158	-155	-160	-166	-157	-155	-147	-155	-166	-146	-163	-167
	GEV	-176	-151	-162	-178	-181	-175	-165	-170	-167	-142	-161	-166
WINNI	**Fréchet**	-140	-159	-151	-117	-79	-103	-164	-177	-183	-180	-177	-165
	Weibull	-120	-143	-136	-157	-151	-178	-145	-156	-144	-118	-137	-140
	GBL	-117	-161	-159	-187	-164	-179	-131	-159	-150	-135	-138	-142
	GEV	-149	-172	-157	-184	-160	-180	-175	-197	-189	-181	-183	-189

Table A.3 Critical values of the Chi-square distribution with df degree of freedom

	Level of Significance α								
df	0.200	0.100	0.075	0.050	0.025	0.010	0.005	0.001	0.0005
1	1.642	2.706	3.170	3.841	5.024	6.635	7.879	10.828	12.116
2	3.219	4.605	5.181	5.991	7.378	9.210	10.597	13.816	15.202
3	4.642	6.251	6.905	7.815	9.348	11.345	12.838	16.266	17.731
4	5.989	7.779	8.496	9.488	11.143	13.277	14.860	18.467	19.998
5	7.289	9.236	10.008	11.070	12.833	15.086	16.750	20.516	22.106
6	8.558	10.645	11.466	12.592	14.449	16.812	18.548	22.458	24.104
7	9.803	12.017	12.883	14.067	16.013	18.475	20.278	24.322	26.019
8	11.030	13.362	14.270	15.507	17.535	20.090	21.955	26.125	27.869
9	12.242	14.684	15.631	16.919	19.023	21.666	23.589	27.878	29.667
10	13.442	15.987	16.971	18.307	20.483	23.209	25.188	29.589	31.421
11	14.631	17.275	18.294	19.675	21.920	24.725	26.757	31.265	33.138
12	15.812	18.549	19.602	21.026	23.337	26.217	28.300	32.910	34.822
13	16.985	19.812	20.897	22.362	24.736	27.688	29.820	34.529	36.479
14	18.151	21.064	22.180	23.685	26.119	29.141	31.319	36.124	38.111
15	19.311	22.307	23.452	24.996	27.488	30.578	32.801	37.698	39.720
16	20.465	23.542	24.716	26.296	28.845	32.000	34.267	39.253	41.309
17	21.615	24.769	25.970	27.587	30.191	33.409	35.719	40.791	42.881
18	22.760	25.989	27.218	28.869	31.526	34.805	37.157	42.314	44.435
19	23.900	27.204	28.458	30.144	32.852	36.191	38.582	43.821	45.974
20	25.038	28.412	29.692	31.410	34.170	37.566	39.997	45.315	47.501
21	26.171	29.615	30.920	32.671	35.479	38.932	41.401	46.798	49.013
22	27.301	30.813	32.142	33.924	36.781	40.289	42.796	48.269	50.512
23	28.429	32.007	33.360	35.172	38.076	41.639	44.182	49.729	52.002
24	29.553	33.196	34.572	36.415	39.364	42.980	45.559	51.180	53.480
25	30.675	34.382	35.780	37.653	40.646	44.314	46.928	52.620	54.950
26	31.795	35.563	36.984	38.885	41.923	45.642	48.290	54.053	56.409
27	32.912	36.741	38.184	40.113	43.195	46.963	49.645	55.477	57.860
28	34.027	37.916	39.380	41.337	44.461	48.278	50.994	56.894	59.302
29	35.139	39.087	40.573	42.557	45.722	49.588	52.336	58.302	60.738
30	36.250	40.256	41.762	43.773	46.979	50.892	53.672	59.704	62.164
40	47.269	51.805	53.501	55.759	59.342	63.691	66.766	73.403	76.097
50	58.164	63.167	65.030	67.505	71.420	76.154	79.490	86.662	89.564
60	68.972	74.397	76.411	79.082	83.298	88.380	91.952	99.609	102.698
70	79.715	85.527	87.680	90.531	95.023	100.425	104.215	112.319	115.582
80	90.405	96.578	98.861	101.880	106.629	112.329	116.321	124.842	128.267
90	101.054	107.565	109.969	113.145	118.136	124.117	128.300	137.211	140.789
100	111.667	118.498	121.017	124.342	129.561	135.807	140.170	149.452	153.174

3.2 Assessing the Moisture Load in a Vinyl-Clad Wall Assembly through Watertightness Test

Zhe Xiao, Michael A. Lacasse, Maurice Defo and Elena Dragomirescu

Buildings 2021, 11, 117

3.2.1 Abstract

The moisture load in wall assemblies is typically considered as 1% of the Wind Driving Rain (WDR) load that is deposited on the surface of wall assemblies as specified in the ASHRAE-160 standard whereas this ratio has been shown to be inaccurate as compared to results derived from several watertightness tests. Accurate assessment of moisture loads arising from WDR can be obtained through the watertightness test during which different levels of WDR intensities and Driving Rain Wind Pressures (DRWPs) are applied to a test specimen and water that penetrates wall assembly can thus be quantified. Although many previous studies have included water-tightness tests, only a few of these have attempted to correlate the moisture loads to WDR conditions as may occur in specific locations within a country. To improve the assessment of moisture loads for a vinyl-clad wall assembly, a wall test specimen was tested following a test protocol based on local climate data using National Research Council of Canada's Dynamic Wind and Wall Testing Facility (DWTF). The use of this test protocol permitted quantifying the moisture load in the vinyl wall assembly when subjected to several different simulated WDR conditions. The moisture load was formulated as a function of the WDR intensity and DRWP which thereafter allowed evaluating the moisture load based on a given climate's hourly rainfall intensity and wind velocity. Such work is particularly relevant considering that the intensity, duration and frequency of WDR events across Canada will in some regions increase due to the effects of climate change.

Keywords: wood frame wall; vinyl cladding; wind-driven rain; watertightness test; moisture load; water entry function

3.2.2 Introduction

The long-term moisture performance and hence, durability of building façades are adversely affected by the moisture load, in particular those arising from the wind-driven rain (WDR) (Kumaran et al., 2003; Lacasse & Vanier (Eds.), 1999a, 1999b). This is particularly relevant considering that the intensity, duration, and frequency of WDR events across Canada will in some regions increase due to the effects of climate change. Hygrothermal simulation models are often used as a means to assess the long-term performance of building façades and façade components. The simulation models do however require inputs of the moisture load which can be obtained from either of two typical approaches. The first is to simply consider the moisture load as 1% of the WDR load that is deposited on the exterior surface of the wall assembly as specified in the ASHRAE-160 Standard (ASHRAE, 2016); and, the other approach is to directly measure the amount of water that has penetrated into a wall assembly during watertightness testing of a test specimen. Rainwater that is deposited on building surfaces can be absorbed and accumulated by porous materials or can run off from the façade surface. In respect to the moisture load in porous materials, it may lead to frost damage (Van Balen, 1996), salt migration (Charola & Lazzarini, 1986) or discoloration (Franke et al., 1998) of the material. In respect to run off, water can penetrate the exterior sur-face of the building façade when deficiencies are present and result in mould growth at the interior surface of the cladding (Abuku et al., 2009) or decay of wood-based materials (Chouinard & Lawton, 2001).

A watertightness test simulating WDR is commonly used to investigate the performance of standard size wall assemblies (AS 2047, 1999; BS 6375, 2009; CSA 440-08, 2008; NBN B 25-002-1, 2009), to their resistance to water entry, and perhaps as well, quantify the rate of water entry across wall cladding into the wall assembly (Lacasse et al., 2003a; Sahal & Lacasse, 2004, 2005). Additionally, such tests can be performed at different pressure and water spray rates, thereby replicating a range of WDR conditions that may exist, and to which the exterior surface of a wall assembly may be subjected during a rain event. Facilities to implement such types of tests impose a pressure difference across the test specimen by aid of a pressure chamber (Norwegian Standard, 1993), aero engines (Mayo, 1998), or both. These devices are used to replicate the static and dynamic wind effects to which a building façade would be subjected from the action of wind on the building in an exposed environment. At the same time, the WDR can be replicated by a water spray system integrated to the experimental facility. The simultaneous actions of both systems in a test set-up are considered as the WDR load acting on the wall assembly. It is usual for a WDR laboratory test to comply with a test protocol, as following this protocol would have an impact on the water entry results (Van Den Bossche, 2011). It would permit experimental conditions in the test facility to be repeatable as test conditions would be clearly defined and generated by calibrated devices employed in the laboratory. As such, different types of specimens can be tested using the predefined set of WDR conditions and test results obtained can then be readily compared. A watertightness test proto-col ought, however, to be developed on the basis of climate loads, where the water deposition to the wall surface can be obtained from existing semiempirical equations relating water deposition to the WDR load to the wall (ASHRAE, 2016; ISO 15927-3, 2009; Straube, 2010).

According to the results obtained from previously conducted watertightness tests (Bossche et al., 2012; Lacasse et al., 2003b; Sahal & Lacasse, 2004), the water entry rates for different types of wall assemblies and having different configurations varied significantly. It was evident that the water entry rates as measured were greatly affected by water spray rates and pressures applied to the exterior surface of the wall assembly. Several studies (Brown et al., 1997; Moore et al., 2019; Sahal & Lacasse, 2004; St-Hilaire et al., 2003) have established mathematical expressions to describe the relation between the water entry rate and simulated WDR intensities and DRWPs. Sahal and Lacasse (Sahal & Lacasse, 2004) established a systematic approach to derive the water entry equation based on the results of a watertightness test for a hardboard siding-clad wall assembly. The water entry load Q (L/min) into the stud cavity of the test specimen was defined as the product of water entry potential m_p and the spray rate Rp, as shown in Eq. (3.12).

$$Q = m_p \times R_p \tag{3.12}$$

The water entry potential, m_p, was an empirical function using the static pressure differences across the wall assembly as the variable and the constant factors which were de-rived from fitting a cubic polynomial to the results of the watertightness test. Eq. (3.13) shows the water entry potential for the tested hardboard siding-clad wall assembly in which ΔP (Pa) is the static pressure difference across the assembly.

$$m_p = 3 \times 10^{-11}(\Delta P)^3 - 8 \times 10^{-7}(\Delta P)^2 + 5 \times 10^{-5}(\Delta P) + 0.0123 \quad (3.13)$$

The water entry rates were accurately captured using this approach where rates of water entry were determined for different rates of water spray and for given pressure differences across the wall assembly. However, the constant factor in the water entry potential function (i.e., water spray rate) only corresponded to one specific spray rate at any one time whereas, WDR intensities in fact vary considerably due to the constant moving of air in the atmosphere during a rain event. Therefore, to be able to cover a broad range of WDR conditions, and using this approach, several water entry potential equations would need to be generated and as well, the number of these equations would be limited by the number of spray rates implemented in the watertightness test.

Moore et al. (Moore et al., 2019) proposed another equation for the water entry potential function given in Eq. (3.14) using a power function and given as:

$$WE = WDR \times WE\% \quad (3.14)$$

Where: WE is the water entry (L/hr-m^2), WDR is the WDR intensity (L/hr-m^2), and $WE\%$ is the percentage of water entry for each cladding type as shown in Eq. (3.15).

$$WE\% = a \times P^b \quad (3.15)$$

Where: a and b are fitting factors derived from results of watertightness tests, and P is the wind induced pressure (Pa) calculated using Bernoulli's Equation. The fitting factors a and b were generated from fitting the percentage of water entry in Eq (3.15) to water entry results for all spray rates. Thus, this equation covers a continuous range of WDR in-tensities and DRWPs. Despite that, both water entry equations (Eqs. (3.12) and (3.14)) have a mutual weakness: the effect of the WDR intensity is not considered when calculating the water entry ratio (%) which is the ratio of the water entry rate to that of the water spray rate.

To improve the assessment of moisture load using the water entry equation, a revised two-step approach is proposed in this study to permit more accurately determining the relation between the WDR intensity, the DRWP and the water entry rate. As compared to existing water entry equations, the impact of WDR intensity on the water entry rate is considered.

To validate this two-step approach for determining the relation between WDR load and degree of water entry to a wall, a vinyl-clad wall assembly installed with frequently-used wall components (i.e., electrical outlet, ventilation duct and window) was tested in the Dynamic Wind and Wall Testing Facility (DWTF) at the National Research Council Canada (NRC). In addition, the test followed a preliminary established test protocol on the basis of climate data collected in Canada (Xiao et al., 2020). Using this procedure, the air-leakage rate and pressure equalization of the tested wall assembly was also investigated.

3.2.3 Methods

The overall procedure of this study included constructing a National Building Code of Canada (NBCC) (NRCC, 2015) compliant vinyl-clad wall assembly, conducting the test with ap-propriate testing devices, and correlating the water entry results to the experimental input and other measurements from the test.

3.2.3.1 Configuration of wall specimen

The wall assembly test specimen (Figure 3.8) measures 2.44 × 2.44 m^2 (8-ft. by 8-ft.) and incorporates a 600 × 600 mm^2 window, 100-mm diameter circular pipe, and a standard exterior electrical outlet box. Other than the cladding layer, the specimen also included a 30-min asphalt impregnated membrane, 3/8-in transparent polycarbonate sheathing, 51 × 152 mm^2 (2" × 6" wood) (SPF) studs spaced at 600 mm (24") on center, and a 9.5 mm (3/8") clear polycarbonate air and vapor barrier having an air leakage rate of 0.2 L/s-m^2. No insulation material was installed in the tested specimen.

(a)

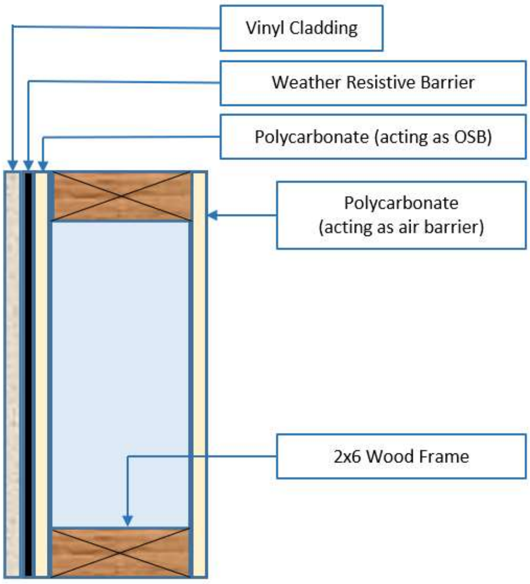

(b)

Figure 3.8 (a) The NBCC complied vinyl-clad wall assembly with a window, a ventilation duct, and an electrical outlet; (b) Cross-section of the test specimen.

Pressure differences were measured by pressure transducer and infiltrated water was collected at several locations of the test specimen as shown in Figure 3.9. Specifically, in this test, pressure differences between the stud cavity and chamber were measured at locations shown in Figure 2 as P3, P5 and P7, and that between chamber and behind the cladding layer were measured at locations P2, P4, P6. These pressure differences could then be used to estimate the potential for water to be driven though the cladding and onto the weather resistant barrier.

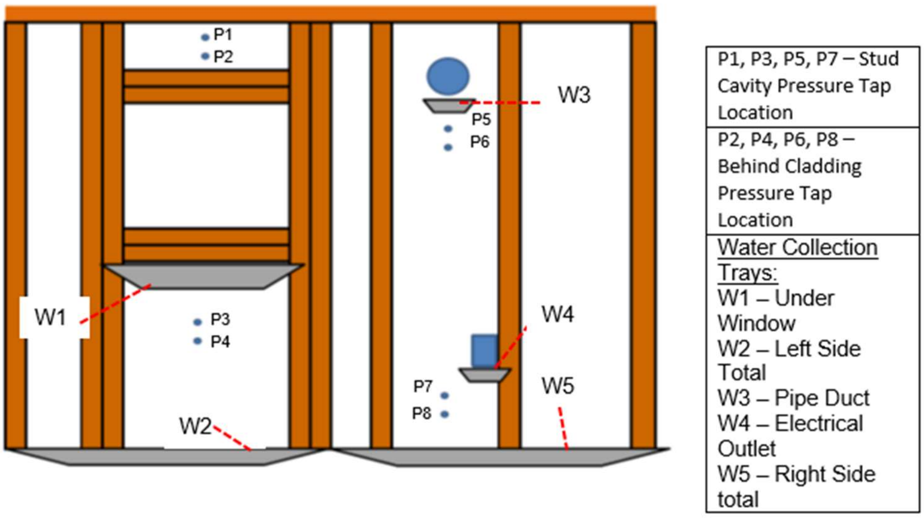

Figure 3.9 Locations of pressure taps and water collection troughs.

Three, 3-mm diameter, holes were bored at the top center of the caulking around the pipe, the bottom left of the caulking near the electrical outlet, and at the bottom corner of the window frame to simulate failures at these locations. Water collection troughs were installed below the window, ventilation pipe and electrical outlet box, at the bottom of the left-side and right-side of the wall represented by W1, W3, W4, W2, and W5, respectively. Details of collection trays for the window, pipe and electrical outlet box are shown in Figure 3.10. Yellow plastic mesh was installed to direct water that has penetrated the cladding into the aluminum collection trough. Water in the trough was then drained to a water reservoir that could be weighed before and after each test; this permitted quantifying the water that had penetrated the cladding and reached the sheathing membrane. The portion of water that had entered the wall assembly but was not collected in the water troughs, could be observed through transparent polycarbonate panels, these panels replacing the sheathing and gypsum boards as is typically used in real wall assemblies.

(a)

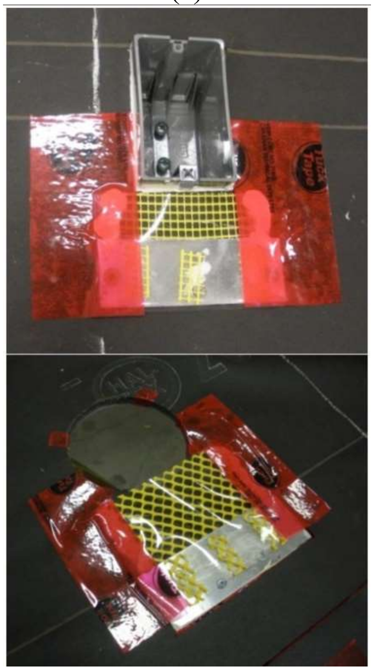

(b)

Figure 3.10 (a) Water collection troughs below the window; (b) water collection troughs below the electrical outlet and ventilation duct.

3.2.3.2 Watertightness test protocol

A preliminary test protocol was established based on climate data collected in Ottawa, Canada for watertightness tests which would be carried out by using the DWTF. The experimental inputs in the protocol ensured that the specimen was subjected to all possible WDR conditions that could occur at the location of interest in the test. The results of testing using this protocol were expected to provide comprehensive information regarding the moisture load in the tested wall assembly.

The entire protocol included five steps. The first step, Air-Leakage Test, was intended to measure the air-leakage in wall assemblies which occurs primarily through cracks, gaps, poorly designed or constructed joints, junctions at perimeters of window and door frames, or pass directly through porous materials under pressure differential. The air-leakage test was added to the protocol given an appreciation of its effects on water entry, as well as the requirement for a maximum air-leakage rate (i.e., 0.2 L/s-m^2 at 75 Pa static pressure), as specified in NBCC (NRCC, 2015) to help ensure reduced consumption in building heating loads. Other than satisfying this requirement, additional static pressure levels up to 250 Pa were also added to the test protocol. Thus air-leakage rates of the wall assembly were measured from those pressure levels and thereafter correlated with the water entry rates.

The primary force that drives water inward of wall assemblies are induced by the pressure differential across different layers of wall (Rousseau et al., 1998). Ideally, a perfectly pressure equalized wall assembly can mitigate part of these driving forces. However, due to the inevitable presence of air flow paths in the wall assembly, in real wall applications the pressure differential more likely is altered from the ideal case and thus ought to be characterized. Thus, the pressure equalization of the wall assembly, and that could potentially affect the degree of water entry, was characterized at the second step of the test protocol. The pressure equalization step was conducted by simultaneously measuring pressure at different layers, and several locations, of the wall assembly test specimen when different levels of pressure were applied to the wall specimen. Pressures applied to the façade surface, in the drainage cavity and in the stud cavity, were measured under a succession of dynamic pressure fluctuations; they are presented as sine functions at several locations of the wall assembly. Discrepancies between measured pressures were not the only concern; shifts between sine functions which were plotted from the pressure data at different layers were also of interest. The dynamic pressure cycles applied to the test specimen in later steps of this protocol were in accordance with those implemented at this step. The base pressure for dynamic pressure cycles was the same as the static pressure steps. The amplitude of the dynamic pressure was calculated by multiplying the base pressure with the 0.85 which was derived from the maximum pressure coefficient on wall assemblies specified by the NBCC (NRCC, 2015). The frequencies of dynamic pressure cycles were tentatively suggested as 0.1 Hz considering the wind velocity spectrum near the ground (<10 m) (Teunissen, 1970). Profound discussions were made at the section for watertightness results.

Third and fourth steps of the protocol include the Water Penetration Trials and the Effects of Continuous Water Spray. The Water Penetration Trials were used to determine the ability of the wall assembly to resist water penetration when exposed to static and dynamic pressures, at a nominal spray rate of 3.4 L/min-m^2. Occurrence of any form of water penetration was recorded after visual inspection of the wall assembly. At the fourth step, the test specimen would be subjected to long-lasting water spray to simulate exposure of real wall assemblies to up to 24-h consecutive WDR events in Ottawa (Xiao et al., 2020). Observations in regard to water penetration was conducted and recorded every 10 min.

The final step of the protocol is the Water Entry Assessment. At this step, several levels of spray rates and multiple steps of static and dynamic pressure derived from Ottawa observed historical climate data were applied to the test specimen to investigate the relation between the applied conditions and the water entry results. Water collected by reservoirs was weighed and recorded after each step. Pressure readings in different layers of the wall assembly were also monitored during wet test conditions. The duration for each step was 10 min. The applied spray rate of 3.4 L/min-m^2 is equivalent to the maximum 1-min WDR intensity for the Ottawa region (Xiao et al., 2020) calculated from a WDR intensity of 35 mm/h. Spray rates of 1.3 and 2.1 L/min-m^2 were also implemented to investigate effect of water spray rate to the water entry results. An overview of the test protocol is given in Figure 3.11.

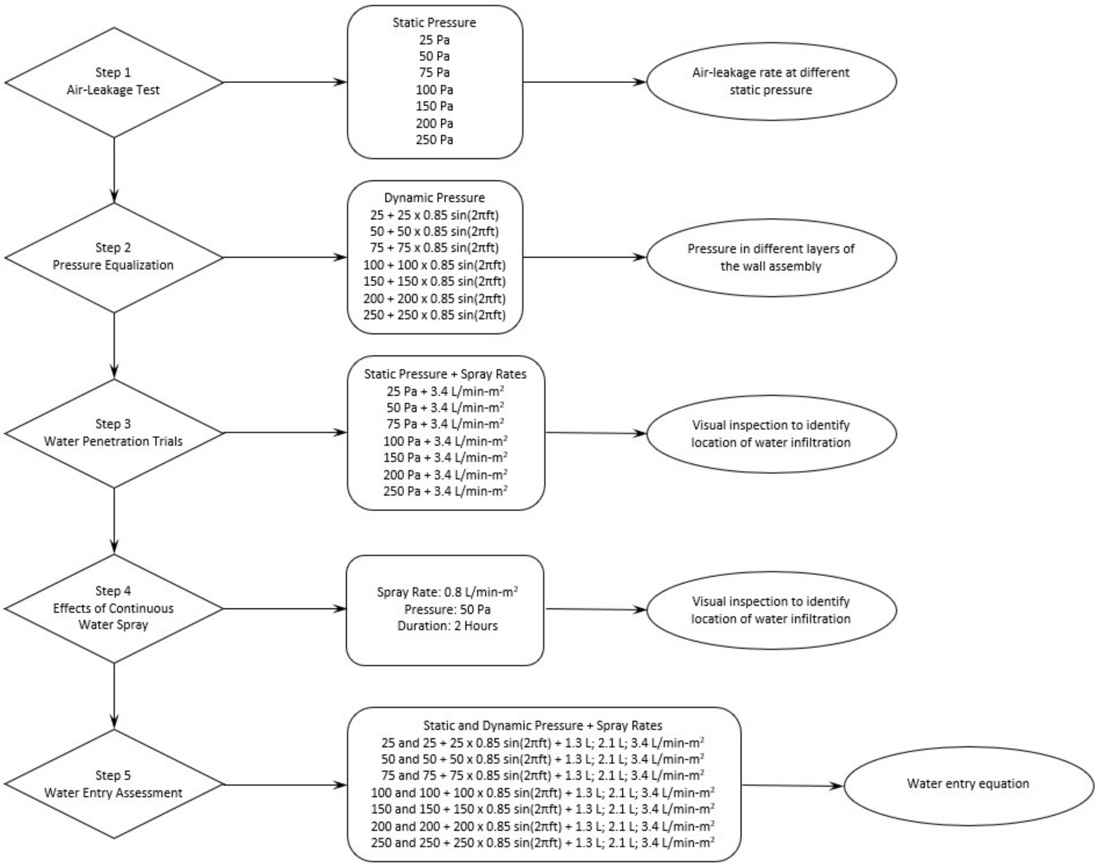

Figure 3.11 Overview of the watertightness test protocol.

3.2.3.3 Experimental Facilities

Air leakage testing on the wall assembly was performed in accordance with ASTM E2357 to characterize wall performance with respect to air leakage at static pressure differentials of 25, 50, 75, 100, 150, 200, and 250 Pa. Testing was also performed to ensure that the wall assembly had an air leakage rate less than or equal to 0.20 L/(s-m^2) at a pressure differential of 75 Pa to meet airtightness requirements of a continuous air barrier system as stated in the NBCC (NRCC, 2015). The actuator unit shown in Figure 3.12a, was used to measure the pressure differential within the air leakage testing assembly as well as record pressure data and the air flow rate. The air leakage testing assembly consisted of a steel frame as shown in Figure 3.12b and a 9.5 mm (3/8") polycarbonate sheet as shown in Figure 3.12c. With the wall assembly secured to the steel frame, the polycarbonate was attached and sealed to the lab side of the wall to measure the base air leakage which is the air leakage occurring through the perimeter seals of the specimen and steel frame. Once the base air leakage was obtained, the polycarbonate sheet would be removed to measure the total air leakage. The air leakage rate of a wall assembly can be calculated by subtracting the base air leakage rate from the total air leakage rate.

(a)

(b)

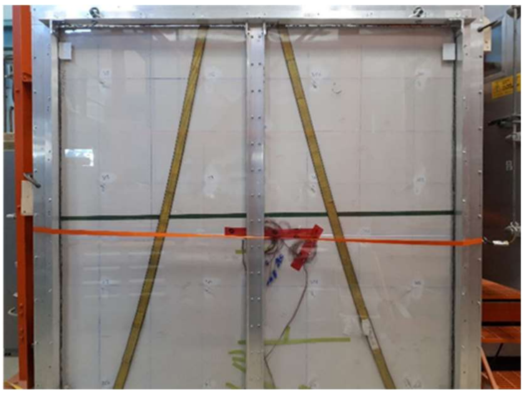

(c)

Figure 3.12 (a) Pressure actuator and data acquisition unit; (b) Steel frame on the exterior side of wall specimen; (c) A 3/8” poly-carbonate sheet on the interior side of wall specimen.

The DWTF is an integrated watertightness and water entry test chamber that is composed of a Rain Effects System (RES), a Wind Effects System (WES) and a Data Acquisition System (DAS) as shown in Figure 3.13. The RES is mounted within the test chamber and allows a regulated amount of water to be deployed by spraying on the test specimen. The setup and calibration of the RES comply with the ASTM E331 standard (ASTM E331-00, 2016). The WES applies pressure to the exterior surface of the wall assembly by using an air blower. Dynamic pressure fluctuations are achieved by controlling an Exhaust Flap System (EFS). All the systems can be controlled and operated from a single computer. The DWTF test chamber, made of stainless steel, is 3.7 m high, 3.7 m wide and 1.22 m deep and has a 2.44×2.44 m^2 opening at the front face for installing and securing a test specimen. A 1×2 m^4 water and airtight door located on one side of the test chamber provides entrance to the inside of the DWTF chamber. On the opposite side of the chamber, a motorized flap system is installed for exhausting air supplied by a blower that is connected to the inlet at the rear of the DWTF though a conduit and controls the pressure that is applied to the test specimen. Additional openings located at the rear of the test chamber provide access for electrical power and water supply to the RES. The open mesh flooring inside the chamber allows water to be drained during or after a test. The WES is designed to produce pressures up to 2400 Pa and the RES is calibrated to provide up to 3.4 L/min-m^2 water deposition in the form of a conical spray.


(a)


(b)


(c)

Figure 3.13 (a) Dynamic Wind and Wall Testing Facility (DWTF); (b) Rain Effect System (RES); (c) Exhaust Flap System (EFS)

3.2.4 Experimental results and discussion

The output of the experiment included the air-leakage rate for different levels of static pressure across the wall assembly, pressure equalization of the wall assembly under dynamic pressure, water penetration observed at different locations of the wall assembly, and water entry rate for different spray rates and applied pressure. The correlations between the air-leakage rate and the water entry rate under static pressure are discussed, and as well, those between the pressure equalization and the water entry rate under dynamic pressure. As well, a two-step approach was developed to establish the water entry equation.

3.2.4.1 Water entry results and water entry functions

3.2.4.1.1 Static results

Water entry results obtained from tests under static pressure for different spray rates are shown in Figure 3.14. The trough below the window collected water for most of cases tested at spray rates of 1.3 and 2.1 L/min-m^2. More water penetrated through the deficiency at the window than the other two types of components under most of the static pressure steps. No clear correlation was observed between the static pressure and the water entry rate, and between the spray rate and the water entry rate at the window. As to the electrical outlet box, the greatest amount of water was collected at 3.4 L/min-m^2 spray rate whereas almost no water was collected at a spray rate 2.1 L/min-m^2. For deficiency at this location, a positive relation was found between the pressure level and water entry rate for 1.3 and 3.4 L/min-m^2 spray rates. The amount of water that penetrated through the ventilation duct was not sensitive to the test pressure level. Compared with the other two types of appliances, a relatively low amount of water was collected by the trough at the ventilation duct. In addition, no water was collected at the bottom of the wall assembly in the drain-age cavity for the entire static pressure test period, as well as by all water reservoirs at a water spray rate of 1.3 L/min-m^2 under pressure level of 25 Pa.

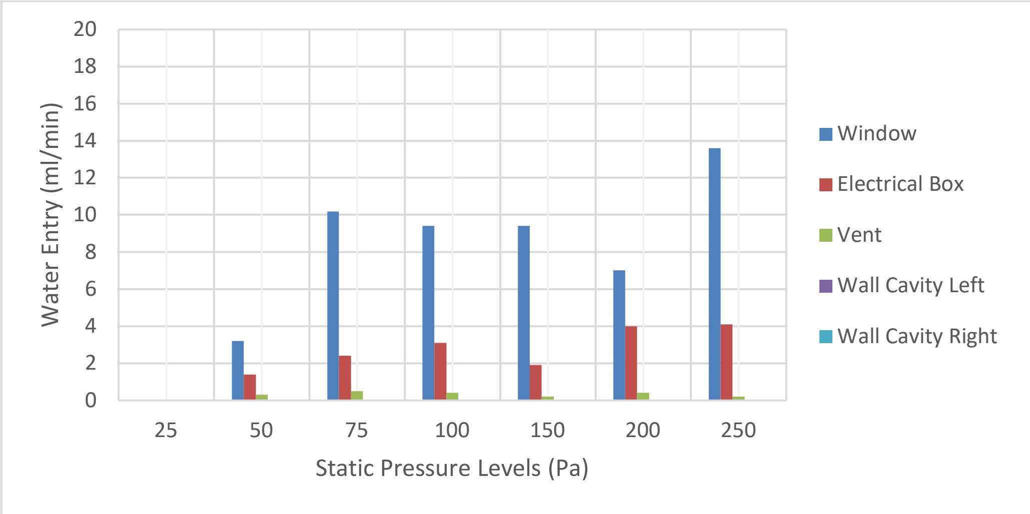

20
18
16
14
12
10
8
6
4
2
0
Water Entry (ml/min)
25
50
75
100
150
200
250
Static Pressure Levels (Pa)
Window
Electrical Box
Vent
Wall Cavity Left
Wall Cavity Right

(a)

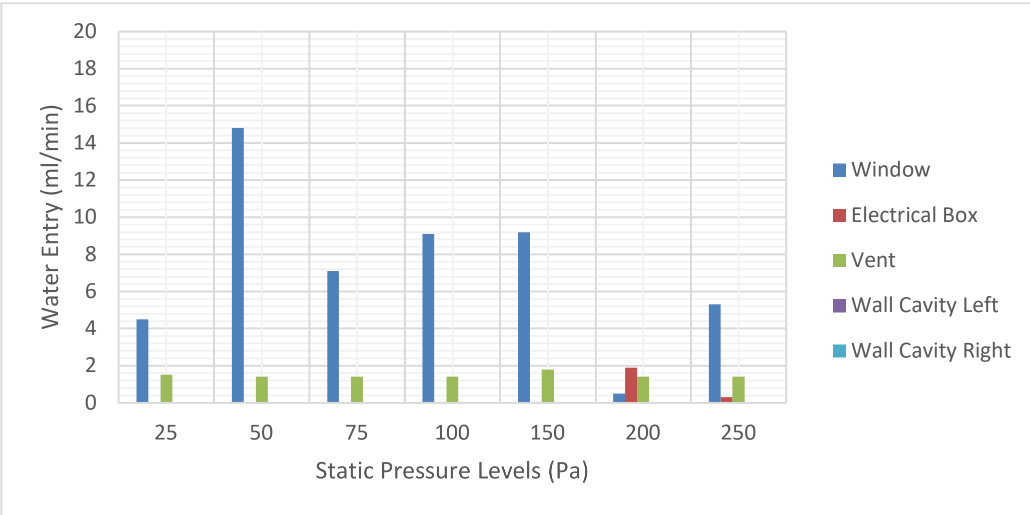

20
18
16
14
12
10
8
6
4
2
0
Water Entry (ml/min)
25
50
75
100
150
200
250
Static Pressure Levels (Pa)
Window
Electrical Box
Vent
Wall Cavity Left
Wall Cavity Right

(b)

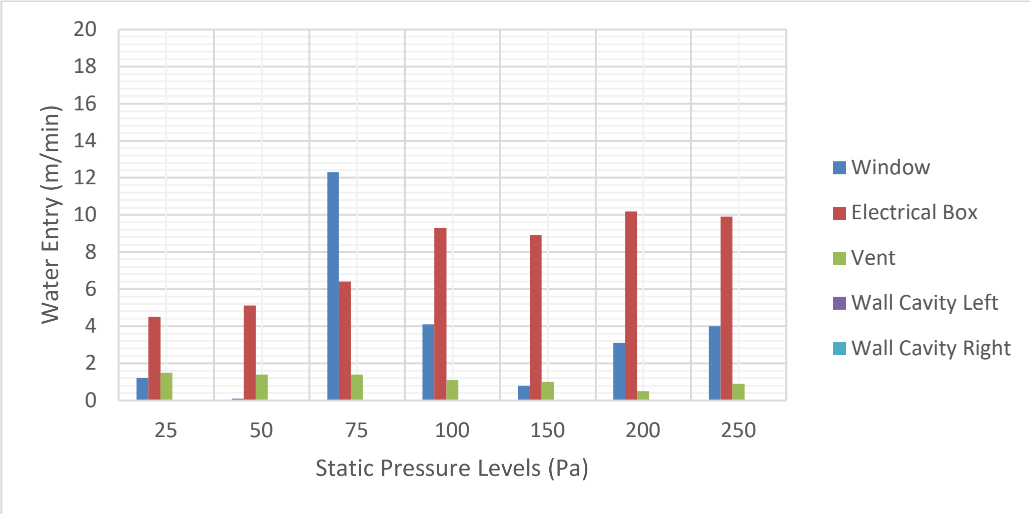

(c)

Figure 3.14 Water entry results under static pressure with (a) 1.3 L/min-m^2 spray rate, (b) 2.1 L/min-m^2 spray rate, and (c) 3.4 L/min-m^2 spray rate.

The sum of infiltrated water from all deficiencies for each spray rate under static pressure is depicted in Figure 3.15. Neither the spray rate nor the pressure level determined any level of monotonous tendency for the water entry amount.

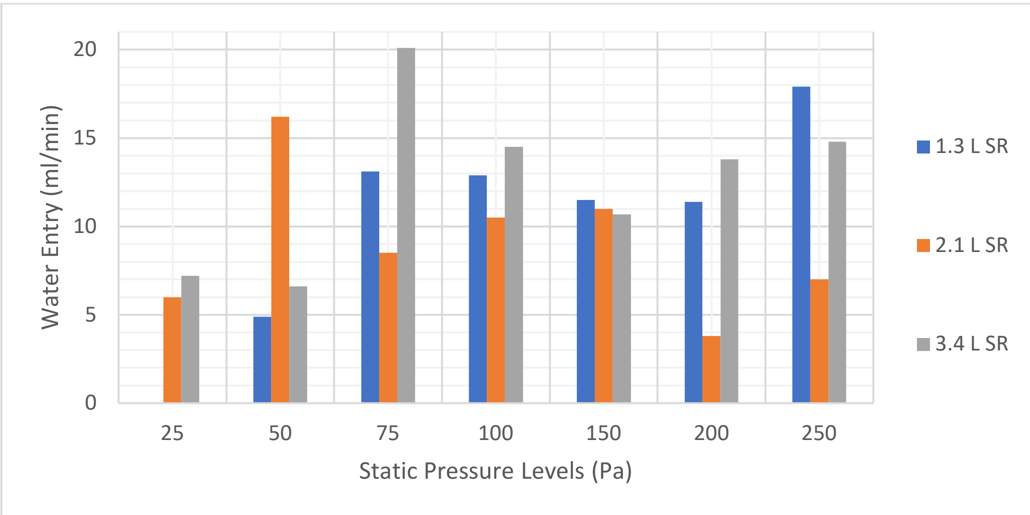

Figure 3.15 Water entry results under static pressure for all deficiencies (SR in the legend means spray rate)

3.2.4.1.2 Dynamic pressure results

The watertightness test results under the dynamic pressure for each spray rate are shown in Figure 3.16. The trough under the window collected more water than all troughs at other locations for most cases. Moreover, water collected under the window from the 200 Pa dynamic pressure level was more than that collected from all other pressure levels for all spray rates. As well, more water was collected at the 2.1 L/min-m^2 spray rate than the other two spray rates. As for the electrical box, no water was collected at pressure levels under 100 Pa with spray rates of 1.3 and 2.1 L/min-m^2, and under 75 Pa with a spray rate of 3.4 L/min-m^2. At the same time, and for all spray rates, most water collected at the electrical box was at the 250 Pa dynamic pressure level. The amount of water that penetrated the ventilation duct was less than 1 mL/min for all cases and the highest water entry rate occurred at the 25 Pa pressure level for all spray rate levels. In some cases, a portion of water reached the bottom of the wall assembly. All of which would be drained away in real applications.

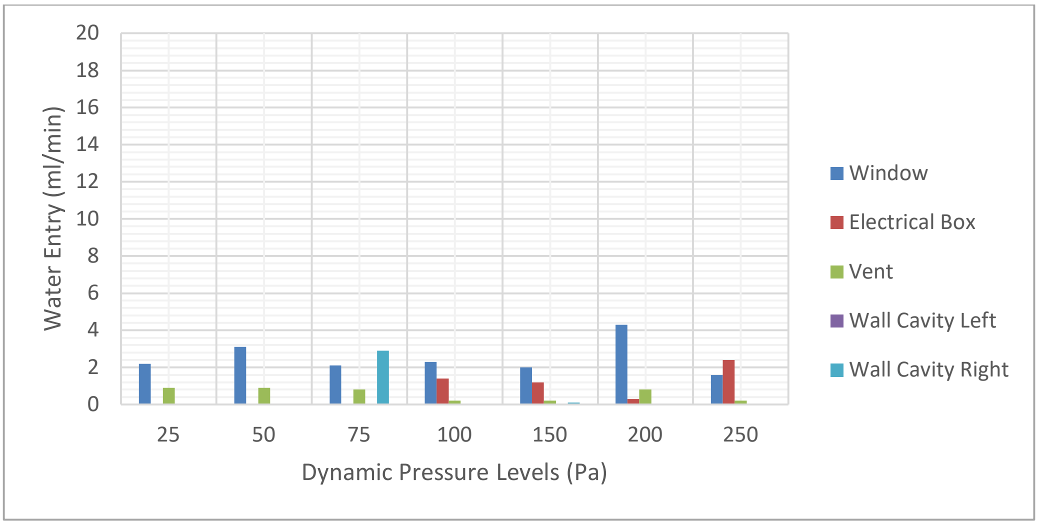

(a)

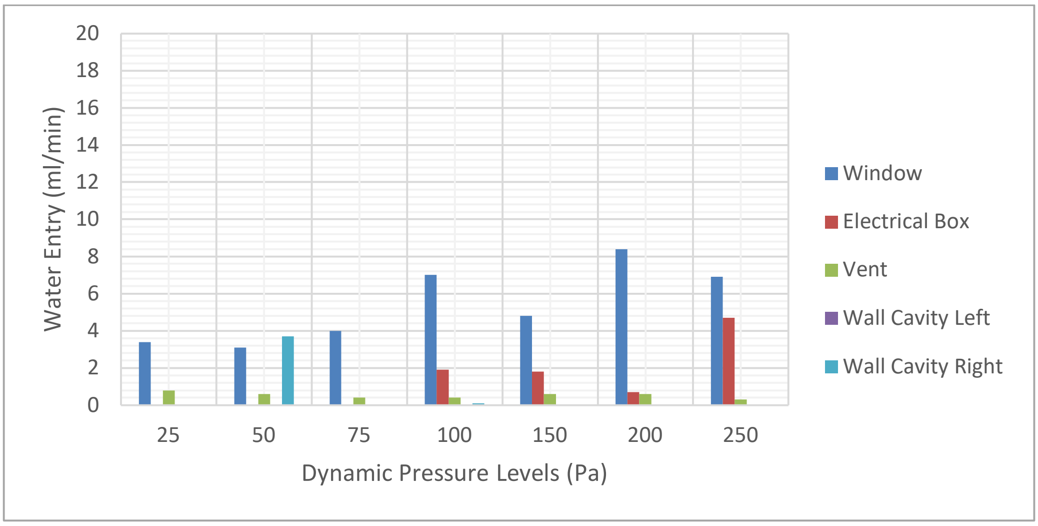

(b)

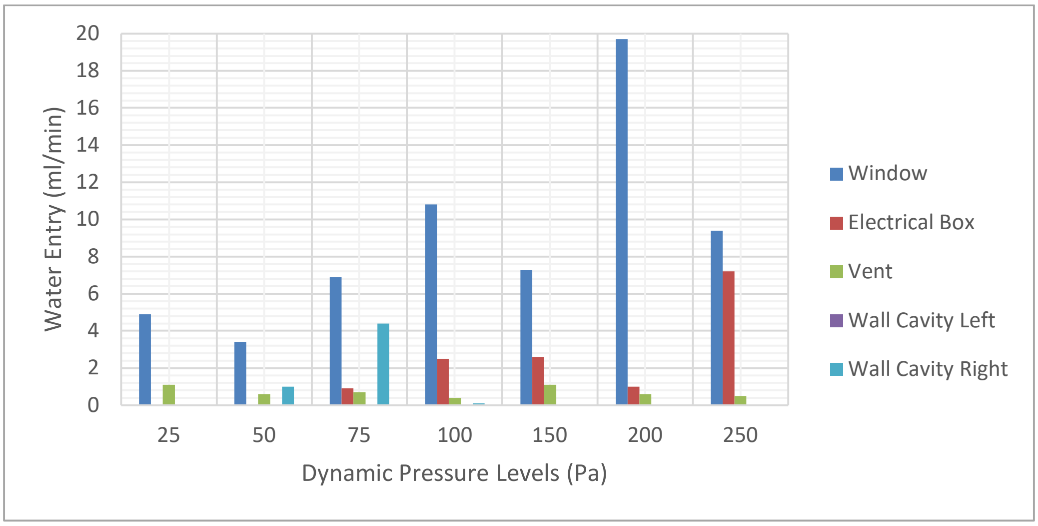

(c)

Figure 3.16 Water entry results under static pressure with (a) 1.3 L/min-m^2 spray rate, (b) 2.1 L/min-m^2 spray rate, and (c) 3.4 L/min-m^2 spray rate.

The total water collected by all three components at each water spray rate tested under dynamic pressure fluctuations is shown in Figure 3.17. Clear tendencies in respect to the water entry amount, dynamic pressure levels and spray rates were revealed. In general, both the level of dynamic pressure and the spray rate were positively correlated with the amount of water entry. Some results were inconsistent with the expected response of the test specimen in relation to applied WDR loads in this test; for example, the water collect-ed at the 200 Pa dynamic pressure level and with a water spray rate of 3.4 L/min-m^2 is more than that at the 250 Pa dynamic pressure level with the same spray rate; such results could be mitigated by increasing the number of repeated tests.

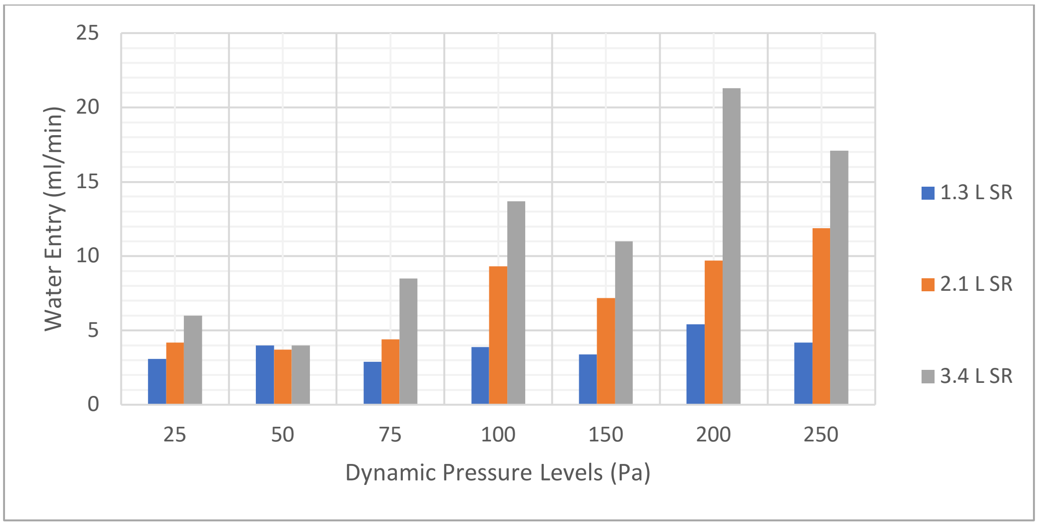

Figure 3.17 Water entry results under dynamic pressure for all deficiencies (SR in the legend means spray rate).

3.2.4.1.3 Water entry equation

The first step to obtain the water entry function that can most accurately estimate the water entry rate to a wall assembly is to determine the adjustment coefficients for the WDRP Index (Xiao et al., 2021). The WDRP Index (WDRPI), as shown in Equation (5), has been pro-posed to determine the joint effects of WDR intensity (mm/h) and co-occurring DRWP (Pa) to the water entry rate of a wall assembly. The spray rates used in the watertightness test have a unit of L/min-m^2 and it is equivalent to 1/60 of value of the WDR intensity (mm/h). The exponential adjustment coefficients α and β represent the relative impact of these two parameters on the water entry rate. As an example, larger values of α than β means that the water entry rate of the wall assembly is more sensitive to the WDR intensity than the DRWP applied to the surface of the wall assembly.

$$WDRP\ Index = WDR^{\alpha} \times DRWP^{\beta} \tag{3.16}$$

The values of these two coefficients were obtained from correlating the WDRPI to the measured water entry rates under different levels of spray rates and applied pressures which, respectively, represent WDR intensity and DRWP. In this study, the water entry rate for all deficiencies under the dynamic pressure was used to fit with the WDRPI and generate values for the coefficients. The values for α and β were determined as 1.342 and 0.671, respectively, as obtained from the fitting process where the function given in Eq. (3.16) had an R-Squared value of 0.851.

An exponential function (Eq. (3.17)) using the WDRPI as the variable was thereafter fitted to the measured water entry rate. Its coefficients, a and b, were determined by the least-square method and their respective values for the vinyl-clad wall assembly, as tested, were 0.00452 and 0.763.

$$Water\ Entry\ Rate = a \times WDRPI^{b} \tag{3.17}$$

The fitting process and the correlation between the measured and calculated water entry rate are shown in Figure3.18. A summary for determining the water entry function of the tested vinyl-clad wall assembly is given in Table 3-6. By using this approach, the moisture load for the test specimen could be determined based on hourly WDR intensity and hourly DRWP which are available for most locations in Canada over a long period of time

Table 3-6 Summary of steps to determine test specimen water entry function

Step 1	$WDRPI = WDR^{\alpha} \times DRWP^{\beta}$	$\alpha = 1.342$, $\beta = 0.671$, $R^2 = 0.851$
Step 2	$Water\ Entry\ Rate = a \times WDRPI^{b}$	$a = 0.00452$, $b = 0.763$, $R^2 = 0.839$

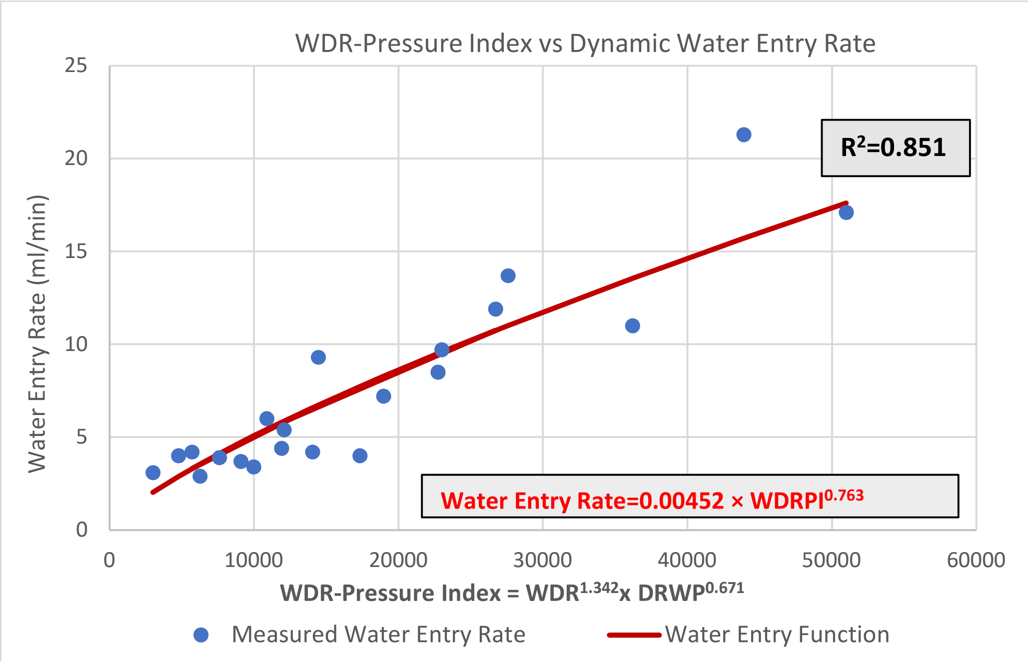

(a)

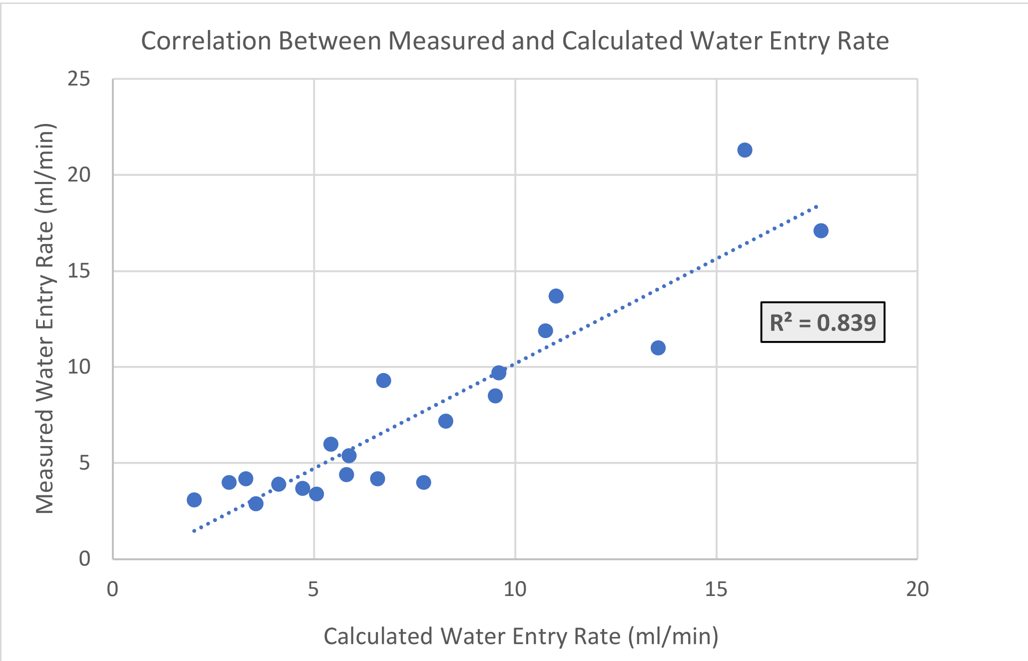

(b)

Figure 3.18 (a) Correlations between the WDRPI and the water entry rate; (b) correlation between the measured water entry rate and the calculated water entry rate

3.2.4.2 Air leakage rate and water entry rate

The flow rates, the volume of air that inflated the air-leakage test apparatus, for different static pressures applied to the surface of wall assembly are shown in Table 3-7. The total leakage was calculated by dividing the flow rate by the area of the wall assembly and 60 s/min. The inherent leakage of the steel frame and wall assembly perimeter seals were denoted as the base leakage. The air-leakage rate of the wall assembly, wall leakage, was then calculated by subtracting the base leakage from the total leakage. The wall leakage for the tested vinyl-clad wall assembly was 0.119 L/s-m^2 which was lower than the 0.2 L/s-m^2 requirement in the National Building Code (NRCC, 2015). The wall leakage rates increased at each increment of static pressure.

Table 3-7 Air-leakage test results

Pressure	**Flow Rate (L/min)**	**Total Leakage (L/s-m^2)**	**Base Leakage (L/s-m^2)**	**Wall Leakage (L/s-m^2)**
25 Pa	22.9	0.064	0.009	0.054
50 Pa	37.5	0.105	0.015	0.090
75 Pa	49.2	0.137	0.018	0.119
100 Pa	59.7	0.167	0.023	0.144
150 Pa	77.3	0.216	0.032	0.184
200 Pa	93.8	0.262	0.037	0.225
250 Pa	109	0.305	0.045	0.261

Coefficients of determination between the wall leakage rate and the water entry rate for different deficiencies and different spray rates are given in Table 3-8. Relatively strong correlations between these two parameters were observed for deficiency at the window with a 1.3 L/min-m^2 spray rate, at the electrical box with spray rates of 1.3 and 3.4 L/min-m^2, at ventilation duct with 3.4 L/min-m^2, as well as the total water entry rate from all deficiencies at a spray rate of 1.3 L/min-m^2. No meaningful relationship could be established for the remaining cases. These observations also indicate that the response of water entry rates to the applied pressure varied when subjected to different spray rates.

Table 3-8 Coefficients of determination between air-leakage rate and water entry rate for different deficiencies and spray rates.

R-Squared	Window	Electrical Box	Ventilation Duct	Sum from All Deficiencies
1.3 L/min-m^2	0.605	0.785	0.043	0.688
2.1 L/min-m^2	0.182	N/A	0.001	0.144
3.4 L/min-m^2	0.002	0.841	0.761	0.185

3.2.4.3 Pressure equalization of the wall assembly

The pressure measurements for each experimental condition at different deficiencies across the wall assembly were concluded as three pairs of comparisons as shown in Table 3-9. One pair was the differences between the pressure on the exterior surface of the cladding, which is also the pressure in the DWTF chamber, and the pressure in the drainage cavity of the tested wall assembly. The second comparison was made between the pressure in the DWTF chamber and the pressure in the stud cavity of the tested wall assembly. In addition, the phase shift between sine waves, which were plotted by the pressure measured in the drainage cavity and in the stud cavity under dynamic pressure conditions, were also determined. An example of shifts between plotted sine waves is depicted in Figure 12. The root-mean-square values of each set of pressure data were used for com-parison and the two sets of compared data were measured from the same location but different layers of the wall assembly.

The results shown in Table 3-9 indicate that pressure differences between the exterior surface of the cladding and the drainage cavity of the wall assembly were almost negligible for all locations and under all applied pressure levels. As well, pressure differences between the exterior surface of the cladding and the stud cavity were larger than that be-tween the exterior surface of the cladding and the drainage cavity. At the same dynamic pressure step, the pressure in the stud cavity around the window seems slightly lower than the pressure around the electrical outlet box and ventilation duct. The ratio between the pressures on the exterior surface and in the stud cavity of the wall assembly were all very close to the averaged ratio regardless of the magnitude of pressure applied to the test specimen. This also meant that the absolute value of the pressure differences steadily increased with changes in applied dynamic pressure to the test specimen. The phase shift between the sine waves plotted by the pressure readings in drainage cavity and stud cavity was positively correlated with the magnitude of the pressure. Shifts that occurred around the window were larger than that which occurred at the other two locations. The pressure differences obtained from this step were determined by the airtightness of the wall assembly. The shift between each cyclic pressure wave is affected by the airtightness of the wall assembly as well as the flexibility of materials that compose the test specimen.

Table 3-9 Pressure differences at each type of deficiency under different dynamic pressure steps.

Deficiencies	Dynamic Pressure	Drainage Cavity to Ext. Cladding	Stud Cavity to Ext. Cladding	Time Shifts
Window	25 +25 × 0.85 sin (2πft *)	99.9%	98.6%	0.08%*
	50 +50 × 0.85 sin (2πft)	99.9%	98.5%	0.43%
	75 +75 × 0.85 sin (2πft)	99.9%	98.9%	0.46%
	100 +100 × 0.85 sin (2πft)	99.6%	98.1%	0.56%
	150 +150 × 0.85 sin (2πft)	99.6%	97.5%	0.53%
	200 +200 × 0.85 sin (2πft)	99.8%	97.7%	0.64%
	250 + 250 × 0.85 sin (2πft)	99.9%	97.9%	0.57%
Electrical Outlet	25 +25 × 0.85 sin (2πft)	99.9%	95.7%	0.37%
	50 +50 × 0.85 sin (2πft)	99.5%	95.8%	0.05%
	75 +75 × 0.85 sin (2πft)	99.9%	97.2%	0.25%
	100 +100 × 0.85 sin (2πft)	99.7%	96.5%	0.40%
	150 +150 × 0.85 sin (2πft)	99.9%	96.8%	0.37%
	200 +200 × 0.85 sin (2πft)	99.9%	97.2%	0.46%
	250 + 250 × 0.85 sin (2πft)	99.9%	97.7%	0.37%
Ventilation Duct	25 +25 × 0.85 sin (2πft)	99.9%	97.1%	0.35%
	50 +50 × 0.85 sin (2πft)	99.9%	95.9%	0.38%
	75 +75 × 0.85 sin (2πft)	99.9%	96.7%	0.38%
	100 +100 × 0.85 sin (2πft)	99.8%	95.9%	0.43%
	150 +150 × 0.85 sin (2πft)	99.8%	96.3%	0.49%
	200 +200 × 0.85 sin (2πft)	99.9%	97.7%	0.37%
	250 + 250 × 0.85 sin (2πft)	99.5%	97.0%	0.53%
	Averaged	99.8%	97.2%	0.41%

* f: frequency (Hz), t: time, ratio between time shift and period.

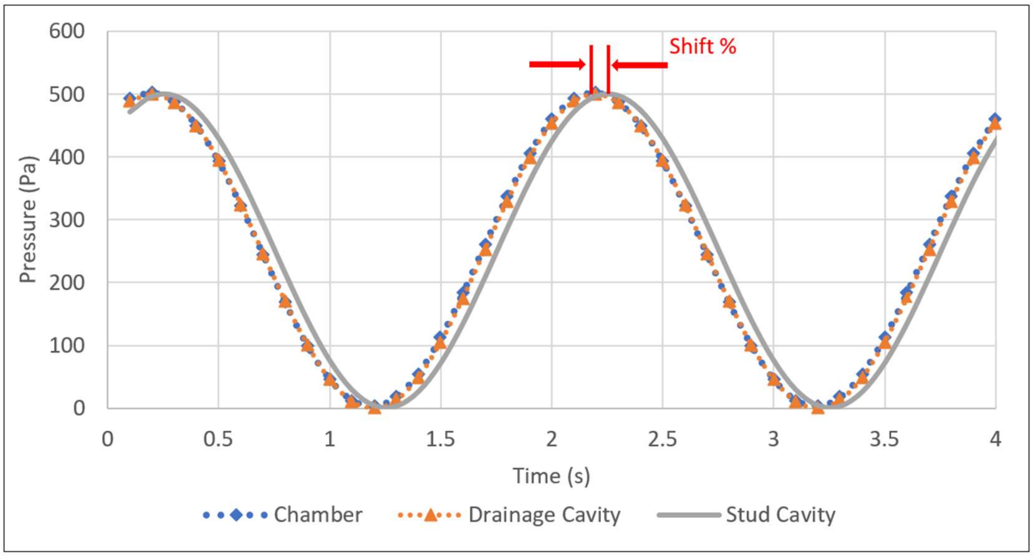

Figure 3.19 Shift between the pressure readings in different layers of wall assembly.

3.2.4.4 Observed water penetration

During the Water Penetration Trials test, water penetration was observed penetrating into the stud cavity via fasteners used to secure either the vent duct or electrical box as shown in Figures 3.20a. The observations for the Continuous Water Spray test are shown in Figure 3.20b and c. Similar to the prior observations, water penetrated into the stud cavity through fasteners located near the electrical box and the pressure tube for pressure readings near the ventilation duct. To reduce the risk of exposure to moisture loads, in real wall assembly applications, these types of through-wall components should be properly sealed with appropriate products and installation methods.

(a) (b) (c)

Figure 3.20 (a) Water entry and drip by electrical box; (b) Water entry through electrical box screw; (c) Water entry through vent screw.

3.2.5 Conclusion

By testing the wall assemblies following the protocol and using the approach to establish the water entry function based on the test results, the relation between the simulated WDR conditions and the moisture load in wall assembly with designated deficiencies were established. The water entry rates derived from the water entry function were in a good agreement with those measured. The moisture load as calculated from this function could readily be implemented in a hygrothermal simulation to more accurately assess the performance and durability of wall assemblies. For this wall assembly, the moisture load function was found to be:

Table 3-10 Values of coefficients for WDRPI and water entry equation.

$WDRPI = WDR^{\alpha} \times DRWP^{\beta}$	α = 1.342, β = 0.671, R^2 = 0.851
$Water\ Entry\ Rate = a \times WDRPI^{b}$	a = 0.00452, b = 0.763, R^2 = 0.839

The moisture load in the tested vinyl-clad wall assembly can be estimated based on hourly WDR loads and DRWPs from a given location. Naturally, this function can also be used to calculate the moisture load and assess the durability of wall assemblies subjected to the anticipated future projected WDR loads and DRWPs arising from climate change and that are generated from climate models (Scinocca et al., 2016). In the subsequent studies other types of wall assemblies will be tested through the same procedure thereby permitting a broader application of the water entry function. This future work will also include investigation of aged wall assemblies as the configurations of deficiencies have an effect on the water entry results.

The air-leakage rate of the wall assembly was positively correlated with the static pressure acting on its surface and complied with requirements in the building code. The correlations between the water entry rate and the air-leakage rate varied with the spray rates and types of deficiencies. Differences of pressure on exterior surface and in the drainage cavity of the wall assembly were almost the same for the tested vinyl-clad wall assembly under dynamic pressure steps. The pressure in the stud cavity was, on average, 97.2% of that on the exterior surface regardless of the magnitude of the pressure. The phase shift ratio of the sine wave plotted by the pressure reading in the stud cavity and on the exterior surface of the wall assembly tended to increase with the pressure magnitude. Other than the water collected at designed deficiencies, water infiltration was also observed at through-wall components, such as fastener and pressure tubes locations, during both the Water Penetration Trails test and Continued Water Spray test.

3.2.6 References

Abuku, M., Janssen, H., & Roels, S. (2009). Impact of wind-driven rain on historic brick wall buildings in a moderately cold and humid climate: Numerical analyses of mould growth risk, indoor climate and energy consumption. *Energy and Buildings*, *41*(1), 101–110. https://doi.org/10.1016/j.enbuild.2008.07.011

AS 2047. (1999). *Windows in buildings - selection and installation*. Standards Australia International.

ASHRAE. (2016). ASHRAE standard 160P-criteria for moisture control design analysis in buildings. In *ASHRAE Transactions*.

ASTM E331-00. (2016). *Standard Test Method for Structural Performance of Exterior Windows , Curtain Walls , and Doors by Uniform Static Air Pressure Difference*. ASTM International. https://doi.org/10.1520/E0331-00R16

Bossche, N. Van Den, Lacasse, M., Moore, T., & Janssens, A. (2012). Water infiltration through openings in a vertical plane under static boundary conditions. *Proceedings of the 5th IBPC*.

Brown, W., Ullett, J., Karagiozis, A., & Tonyan, T. (1997). Barrier EIFS Clad Walls: Results from a Moisture Engineering Study. *Journal of Thermal Insulation and Building Envelopes*, *20*(3), 206–226. https://doi.org/10.1177/109719639702000304

BS 6375. (2009). *Performance of windows and doors*. British Standards Institution.

Charola, A. E., & Lazzarini, L. (1986). Deterioration of Brick Masonry Caused by Acid Rain. In *ACS Symposium Series* (pp. 250–258). https://doi.org/10.1021/bk-1986-0318.ch017

Chouinard, K. L., & Lawton, M. D. (2001). Rotting wood framed apartments-Not just a Vancouver problem. *Proc of the 8th Canadian Conference on Building Science and Technology*, 304–318.

CSA 440-08. (2008). *North American fenestration standard/specification for windows, doors, and skylights*. Canadian Standards Association.

Franke, L., Schumann, I., van Hees, R. P. J., van der Klugt, L., Naldini, S., Binda, L., Baronio, G., Van Balen, K., & Mateus, J. (1998). Damage Atlas: Classification and Analyses of Damage Patterns Found in Brick Masonry. In *Protection and Conservation of European Cultural Heritage, Research Report No. 8, Volume 2*. Fraunhofer IRB Verlag.

ISO 15927-3. (2009). *ISO 15927-3, Hygrothermal performance of buildings Calculation and presentation of climatic data Part 3: Calculation of a driving rain index for vertical surfaces from hourly wind and rain data*.

Kumaran, M. K., Mukhopadhyaya, P., Cornick, S. M., Lacasse, M. A., Rousseau, M. Z., Maref, W., Nofal, M., Quirt, J. D., & Dalgliesh, W. A. (2003). An Integrated methodology to develop moisture management strategies for exterior wall systems. *Proceedings of the 9th Canadian Conference on Building Science and Technology*.

Lacasse, M. A., Oe 9th Canadian Conference on Building Science and TReport from Task 6 of MEWS Project: Experimental Assessment of Water Penetration and Entry into Wood-Frame Wall Specimens - Final Report. In *Research Report (National Research Council of Canada. Institute for Research in Construction); no. RR-133*.

Lacasse, M. A., ONational Research Council of Canada. Institute for Report from Task 6 of MEWS Project: Experimental Assessment of Water Penetration and Entry into Wood-Frame Wall Specimens - Final Report. In *Research Report (National Research Council of Canada. Institute for Research in Construction); no. RR-133*. National Research Council of Canada. https://doi.org/10.4224/20386351

Lacasse, M. A., & Vanier (Eds.), D. J. (1999a). *Durability of building materials and components 8: service life and asset management, Durability of Building Assemblies and Methods of Service Life Prediction, vol. 2*. NRC Research Press.

Lacasse, M. A., & Vanier (Eds.), D. J. (1999b). *Durability of building materials and components 8: service life and asset management, Service Life and Durability of Materials and Components, vol. 1*. NRC Research Press.

Mayo, A. (1998). *To develop a European standard dynamicwatertightness test for curtain walling. Task 4: compare the conditions produced by existing test methods with the standard test conditions*.

Moore, T. V., Lacasse, M. A., & Defo, M. (2019). Determining Moisture Source due to Wind Driven Rain for Input to Hygrothermal Simulations Using Experimental Methods. *ASHRAE*.

NBN B 25-002-1. (2009). *External window work*. BIN.

Norwegian Standard. (1993). *ROOF, ROFFINGS: Test method for watertightness under pulsating air pressure* (p. 116). Nordtest –NT Build.

NRCC. (2015). National Building Code of Canada. *Institute for Research in Construction*.

Rousseau, M. Z., Poirier, G. F., & Brown, W. C. (1998). *Pressure Equalization in Rainscreen Wall Systems*. Construction Technology Updates No17.

Sahal, N., & Lacasse, M. A. (2004). Experimental assessment of water penetration and entry into siding-clad wall specimen. In *Internal Report (National Research Council* *of Canada. Institute for Research in Construction); no. IRC-IR-862*. National Research Council of Canada. https://doi.org/10.4224/20377802

Sahal, N., & Lacasse, M. A. (2005). Water entry function of a hardboard siding-clad wood stud wall. *Building and Environment*, *40*(11), 1479–1491. https://doi.org/10.1016/j.buildenv.2004.11.019

Scinocca, J. F., Kharin, V. V., Jiao, Y., Qian, M. W., Lazare, M., Solheim, L., Flato, G. M., Biner, S., Desgagne, M., & Dugas, B. (2016). Coordinated global and regional climate modeling. *Journal of Climate*. https://doi.org/10.1175/JCLI-D-15-0161.1

St-Hilaire, A., Derome, D., & Fazio, P. (2003). Approach for the simulation of wetting due to rain infiltration for building envelope testing. *Proceedings of the Ninth Canadian Conference on Building Science and Technology*, 459–474.

Straube, J. (2010). Simplified Prediction of Driving Rain on Buildings : ASHRAE 160P and WUFI 4.0. *Building Science Digest*.

Teunissen, H. W. (1970). *Characteristics of the Mean Wind and Turbulence in the Planetary Boundary Layer* (Issue 32). Institute for Aerospace Studies, University of Toronto.

Van Balen, K. (1996). Expert system for evaluation of deterioration of ancient brick masonry structures. *Science of The Total Environment*, *189–190*, 247–254. https://doi.org/10.1016/0048-9697(96)05215-1

Van Den Bossche, N. (2011). *Watertightness of building components: principles, testing and design guidelines. PhD thesis*. Ghent, Belgium.

Xiao, Z., Lacasse, M. A., & Dragomirescu, E. (2021). An analysis of historical wind-driven rain loads for selected Canadian cities. *Journal of Wind Engineering and Industrial Aerodynamics*, *213*, 104611. https://doi.org/10.1016/j.jweia.2021.104611

Xiao, Z., Lacasse, M. A., Gaur, A., & Dragomirescu, E. (2020). Climate data analysis to assess resilience of wall assemblies to moisture loads arising from the effects of wind-driven rain. *E3S Web of Conferences*, *172*, 11003. https://doi.org/10.1051/e3sconf/202017211003

Chapter 4 Future WDR and moisture load assessment

4.1 Projected changes of Wind-Driven Rain and moisture load in wall assemblies across Canada (Part I)

Zhe Xiao, Michael A. Lacasse, Elena Dragomirescu and Maurice Defo

Note: Z. Xiao brought the main contribution for experiment, data acquisition, formal analysis and paper writing. The co-supervisors, Dr. Lacasse and Dr. Dragomirescu contributed to this article with conceptualizing and data interpretation, while Dr. Defo contributed by providing guidelines in using numerical tools.

4.2 Abstract

The changing climate is affecting many aspects of the built environment. In respect to the wall assemblies of buildings, any change in the moisture load to the wall would influence its long-term moisture performance. Given that Wind-Driven Rain (WDR) is the primary source of the moisture load to the wall and that this load may also change as a result of changes to the climate in the future, it is expected then, that such changes will subsequently affect the moisture performance of wall assemblies. In this study, climate data for two future projected climate scenarios, 2.0°C (2034-2064) and 3.5°C (2062-2092), as generated from the Canadian Regional Climate Model (CanRCM4), and based on historical (1986-2016) baseline climate, data have been analyzed for 11 selected Canadian cities to investigate changes in climatic parameters such as, WDR and Driving Rain Wind Pressure (DRWP), as well as the Wind-Driven Rain Pressure Index (WDRPI), where the WDRPI reflects the concurrent effects of WDR and DRWP. Intensity-Duration-Frequency (IDF) curves for the WDR and WDRPI were also produced to explore the changes in probabilities of occurrence. In addition, watertightness tests were conducted for a vinyl and brick masonry veneer-clad wall assemblies, the results of which were used to establish a two-step approach to estimate the moisture loads in these two wall assembly types based on hourly WDR load and hourly averaged DRWP. Moisture loads of each wall assembly type during future projected climate scenarios were compared to those of the historical baseline periods. Increase in moisture load to both wall assembly types were found for most of cities analyzed in this study.

Keywords: climate change, wind-driven rain, driving rain wind pressure, climate loads, intensity-duration-frequency curves, watertightness test, water entry equations, moisture load

4.3 Introduction

According to the Intergovernmental Panel on Climate Change (IPCC), it is virtually certain that the global averaged precipitation will increase with an increase in surface temperature (Krinner et al., 2013). Depending on different future emission scenarios, the degree of changes in intensity and durations of precipitation events will vary. For the RCP2.6 emission scenario, for which the increase in mean temperature is limited to 2°C by the end of 21st century, precipitation will likely increase by 0.5% to 4% $°C^{-1}$ and for all other scenarios, by 1% to 3% $°C^{-1}$. In addition, both the observational and projected climate data are positively correlated to the extreme precipitation and global warming (Mirle et al., 2013). In Canada, by mid-century under the RCP2.6 scenario, the median projections for annual mean surface temperature will increase by 1.8°C. Whereas under a high emission scenario (RCP 8.5), the increase in surface temperature is projected to be 6°C by the end of 21st century (Bush & Lemmen, 2019). The increase in precipitation under these two scenarios are 7 % and 24 % respectively; such increase is mainly attributable to the shift from snow to rain in the spring and autumn. In addition, it is projected in the future with a high degree of confidence, that the daily extreme precipitation is to increase (Bush & Lemmen, 2019; Il Jeong & Sushama, 2018). These projected changes in precipitation will inevitably affect corresponding WDR loads and subsequently influence the performance of parts of the building envelope exposed to WDR.

Several previous studies have investigated the possible changes of moisture load and its impact on the building envelope under climate change. Nik et al. (Nik et al., 2015) studied the variation of hygrothermal performance of building façades in Sweden due to climate uncertainties which included global climate models, emissions scenarios and spatial resolutions. The discussion was focused on the variation of moisture content arising from WDR which was calculated from the precipitation and wind velocity of projected climate data affected by those climate uncertainties. Future risks of degradation of heritage buildings at 8 sites in the UK when subjected to the projected WDR were evaluated by Orr et al. (Orr et al., 2018). The projected climate data used was generated by the UKCP09 Weather Generator under a high-emissions scenario. The criteria for quantifying the impact in this study was the number of rain spells, the average number of which was predicted to remain constant while the WDR intensity was found to increase. In addition, the periods of time between rain spells were expected to be longer. It was concluded that building element failure would be more frequent under the scenario analyzed due to an increase in moisture ingress of the building fabric. In respect to Canada, Jeong & Cannon (Jeong & Cannon, 2020) investigated the projected changes of the moisture index, an the indicator useful for the design and management of building envelope. The climate data used in this study was generated from CanRCM4. As well, a simple linear bias correction scheme had been applied to the data generated from the CanRCM4 model to obtain unbiased moisture indices. It was determined that the projected moisture load over the western and eastern coastal regions of Canada was to substantially increase due to a warming-induced shift from snow to rain whereas that over south-central and northern Canada would decrease dramatically attributed to the increase in surface temperature with a concurrent unchanged relative humidity. The projected climate data have also been considered in many other fields to permit investigating different aspects of its impacts on the built environment. Studies have assessed the performance of the building envelope under the effects of climate change (Gaur et al., 2019; Lankester & Brimblecombe, 2012; Nik, 2017; Sanderson et al., 2017). Building energy consumption under projected climate conditions were evaluated by conducting whole building simulations (Salamanca et al., 2015, 2016; Tewari et al., 2017). Possible climate load effects on structural design and infrastructure applications have also been explored (Jeong, Cannon, et al., 2018; Jeong, Sushama, et al., 2018; Jeong & Sushama, 2018; Murdock et al., 2013; Picketts et al., 2016).

In the work described in this paper, the possible changes of WDR conditions were investigated for selected Canadian cities, as shown in Figure 4.1, and for two (2) future projected global warming scenarios, of 2°C (2034-2064) and 3.5°C (2062-2092) as compared to the historical baseline climate scenario (1986-2016). The analysis included changes in the number of rain hours, rain spell gap, WDR load, Driving Rain Wind

Pressure (DRWP), Wind Driven Rain Pressure Index (WDRPI) (3), and prevailing wind directions during rain events. Intensity-Duration-Frequency (IDF) curves for WDR and WDRPI were generated using the Gumbel distribution (4) to explore changes in probability of occurrence for different magnitudes of WDR and WDRPI. Thereafter, and given that the moisture load to the wall is the primary cause of the many detrimental effects that occur in wall assembly components (Desjarlais et al., 2001; Rousseau, 1999; Smegal et al., 2013), the moisture load was assessed based on hourly WDR loads and hourly averaged DRWPs for a vinyl-clad and a brick masonry veneer-clad wall assemblies using a two-step approach (Xiao, Lacasse, Defo, et al., 2021) derived from watertightness tests. Changes in moisture load of wall assemblies for selected cities based on the historical and future projected climate scenarios are also discussed.

Figure 4.1 Canadian Cities analyzed from West to East: VAN-Vancouver, CAL-Calgary, SAS-Saskatoon, WIN-Winnipeg, TOR-Toronto, OTT-Ottawa, MON-Montreal, MNC-Moncton, CHA-Charlottetown, HAL-Halifax, and STJ-St. John’s.

4.3 Climate data and methodology

4.3.1 Climate data

In this study, 15 bias-corrected datasets (realizations) with different initial conditions for the time period 1986-2016, were generated from historical data (Xiao, Lacasse, Dragomirescu, et al., 2021) collected over the same time period by meteorological stations operated by Environmental and Climate Change Canada (ECCC). Typical bias-correction methods as were used on this data, included simple scaling and additive corrections methods (Berg et al., 2012; Leander & Buishand, 2007), and more complex methods, such as, e.g. histogram equalization (Ashfaq et al., 2010; Li et al., 2010; Piani et al., 2010) and multivariable bias corrections methods (Cannon, 2018). These 15 realizations were thereafter used as the baseline for generating climate data for future projected periods derived from CanRCM4 (Scinocca et al., 2016). The CanRCM4 itself was downscaled from the CanESM2 large ensemble simulation (Environment and Climate Change Canada, 2018) which was obtained from a Global Climate Model considering interactions of the atmosphere, ocean, sea ice, land and carbon cycle components with a 2.8° spatial resolution (Arora et al., 2011) to a 0.44° grid.

With respect to the parameters relating to WDR, the wind speed and wind direction in the dataset were corrected from the bias correction factors that represent the differences between the modelled future and observed historical variables for each combination of hour and month. The additive correction factors were obtained for wind direction whereas the multiplicative correction factors were derived for wind speed. These factors were thereafter added to and multiplied with the projected data generated by the CanRCM4 model to produce the bias-corrected climate data. In regards to precipitation, the correction considered both the total numbers of wet hours and the magnitude of rainfall. The observational and modelled rainfall intensities were firstly sorted in descending order and thereafter rankings were applied. Since the modelled dataset is intended for generating more wet hours than the observational dataset (Berg et al., 2012; Bordoy & Burlando, 2013), the ranking number (n) of the first 0 value for the observational dataset would be smaller than that for the modelled dataset. Thereafter, all the modelled rainfall intensities were subtracted with the n^{th} rank modelled rainfall intensity ($R_{th,0}$) to obtain the first level corrected values $R_{dd(t)}$. Using this approach, the number of dry hours for model and observational data would thus be identical. In addition to the correction for wet hours, the first level corrected values were further adjusted by multiplying a factor which is equivalent to the ratio between the monthly averaged observed rainfall intensity and the monthly averaged corrected rainfall intensity ($R_{dd(t)}$) [8]. The time periods for the two projected periods, 2°C and 3.5°C, were 2034-2064 and 2062-2092 respectively. The consideration of the 2°C scenario is for a typical home mortgage period of 30 years, and the other scenario (3.5°C) was prepared in consideration of the long-term performance of wall assemblies during their life span.

4.3.2 WDR related parameters and the IDF curves

The WDR load in this study was calculated by Eq. (4.1), as given in the ASHRAE standard (ASHRAE, 2016):

$$r_{bv} = r_h \mathrm{F_E F_D F_L} U \cos\theta \tag{4.1}$$

Where, r_{bv} is the WDR intensity (kg/m^2·h); r_h is the horizontal rainfall intensity (mm/h), and F_E, F_D and F_L are respectively, the rain exposure factor, rain deposition factor, and an empirical constant, 0.2 kg·s (m^3·mm); U is the concurrent hourly average wind speed (m/s) and θ is the angle between the wind direction and normal to the wall. The rain exposure factor (F_E), and the deposition factor (F_D) are determined by the building configurations and topography surrounding the building which in this study were considered both equal to 1 when analyzing the WDR load.

The DRWP was calculated using the Bernoulli principle (4.2). The value of air density ρ used in this study was 1.225 kg/m^3 and V is the hourly averaged wind velocity.

$$DRWP = \frac{1}{2}\rho V^2 \tag{4.2}$$

As reported in many watertightness tests (Bossche et al., 2012; Sahal & Lacasse, 2004, 2005), both the WDR intensity and DRWP have an effect on the rate of water entry to the wall assembly. However, no meaningful correlation between these two factors could be concluded from an analysis of climate data(Xiao, Lacasse, Dragomirescu, et al., 2021). To better describe the severity of risk to water entry from the concurrent effects of WDR intensity and DRWP, the Wind Driven Rain Pressure Index (WDRPI) was introduced as show in Eq. (4.3). The coefficients α and β are determined from watertightness tests for different wall assembly configurations based on their response, respectively, to the WDR intensity and DRWP during a test. When analyzing the climate data, both these factors were considered equal to 1.

$$WDRPI = \mathrm{WDR}^{\alpha} \times DRWP^{\beta} \tag{4.3}$$

Other than investigating the changes in distributions of WDR conditions, the magnitude and probability of occurrence of extreme WDR events were also of interest. The Gumbel distribution (4.4) was selected (Xiao, Lacasse, Dragomirescu, et al., 2021) to generate intensity-duration-frequency curves for each realization of future projected climate scenarios in which the extreme WDR conditions for different lengths of rain events during projected periods were compared to that which occurred during the historical climate period.

$$F_{(\mu,\sigma)}(x) = EXP\left(-(e)^{\frac{-(x-\mu)}{\sigma}}\right) \tag{4.4}$$

4.3.3 Moisture load

There are two typical approaches to estimate the moisture load in a wall assembly. One is to consider the moisture as 1 % of the WDR load that is deposited onto the exterior surface of a wall assembly as stated in ASHRAE standard 160 (ASHRAE, 2016); the other approach is to directly measure the moisture load during watertightness tests. The results obtained from tests can be used to establish the water entry equations to derive moisture loads based on hourly WDR loads and concurrent hourly averaged DRWPs (Moore et al., 2019; Xiao, Lacasse, Defo, et al., 2021).

In this study, watertightness test results of a vinyl clad and a brick veneer-clad wall assembly were used to assess the moisture load in these two wall assemblies when subjected to different WDR loads and DRWPs. The assessment procedure included two steps (Xiao, Lacasse, Defo, et al., 2021): (i) determine the values of the adjustment coefficients α and β for the WDRPI by fitting equation (3) to the water entry rates measured from watertightness tests; and, (ii) an exponential function is used to depict the relation between water entry rates and the adjusted WDRPIs as given in Eq. (4.5).

$$Water\ Entry\ Rate = a \times WDRPI^{b} \tag{4.5}$$

The two adjustment coefficients, a and b, were derived from fitting the plot of the water entry rates to the corresponding values of WDRPIs. The exponential function was thereafter used to calculate water entry rates based on hourly WDR loads and hourly averaged DRWPs through the use of the WDPRI.

4.4 Projected Changes for WDR, DRWP and WDRPI

The hourly WDR loads and hourly averaged DRWPs are the factors considered to assess the moisture load in wall assemblies. Any changes to the WDR load and DRWP in the future due to the climate change will inevitably affect the performance of wall assemblies in relation to the moisture load to which they are subjected. Thus, analyzing possible changes of parameters relating to the WDR load and DRWP would provide information on conditions to which wall assemblies may be subjected during future projected climate scenarios.

4.4.1 Rain hours and rain spell gaps

Changes in frequency of rain hours and frequency of gaps between rain spells, defined as 96 or more consecutive dry hours (ISO 15927-3, 2009) between rain events, are shown in Table 4-1. The number of rain hours is the number of hours recorded as non ice or snow precipitation during the assessment period. The mean number of rain hours for each scenario is averaged from 15 realizations generated by the climate model. The 95% confidence interval is also for the 15 values for rain hours derived from each of the 15 realizations. Opposite to this are hours recorded with zero precipitation; these are considered as dry hours. When generating the projected climate dataset, the dry hours of the future projected climate scenarios have been corrected to match that of the historical climate dataset. In another words, the variation of rain hours between the historical and projected periods are attributed to changes in ice and snow hours which are sensitive to temperature. Considering that the duration of the winter period in Canada is longer than most other counties around the World, it is reasonable to speculate that global climate change in Canada would more significantly affect the future projected number of rain hours. The rain spell, as defined in the ISO standard [32], indicates the level of moisture exposure risk arising from WDR deposited on the cladding of the building envelope. The rain spell gaps, a period that has no (=0) precipitation, is therefore negatively correlated to the moisture exposure risk.

Table 4-1 Change in rain hours and rain spell gaps

Scenarios:		Hist. 1986-2016	2°C 2034-2064		3.5°C 2062-2092	
Cities		Mean	Mean	95% CI	Mean	95% CI
Calgary	*Rain Hours*	7127	9251	± 265	10373	± 264
	Diff. to Hist. (%)		**130%**	**± 2.86%**	**146%**	**± 2.55%**
	Rain Spell Gaps	1791	1572	± 24	1428	± 23
	Diff. to Hist. (%)		**87.7%**	**± 1.52%**	**79.7%**	**± 1.65%**
Charlottetown	*Rain Hours*	18502	20895	± 541	21996	± 513
	Diff. to Hist. (%)		**113%**	**± 2.59%**	**119%**	**± 2.33%**
	Rain Spell Gaps	1203	923	± 29	784	± 32
	Diff. to Hist. (%)		**76.7%**	**± 3.13%**	**65.1%**	**± 4.12%**
Halifax	*Rain Hours*	19775	23002	± 420	22315	± 432
	Diff. to Hist. (%)		**116%**	**± 1.83%**	**113%**	**± 1.94%**
	Rain Spell Gaps	1001	708	± 16	610	± 13
	Diff. to Hist. (%)		**70.7%**	**± 2.21%**	**60.9%**	**± 2.1%**
Moncton	*Rain Hours*	15341	17013	± 268	18124	± 272
	Diff. to Hist. (%)		**111%**	**± 1.57%**	**118%**	**± 1.5%**
	Rain Spell Gaps	1231	962	± 23	781	± 19
	Diff. to Hist. (%)		**78.1%**	**± 2.4%**	**63.5%**	**± 2.41%**
Montreal	*Rain Hours*	21746	22766	± 466	23450	± 473
	Diff. to Hist. (%)		**105%**	**± 2.04%**	**108%**	**± 2.02%**
	Rain Spell Gaps	1053	860	± 14	740	± 18
	Diff. to Hist. (%)		**81.7%**	**± 1.62%**	**70.2%**	**± 2.48%**
Ottawa	*Rain Hours*	15546	16608	± 304	17360	± 337
	Diff. to Hist. (%)		**107%**	**± 1.83%**	**112%**	**± 1.94%**

	Rain Spell Gaps	1217	1028	± 21	888	± 25
	Diff. to Hist. (%)		**84.5%**	**± 2.05%**	**73%**	**± 2.84%**
Saskatoon	*Rain Hours*	8465	9452	± 302	9996	± 375
	Diff. to Hist. (%)		**112%**	**± 3.2%**	**118%**	**± 3.75%**
	Rain Spell Gaps	1656	1515	± 20	1430	± 21
	Diff. to Hist. (%)		**91.5%**	**± 1.31%**	**86.4%**	**± 1.48%**
St. John's	*Rain Hours*	19393	22007	± 494	23003	± 343
	Diff. to Hist. (%)		**113%**	**± 2.24%**	**119%**	**± 1.49%**
	Rain Spell Gaps	1208	816	± 31	658	± 19
	Diff. to Hist. (%)		**67.6%**	**± 3.75%**	**54.5%**	**± 2.84%**
Toronto	*Rain Hours*	18868	18730	± 548	18712	± 260
	Diff. to Hist. (%)		**99.3%**	**± 2.93%**	**99.2%**	**± 1.39%**
	Rain Spell Gaps	1118	1000	± 16	942	± 18
	Diff. to Hist. (%)		**89.4%**	**± 1.57%**	**84.2%**	**± 1.88%**
Vancouver	*Rain Hours*	48903	51589	± 1259	50725	± 1116
	Diff. to Hist. (%)		**106%**	**± 2.44%**	**104%**	**± 2.2%**
	Rain Spell Gaps	765	632	± 22	657	± 17
	Diff. to Hist. (%)		**82.6%**	**± 3.53%**	**85.8%**	**± 2.66%**
Winnipeg	*Rain Hours*	7480	8181	± 256	8586	± 305
	Diff. to Hist. (%)		**109%**	**± 3.14%**	**115%**	**± 3.56%**
	Rain Spell Gaps	1655	1538	± 17	1453	± 26
	Diff. to Hist. (%)		**92.9%**	**± 1.13%**	**87.8%**	**± 1.76%**

When comparing the average number of rain hours from the future projected climate scenario to that of the historical baseline period each of average number of rain hours for the two future projected periods, 2.0°C and 3.5°C, increased for majority of cities, with the exception of Toronto, where the total number of rain hours remained almost the same. In Calgary, Charlottetown, Moncton, Montreal, Ottawa, Saskatoon, St. John's, and Winnipeg, the rain hours for the 3.5°C scenario was greater than that for the 2.0°C scenario. The most significant increase in rain hours was observed in Calgary and the climate model predicted, respectively, 30% and 46% more rain hours for the 2.0°C and 3.5°C future climate scenarios.

Compared to the historical baseline periods, a notable reduction in the number of rain spell gaps were predicted for both future projected periods in all cities. Except for

Vancouver, the numbers of rain spell gaps for the 3.5°C future scenario were fewer than that for the 2.0°C scenario. The east coast cities of Charlottetown, Moncton, Halifax, and St. John's had a greater reduction in rain spell gaps than other cities across Canada. From the magnitude of the 95% confidence interval, the discrepancies between realizations generated from different initial conditions for the rain hours and number of rain spell gaps were not significant.

4.4.2 WDR intensities, DRWP and WDRPI

It is evident that any changes in the WDR load, which is the primary source of moisture load in wall assemblies, could subsequently affect the moisture load used in the hygrothermal simulation of wall assemblies. Also, in respect to the watertightness test, that provides a mean to replicate WDR conditions and permits a more accurate estimate of the moisture load in a wall assembly, knowledge of the ranges of WDR related parameters is beneficial when establishing boundary conditions for test parameters.

The WDR intensity, DRWP and WDRPI in different cities for the historical baseline periods and the two future projected periods are shown in Figure 4.2, Figure 4.3 and Figure 4.4, respectively. The range of values over 31 years for each different parameter was described in terms of the six following categories: mean, 50-percentile, 90-percentile, 99-percentile, 99.5-percentile, and 100-percentile. The range of values depicted in the boxplots for the different parameters relate to values for each category that encompasses all the 15 realizations. The upper and lower whisker were 1.5 times the interquartile range (IQR) from the first and third quartiles. Boxplots for each category are shown in different palette colors and for the different scenarios (i.e., historical; future 2.0°C; future 3.5°C), the colors of the boxplots were selected from the same color palette but with a different shade. The magnitude of the values in vertical axis was set as a Log scale.

The value at the 100-percentile was the maximum value for the scenario analyzed. It was noted that the values within this category as generated by different realizations varied substantially for all 3 parameters analyzed, i.e., WDR intensity, DRWP, and WDRPI. For example, the upper limit and lower limit of the 100-percentile WDR intensity in Calgary for the 3.5°C scenario generated from 15 realizations were, respectively, 160mm/h and 33 mm/h. The third and first quantiles for the same case were 107mm/h and at 58mm/h. Such large discrepancies between single values, as was selected from each realization, suggests that the generation of the maximum value by the climate model was randomly produced. Thus, to produce reliable conclusions it was not considered useful to use 100-percentile values.

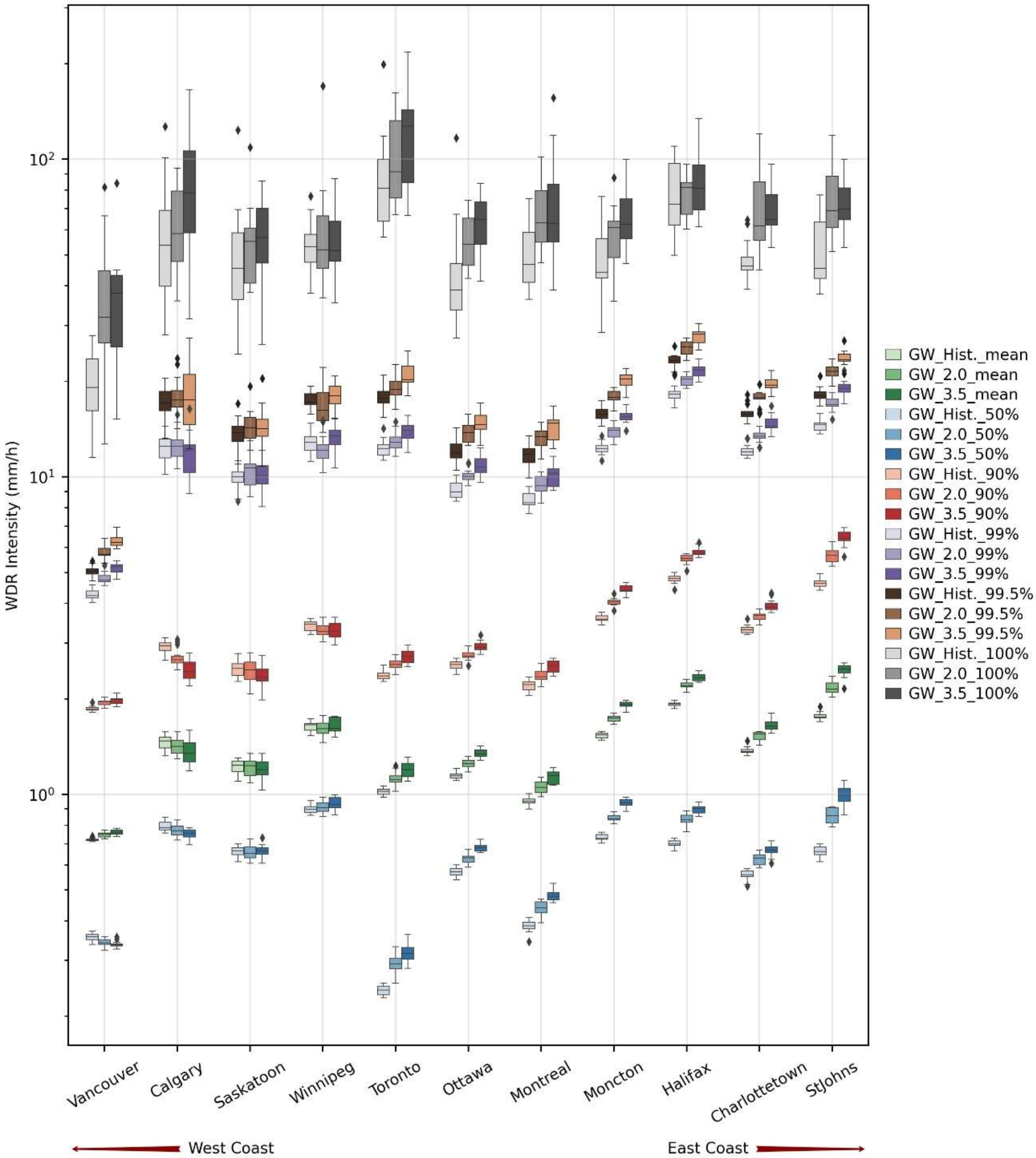

Figure 4.2 WDR intensities for historical and future projected scenarios

The WDR intensities for St. John's, Charlottetown, Halifax, Moncton, Montreal, Ottawa, and Toronto were predicted to increase for the mean, 50-percentile, 90-percentile, 99-percentile, and 99.5 percentile for the future projected periods of 2034-2064 and

2062-2092, where, respectively, temperature increases of 2.0°C and 3.5°C are expected, as compared to the historical baseline time period of 1986-2016. Also, the WDR intensities during the 2062-2092 period were higher than that during the 2034-2064 period. For other cities, the WDR intensities in Calgary decreased over the future time periods for the mean, 50-percentile, 90-percentile, and 99-percentile categories whereas the 99.5-percentile value remained almost the same for over the 3 time periods. In Saskatoon and Winnipeg, the WDR intensities did not change significantly over time at all levels. Whereas in Vancouver, the WDR intensities were predicted to decrease for the 50-percentile value and increase for all other categories in the future. In general, the WDR intensities in east coast cities, such as St. John’s, Charlottetown, Halifax, and Moncton, were higher than other cities for almost all categories. Only Calgary and Winnipeg had slightly higher WDR intensities for the 50-percentile category. The maximum median value of WDR intensities for the 15 realizations was Halifax for the 3.5°C future scenario with a magnitude of 38mm/h.

The DRWP is calculated using Bernoulli's principle (2). For a watertightness test, the DRWP is an important input test parameters together with the water spray rate, although its significance to the rate of water entry to the wall assembly largely depends on the type of deficiency (Bossche et al., 2012; Lacasse et al., 2003) through which water may penetrate. The predicted changes for DRWP are given in Figure 4.3.

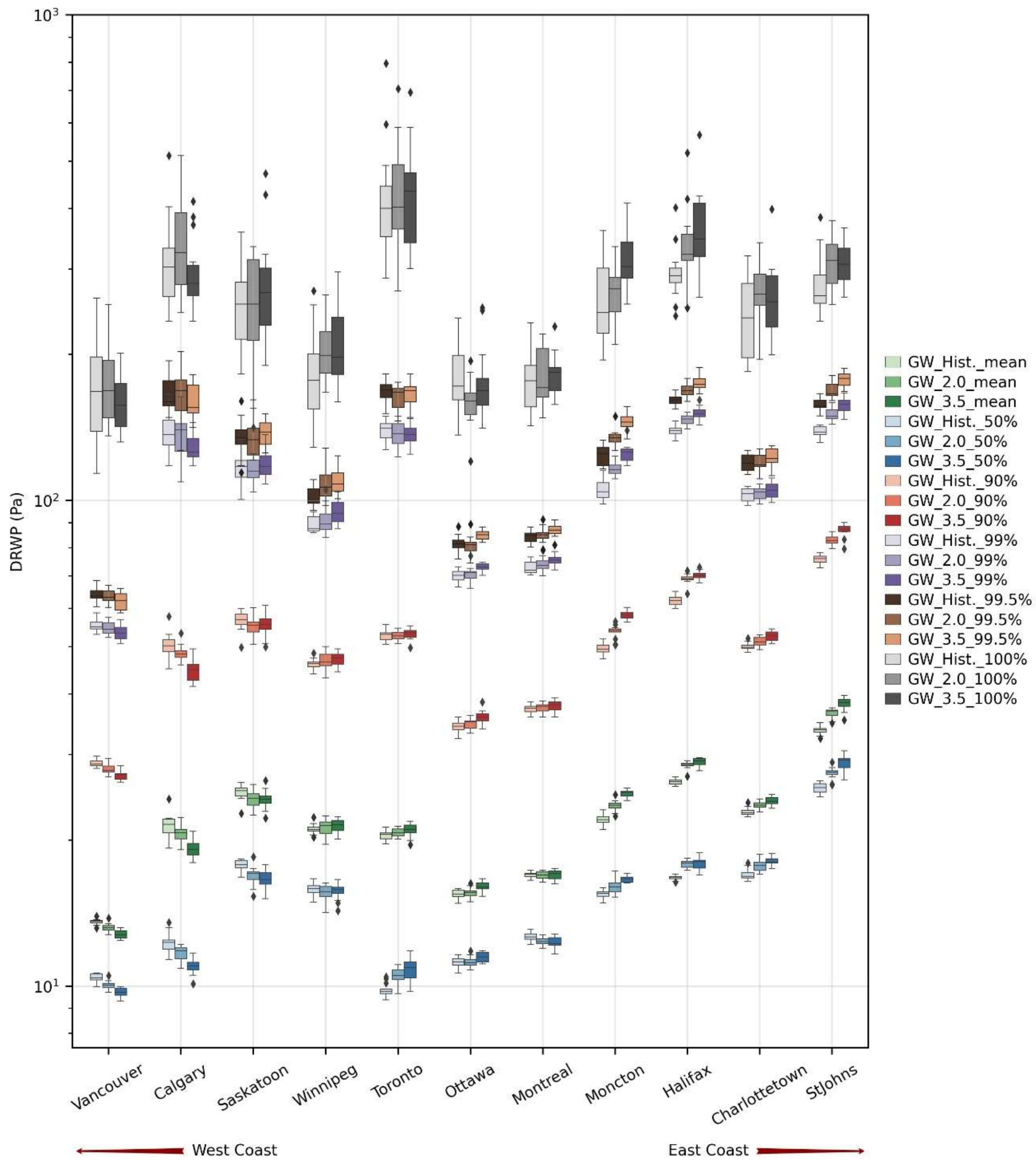

Figure 4.3 DRWP for historical and projected periods

Except for the100-percentile category, the DRWPs for the four (4) east coast cities were predicted to increase for the two future projected periods in which DRWPs for the 3.5°C scenario were higher than that for the 2.0°C scenario. Conversely, for the cities Calgary and Vancouver, which are located in the western part of Canada, their DRWPs dropped over the predicted time periods in all categories. For the remaining cities of

Winnipeg, Toronto, Ottawa, and Montreal, the DRWPs remain almost the same. Most of DRWPs at the 99.5- percentile were lower than 200 Pa. Only the upper limit of the boxplot in Calgary for 2.0°C future scenario was barely larger than 200Pa. It was noted that the DRWPs in all cities at or below 90-percentile were lower than 100 Pa. When establishing pressure steps applied to test specimens during a watertightness test, the distributions of these values should also be taken into account.

As shown in Figure 4.4, the WDRPI were predicted to increase in the cities of Toronto, Ottawa, Montreal, Moncton, Halifax, Charlottetown, and St. John's which are situated on the east of Canada for all analyzed categories except for the 100-percentile value. Between the two future projected periods, higher WDRPIs were seen in all these cities for the 3.5°C scenario. The incremental values for the WDRPIs were positively correlated with the percentile level which implies that more extreme WDR events will occur in the future. In Winnipeg, the WDRPIs almost remained the same for the mean, 50-percentile, and 90-percentile categories and increased for the 3.5°C future scenario as compared to the historical scenario for the 99-percentile and 99.5-percentile categories. The WDRPIs were projected to slightly decrease in the future for all categories in Calgary and Saskatoon, which are cities located in the Prairie Provinces, as well as for the 50-percentile category in Vancouver, a west coast city. Nevertheless, the 99-percentile and 99.5-percentile WDRPI values for Vancouver would increase with a warmer climate.

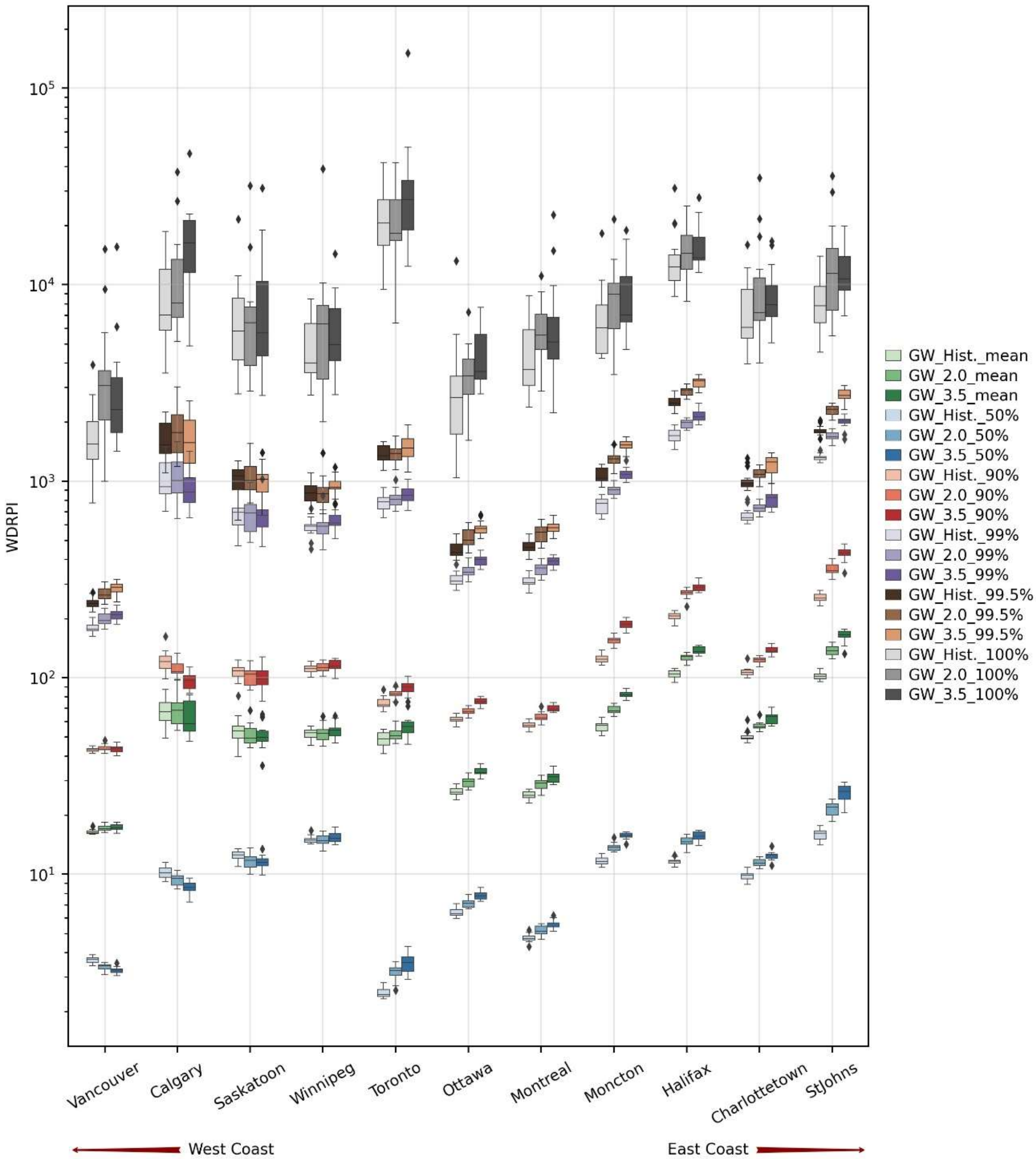

Figure 4.4 WDRPI for historical and projected periods

The plots given in Figure 4.5 show the distributions of frequencies of wind directions during WDR events for the historical baseline and future projected periods. The north direction was 0° in the plot and 90°, 180° and 270° represent east, south, and west directions respectively. The minimum wind direction resolution was 10 °. The frequencies of occurrence of each wind direction were presented as a percentage and the total sum for the weight of frequencies of occurrence for all wind directions was 100%.

The wind direction is a major factor considered to determine the magnitude of the WDR load. The changes in wind direction during WDR events generated by the climate model did not seem very promising. The projected distributions of wind directions for the three (3) time periods analyzed were almost identical which is not likely given a changing climate and stochastic atmospheric flows. However, the projected prevailing wind direction could still be considered a useful projected value, given that the atmospheric flow was computed by the numerical formulation of the large-scale climate model (Laprise et al., 1997).

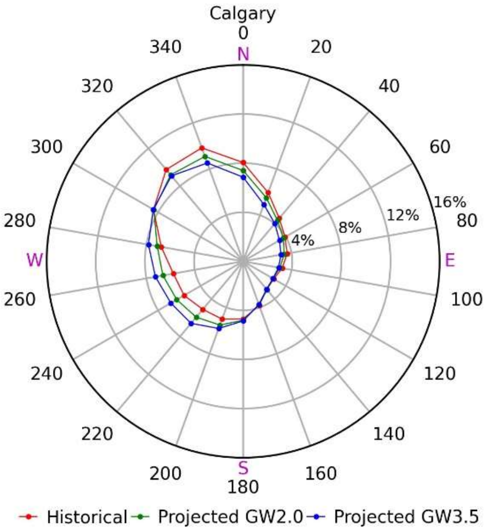
Calgary
0
N
20
40
60
80
E
100
120
140
160
S
180
200
220
240
260
W
280
300
320
340
4%
8%
12%
16%
Historical
Projected GW2.0
Projected GW3.5

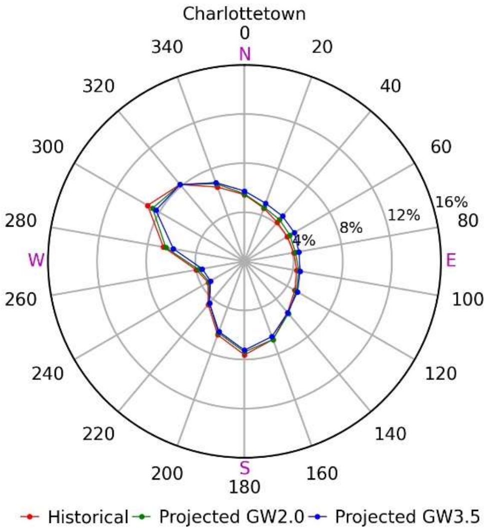
Charlottetown
0
N
20
40
60
80
E
100
120
140
160
S
180
200
220
240
260
W
280
300
320
340
4%
8%
12%
16%
Historical
Projected GW2.0
Projected GW3.5

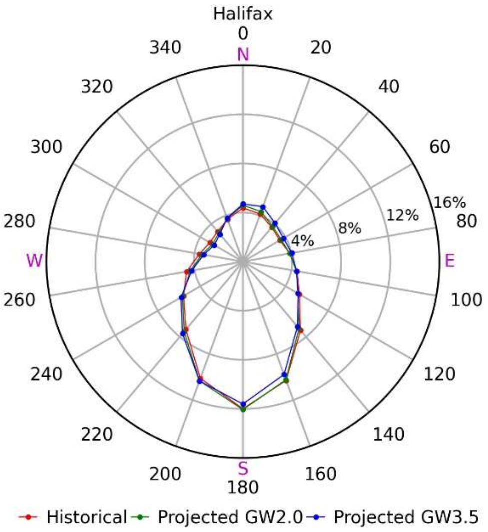
Halifax
0
N
20
40
60
80
E
100
120
140
160
S
180
200
220
240
260
W
280
300
320
340
4%
8%
12%
16%
Historical
Projected GW2.0
Projected GW3.5

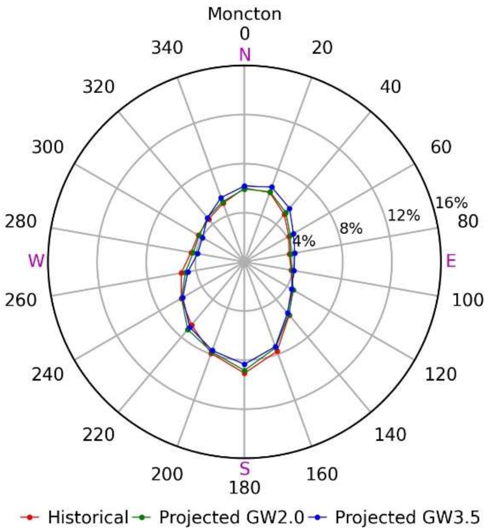
Moncton
0
N
20
40
60
80
E
100
120
140
160
S
180
200
220
240
260
W
280
300
320
340
4%
8%
12%
16%
Historical
Projected GW2.0
Projected GW3.5

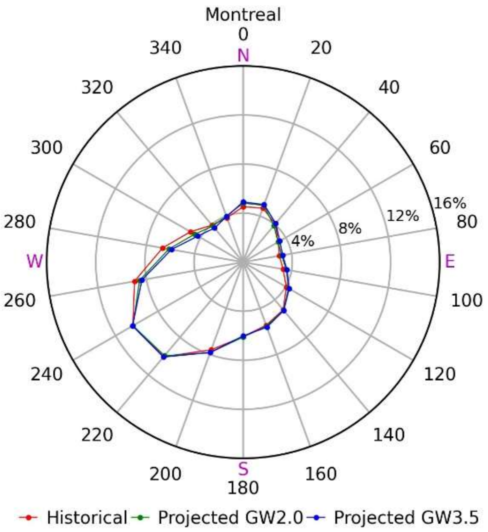
Montreal
0
N
20
40
60
80
E
100
120
140
160
S
180
200
220
240
260
W
280
300
320
340
4%
8%
12%
16%
Historical
Projected GW2.0
Projected GW3.5

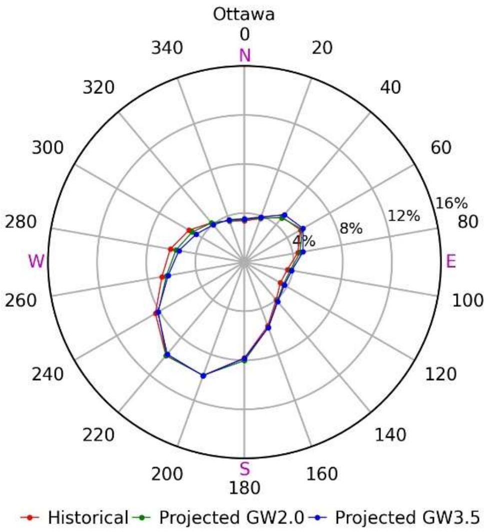
Ottawa
0
N
20
40
60
80
E
100
120
140
160
S
180
200
220
240
260
W
280
300
320
340
4%
8%
12%
16%
Historical
Projected GW2.0
Projected GW3.5

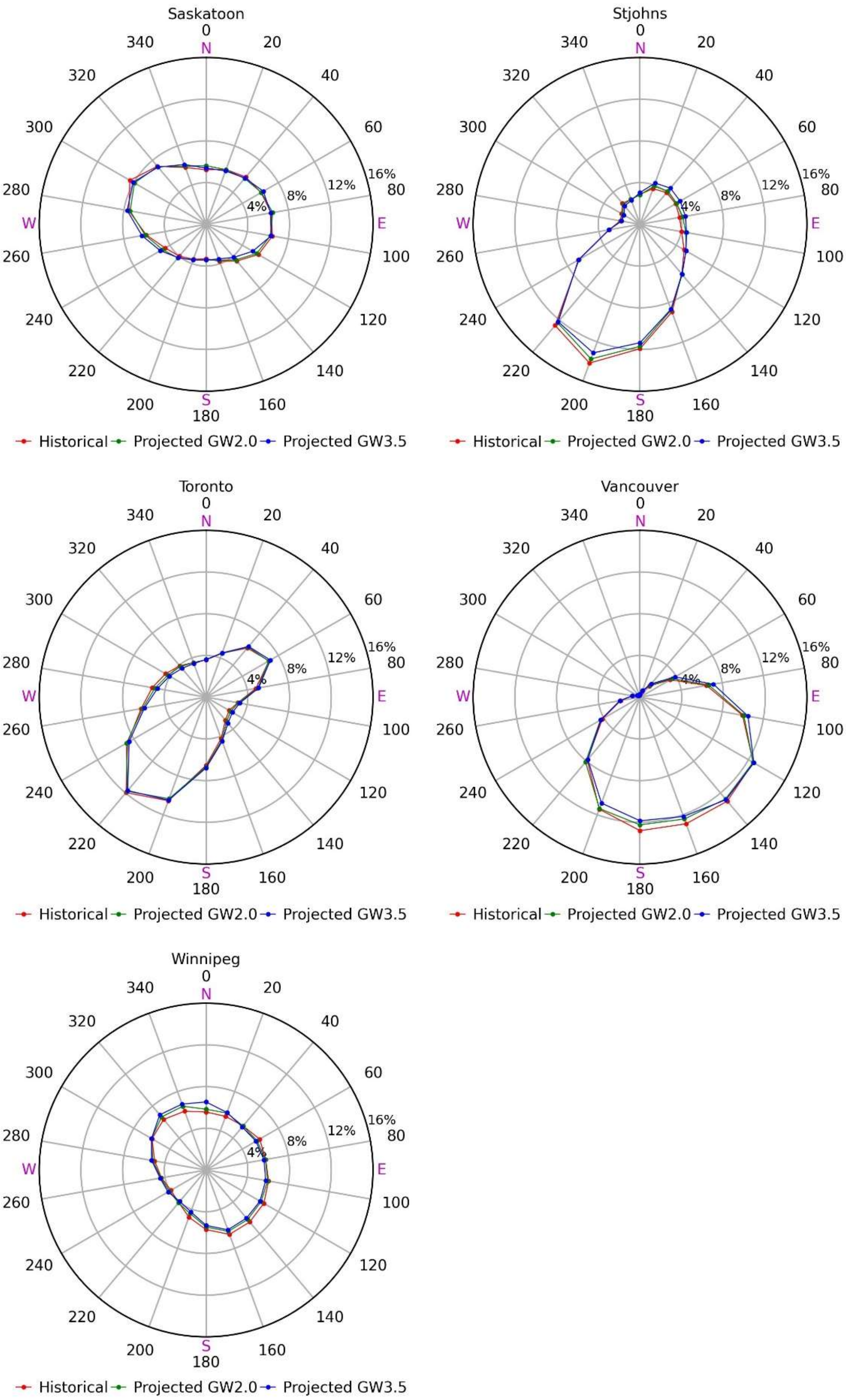

Figure 4.5 Projected Changes of Wind Directions

4.4.3 Intensity-Frequency-Duration curves

The Intensity-Frequency-Duration (IDF) curves were generated for the WDR load and the WDRPI values for the future projected periods to permit estimating the extreme WDR conditions for different probabilities of occurrence. The annual maximum values of 31 years of data for each realization were fitted to a Gumbel distribution (4). The parameters determined from the fitting process were then used to generate values of Gumbel distribution parameters for different return periods. The WDR loads for 1, 2, 4, 8, 12 and 24-consecutive hours events for different return periods were produced and the values for each city averaged from the 15 realizations.

As shown in Figure 4.6, different durations of WDR loads were considered for the 2-year, 5-year, 10-year, 20-year,30-year, 50-year and 100-year return periods. For all analyzed cities, the WDR loads for the future projected periods were higher than that of the historical scenario, and the extreme WDR loads for the 3.5°C future scenario were greater than that for 2.0°C scenario for all return periods. The highest 1-hour WDR load for a 100-year return period was observed in Toronto with a value of 78 mm/hour and the highest 24-hour WDR load for a 100-year return period was found in St. John's. Whereas, Vancouver had the lowest WDR load for all durations categories and all return periods. The most significant changes for extreme WDR loads between the historical and future projected periods were observed for Moncton: an increase of over 20% was noted between historical and the 2.0°C future scenario for the100-year return period and for the 1-hour WDR load, over 20% increase between the 2.0°C and 3.5°C future scenarios.

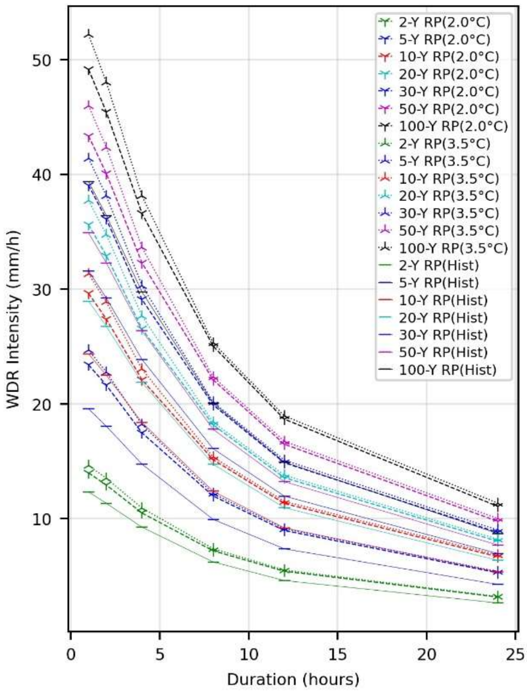

(a) Calgary

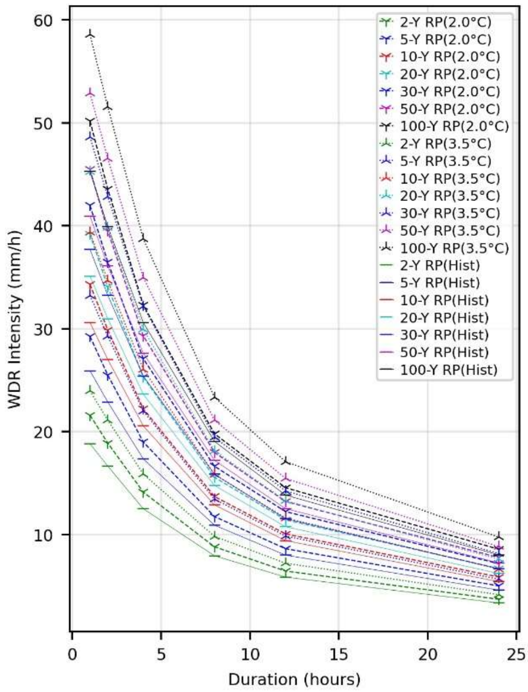

(b) Charlottetown

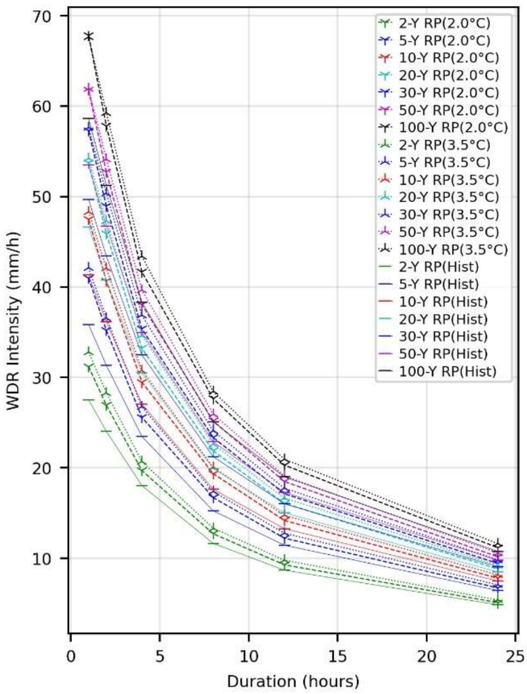

(c) Halifax

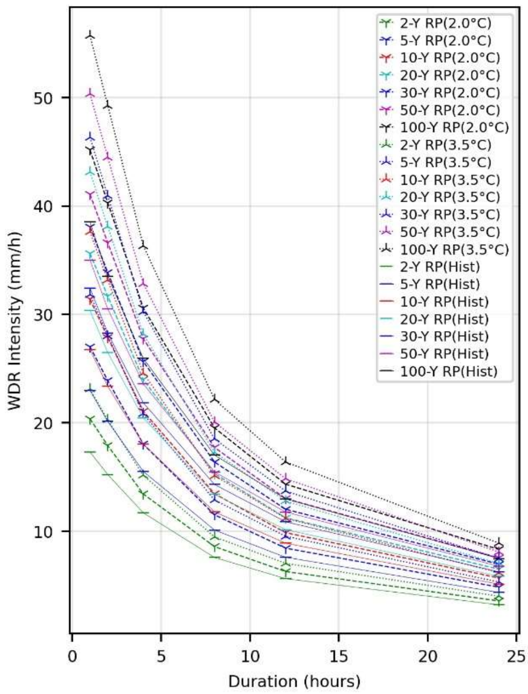

(d) Moncton

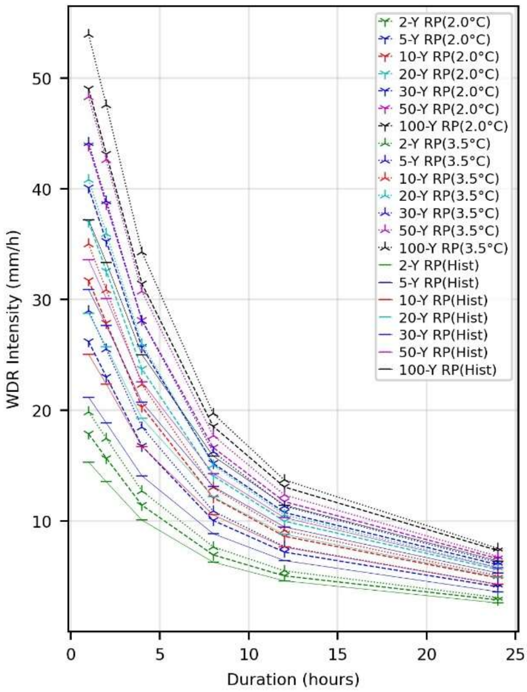

(e) Montreal

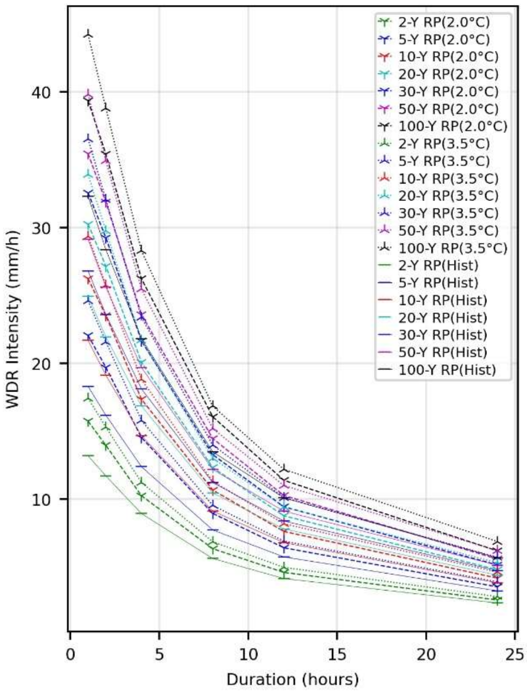

(f) Ottawa

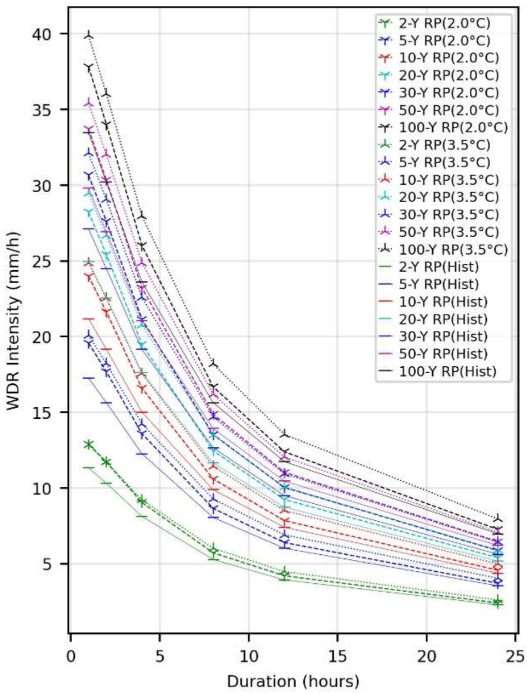

(g) Saskatoon

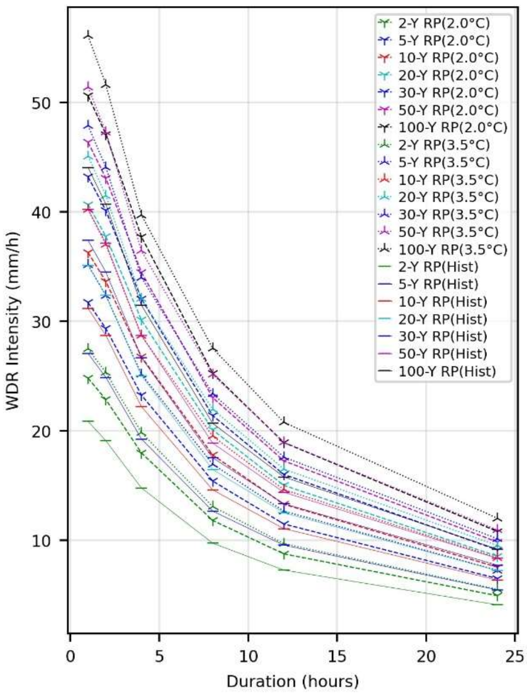

(h) St. John’s

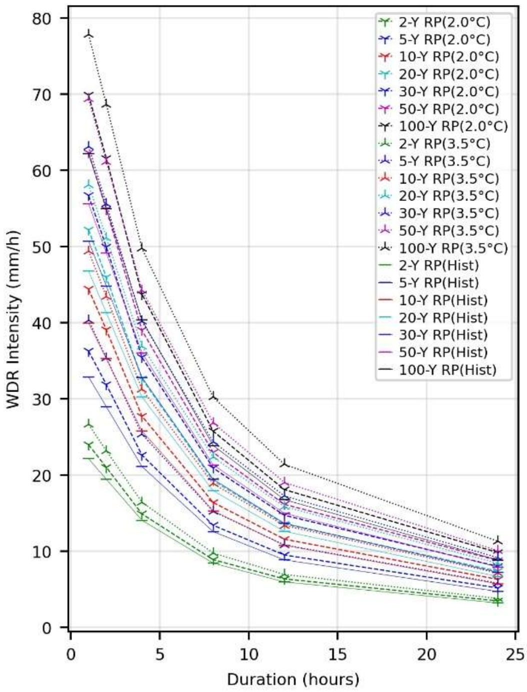

(i) Toronto

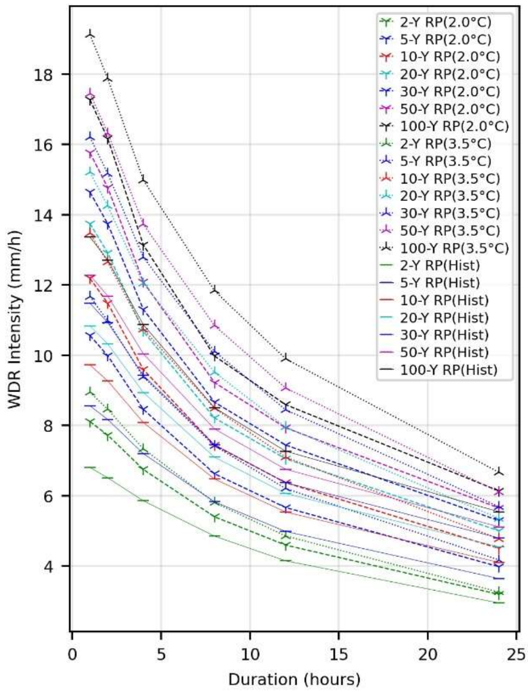

(j) Vancouver

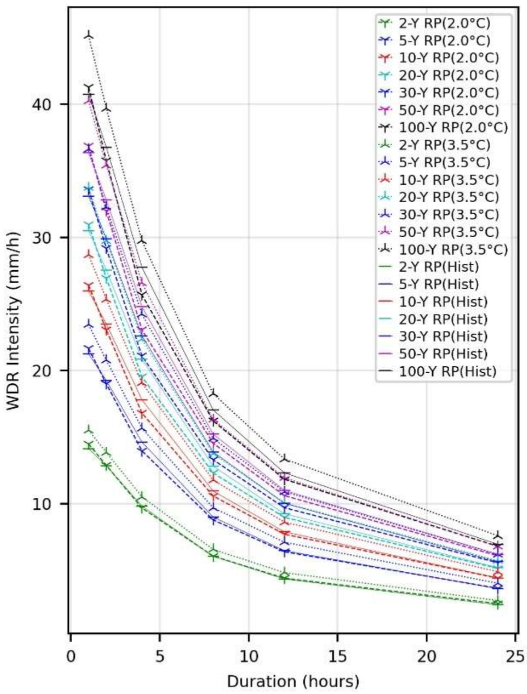

(k) Winnipeg

Figure 4.6 IDF curves for WDR load in selected cities

The IDF curves for WDRPI values of each city are given in Figure 4.7. The duration of events and return periods considered were the same as those used for the WDR load IDF curves. The greatest WDRPI values for all duration categories and all return periods were for Halifax. The values of WDRPIs for the same duration category in Halifax were at least two times greater than in other cities excepted for that of St. John's and Toronto. Considering the differences in extreme WDR loads between Halifax and other cities were much lower than this ratio, it is noted that the extreme DRWP conditions for Halifax were much more severe than the other cities considered in this work. Similar to the extreme WDR load, the least extreme WDRPI values were observed in Vancouver for all duration categories and return periods. The WDRPI values during future projected periods were greater than that for the historical scenario in all cities and for all duration categories and return periods. The discrepancies in WDRPI values between the historical and future projected periods were relatively small for shorter return periods and tended to increase for longer return periods. For instance, the 1-hour WDRPI value in Calgary for a 2-year return period was 1114 for the historical scenario, 1327 for the 2.0°C future scenario, and 1377 for the 3.5°C future scenario. The increase in WDRPI values between historic and the 2.0°C and 3.5°C future projected periods was 19% and 24% respectively. Whereas, for a 100-year return period, the WDRPI respective values for the historical, 2.0°C, and 3.5°C scenarios were 4550, 5838, and 6317. Thus, these increases from the historical periods were 28% and 39% respectively for the 2.0°C and 3.5°C future projected periods.

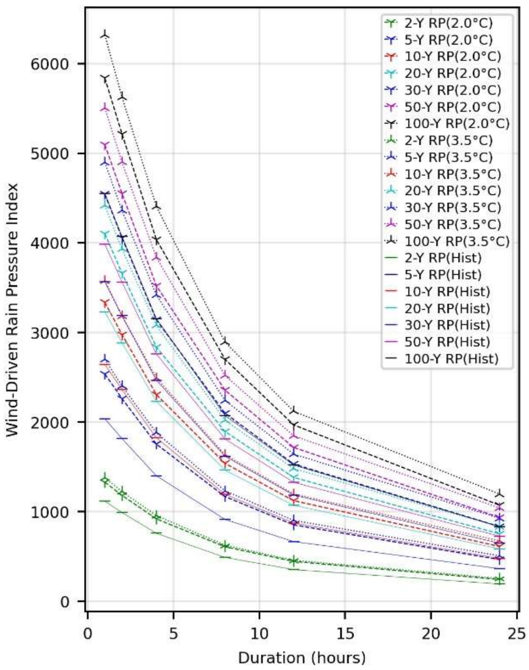

(a) Calgary

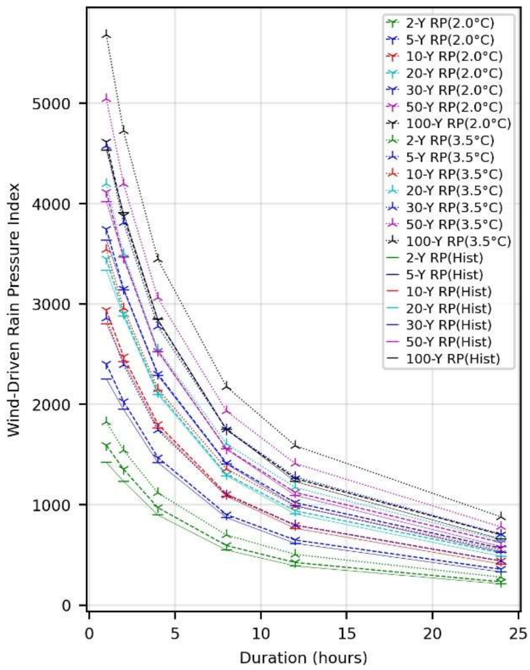

(b) Charlottetown

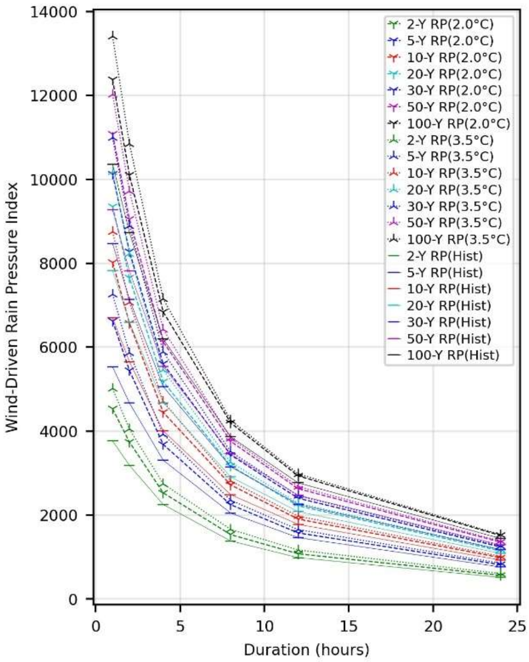

(c) Halifax

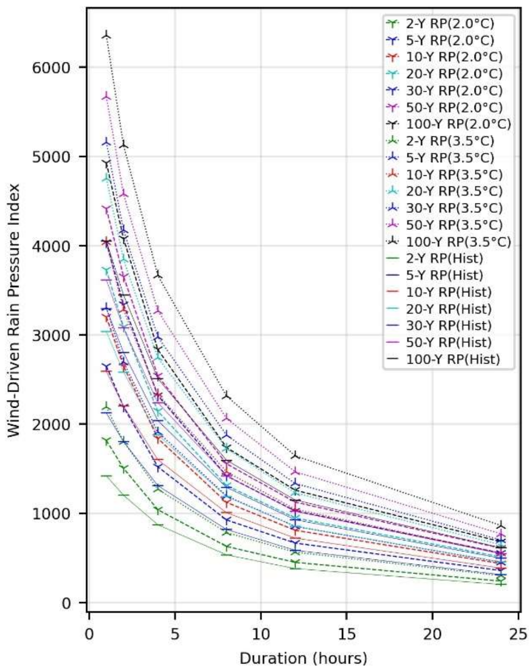

(d) Moncton

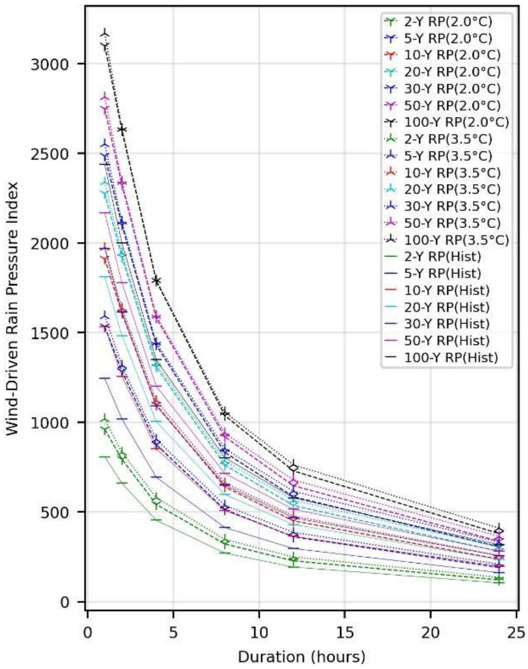

(e) Montreal

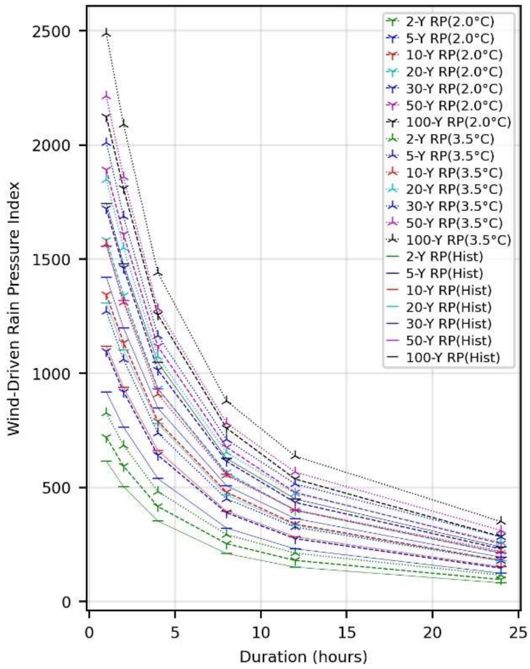

(f) Ottawa

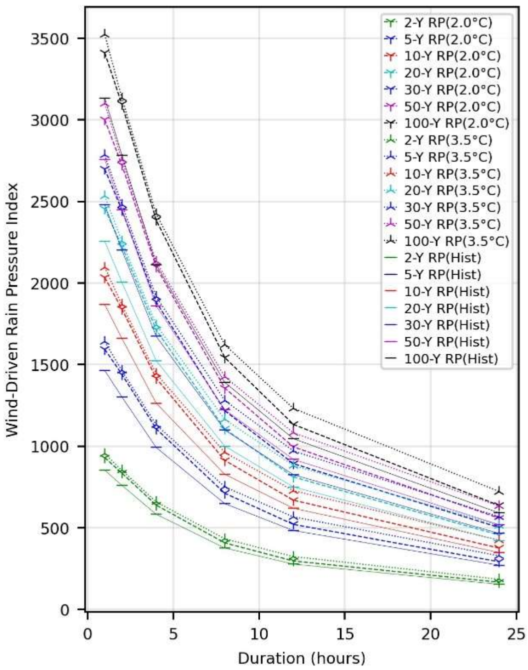

(g) Saskatoon

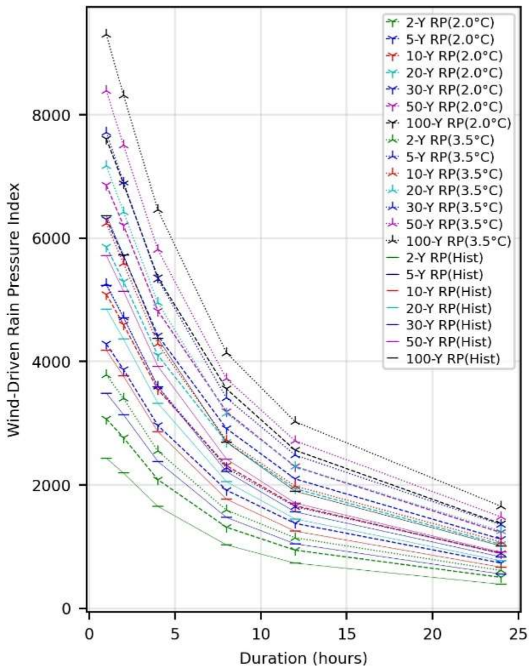

(h) St. John’s

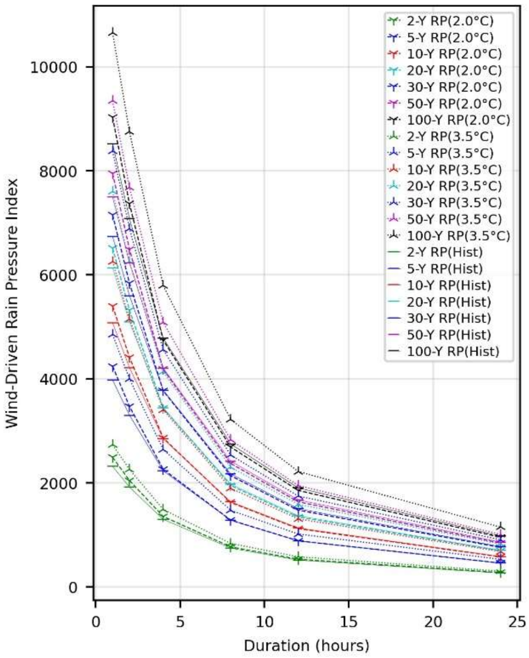

(i) Toronto

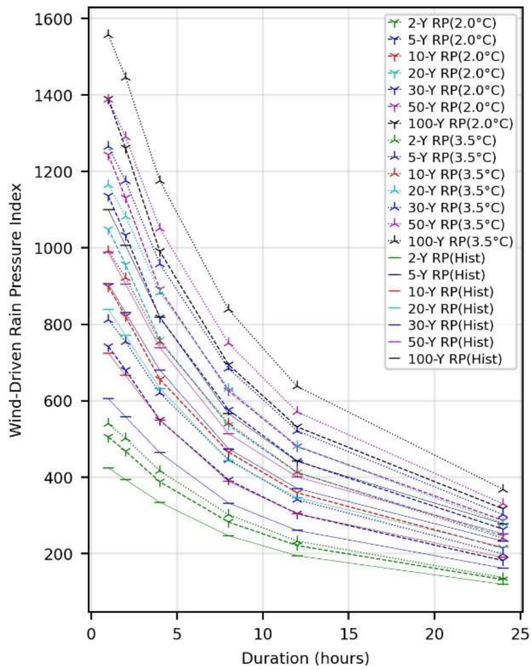

(j) Vancouver

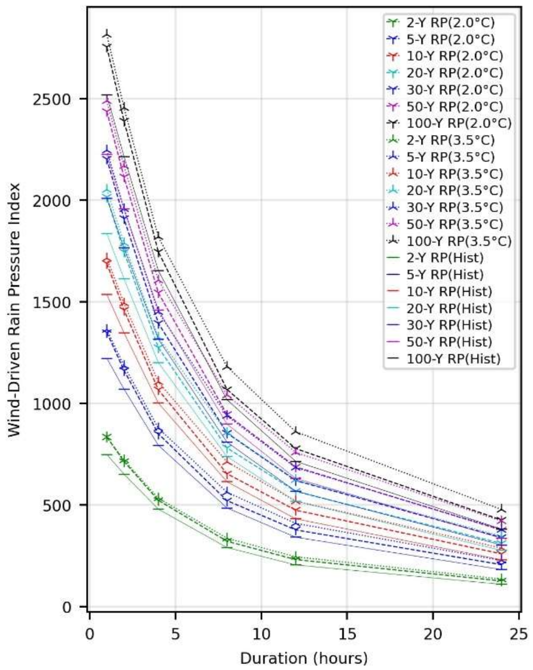

(k) Winnipeg

Figure 4.7 IDF curves for WDRPI in selected cities

4.5 Moisture loads within wall assemblies

The moisture load in each wall assembly type was calculated using a two-step approach in which the hourly WDR intensity and hourly averaged DRWP from the climate dataset were considered as variables. In addition, and for comparison to that given in ASHRAE 160 Standard, the moisture load of 1 % of the WDR load was also produced. Discussions focus on the changes in moisture load under different climatic scenarios, as well as the characteristics of the moisture load for each selected city.

4.5.1 Watertightness test and water entry equation

Water entry equations for each wall type were derived from the results of water entry as obtained from watertightness tests. The two types of wall assemblies analyzed in this study were tested in the Dynamic Wind and Wall Testing Facility (Figure 4.8) located at the National Research Council Canada. Both test specimens had the same dimensions of: 2.44m x 2.44m (8ft by 8ft). The construction of both wall assemblies complied with the minimum requirements of the National Building Code of Canada (NBCC) (NRCC, 2015) for wood frame wall assemblies.

Figure 4.8 Dynamic wind and wall testing facility

The vinyl wall assembly, as shown in Figure 4.9a, was comprised of a layer of vinyl cladding, an asphalt impregnated paper-based membrane (30-minute), a 10-mm (3/8in.) transparent polycarbonate sheathing panel acting as the OSB, 51mm x 152mm (2in. x 6in.) wood stud frames and another 10-mm (3/8in.) transparent polycarbonate sheathing acting as the interior sheathing and part of the air barrier system. In addition, three through-wall components were added to the wall assembly, these components being those typically found in light-weight wood-frame wall assemblies representative of North American construction practice. These components included: a 600mm x 600mm (30in. x

30in.) window; a 100-mm diameter (4in.) circular ventilation duct; and an exterior electrical outlet (2in. x 4in.) installed to the exterior surface of the wall assembly. When the vinyl wall assembly was constructed roughly 7 years ago, openings of 3mm diameter (~1/8in.) were bored through the cladding at the top center of the ventilation duct through the caulking seal, the bottom left of the caulking surrounding the electrical outlet, and at the bottom corner of the window frame to represent deficiencies in wall assemblies. Prior to this test, those holes bored at different locations of the wall assembly were plugged, whereas all water collection mechanisms in the wall assembly remained the same. The configuration of the brick wall assembly (Figure 4.9b) was similar to that of the vinyl wall assembly with the exception that a red matt clay brick veneer was used as cladding and the wall assembly also included a 25mm (1in.) drainage cavity. This brick veneer wall assembly was fabricated almost 20 years ago (Lacasse et al., 2003). No intentional deficiencies were applied to the wall. Water collection gutters (Figure 4.9c) were installed below the window, ventilation duct, and electrical outlet to collect and guide infiltrated water into reservoirs where the quantity of the water can be gauged.

(a)

(b)

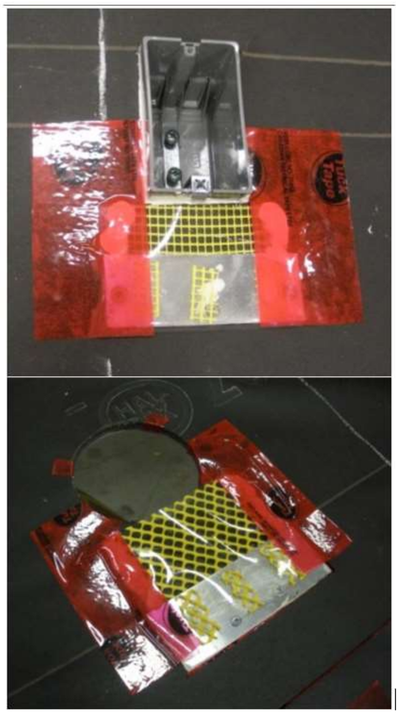

(c)

Figure 4.9 (a) Vinyl wall assembly; (b) Brick-veneer wall assembly; and (c) Water collection gutter attach to the asphalt impregnated membrane below each appliance. The yellow plastic mesh was to guide the infiltrated water into the steel gutter

During the watertightness test, 8 levels of dynamic pressure and 4 levels of water spray rate (Table 4-2), which considered the magnitude of the WDR and DRWPs during the future projected time periods, were applied to the test specimen. The value for WDRPI given on horizontal axis for plots of Figure 4.10 were calculated from these experimental inputs and corresponding adjustment coefficients. The magnitudes for the dynamic pressure and spray rates were based on the distributions for the WDR load and DRWPs from the analyzed climate dataset. A 0.1 Hz frequency was selected to fluctuate the dynamic pressure according to the wind velocity spectrum measured near the ground (<10m) (Teunissen, 1970).

Table 4-2 Watertightness test input

Steps	Dynamic Pressure Steps	Spray Rates
1	25 ± 25 * 0.2 sin (2πft*)	0.6 L; 1.3 L; 2.0 L; 2.7L/min-m^2
2	50 ± 50 * 0.2 sin (2πft)	0.6 L; 1.3 L; 2.0 L; 2.7L/min-m^2
3	75 ± 75 * 0.2 sin (2πft)	0.6 L; 1.3 L; 2.0 L; 2.7L/min-m^2
4	100 ± 100 * 0.2 sin (2πft)	0.6 L; 1.3 L; 2.0 L; 2.7L/min-m^2
5	150 ± 150 * 0.2 sin (2πft)	0.6 L; 1.3 L; 2.0 L; 2.7L/min-m^2
6	200 ± 200 * 0.2 sin (2πft)	0.6 L; 1.3 L; 2.0 L; 2.7L/min-m^2
7	250 ± 250 * 0.2 sin (2πft)	0.6 L; 1.3 L; 2.0 L; 2.7L/min-m^2
8	300 ± 300 * 0.2 sin (2πft)	0.6 L; 1.3 L; 2.0 L; 2.7L/min-m^2

*f: frequency (Hz); t: time (s)

4.5.2 Water entry equations

The water entry results and the fitting process are shown in Figure 4.10. For the vinyl wall assembly, the adjustment coefficients α and β for the WDRPI are 1.54 and 0.515 respectively and the adjustment coefficients a and b for the exponential function are 0.000109 and 0.554. In respect to the brick wall assembly, the adjustment coefficients α and β are 0.951 and 1.04 and the adjustment coefficients a and b for the exponential function are 0.000008 and 0.674. The water entry rate for the vinyl wall assembly was more sensitive to the WDR load than the DRWP whereas that for the brick veneer wall assembly was slightly more affected by the DRWP.

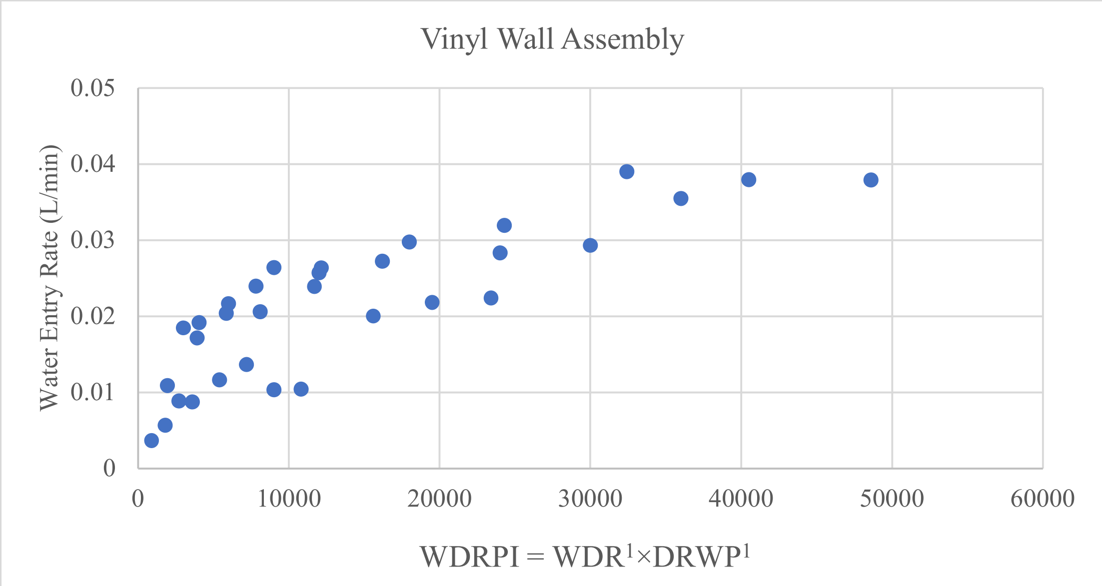

(a)

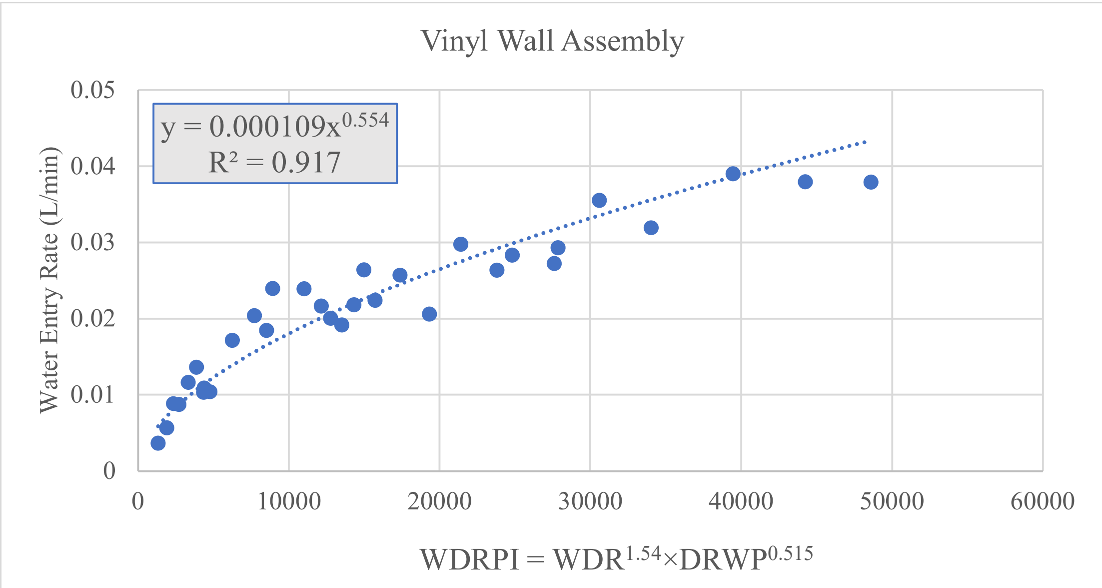

(b)

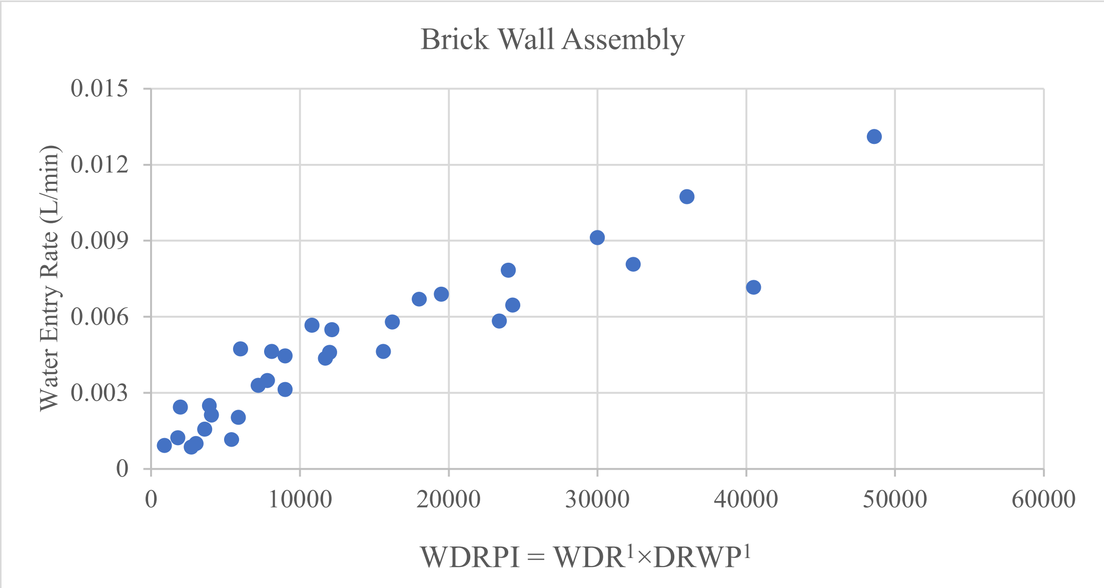

(c)

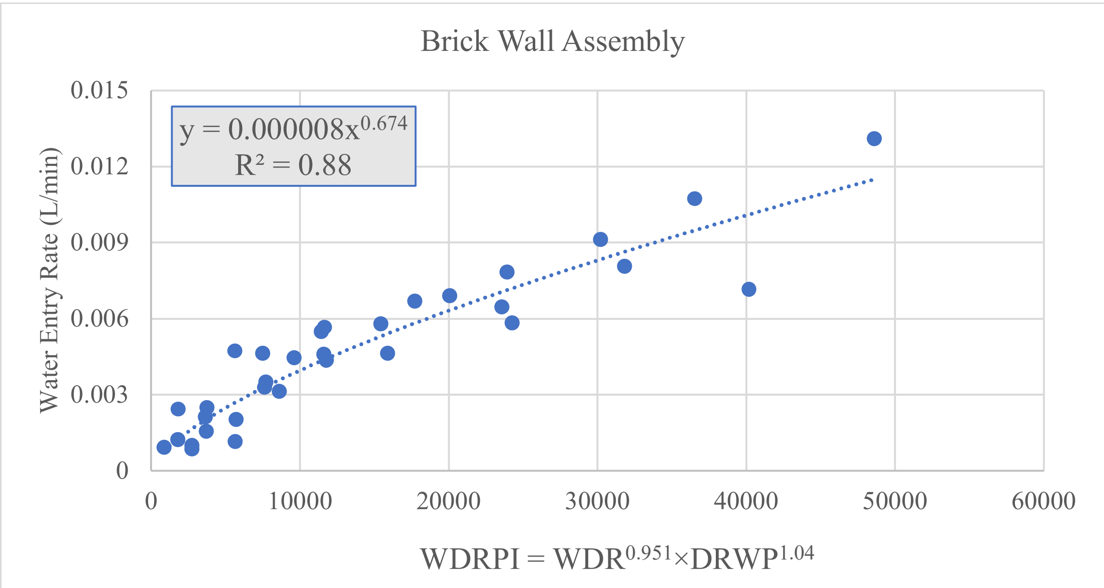

(d)

Figure 4.10(a) Water entry results of vinyl wall assembly plot with WDRPI prior to adjustment; (b) Water entry results of vinyl wall assembly plot with adjusted WDRPI and fit with the exponential function; (c) Water entry results of brick veneer wall assembly plot with WDRPI prior to adjustment; (d) Water entry results of brick veneer wall assembly plot with adjusted WDRPI and fit with the exponential function.

4.5.3 Moisture loads within vinyl and brick veneer clad wall assemblies

The moisture loads at different percentiles for the two tested wall assemblies calculated from equation (3) and equation (5) for the different cities are shown in Figure 4.11. The moisture loads for the same percentile category were plotted in the same color palette. Each percentile category for each city included 6 box plots, 3 of which, on the left, represent the moisture load calculated as 1 % of the WDR load; the other 3, on the right, were for the moisture load calculated using the water entry equations. In addition, each box plot was representative of the range of values generated from the 15 climate realizations. The values for the mean, 50-percentile, 90-percentile, 99-percentile, 99.5-percentile and 100-percentile of moisture load were generated for each city. The y-axis of the plots was in logarithmic scale. When calculating the moisture load, the prevailing wind directions, as shown in Figure 4.5, were considered as the wall orientation for both wall assembly types.

As to the moisture loads in the vinyl wall assembly (Figure 4.11), the water entry equation generated greater moisture loads in all cities for all percentile categories. For the mean category, i.e., the box plot in green colors in Figure 4.11, the moisture loads generated by the water entry equation were 65% to 99% more than that equivalent to 1 % of the WDR load. The trend in changes to the moisture loads derived from theses two approaches were consistent with each other. As an example, the moisture loads generated from the water entry equation and considered as 1 % of the WDR load tended to increase for the future projected climate scenarios as compared to the historical period. The trend in changes to the moisture load in the same city are similar to those changes for the WDRPI values as shown in Figure 4.4.

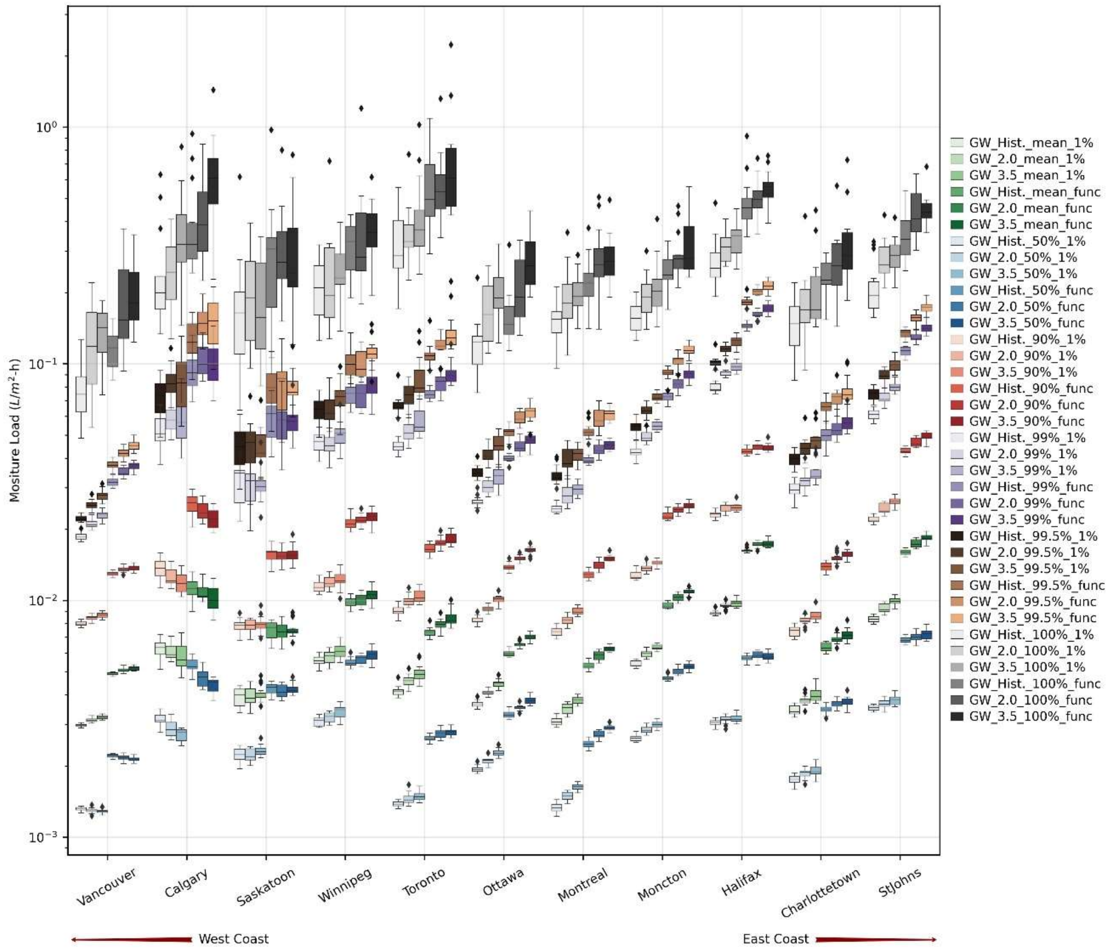

Figure 4.11 Moisture loads in the vinyl wall assembly in analyzed cities for different scenarios

The average changes of moisture load at different percentile categories for the vinyl wall assembly are shown in Figure 4.11 and are listed in Table A.1 in the appendix. The changes are given in percentages, representing the average difference of 15 realizations between each projected and historical climate scenario. In general, the changes in moisture load, generated either from the water entry equation or that considered as 1% of the WDR load, at higher percentile categories were greater than that at lower percentile categories. This implies that the extreme moisture loads would occur more frequently during future projected climate scenarios. In addition, the changes in moisture load for the 3.5°C future climate scenario is greater than those for the 2.0°C scenario, and for most cases, the changes in moisture load generated by the water entry equation would be less than that given by 1% WDR load.

In respect to the changes in mean moisture load for different regions of Canada between the historical and the two future projected climate scenarios, the greatest changes were observed in three (3) inland cities, specifically: Montreal, Ottawa and Toronto. The regions with fewer changes were found in cities located on the east coast of Canada, and include: Charlottetown, Halifax, Moncton and St. John's. Amongst these cities, St. John's had the greatest changes in mean moisture load whereas changes for Halifax were the smallest. For the west coast and central regions of Canada, the mean moisture load in Vancouver and Winnipeg increased slightly for the two future projected climate scenarios whereas that in Saskatoon essentially remained the same and in Calgary, was moderately reduced.

The moisture loads in the brick veneer wall assembly for different cities and different climate scenarios are given in Figure 4.12. The plot has the same scheme as that for the vinyl wall assembly (Figure 4.11). The averaged moisture loads of 15 realizations and their changes are listed in Table A.2 in appendix. The mean moisture loads generated from the water entry equation ranged between 46.3% and 82.2% of that given by the 1 % WDR load. However, their trends of changes, in general, were similar to each other. Compared to the vinyl wall assembly, the extent of increase in moisture load generated from the water entry equation between the historical and the two future projected climate scenarios in the brick veneer wall assembly was relatively minor whereas the decrease of that was greater. For most cases, the changes in moisture load in the brick veneer wall assembly were greater for the 3.5°C future climate scenario than the 2.0°C future scenario. It was also noted that, the changes of the mean moisture load generated by the water entry equation for the brick veneer wall assembly for inland and east coast cities were almost the same percentage level except that for Halifax. In the remaining cities, decreases of moisture loads were observed for the brick veneer wall assembly for the locations of Calgary and Saskatoon. Slight increases were found for the location of Vancouver and Winnipeg.

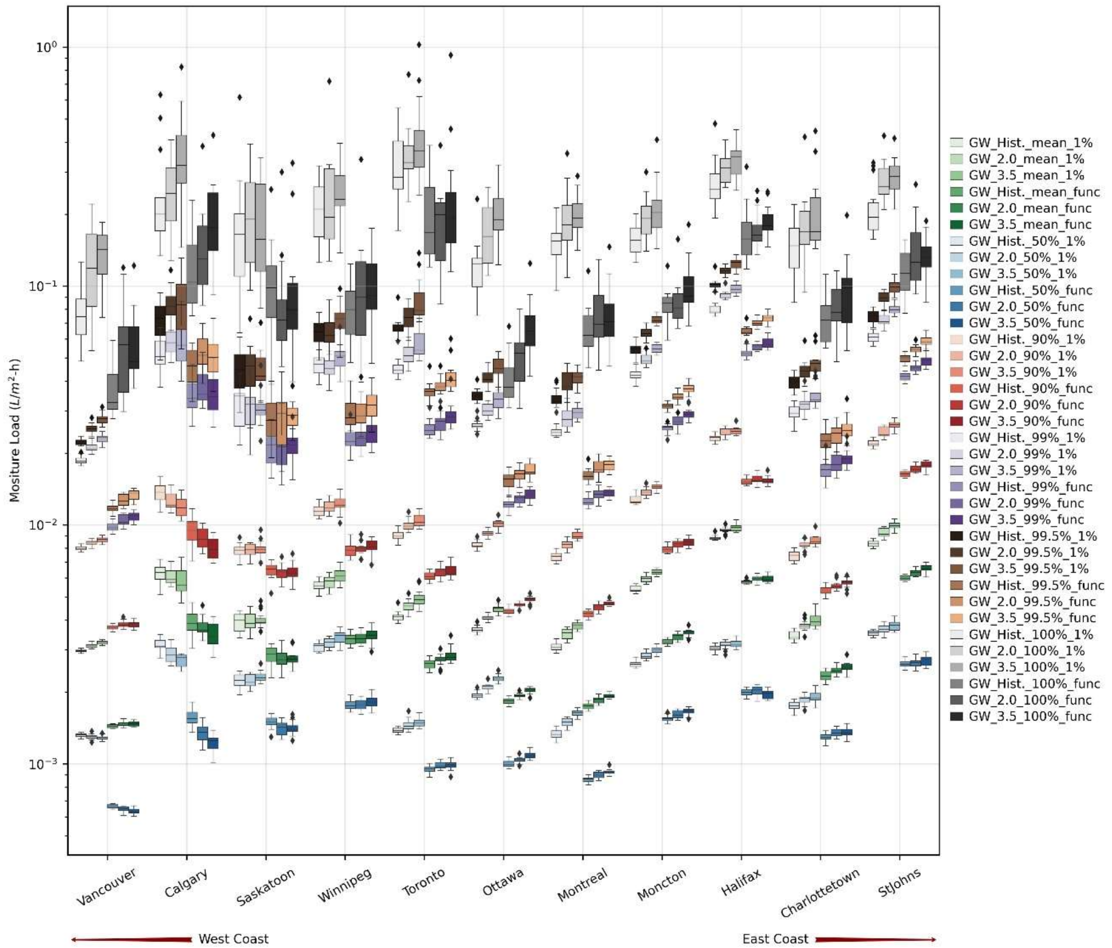

Figure 4.12 Moisture loads in the brick wall assembly in analyzed cities for different scenarios.

The average mean and 50-percentile water entry ratios for the 15 realizations, which are the ratios between the moisture load generated from the water entry equation and the over all WDR load, are listed in Table 4-3. It is evident that the ratios would vary for different configurations of wall assembly and different locations due to diverse WDR and DRWP conditions. For both types of wall assemblies, decreases in water entry ratios between the historical and future projected climate scenario was observed in all cities, and the water entry ratios for the 3.5°C future scenario were less than that for the 2.0°C future scenario. Increases in moisture loads were evidently found for the future projected climate scenarios whereas the water entry ratios slightly decreased for the same scenarios. The contrary changes in these two parameters were primarily because changes in WDR were greater than changes in moisture load. The magnitudes for the water entry ratios did not reveal any regional characteristics and only depended on the WDR conditions for the specific city locations. Thus, the water entry ratios for different cities might be significantly different and the moisture load given by the 1% of the WDR load should not be applied identically to all locations. The highest water entry ratios for the vinyl wall assembly were located in Charlottetown and St. John's, whereas the lowest water entry ratios were found in Vancouver. For the tested brick veneer wall assembly, the highest mean and 50-percentile water entry ratios were observed in Toronto and St. John's. Conversely, both the lowest mean and 50-percentile water entry ratios were evident for Vancouver.

Table 4-3 Ratio (%) between WDR load and moisture load in each wall assembly

City	Wall Typ.	Category	Hist.	*GW 2.0 C*	*GW 3.5 C°*
Calgary	Vinyl	*Mean*	1.72%	1.69%	1.67%
		50-Perc.	1.70%	1.67%	1.65%
	Brick	*Mean*	0.582%	0.561%	0.546%
		50-Perc.	0.499%	0.479%	0.463%
Charlot.	Vinyl	*Mean*	1.96%	1.95%	1.92%
		50-Perc.	1.97%	1.95%	1.93%
	Brick	*Mean*	0.797%	0.769%	0.779%
		50-Perc.	0.719%	0.685%	0.702%
Halifax	Vinyl	*Mean*	1.89%	1.86%	1.85%
		50-Perc.	1.89%	1.87%	1.84%
	Brick	*Mean*	0.726%	0.705%	0.694%
		50-Perc.	0.652%	0.629%	0.612%
Monc.	Vinyl	*Mean*	1.81%	1.79%	1.77%
		50-Perc.	1.81%	1.78%	1.76%
	Brick	*Mean*	0.669%	0.643%	0.628%
		50-Perc.	0.581%	0.561%	0.547%
Mont.	Vinyl	*Mean*	1.87%	1.83%	1.8%
		50-Perc.	1.86%	1.82%	1.78%
	Brick	*Mean*	0.714%	0.681%	0.656%
		50-Perc.	0.629%	0.592%	0.564%
Otto.	Vinyl	*Mean*	1.72%	1.69%	1.67%
		50-Perc.	1.71%	1.68%	1.65%
	Brick	*Mean*	0.577%	0.555%	0.540%
		50-Perc.	0.508%	0.484%	0.467%
Sask.	Vinyl	*Mean*	1.93%	1.89%	1.88%
		50-Perc.	1.91%	1.87%	1.84%
	Brick	*Mean*	0.772%	0.740%	0.728%
		50-Perc.	0.665%	0.633%	0.610%

St. J.	Vinyl	*Mean*	1.96%	1.94%	1.92%
		50-Perc.	1.99%	1.96%	1.94%
	Brick	*Mean*	0.811%	0.786%	0.773%
		50-Perc.	0.736%	0.708%	0.693%
Toro.	Vinyl	*Mean*	1.93%	1.92%	1.90%
		50-Perc.	1.92%	1.90%	1.87%
	Brick	*Mean*	0.825%	0.811%	0.795%
		50-Perc.	0.676%	0.659%	0.638%
Vanc.	Vinyl	*Mean*	1.70%	1.69%	1.68%
		50-Perc.	1.67%	1.66%	1.65%
	Brick	*Mean*	0.552%	0.545%	0.533%
		50-Perc.	0.477%	0.472%	0.464%
Winni.	Vinyl	*Mean*	1.81%	1.79%	1.77%
		50-Perc.	1.81%	1.78%	1.76%
	Brick	*Mean*	0.662%	0.640%	0.628%
		50-Perc.	0.584%	0.557%	0.542%

4.6 Conclusions

In this study, the changes in WDR related climatic conditions for selected Canadian cities and for future projected time periods of 2034-2064 and 2062-2092, respectively representative of a 2.0°C and 3.5°C increase in global temperature, have been investigated in terms of moisture loads to wall assemblies, directly associated with the atmospheric phenomena of wind and rain. Specifically, changes in hourly WDR load, hourly averaged DRWP, WDRPI and the prevailing wind direction during rain events were explored. Other than the changes of these parameters in different percentiles, IDF curves of the WDR load and WDRPI were also generated to demonstrate changes of climate parameters at different risk levels. To further demonstrate the effects of changes of those climatic parameters in respect to wall assemblies, a two-step approach was used to estimate the moisture load in wall assemblies based on two governing water entry equations. The parameters for these equations were obtained from watertightness tests for a vinyl and a brick wall assembly. Moisture loads for these two types of wall assembly in selected Canadian cities and for different climate scenarios were compared and discussed.

The number of rain hours in all cities analyzed increased for future projected periods except for Toronto where the number of rain hours remained essentially unchanged; the only increase in the number of rain spell gaps for the same climate scenarios considered was observed for Vancouver. The mean, 50-percentile, 90-percentile, 99-percentile, and

99.5-percentile, values for the WDR load, DRWP and WDRPI for the selected cities were plotted and results discussed. For the east coast cities of Charlottetown, Halifax, Moncton and St. John's, all percentiles of WDR load, DRWP and WDRPI increased noticeably for the future projected climate scenarios when compared to the historical scenario. For the inland cities of Montreal, Ottawa and Toronto, the WDR load increased whereas the DRWP remained essentially the same between different climate scenarios. Consequently, the WDRPI value also increased as it represents the con-current effect of WDR and DRWP. For cites located in the Prairies region of Canada, there was an evident decrease in WDR load, DRWP and WDRPI value for Calgary, whereas, these parameters for Saskatoon and Winnipeg did not change significantly. The 50-percentile WDR load, 50-percentile WDRPI, and all categories of DRWP for the city of Vancouver only slightly decreased. The prevailing wind directions during rain events were almost unchanged for the future projected climate scenarios. According to the IDF curves, based on averaged data from 15 climate realizations and for each different climate scenario, the magnitude of WDR and WDRPI at the same occurrence probability level increased for future projected climate scenarios in all cities. For all the comparison mentioned, the changes occurred for the 3.5 °C future climate scenario were usually greater than that for the 2.0°C scenario.

To permit more accurate assessment of the moisture load in wall assemblies, watertightness tests were conducted for a vinyl and a brick veneer wall assembly. The results of the test were used to establish water entry equations that permitted calculating the moisture load based on hourly WDR loads and hourly averaged DRWPs. Obvious changes to the moisture load were identified for wall assemblies located on the east coast and inland cities. A minor increase in the moisture load was evident for the centrally located cities of Saskatoon and Winnipeg and the west coast city of Vancouver. Slight decreases in the moisture load were observed for Calgary. The water entry ratio assessed on the basis of watertightness testing for the vinyl wall assembly ranged between 1.65% and 1.99% whereas this ratio ranged between 0.463% and 0.822% for the brick veneer wall assembly. These values are different from that of 1% WDR suggested in ASHRAE 160 standard.

The next phase of this study is to conduct hygrothermal simulations to explore the resilience of wall assemblies subjecting to future projected climate load using the different criterion. It is also intended that further investigation for other types and configurations of wall assemblies using the watertightness tests described in this paper will also be carried out.

4.6 References

Arora, V. K., Scinocca, J. F., Boer, G. J., Christian, J. R., Denman, K. L., Flato, G. M., Kharin, V. V., Lee, W. G., & Merryfield, W. J. (2011). Carbon emission limits required to satisfy future representative concentration pathways of greenhouse gases. *Geophysical Research Letters*. https://doi.org/10.1029/2010GL046270

Ashfaq, M., Bowling, L. C., Cherkauer, K., Pal, J. S., & Diffenbaugh, N. S. (2010). Influence of climate model biases and daily-scale temperature and precipitation events on hydrological impacts assessment: A case study of the United States. *Journal of Geophysical Research Atmospheres*. https://doi.org/10.1029/2009JD012965

ASHRAE. (2016). ASHRAE standard 160P-criteria for moisture control design analysis in buildings. In *ASHRAE Transactions*.

Berg, P., Feldmann, H., & Panitz, H. J. (2012). Bias correction of high resolution regional climate model data. *Journal of Hydrology*. https://doi.org/10.1016/j.jhydrol.2012.04.026

Bordoy, R., & Burlando, P. (2013). Bias correction of regional climate model simulations in a region of complex orography. *Journal of Applied Meteorology and Climatology*. https://doi.org/10.1175/JAMC-D-11-0149.1

Bossche, N. Van Den, Lacasse, M., Moore, T., & Janssens, A. (2012). Water infiltration through openings in a vertical plane under static boundary conditions. *Proceedings of the 5th IBPC*.

Bush, E., & Lemmen, D. S. (2019). *Canada's Changing Climate Report*. Government of Canada. http://www.changingclimate.ca/CCCR2019

Cannon, A. J. (2018). Multivariate quantile mapping bias correction: an N-dimensional probability density function transform for climate model simulations of multiple variables. *Climate Dynamics*. https://doi.org/10.1007/s00382-017-3580-6

Desjarlais, A. O., Karagiozis, A. N., & Aoki-Kramer, M. (2001). Wall moisture problems in Seattle. *Buildings VIII Proceedings, ASHRAE, 8p*, *July*.

Environment and Climate Change Canada. (2018). *Memorandum ofUnderstanding between National Research Council and Environment and Climate Change Canada on Climate Resilient Buildings and Core Public Infrastructure: Future Projections ofClimate Design Values. Tier 1 Climate Projections* (p. 48). Government of Canada.

Gaur, A., Lacasse, M. A., & Armstrong, M. (2019). Climate data to undertake hygrothermal and whole building simulations under projected climate change influences for 11 Canadian cities. *Data*, *4*(2). https://doi.org/10.3390/data4020072

Il Jeong, D., & Sushama, L. (2018). Rain-on-snow events over North America based on two Canadian regional climate models. *Climate Dynamics*, *50*(1–2), 303–316. https://doi.org/10.1007/s00382-017-3609-x

ISO 15927-3. (2009). *ISO 15927-3, Hygrothermal performance of buildings Calculation and presentation of climatic data Part 3: Calculation of a driving rain index for vertical surfaces from hourly wind and rain data*.

Jeong, D. Il, & Cannon, A. J. (2020). Projected changes to moisture loads for design and management of building exteriors over Canada. *Building and Environment*, *170*, 106609. https://doi.org/10.1016/j.buildenv.2019.106609

Jeong, D. Il, Cannon, A. J., & Zhang, X. (2018). Projected changes to extreme freezing precipitation and design ice loads over North America based on a large ensemble of Canadian regional climate model simulations. *Natural Hazards and Earth System Sciences Discussions*. https://doi.org/10.5194/nhess-2018-395

Jeong, D. Il, & Sushama, L. (2018). Projected changes to extreme wind and snow environmental loads for buildings and infrastructure across Canada. *Sustainable Cities and Society*. https://doi.org/10.1016/j.scs.2017.10.004

Jeong, D. Il, Sushama, L., Vieira, M. J. F., & Koenig, K. A. (2018). Projected changes to extreme ice loads for overhead transmission lines across Canada. *Sustainable Cities and Society*. https://doi.org/10.1016/j.scs.2018.03.017

Krinner, G., Germany, F., Shongwe, M., Africa, S., France, S. B., Uk, B. B. B. B., Germany, V. B., Uk, O. B., France, C. B., Uk, R. C., Canada, M. E., Erich, M., Uk, R. W. L., Uk, S. L., & Lucas, C. (2013). Long-term Climate Change: Projections, Commitments and Irreversibility Pages 1029 to 1076. In Intergovernmental Panel on Climate Change (Ed.), *Climate Change 2013 - The Physical Science Basis* (Vol. 9781107057, pp. 1029–1136). Cambridge University Press. https://doi.org/10.1017/CBO9781107415324.024

Lacasse, M. A., O'Connor, T., Nunes, S. C., & Beaulieu, P. (2003). Report from Task 6 of MEWS Project: Experimental Assessment of Water Penetration and Entry into Wood-Frame Wall Specimens - Final Report. In *Research Report (National Research Council of Canada. Institute for Research in Construction); no. RR-133*.

Lankester, P., & Brimblecombe, P. (2012). The impact of future climate on historic interiors. *Science of the Total Environment*. https://doi.org/10.1016/j.scitotenv.2011.12.026

Laprise, R., Caya, D., Bergeron, G., & Giguère, M. (1997). The Formulation of the André Robert MC2 (Mesoscale Compressible Community) Model. *Atmosphere-Ocean*, *35*(sup1), 195–220. https://doi.org/10.1080/07055900.1997.9687348

Leander, R., & Buishand, T. A. (2007). Resampling of regional climate model output for the simulation of extreme river flows. *Journal of Hydrology*. https://doi.org/10.1016/j.jhydrol.2006.08.006

Li, H., Sheffield, J., & Wood, E. F. (2010). Bias correction of monthly precipitation and temperature fields from Intergovernmental Panel on Climate Change AR4 models using equidistant quantile matching. *Journal of Geophysical Research Atmospheres*. https://doi.org/10.1029/2009JD012882

Mirle, K., Uk, M. R. A., Canada, N. G., Gutzler, D., Uk, J. G., Quintana, J. I., Republic, S. M., Uk, D. M., Germany, T. M., Uk, D. P., & France, A. R. (2013). Detection and attribution of climate change: From global to regional. In *Climate Change 2013 the Physical Science Basis: Working Group I Contribution to the Fifth Assessment Report of the Intergovernmental Panel on Climate Change* (Vol. 9781107057). https://doi.org/10.1017/CBO9781107415324.022

Moore, T. V., Lacasse, M. A., & Defo, M. (2019). Determining Moisture Source due to Wind Driven Rain for Input to Hygrothermal Simulations Using Experimental Methods. *ASHRAE*.

Murdock, T. Q., Sobie, S. R., Zwiers, F. W., & Eckstrand, H. D. (2013). Climate change and extremes in the Canadian Columbia basin. *Atmosphere - Ocean*. https://doi.org/10.1080/07055900.2013.816932

Nik, V. M. (2017). Application of typical and extreme weather data sets in the hygrothermal simulation of building components for future climate – A case study for a wooden frame wall. *Energy and Buildings*. https://doi.org/10.1016/j.enbuild.2017.08.042

Nik, V. M., Mundt-Petersen, S. O., Kalagasidis, A. S., & De Wilde, P. (2015). Future moisture loads for building façades in Sweden: Climate change and wind-driven rain. *Building and Environment*, *93*(P2), 362–375. https://doi.org/10.1016/j.buildenv.2015.07.012

NRCC. (2015). National Building Code of Canada. *Institute for Research in Construction*.

Orr, S. A., Young, M., Stelfox, D., Curran, J., & Viles, H. (2018). Wind-driven rain and future risk to built heritage in the United Kingdom: Novel metrics for characterising rain spells. *Science of The Total Environment*, *640–641*, 1098–1111. https://doi.org/10.1016/j.scitotenv.2018.05.354

Piani, C., Weedon, G. P., Best, M., Gomes, S. M., Viterbo, P., Hagemann, S., & Haerter, J. O. (2010). Statistical bias correction of global simulated daily precipitation and temperature for the application of hydrological models. *Journal of Hydrology*. https://doi.org/10.1016/j.jhydrol.2010.10.024

Picketts, I. M., Andrey, J., Matthews, L., Déry, S. J., & Tighe, S. (2016). Climate change adaptation strategies for transportation infrastructure in Prince George, Canada. *Regional Environmental Change*. https://doi.org/10.1007/s10113-015-0828-8

Rousseau, M. (1999). An Overview of the Survey of Building Envelope Failures in the Coastal Climate of British Columbia, Performed by Morrisson-Hershfield Limited for CMHC (1996). *Journal of Thermal Envelope and Building Science*, *22*(4), 364–367. https://doi.org/10.1177/109719639902200411

Sahal, N., & Lacasse, M. A. (2004). *Experimental Assessment of Water Penetration and Entry into Siding-Clad Wall Specimen*. NRC Publications Archive. https://doi.org/10.4224/20377802

Sahal, N., & Lacasse, M. A. (2005). Water entry function of a hardboard siding-clad wood stud wall. *Building and Environment*, *40*(11), 1479–1491. https://doi.org/10.1016/j.buildenv.2004.11.019

Salamanca, F., Georgescu, M., Mahalov, A., & Moustaoui, M. (2015). Summertime response of temperature and cooling energy demand to urban expansion in a semiarid environment. *Journal of Applied Meteorology and Climatology*. https://doi.org/10.1175/JAMC-D-14-0313.1

Salamanca, F., Georgescu, M., Mahalov, A., Moustaoui, M., & Martilli, A. (2016). Citywide Impacts of Cool Roof and Rooftop Solar Photovoltaic Deployment on Near-Surface Air Temperature and Cooling Energy Demand. *Boundary-Layer Meteorology*. https://doi.org/10.1007/s10546-016-0160-y

Sanderson, M., Arbuthnott, K., Kovats, S., Hajat, S., & Falloon, P. (2017). The use of climate information to estimate future mortality from high ambient temperature: A

systematic literature review. In *PLoS ONE*. https://doi.org/10.1371/journal.pone.0180369
Scinocca, J. F., Kharin, V. V., Jiao, Y., Qian, M. W., Lazare, M., Solheim, L., Flato, G. M., Biner, S., Desgagne, M., & Dugas, B. (2016). Coordinated global and regional climate modeling. *Journal of Climate*. https://doi.org/10.1175/JCLI-D-15-0161.1
Smegal, J., Lstiburek, J., Straube, J., & Grin, A. (2013). Moisture-related durability of walls with exterior insulation in the pacific northwest. *Thermal Performance of the Exterior Envelopes of Whole Buildings - 12th International Conference*.
Teunissen, H. W. (1970). *Characteristics of the Mean Wind and Turbulence in the Planetary Boundary Layer* (Issue 32). Institute for Aerospace Studies, University of Toronto.
Tewari, M., Salamanca, F., Martilli, A., Treinish, L., & Mahalov, A. (2017). Impacts of projected urban expansion and global warming on cooling energy demand over a semiarid region. *Atmospheric Science Letters*. https://doi.org/10.1002/asl.784
Xiao, Z., Lacasse, M. A., Defo, M., & Dragomirescu, E. (2021). Moisture Load to a Vinyl-Clad Wall Assembly for Selected Canadian Cities. *ASTM International*.
Xiao, Z., Lacasse, M. A., Dragomirescu, E., & Defo, M. (2021). An Analysis of Historical Wind-driven Rain Loads for selected Canadian Cities. *Journal of Wind Engineering and Industrial Aerodynamics*.

4.7 Appendix B

Table A1. Averaged moisture loads from 15 realizations and their changes between scenarios for the vinyl wall assembly

		Percentiles	Mean	50%	90%	99%	99.5%
Cities	Methods	Scenario					
Calgary	W.E.E.*	***Hist.***	**0.0113**	**0.00533**	**0.0257**	**0.0944**	**0.127**
		GW 2.0 C°	0.0109 ↓ 3.27%	0.00472 ↓ 11.3%	0.0239 ↓6.68%	0.104 ↑10.7%	0.152 ↑19.3%
		GW 3.5 C°	0.0104 ↓ 7.84%	0.00438 ↓ 17.8%	0.0223 ↓ 13.3%	0.102 ↑7.57%	0.151 ↑18.2%
	1%	***Hist.***	**0.00626**	**0.00314**	**0.0137**	**0.0527**	**0.072**
		GW 2.0 C°	0.00610 ↓ 2.58%	0.00288 ↓ 8.48%	0.01262 ↓ 7.52%	0.05944 ↑12.8%	0.08457 ↑17.4%
		GW 3.5 C°	0.00592 ↓ 5.5%	0.00271 ↓ 13.9%	0.0119 ↓ 12.7%	0.0587 ↑11.4%	0.0857 ↑19%
Charlot.	W.E.E.	***Hist.***	**0.00637**	**0.00346**	**0.01386**	**0.0498**	**0.0658**
		GW 2.0 C°	0.00687 ↑ 7.97%	0.00366 ↑ 5.59%	0.0152 ↑ 9.48%	0.0531 ↑ 6.79%	0.072 ↑ 9.43%
		GW 3.5 C°	0.00719 ↑ 12.9%	0.00373 ↑ 7.75%	0.0158 ↑ 13.8%	0.0573 ↑ 15.1%	0.0777 ↑ 18.1%
	1%	***Hist.***	**0.00345**	**0.00174**	**0.00742**	**0.0295**	**0.0395**
		GW 2.0 C°	0.00379 ↑ 9.88%	0.00186 ↑ 6.17%	0.00823 ↑ 10.9%	0.0322 ↑ 9.06%	0.0444 ↑ 12.3%
		GW 3.5 C°	0.00401 ↑ 16.3%	0.00191 ↑ 9.3%	0.00865 ↑ 16.5%	0.0352 ↑ 19.4%	0.0489 ↑ 23.7%

Halifax	W.E.E.	***Hist.***	**0.0163**	**0.00571**	**0.0427**	**0.146**	**0.183**
		GW 2.0 C°	0.0172 ↑ 5.7%	0.00586 ↑ 2.64%	0.0446 ↑ 4.46%	0.162 ↑10.6%	0.202 ↑ 10.9%
		GW 3.5 C°	0.0174 ↑ 6.84%	0.00579 ↑ 1.54%	0.0443 ↑ 4%	0.171 ↑ 16.8%	0.215 ↑ 17.7%
	1%	***Hist.***	**0.00884**	**0.00305**	**0.0231**	**0.0802**	**0.102**
		GW 2.0 C°	0.00954 ↑ 7.87%	0.00315 ↑ 3.17%	0.0247 ↑ 6.87%	0.0919 ↑ 14.6%	0.116 ↑ 13.7%
		GW 3.5 C°	0.00973 ↑ 10.12%	0.00317 ↑ 3.85%	0.0248 ↑ 7.31%	0.0977 ↑ 21.8%	0.124 ↑ 22.1%
Monc.	W.E.E.	***Hist.***	**0.00953**	**0.00472**	**0.02278**	**0.07227**	**0.09111**
		GW 2.0 C°	0.0103 ↑ 8.08%	0.00503 ↑ 6.6%	0.0242 ↑ 6.02%	0.082 ↑ 13.4%	0.103 ↑ 12.7%
		GW 3.5 C°	0.0109 ↑ 14.1%	0.00525 ↑ 11.1%	0.02514 ↑ 10.4%	0.0901 ↑ 24.8%	0.115 ↑ 26%
	1%	***Hist.***	**0.00540**	**0.00262**	**0.0128**	**0.0426**	**0.0543**
		GW 2.0 C°	0.00595 ↑ 10.1%	0.00283 ↑ 8.05%	0.0137 ↑ 7.37%	0.0492 ↑ 15.6%	0.0632 ↑ 16.5%
		GW 3.5 C°	0.00634 ↑ 17.5%	0.00299 ↑ 14.1%	0.0145 ↑ 13%	0.0547 ↑ 28.6%	0.0723 ↑33.4%
Mont.	W.E.E.	***Hist.***	**0.00532**	**0.00248**	**0.0129**	**0.0393**	**0.0523**
		GW 2.0 C°	0.00584 ↑ 9.83%	0.00271 ↑ 9.36%	0.0141 ↑ 9.7%	0.0435 ↑ 10.5%	0.0588 ↑ 12.3%
		GW 3.5 C°	0.00624 ↑ 17.4%	0.00289 ↑ 16.7%	0.0151 ↑ 17.8%	0.0454 ↑ 15.4%	0.0611 ↑ 16.8%
	1%	***Hist.***	**0.00310**	**0.00133**	**0.00736**	**0.0247**	**0.0342**
		GW 2.0 C°	0.00348 ↑ 12.5%	0.00150 ↑ 12.7%	0.00826 ↑ 12.2%	0.028 ↑ 13.2%	0.0392 ↑ 14.7%
		GW 3.5 C°	0.0038 ↑ 22.7%	0.00163 ↑ 23%	0.00902 ↑ 22.5%	0.0294 ↑ 18.9%	0.0415 ↑ 21.5%
Ott.	W.E.E.	***Hist.***	**0.00598**	**0.0033**	**0.0139**	**0.0401**	**0.0517**
		GW 2.0 C°	0.00654 ↑ 9.32%	0.00353 ↑ 6.76%	0.0152 ↑ 9.18%	0.0446 ↑11.4%	0.0591 ↑ 14.4%
		GW 3.5 C°	0.00654 ↑ 17.4%	0.00353 ↑ 14.7%	0.0152 ↑ 17.5%	0.0446 ↑ 18.4%	0.0591 ↑ 20.7%
	1%	***Hist.***	**0.00366**	**0.00194**	**0.00828**	**0.0262**	**0.0351**
		GW 2.0 C°	0.0041 ↑ 12.05%	0.0021 ↑ 8.4%	0.00923 ↑ 11.6%	0.0302 ↑ 15.5%	0.0416 ↑ 18.4%
		GW 3.5 C°	0.00447 ↑ 22.1%	0.00228 ↑ 17.7%	0.0101 ↑ 21.8%	0.0331 ↑ 26.6%	0.0456 ↑ 30%
Sask.	W.E.E.	***Hist.***	**0.00755**	**0.00424**	**0.0157**	**0.0579**	**0.0796**
		GW 2.0 C°	0.00743 ↓ 1.55%	0.00414 ↓ 2.19%	0.0155 ↓ 1.41%	0.0567 ↓ 2.11%	0.081 ↑ 1.75%

		GW 3.5 C°	0.00756 ↑ 0.194%	0.00423 ↓ 0.14%	0.0157 ↑0.357%	0.0575 ↓0.693%	0.07982 ↑ 2.44%
	1%	***Hist.***	**0.00394**	**0.00224**	**0.00779**	**0.0318**	**0.0453**
		GW 2.0 C°	0.00394 ↑ 0.173%	0.00223 ↓0.504%	0.00782 ↑0.306%	0.0311 ↓2.05%	0.0459 ↑1.32%
		GW 3.5 C°	0.00403 ↑ 2.34%	0.00232 ↑ 3.69%	0.00795 ↑ 1.94%	0.0311 ↓2.1%	0.04510 ↓0.338%
St. J.	W.E.E.	***Hist.***	**0.016**	**0.00681**	**0.043**	**0.113**	**0.134**
		GW 2.0 C°	0.0174 ↑ 8.68%	0.00699 ↑ 2.72%	0.0465 ↑ 8.43%	0.129 ↑ 15%	0.157 ↑ 16.5%
		GW 3.5 C°	0.0184 ↑ 14.9%	0.00722 ↑ 6.15%	0.0492 ↑ 14.6%	0.142 ↑ 25.9%	0.173 ↑ 28.9%
	1%	***Hist.***	**0.00833**	**0.00352**	**0.02195**	**0.06091**	**0.07466**
		GW 2.0 C°	0.00928 ↑ 11.4%	0.00366 ↑ 4.01%	0.0244 ↑11.2%	0.0721 ↑ 18.3%	0.0896 ↑ 20%
		GW 3.5 C°	0.00994 ↑ 19.3%	0.0038 ↑ 7.96%	0.0262 ↑ 19.5%	0.08 ↑ 31.4%	0.0991 ↑ 32.7%
Toro.	W.E.E.	***Hist.***	**0.00735**	**0.00261**	**0.0166**	**0.0755**	**0.11**
		GW 2.0 C°	0.00791 ↑ 7.69%	0.00274 ↑ 4.81%	0.0176 ↑ 6.13%	0.0828 ↑ 9.66%	0.119 ↑ 7.69%
		GW 3.5 C°	0.00845 ↑ 15%	0.00278 ↑ 6.55%	0.0183 ↑ 10.6%	0.0917 ↑ 21.4%	0.139 ↑ 26.1%
	1%	***Hist.***	**0.00413**	**0.00138**	**0.00905**	**0.0455**	**0.0672**
		GW 2.0 C°	0.00457 ↑ 10.6%	0.00145 ↑ 5.36%	0.00998 ↑ 10.3%	0.0518 ↑ 13.9%	0.0738 ↑ 9.94%
		GW 3.5 C°	0.00495 ↑ 19.8%	0.00149 ↑ 7.99%	0.0105 ↑ 16.2%	0.057 ↑ 25.4%	0.0886 ↑ 31.9%
Vanc.	W.E.E.	***Hist.***	**0.00489**	**0.00221**	**0.013**	**0.0316**	**0.0375**
		GW 2.0 C°	0.00509 ↑ 3.96%	0.00217 ↓1.83%	0.0136 ↑ 4.75%	0.0349 ↑ 10.3%	0.042 ↑ 12%
		GW 3.5 C°	0.00518 ↑ 5.88%	0.00214 ↓3.12%	0.0138 ↑ 6.13%	0.0371 ↑ 17.2%	0.0453 ↑ 20.9%
	1%	***Hist.***	**0.00297**	**0.00132**	**0.00799**	**0.0187**	**0.022**
		GW 2.0 C°	0.00312 ↑ 5.09%	0.0013 ↓1.67%	0.00844 ↑ 5.64%	0.0211 ↑ 13%	0.0254 ↑ 15%
		GW 3.5 C°	0.00322 ↑ 8.3%	0.00129 ↓2.44%	0.00866 ↑ 8.4%	0.023 ↑ 23.1%	0.028 ↑ 27%
Winni.	W.E.E.	***Hist.***	**0.00984**	**0.00548**	**0.0213**	**0.0743**	**0.1002**
		GW 2.0 C°	0.0101 ↑ 2.83%	0.00565 ↑ 2.97%	0.022 ↑ 3.36%	0.0739 ↓0.551%	0.1005 ↓0.296%
		GW 3.5 C°	0.0105 ↑ 7.165%	0.0059 ↑ 7.58%	0.0225 ↑ 5.72%	0.0808 ↑ 8.78%	0.113 ↑ 11.1%

	1%	*Hist.*	0.0056	0.00308	0.0115	0.0467	0.0642
		GW 2.0 C°	0.0058 ↑ 3.55%	0.00321 ↑ 4.12%	0.012 ↑ 3.93%	0.046 ↓1.43%	0.0641 ↓0.192%
		GW 3.5 C°	0.00612 ↑ 9.25%	0.00339 ↑ 9.98%	0.0122 ↑ 6.46%	0.0504 ↑ 8.07%	0.0732 ↑ 13.9%
* W.E.E: Water Entry Equation							

Table A2. Averaged moisture loads from 15 realizations and their changes between scenarios for the brick wall assembly

		Percentiles:	Mean	50%	90%	99%	99.5%
Cities	Methods	Scenario					
Calgary	W.E.E.	***Hist.***	**0.00391**	**0.00157**	**0.00955**	**0.0352**	**0.0458**
		GW 2.0 C°	0.00375 ↓ 4.14%	0.00135 ↓ 13.6%	0.00881 ↓ 7.66%	0.0382 ↑ 8.58%	0.0538 ↑ 17.49%
		GW 3.5 C°	0.00348 ↓ 11.1%	0.00122 ↓ 21.9%	0.00798 ↓ 16.4%	0.036 ↑ 2.21%	0.0518 ↑ 13.1%
	1%	***Hist.***	**0.00626**	**0.00314**	**0.0136**	**0.0527**	**0.072**
		GW 2.0 C°	0.00610 ↓ 2.58%	0.00288 ↓ 8.48%	0.0126 ↓ 7.52%	0.0594 ↑ 12.8%	0.0846 ↑ 17.4%
		GW 3.5 C°	0.00592 ↓ 5.5%	0.00271 ↓ 13.9%	0.0119 ↓ 12.7%	0.0586 ↑ 11.4%	0.0857 ↑ 19%
Charlot.	W.E.E.	***Hist.***	**0.00234**	**0.00129**	**0.00528**	**0.0171**	**0.0225**
		GW 2.0 C°	0.00247 ↑ 5.43%	0.00135 ↑ 4.53%	0.00557 ↑ 5.41%	0.0181 ↑ 5.64%	0.0239 ↑ 6.45%
		GW 3.5 C°	0.00254 ↑ 8.51%	0.00135 ↑ 4.59%	0.00573 ↑ 8.43%	0.0191 ↑ 11.8%	0.0256 ↑ 13.9%
	1%	***Hist.***	**0.00345**	**0.00174**	**0.00742**	**0.0295**	**0.0395**
		GW 2.0 C°	0.00379 ↑ 9.88%	0.00186 ↑ 6.37%	0.00823 ↑ 10.9%	0.0322 ↑ 9.06%	0.0444 ↑ 12.3%
		GW 3.5 C°	0.00401 ↑ 16.2%	0.00191 ↑ 9.26%	0.00865 ↑ 16.5%	0.0353 ↑ 19.3%	0.0489 ↑ 23.7%
Halifax	W.E.E.	***Hist.***	**0.00579**	**0.002**	**0.0152**	**0.0526**	**0.065**
		GW 2.0 C°	0.00596 ↑ 3.07%	0.00202 ↑ 1.22%	0.0155 ↑ 2.12%	0.0556 ↑ 5.67%	0.0702 ↑ 8.09%
		GW 3.5 C°	0.00596 ↑ 3.04%	0.00196 ↓ 1.9%	0.0153 ↑0.514%	0.0577 ↑ 9.71%	0.0734 ↑ 12.9%
	1%	***Hist.***	**0.00884**	**0.00305**	**0.0231**	**0.0802**	**0.102**
		GW 2.0 C°	0.00954 ↑ 7.78%	0.00315 ↑ 3.17%	0.0247 ↑ 6.87%	0.0919 ↑ 14.6%	0.116 ↑ 13.7%
		GW 3.5 C°	0.00973 ↑ 10.1%	0.00317 ↑ 3.85%	0.0248 ↑ 7.31%	0.0977 ↑ 21.8%	0.124 ↑ 22.1%
Monc.	W.E.E.	***Hist.***	**0.00324**	**0.00154**	**0.00791**	**0.0253**	**0.0312**

		GW 2.0 C°	0.0054 ↑ 5.31%	0.00262 ↑ 4.33%	0.0128 ↑ 4.75%	0.0426 ↑ 7.71%	0.0543 ↑ 9.79%
		GW 3.5 C°	0.00354 ↑ 9.42%	0.00165 ↑ 7.12%	0.00849 ↑ 7.35%	0.0292 ↑ 15.7%	0.0375 ↑ 20.1%
	1%	***Hist.***	**0.0054**	**0.00262**	**0.0128**	**0.0426**	**0.0543**
		GW 2.0 C°	0.00595 ↑ 10.1%	0.00283 ↑ 8.05%	0.0137 ↑ 7.37%	0.0492 ↑ 15.6%	0.0632 ↑ 16.5%
		GW 3.5 C°	0.00634 ↑ 17.5%	0.00299 ↑ 14.1%	0.0145 ↑ 13%	0.0547 ↑ 28.6%	0.0723 ↑ 33.4%
Mont.	W.E.E.	***Hist.***	**0.00174**	**0.000858**	**0.00424**	**0.0125**	**0.0161**
		GW 2.0 C°	0.00185 ↑ 6.13%	0.000897 ↑ 4.55%	0.00452 ↑ 6.59%	0.0134 ↑ 6.83%	0.0174 ↑ 7.87%
		GW 3.5 C°	0.00192 ↑ 10.3%	0.000927 ↑ 7.93%	0.00471 ↑ 10.9%	0.0137 ↑ 9.03%	0.0178 ↑ 10.2%
	1%	***Hist.***	**0.0031**	**0.00133**	**0.00736**	**0.0247**	**0.0342**
		GW 2.0 C°	0.00348 ↑ 12.5%	0.0015 ↑ 12.7%	0.00826 ↑ 12.2%	0.028 ↑ 13.1%	0.0392 ↑ 14.7%
		GW 3.5 C°	0.0038 ↑ 22.7%	0.00163 ↑ 23%	0.00902 ↑ 22.5%	0.0294 ↑ 19%	0.0415 ↑ 21.5%
Otto.	W.E.E.	***Hist.***	**0.00183**	**0.001**	**0.00435**	**0.0121**	**0.0154**
		GW 2.0 C°	0.00193 ↑ 5.67%	0.00104 ↑ 3.93%	0.00463 ↑ 6.53%	0.0129 ↑ 5.89%	0.0163 ↑ 6.04%
		GW 3.5 C°	0.00203 ↑ 11.3%	0.00109 ↑ 8.76%	0.00488 ↑ 12.2%	0.0134 ↑ 10.6%	0.0171 ↑ 11%
	1%	***Hist.***	**0.00366**	**0.00194**	**0.00828**	**0.0262**	**0.0351**
		GW 2.0 C°	0.0041 ↑ 12%	0.0021 ↑ 8.4%	0.00923 ↑ 11.6%	0.0302 ↑ 15.4%	0.0416 ↑ 18.4%
		GW 3.5 C°	0.00447 ↑ 22.1%	0.00228 ↑ 17.7%	0.0101 ↑ 21.8%	0.0331 ↑ 26.6%	0.0456 ↑ 30%
Sask.	W.E.E.	***Hist.***	**0.00287**	**0.00149**	**0.00648**	**0.0211**	**0.0285**
		GW 2.0 C°	0.00276 ↓ 3.74%	0.00142 ↓ 5.23%	0.00632 ↓ 2.46%	0.0211 ↑0.0367%	0.0283 ↓ 0.865%
		GW 3.5 C°	0.0028 ↓ 2.38%	0.00142 ↓ 5.12%	0.00635 ↓ 1.97%	0.0218 ↑ 3.27%	0.0286 ↑ 0.256%
	1%	***Hist.***	**0.00394**	**0.00224**	**0.00779**	**0.0318**	**0.0453**
		GW 2.0 C°	0.00394 ↑ 0.173%	0.00223 ↓0.504%	0.00782 ↑0.306%	0.0311 ↓ 2.05%	0.0459 ↑ 1.32%
		GW 3.5 C°	0.00403 ↑ 2.34%	0.00232 ↑ 3.69%	0.00795 ↑ 1.94%	0.0311 ↓ 2.1%	0.0451 ↓ 0.338%
St. J.	W.E.E.	***Hist.***	**0.00602**	**0.00261**	**0.0163**	**0.0417**	**0.0498**
		GW 2.0 C°	0.00632 ↑ 4.99%	0.00264 ↑ 1.02%	0.0172 ↑ 5.23%	0.0454 ↑ 8.92%	0.0544 ↑ 9.39%
		GW 3.5 C°	0.00657 ↑ 9.17%	0.00271 ↑ 3.7%	0.0178 ↑ 8.81%	0.0487 ↑ 16.8%	0.0587 ↑ 18%
	1%	***Hist.***	**0.00833**	**0.00352**	**0.022**	**0.0609**	**0.0747**

		GW 2.0 C°	0.00928 ↑ 11.4%	0.00366 ↑ 4.01%	0.0244 ↑11.2%	0.0721 ↑ 18.3%	0.0896 ↑ 20%
		GW 3.5 C°	0.00994 ↑ 19.3%	0.0038 ↑ 7.96%	0.0262 ↑ 19.5%	0.08 ↑ 31.4%	0.0991 ↑ 32.7%
Toro.	W.E.E.	***Hist.***	**0.00262**	**0.000948**	**0.00611**	**0.0254**	**0.0364**
		GW 2.0 C°	0.00273 ↑ 4.1%	0.000983 ↑ 3.7%	0.00635 ↑ 382%	0.0269 ↑ 5.75%	0.0381 ↑ 4.58%
		GW 3.5 C°	0.00286 ↑ 8.96%	0.00099 ↑ 4.49%	0.00647 ↑ 5.88%	0.0289 ↑ 13.9%	0.0423 ↑ 16.2%
	1%	***Hist.***	**0.00413**	**0.00138**	**0.00905**	**0.0455**	**0.0672**
		GW 2.0 C°	0.00457 ↑ 10.6%	0.00145 ↑ 5.36%	0.00998 ↑ 10.3%	0.0518 ↑ 13.9%	0.0738 ↑ 9.94%
		GW 3.5 C°	0.00495 ↑ 19.8%	0.00149 ↑ 7.99%	0.0105 ↑ 16.2%	0.057 ↑ 25.4%	0.0886 ↑ 31.9%
Vanc.	W.E.E.	***Hist.***	**0.00144**	**0.000665**	**0.00373**	**0.00979**	**0.0118**
		GW 2.0 C°	0.00147 ↑ 2.32%	0.000648 ↓2.55%	0.00384 ↑ 2.86%	0.0105 ↑ 7.14%	0.0127 ↑ 8.04%
		GW 3.5 C°	0.00147 ↑ 2.48%	0.000633 ↓4.68%	0.00383 ↑ 2.7%	0.0108 ↑ 10.6%	0.0133 ↑ 13.4%
	1%	***Hist.***	**0.00297**	**0.00132**	**0.00799**	**0.0187**	**0.022**
		GW 2.0 C°	0.00312 ↑ 5.09%	0.0013 ↓1.67%	0.00844 ↑ 5.64%	0.0211 ↑ 13%	0.0254 ↑ 15%
		GW 3.5 C°	0.00322 ↑ 8.3%	0.00129 ↓2.44%	0.00866 ↑ 8.4%	0.023 ↑ 23.1%	0.028 ↑ 27%
Winni.	W.E.E.	***Hist.***	**0.00331**	**0.00177**	**0.00784**	**0.0229**	**0.0296**
		GW 2.0 C°	0.00336 ↑ 1.52%	0.00177 ↓0.246%	0.00794 ↑ 1.26%	0.0229 ↓0.0968%	0.0298 ↑ 0.669%
		GW 3.5 C°	0.00346 ↑ 4.3%	0.00182 ↑ 3%	0.00808 ↑ 3.07%	0.0243 ↑ 5.91%	0.0321 ↑ 8.44%
	1%	***Hist.***	**0.0056**	**0.00308**	**0.0115**	**0.0467**	**0.0642**
		GW 2.0 C°	0.0058 ↑ 3.55%	0.00321 ↑ 4.12%	0.012 ↑ 3.93%	0.046 ↓1.43%	0.0641 ↓0.192%
		GW 3.5 C°	0.00612 ↑ 9.25%	0.00339 ↑ 9.98%	0.0122 ↑ 6.46%	0.0504 ↑ 8.07%	0.0732 ↑ 13.9%

Chapter 5 Hygrothermal simulation and the assessment of performance of wall assemblies

5.1 Assessing the Resilience of Wall Assemblies to Moisture Load Arising from the Wind-Driven Rain (Part II)

Zhe Xiao, Michael A. Lacasse, Elena Dragomirescu and Maurice Defo

5.1.1 Abstract

Interpretation of data generated by climate models for future time periods showed that the climate change will substantially affect the moisture load levels in wall assemblies. The moisture load is the main cause of many detrimental effects in wall assemblies which lead to a deterioration of their performance. Thus, it is essential to explore how, and to what extend the wall assemblies may respond to such a variation in moisture load. The first part of the study focused on the projected climate data, as well as the moisture load obtained from the watertightness tests for the vinyl-clad and brick veneer-clad wall assemblies. Climatic conditions corresponding to 11 Canadian cities were implemented in the hygrothermal simulations, to permit evaluating the hygrothermal parameters for different materials in wall assemblies and subsequently for assessing their long-term performance. The mould index on the surface of the Oriented-Strand-Boards (OSB) in each wall assembly was selected as the performance criteria and was sorted into events with different mould index levels and durations. Changes in frequencies of these events for different time periods were compared and discussed. In general, a decrease in the wall assemblies performance will be registered during future projected time periods for all cities analyzed. The extent of responses of wall assemblies to the changing climate varied with geographical positions and types of cladding materials.

5.1.2 Introduction

The first part of this study (Xiao et al., 2021) focused on the moisture load to which vinyl-clad and brick masonry veneer-clad wood frame wall assemblies were subjected arising from the Wind-Driven Rain (WDR) and changes in these loads under different future projected climate scenarios, for which the temperature is predicted to increase comparing to the present temperatures, due to a changing climate. It was evident that the moisture load for the two wall assemblies tested and for majority of cities across Canada as were investigated in that study, would increase for all future projected climate scenarios. The increase in moisture load may aggravate any detrimental moisture induced effects on the wall assembly components, such as decay of materials, mould growth, frost damage, salt migration, erosion and efflorescence (Abuku et al., 2009; Charola & Lazzarini, 1986; Chouinard & Lawton, 2001; Franke et al., 1998; Tang et al., 2004; Van Balen, 1996) or could increase their frequency of occurrence. To permit quantifying these undesired effects, it is necessary to have knowledge of in-service environmental conditions to which components are subjected and that may cause the onset of degradation, as for example, relative humidity, temperature, moisture content. Thus, HAM (heat, air, moisture modelling) models are typically used to undertake hygrothermal simulations given that such tools are capable of simulating the transportation of heat, air and moisture across and within wall assemblies. By using hygrothermal simulations, one can infer the in-service environmental conditions to which components are subjected over the simulation periods.

The development of different HAM models has been thoroughly reviewed in a number of previous studies. 37 different models as developed by different researchers were compiled by Hens (Hens, 1996). Straube and Burnett (Straube & Burnett, 2001) conducted a detailed review regarding the features of different HAM models (Burch et al., 1989; Cunningham, 1990b, 1990a; Karagiozis & Solonvaara, 1994; Kerestecioglu et al., 1989; Kohonen, 1984; Ojanen & Kohonen, 1989; Pedersen, 1989, 1992). More recently, Delgado et al. (Delgado et al., 2010, 2013) identified 57 hygrothermal models and this number may have increased to this day. The most commonly used commercial HAM models are WUFI, DELPHIN and COMSOL Multiphysics which are widely utilized by practitioners all over the world (Defo et al., 2021). Numerical methods, such as Finite Difference Methods (FDM), Finite Control Volume (FCV) Methods and, Finite Element Method (FEM), are usually integrated into the HAM model to discretize both space and time (Delgado et al., 2013).

Based on the output of the HAM simulations, durability criteria for different materials can also be derived. According to CSA S478:19 Standard (National Standard of

Canada, 2019), moisture related failures for wood materials, include: fungal decay, mould growth and drying induced shrinkage perpendicular to the wood grain. Fungal decay causes loss of material, strength and appearance of the wood component. Mould growth can potentially affect to health of humans exposed to some type of mould spores and may also damage appearance of the surface on which the mould may grow. Drying-induced shrinkage could result in floor misalignment and nail popping. In addition, an evaluation process, based on the work of Ojanen et al. (Ojanen et al., 2010), is provided in the ASHRAE 160 standard (ASHRAE, 2016) to assess the severity of mould growth in wall assembly components using a mould growth index which are calculated knowing the time history of relative humidity and temperature of the component.

HAM simulations have been widely used to facilitate evaluating the moisture performance of the building envelope and assessing the effect of environmental loads on envelope components and materials. Vandemeulebroucke et al. (2021) investigated the possibilities of using a ‘reduced’ climate ensemble to represent a relatively larger climate ensemble generated by a climate model. The comparable performance between a brick-clad wood-stud wall assembly and that of an historical solid masonry wall subjected to different climate ensembles were assessed using HAM modeling. Wang and Ge (2017) implemented two air leakage modeling methods in the HAM simulations to explore the impact of air leakage on the moisture performance of wood frame wall assemblies; the advantages and disadvantages of the use of either the two methods were discussed. Jensen et al. (2020) assessed four insulation systems for internal retrofitting solid masonry walls using HAM simulations which were validated by comparison with field measurements retrieved over a period of 2-4 years. The influence of the thickness of the masonry to the hygrothermal response of the wall assemblies was discussed as well as the effect to the brick and mortar type, on the level of relative humidity in the wall assembly. A hygrothermal assessment in respect to brick veneer wall assemblies having thermal insulation added to the interior side of the wall was conducted by Hamid and Wallentén (2017). A comparison was conducted for the mould growth risk of the brick veneer wall assembly with and without the thermal insulation; the HAM models were validated by field measurements. Wang et al. (2020) investigated moisture-safe attic design, where attics had been exposed to an extremely cold climate using HAM simulations. A whole-building HAM model was established in WUFI Plus to study the hygrothermal performance of ventilated and un-ventilated attics. Based on the results obtained from HAM simulations, different attic design options were proposed to achieve acceptable moisture-safe performance in the attics. Frasca el al. (2021) incorporated HAM simulations with the building energy simulations as part of a conservation program for a historical church located in Italy. The combined methodology permitted revealing the moisture-induced conservation risks to which the church structure was subjected to.

To permit further assessing the moisture loads effects on the long-term performance of two wall assemblies, HAM simulations were used to determine the change in moisture performance of brick and vinyl-clad wall assemblies for 11 selected Canadian cities (Figure 5.1) under historical climate loads, as compared to future projected climate data (Xiao et al., 2021). For the study described in this paper, two different moisture loads were considered as input for the HAM simulations: the moisture load estimated as 1 % of the Wind-Driven Rain (WDR) load, and moisture load calculated by using water entry equations for each wall type. The HAM analysis focuses on the moisture performance of the Oriented Strand Board (OSB) components of the wall assemblies. The mould growth index (ASHRAE, 2016) was selected as the criterion to determine the moisture performance of the walls. The hygrothermal performance of these two wall types are compared and discussed in terms of different city locations, for which simulations were completed, and in terms of the hygrothermal response of the walls to historical and future projected climate loads.

Figure 5.1 Location of Canadian cities considered in this study; from left to right: VAN-Vancouver, CAL-Calgary, SAS-Saskatoon, WIN-Winnipeg, TOR-Toronto, OTT-Ottawa, MON-Montreal, MNC-Moncton, CHA-Charlottetown, HAL-Halifax, and STJ-St. John's.

5.1.3 Hygrothermal simulation process parameters

The hygrothermal simulations in this study were conducted using Delphin software version 5.9.5 given that it can solve heat and moisture transport for 1-D and 2-D numerical models within a relative short period of time (Nicolai et al., 2007). The vinyl-clad and brick veneer-clad wall assemblies were modelled in 1-D. The properties of materials and geometric configurations of the models were consistent with the test specimens that had been subjected to watertightness tests in a previous phase of the study (Xiao et al., 2021).

5.1.3.1 Climate input parameters

All 15 ensembles of 31-year climate data during the periods 1986-2016, 2034-2064, and 2062-2092 generated by the climate model used for the analysis of moisture load to wall assemblies located in different cities (Xiao et al., 2021) were implemented in the

HAM simulations. The detailed climate inputs for the simulations are given in Table 5-1. The indoor temperature and relative humidity were set as constant values to eliminate their influence of the assessment results. The liquid water production rate is the moisture load that reached the water resistance barrier derived from the WDR load on wall assemblies. Two sets of moisture loads were implemented in the simulation: one set of the moisture load was considered as 1% of the WDR load and the other set was derived from the water entry equations mentioned in a previous phase of this study (Xiao et al., 2021).

Table 5-1 Climate inputs parameters for the HAM simulation

Climate Input	Descriptions
Indoor Temperature	Constant 20°C
Indoor Relative Humidity	Constant 50%
Outdoor Temperature	Temperature at the HOUR in Celsius
Outdoor Relative Humidity	Relative humidity at the HOUR in %
Wind Velocity	Wind speed at the HOUR in m/s
Wind Direction	Wind direction at the HOUR in ° (measured clockwise from North)
Atmospheric Counter Radiation	Hourly direct normal irradiance in W/m^2
Heat Emission from Surrounding Ground	Measured Ground Emission
Direct Sun Radiation	Hourly direct horizontal irradiance in kJ/m^2
Diffuse Sun Radiation	Hourly diffused horizontal irradiance in W/m^2
Rain Flux Density Normal to the Wall	WDR load on wall assemblies
Liquid Water Production Rate	Water source calculated from WDR load and water entry equation

5.1.3.2 Boundary and field conditions

Boundary and field conditions for the HAM simulation are provided in Table 5-2. Part of conditions were obtained from theoretical concept while the rest were obtained from field measurements. The orientations of wall assemblies were consistent with the directions which had the greatest WDR load during the 31-year period in different cities. The inclination of all simulated wall assemblies was 90°. Latitude, longitude and time zone parameters for each wall assembly followed the cities' geographical information. The moisture load in the simulation was applied to the exterior surface of the water resistive barrier to mimic the penetrated water in the wall assemblies. The moisture load as 1% of the WDR load and the one calculated by the water entry equations (Xiao et al.,

2021) based on hourly WDR load and hourly DRWP were implemented, respectively. Thus, two sets of simulation results using different moisture loads were obtained.

The air change rate (ACH) is a field condition that would significantly affect the moisture performance of wall assemblies and it is calculated by Eq. (5.1).

$$\mathrm{ACH} = \frac{\mathrm{Q} \times 3600}{1000 \times V} \tag{5.1}$$

Where: *ACH* is the air change per hour; *Q* is the air volumetric flow rate in the cavity (L/s); and *V* is the cavity volume (m^3)

For the brick veneer wall, discrete vents are usually distributed at the top and bottom of the cladding. The typical practice in Canada is to have two openings at top and bottom of the wall with a 1.2 m spacing. The area of the opening ranges from 600 mm^2 to 900 mm^2. Finch and Straube (2007) measured the ACH for a brick veneer wall with 38 mm drainage cavity. The range of the measured ACH for the entire year was 0 to 9.6 with an average value of 2.2. Simpson (2010) tested a brick veneer wall with 25 mm cavity in Burnaby, British Columbia. The ACH was recorded between 1 and 11, with an average value of 6 from February to June. Langmans et al. (2016) compared the ACH for a brick veneer wall with a single opening and double openings. The ACH for the single opening case ranged from 1.7 to 6 and the value doubled for the double opening configuration. Based on these observations, the ACH for the 25 mm brick veneer wall assembly analyzed in this study was considered as 5. In respect to the viny-clad wall, Van Straaten (2004) reported the ACH ranged from 41 to 185 with a 19 mm strapping caused cavity for the driving pressure between 1 and 10 Pa. Similar air flow rates were observed in direct applied vinyl-clad cladding and vinyl-clad cladding with 19 mm strapping by Shi and Burnett (2007). The ACH in their study for a vinyl-clad wall with 5mm cavity was 200. As a conservative assumption, a 50 ACH was used in the current simulation, as the filed condition for the vinyl-clad wall.

Table 5-2 Boundary and field conditions for the HAM simulation

Boundary and Field Conditions	Setting and Parameters
Indoor Heat Conduction	Exchange coefficients (8 W/m^2K)
Outdoor Heat Conduction	Boundary layer (Variable air velocity)
Indoor Vapor Diffusion	Exchange coefficient (1.52 x 10^{-8} s/m)
Outdoor Vapor Diffusion	Boundary layer (Variable air velocity)
Rain	Imposed flux (Wall parameters)
Short Wave Radiation	Direct sun radiation model (Medium gray wall 0.6)
Long Wave Radiation	Long wave components (Emission coefficient 0.9)
Moisture Load	Applied to exterior surface of the water resistive barrier (1% of WDR load and water entry functions)
Air Change Rate	Air flow rate per hour in the drainage cavity (m^3/h)

5.1.3.3 Configurations of wall assemblies and materials properties

Configurations and cross-sections of the brick and vinyl-clad wall assemblies subjected to watertightness tests are shown in Figure 5.2. The 1-D numerical models for the two wall assemblies modelled in the HAM simulations were consistent with the cross section as shown in Figs. 5.2 (b) and (d) but excluded wood studs. The depth of air cavity of the vinyl-clad wall assembly was set as 2mm in the numerical model, to represent the actual cavity depth which varied from 0 to 5mm. Thickness of all the other layers in the model were the same as those in the actual wall specimen.

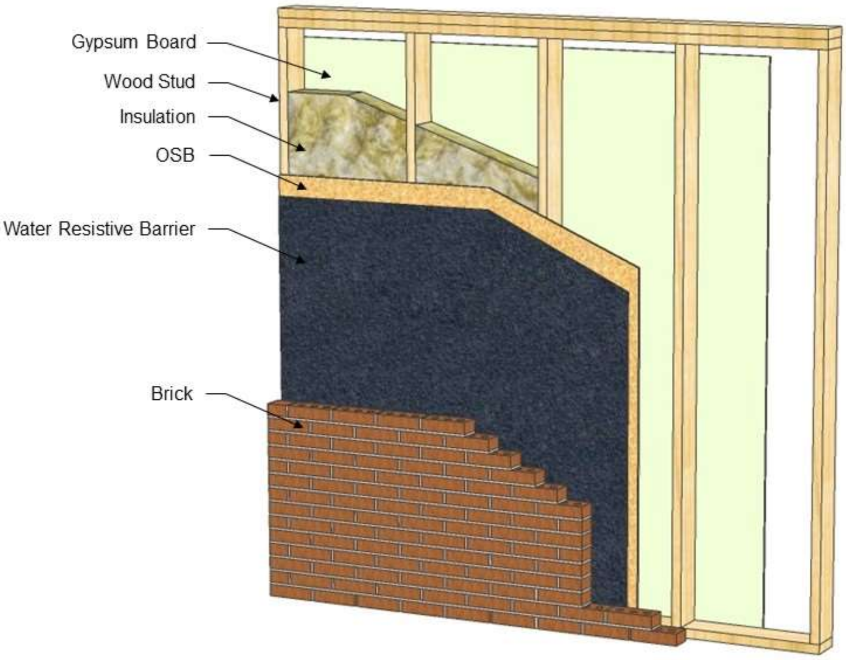
Gypsum Board
Wood Stud
Insulation
OSB
Water Resistive Barrier
Brick

(a)

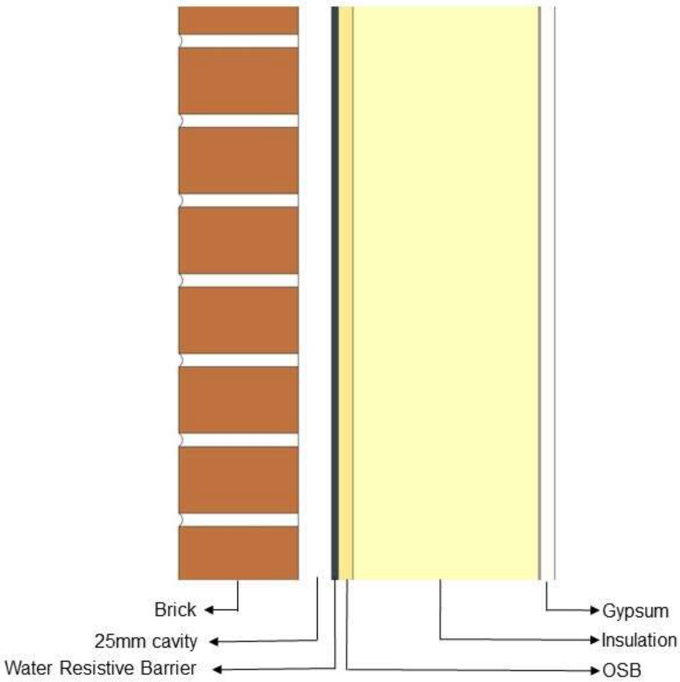
Brick
25mm cavity
Water Resistive Barrier
Gypsum
Insulation
OSB

(b)

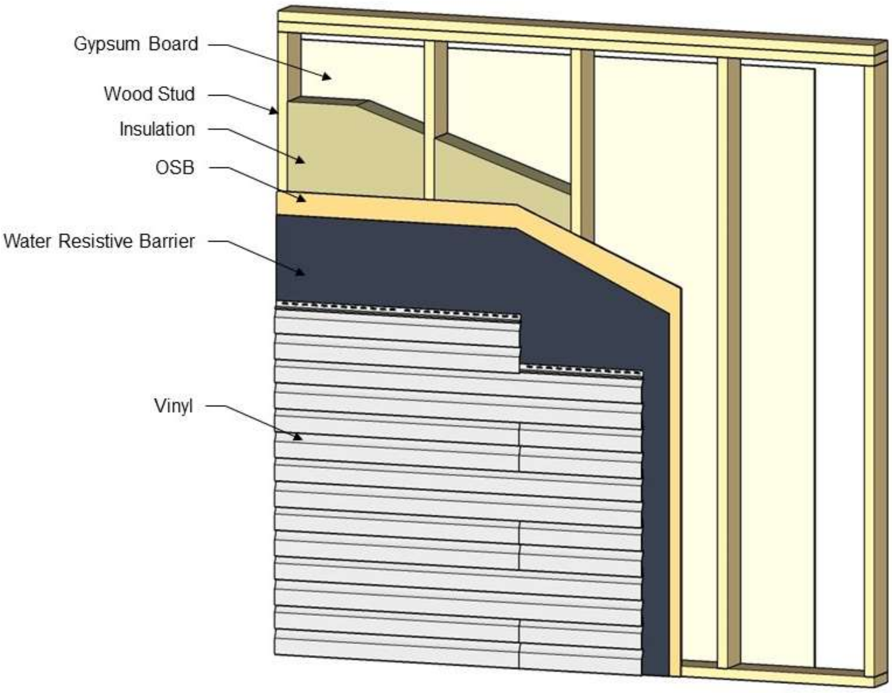
Gypsum Board
Wood Stud
Insulation
OSB
Water Resistive Barrier
Vinyl

(c)

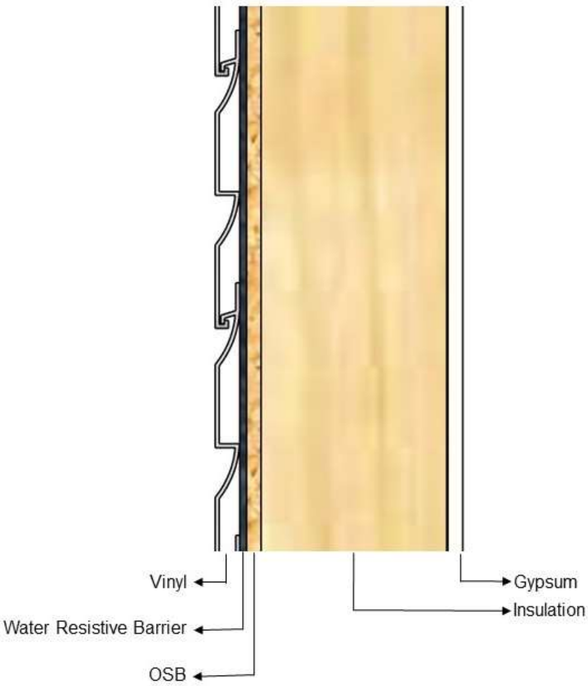
Vinyl
Water Resistive Barrier
OSB
Gypsum
Insulation

(d)

Figure 5.2 (a) Brick veneer wall assembly; (b) Cross section of the brick veneer wall; (c) Vinyl-clad wall assembly; (d) Cross section of the vinyl-clad wall.

The material properties required to carry out the HAM simulation in DELPHIN software include: dry density, material porosity, dry specific heat capacity, moisture storage curve, thermal conductivity, moisture diffusivity or water conductivity and vapour permeability. Such information was obtained from the National Research Council Canada material property database (K. Kumaran et al., 2002; M. Kumaran, 2006). Materials properties that were implemented in this study are listed in Table 5-3.

Table 5-3 Materials properties for brick and vinyl wall assemblies 1-D models

Components/ material	e (mm)	Density (kg/m^3)	kt (W/mk)	CE (J/kg K)	Porosity (m^3/m^3)	vper (s)	vperm (ng/m^2sPa)	A ($kg/m^2s^{0.5}$)	DL (m^2/s)
30-minute paper	0.24	909	0.159	1256	0.97	9.7×10^{-14}	404.2	0.00093	1×10^{-16}
Red matt clay	90	1900	0.5	800	0.21	1.5×10^{-12}	16.2	0.0268	1×10^{-16}
Vinyl-clad	1.1	1500	0.16	1260	0	1×10^{-16}	0.1	-	1×10^{-16}
OSB	11	600	0.094	1880	0.96	2.5×10^{-13}	22.6	0.0022	1.17×10^{-14}
Plywood	12.5	470	0.086	1880	0.8	1.9×10^{-13}	15.4	0.0026	6.14×10^{-14}
Gypsum	13	700	0.15	870	0.4	5.8×10^{-11}	4430	0.001	1.39×10^{-14}
Mineral fibre	140	37	0.032	670	0.66	1.3×10^{-10}	928.6	-	1×10^{-16}

e: thickness; kt: thermal conductivity; CE: specific heat capacity; vper: vapour permeability; veperm: vapour permeance; A: water absorption coefficient; DL: Liquid diffusivity

5.1.3.4 Mould growth index as performance criteria

The mould growth index is a function of relative humidity, temperature and duration. It has been selected as the criteria to assess the performance of the investigated wall assemblies. As developed by Ojanen et al. (2010), the severity of mould growth is determined by visual inspection, to which an index value is assigned ranging from 0 (no growth) to 6 (heavy and tight growth, coverage about 100%). Procedures to derive the mould growth index are outlined in ASHRAE 160 standard (ASHRAE, 2016). The mould growth index is a function of relative humidity, temperature and duration of exposure to conditions suitable for mould growth. The sensitivity class of a material determines parameters used in the calculation of mould growth. The initial value of the mould growth index is considered as 0 and the index value accumulates over time (Eq. 5.2).

$$\mathrm{M}_t = M_{t-1} + \Delta M \tag{5.2}$$

Where, *Mt* is the mould index for the current hour; M_{t-1} is the mould index for the previous hour; ΔM is the change in mould index for each hour calculated using Eq. (5.3) or Eq. (5.5) based on the values of temperature and relative humidity. When the relative humidity (RH_s) at the surface of the materials is greater than the critical relative humidity (RH_{crit}, Eq. 7), an increment of mould index is calculated using Eq. (5.3). If surface temperature, $T_s \leq 0$°C or $RH_s \leq RH_{crit}$, a decline in mould index is calculated using Eq. (5.3).

$$\Delta M = \frac{k_1 k_2}{168 \times \exp(-0.68 \ln T_s - 13.9 \ln RH_s + 0.14W + 66.02)} \tag{5.3}$$

Where: k_1 is the mould growth intensity factor determined based on the sensitivity level of materials as shown in Table 5-4; k_2 – is the mould index attenuation factor calculated using Eq. (5.4); W – is a parameter selected from Table 5-4 based on the sensitivity level of materials.

$$k_2 = \max\{1 - \exp[2.3(M - M_{max})], 0\} \tag{5.4}$$

Where M_{max} – is the maximum mould index as related to the surface temperature and to the relative humidity calculated using Eq. 5.5.

$$M_{max} = \mathrm{A} + \mathrm{B}\left(\frac{RH_{crit} - RH_s}{RH_{crit} - 100}\right) - C\left(\frac{RH_{crit} - RH_s}{RH_{crit} - 100}\right)^2 \tag{5.5}$$

Where, A, B, and C - are coefficients selected from Table 5-4.

$$\Delta M = \begin{cases} -0.00133 \times k_3 \; when \; t_{decl} \leq 6 \\ 0 \; when \; 6 < t_{decl} \leq 24 \\ -0.000667 \times k_3 \; when \; t_{decl} > 24 \end{cases} \tag{6}$$

Where, k_3 is the mould index decline coefficient, and its recommended value is 0.1; t_{decl} is the number of hours from the moment when the conditions for mould growth changed from favorable (T_s > 0°C and RH_s > RH_{crit}) to unfavorable ((Ts ≤ 0°C or RH_s ≤ RH_{crit}).

Table 5-4 Parameters for mould growth index calculation

Sensitivity Class	k_1 (if M < 1)	k_1 (if M ≥ 1)	W	A	B	C
Very sensitive	1	2	0	1	7	2
Sensitive	0.578	0.386	1	0.3	6	1
Medium resistant	0.072	0.097	1	0	5	1.5
Resistant	0.033	0.014	1	0	3	1

The Oriented Strand Board (OSB) is classified as a sensitive material according to the ASHRAE standard (ASHRAE, 2016), thus the corresponding coefficients were selected to proceed with the calculation. The relative humidity and temperature on the material surface for each hour were obtained from the HAM simulations results.

5.1.4 HAM Simulation results and discussion

The HAM simulations were conducted for the brick veneer and viny-clad wall assemblies using both types of moisture loads (ASHRAE 160 Standard and derived from experiments) for 11 city locations each of which was simulated over historical and future projected time periods using 15 ensembles of climate data. In total, 1980 sets of results have been generated. The analysis and discussion focus on the variation of parameters relating to the performance of wall assemblies exposed to climate conditions corresponding to historical and future projected time periods. Results obtained from different types of moisture loads are also discussed. Moreover, the performance of the wall assemblies is characterized geographically. Changes in temperature and relative humidity were used to determine the mould growth index at the exterior surface of the OSB. As well, the levels of mould index and their temporal distributions for different cities and during different time periods were also investigated, and the results are provided below.

5.1.4.1 Changes in temperature and relative humidity

5.1.4.1.1 Changes in OSB surface temperature

Figure 5.3 shows the average temperature at the exterior surface of the OSB during each 31-year time period. The box plots cover the variations of average temperatures for 15 realizations of climate data. The HAM simulations with the same type of moisture source are represented under the same color palette, while colors in different shades represent the temperatures during different time periods. This scheme also applies to the subsequent box plots related to the relative humidity.

It was noticed that, the temperature at the exterior surface of the OSB, for the vinyl-clad wall assembly (Figure 5.3a), obtained from the HAM simulations using different moisture sources were almost identical. The temperature increment at the OSB corresponds to the changes in temperature for the two projected time periods, which were an increase of 2.0°C and 3.5°C, respectively, from the historical time period. This observation also applies to the changes in temperature for the brick veneer wall assembly (Figure 5.3b). However, the temperatures obtained from the HAM simulations using the moisture load derived from the water entry functions for the brick veneer wall assembly were slightly greater than those obtained using the 1% WDR load. According to the previous phase of this study (Xiao et al., 2021), the moisture load obtained from the water entry function was 45% to 80% that of the 1% WDR load. Thus, for the brick veneer wall assembly, a reduced moisture load would result in a greater temperature at the exterior surface of the OSB. It was also evident for simulations conducted of walls located on the west coast (i.e. Vancouver) and as well cities located in central Canada (i.e. Calgary, Saskatoon, and Winnipeg) that under the same climate conditions, the average temperatures on the OSB surface for the brick veneer wall assembly were lower than those for the vinyl-clad wall assembly. Whereas, the opposite was found for the eastern inland cities (i.e. Toronto, Ottawa, Montreal) as well as for the cities located on the east coast Canada (i.e. Moncton, Halifax, Charlottetown and St. John's). The average temperature obtained from the 15 different realizations of climate data did not register changes greater than 2.0°C, and in most instances, the variation was less than 0.5°C. The highest average temperature was found in Vancouver, whereas in cities located in central

Canada (i.e. Calgary, Saskatoon, and Winnipeg) lower average temperatures were experienced, as compared to cities located in the other regions of Canada.

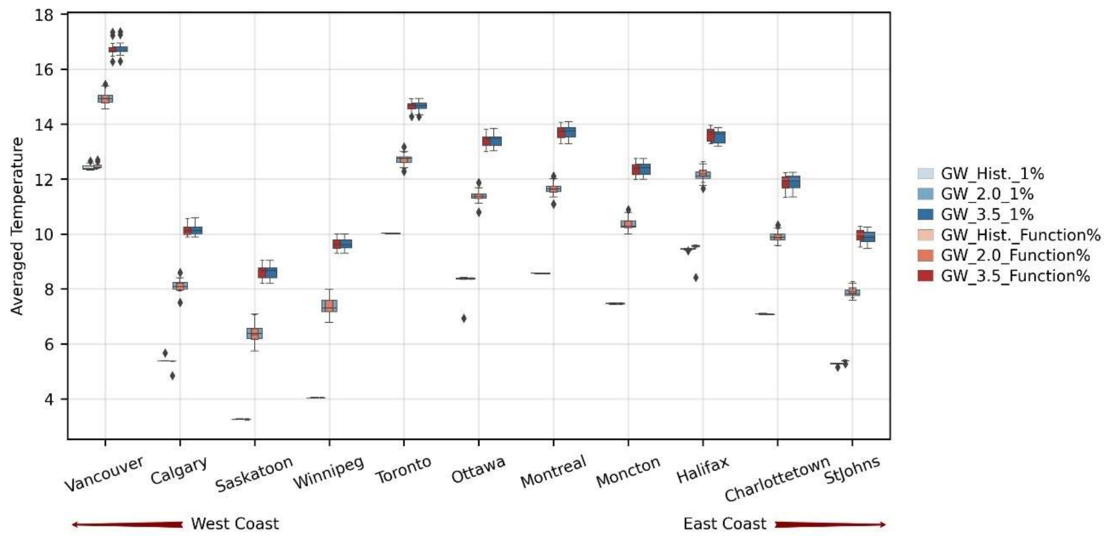

(a)

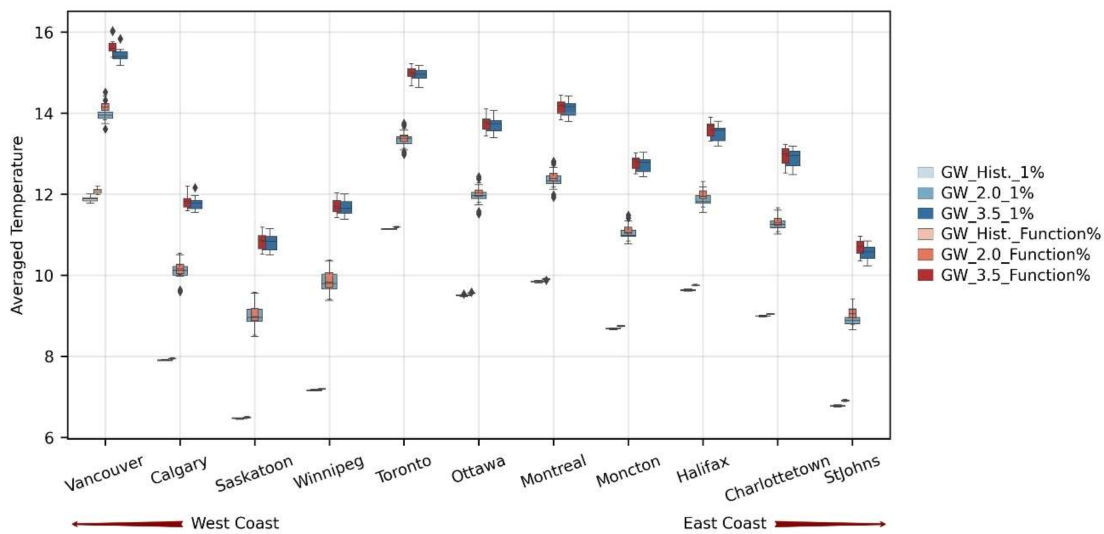

(b)

Figure 5.3 Temperature at the exterior surface of the OSB for the vinyl-clad wall assembly (a) and brick veneer wall assembly (b). 'GW_Hist.' represents time period 1986-2016, 'GW_2.0' represents time period 2034-2064, and 'GW_3.5' represents time period 2062-2092. The '1%' and 'Function%' depict the source of the moisture load.

5.1.4.1.2 Changes in OSB surface relative humidity

The 31-year average relative humidity data for different cities are shown in Figure 5.4. For the vinyl-clad wall assembly (Figure 5.4a), the average moisture load calculated from the water entry function was 65% to 99% greater than that of the 1% WDR load (Xiao et al., 2021). Consequently, discrepancies were evident for average values of relative humidity for instances where HAM simulations used different moisture loads. As it can be noticed in Fig. 5.4, the relative humidity for the different regions of Canada and between different time periods was very different. For Vancouver, the average relative humidity decreased by approximately 10% during the future projected time period of 2062-2092, and the temperature over the same period increased by 3.5°C. For the cities located in central Canada, the relative humidity slightly decreased in Calgary, and essentially remained the same for both Saskatoon and Winnipeg. For the eastern inland city locations, the relative humidity decreased by 3% to 4% in Toronto during the future projected time periods, whereas the relative humidity in Ottawa and Montreal remained at the same levels. The values of relative humidity for east coast cities (i.e. Moncton, Halifax, Charlottetown and St. John's) were much greater than those in the cities located in central Canada and eastern inland. The cities of Moncton and Charlottetown had similar levels of relative humidity. When the moisture load was derived from the water entry equation, the relative humidity in these two cities decreased by 2% to 3% during the future projected time periods. The average level of relative humidity in Halifax and St. John's were close to 100% for all realizations

The relative humidity at the exterior surface of the OSB in the brick veneer wall assembly is shown in Figure 5.4b. The lower moisture load derived from the water entry function for the brick veneer wall assembly rendered a lower relative humidity compared to the cases using a moisture load as 1% of the WDR. The relative humidity of all the cities is shown to increase during the future projected time periods. This observation is contrary to that for the vinyl-clad wall assembly for which the relative humidity remained at the same level or decreased during future projected time periods. The relative humidity for the brick veneer wall assembly in the west coast city of Vancouver was greater than most cities except for Halifax and the variation in values generated from climate data of different realizations was minor compared to the other cities. In regards to the cities located in central Canada (i.e. Calgary, Saskatoon, and Winnipeg), the average relative humidity was lower than for cities located in other regions and Saskatoon had the lowest average relative humidity value. Also, the box plot covered a greater range of values which indicated an increasing uncertainty in climate data generated by the climate model for these city locations. The relative humidity at the OSB surface for the brick veneer wall assembly for inland eastern cities was not significantly different from that for east coast cities, except for Halifax. Compared to the vinyl-clad wall assembly, the relative humidity in the brick veneer wall assembly was over 10% higher for cases using a moisture load of 1% of the WDR, for these cities. In general, the average relative humidity in the brick veneer wall assembly increased by 2% to 5% during the future projected time periods for all city locations. This increase was positively correlated with the corresponding increase in temperature. Considering that both the temperature and the relative humidity would rise, a higher level of mould index would be expected during the future projected time periods.

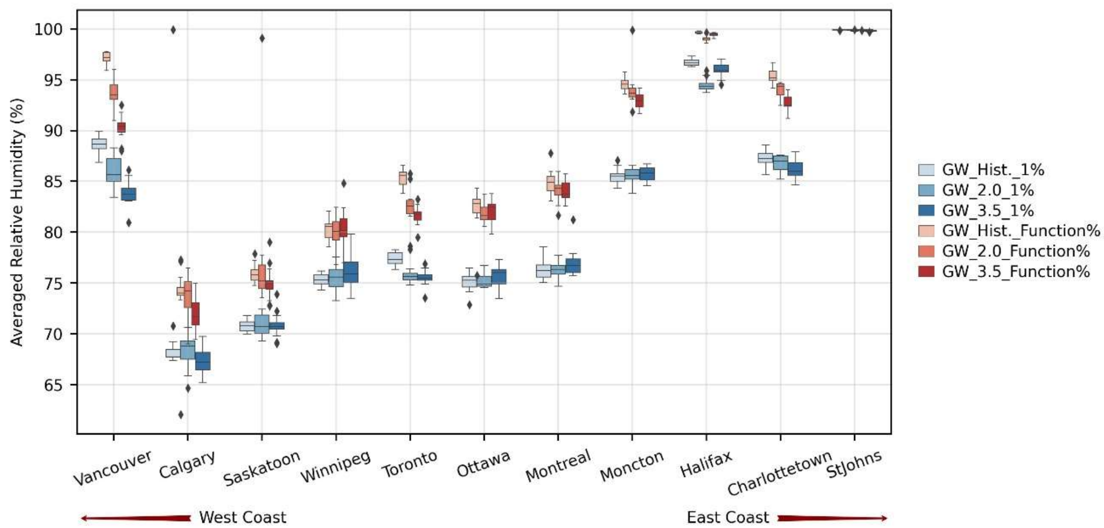

(a)

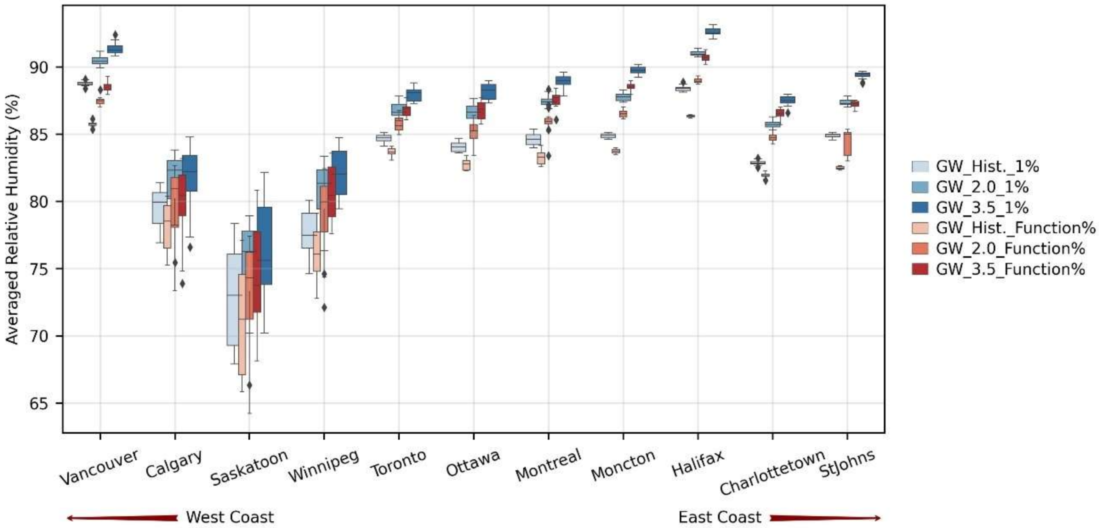

(b)

Figure 5.4 31-year average relative humidity at the exterior surface of the OSB for (a) the vinyl-clad wall assembly and (b) brick veneer wall assembly.

The correlations between the 31-year average moisture load and the 31-year average relative humidity are shown in Figure 5.5. The R-squared value between the two parameters was 0.539 for the vinyl-clad wall assembly and 0.243 for the brick veneer wall assembly. This observation suggests that the relative humidity at the OSB in the vinyl-clad wall assembly was more sensitive to the moisture load than that in the brick veneer wall assembly.

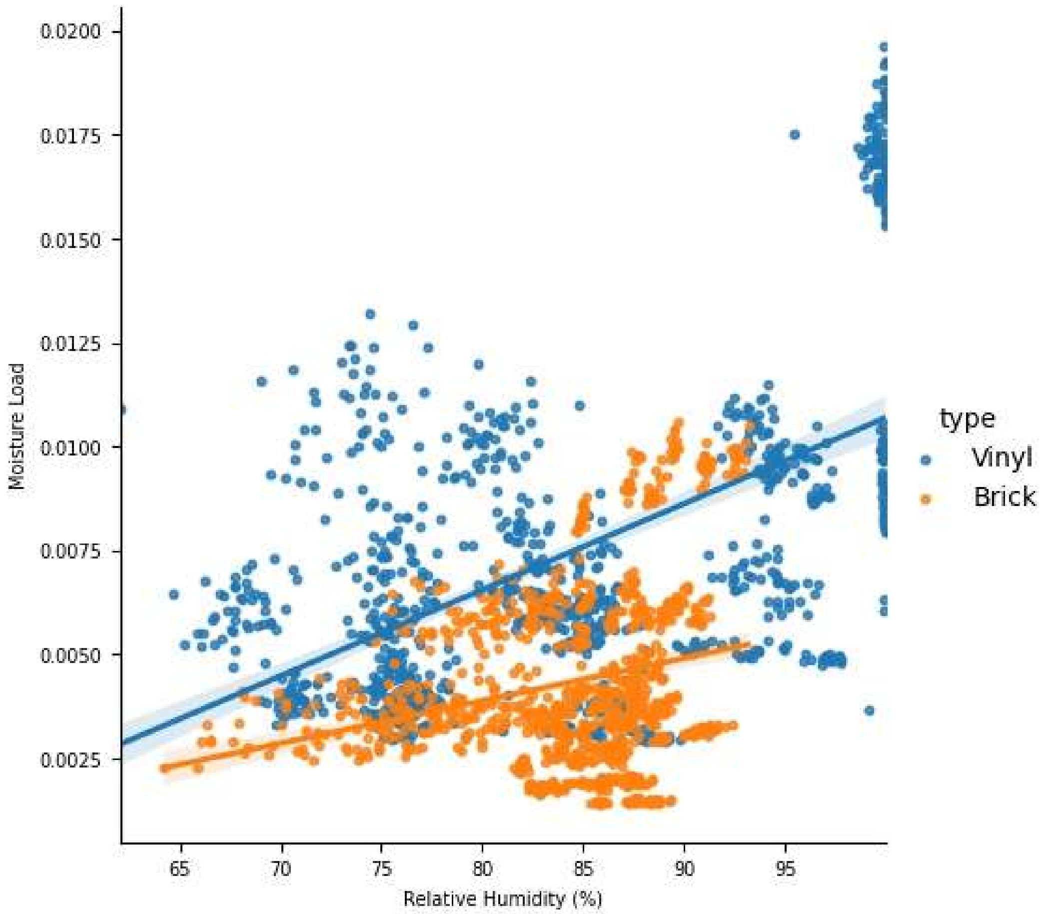

Figure 5.5 Correlations between the 31-year average moisture load and 31-year average relative humidity.

5.1.4.2 Changes in mould index characteristics

5.1.4.2.1 Average mould index

The 31-year average value of mould index for each city are represented as box plots in Figure 5.6. Due to the greater moisture load generated by the water entry function for the vinyl-clad wall assembly, the average mould indices of the corresponding cases were consequently greater (Figure 5.6a). Such discrepancies between cases using a moisture load of 1% of the WDR load and instances where the was moisture load was derived from the water entry function for different cities, varied significantly due to their unique WDR and DRWP conditions, or a combination of both. Since the average mould index in Vancouver for the 1% case was already close to 5, which corresponds to a very severe situation, the gain in mould index due to the extra moisture load derived from water entry function was diminishing. The change in the mould index during projected time periods in this city, was not obvious and small uncertainties were observed for the average mould index derived from different realizations. The mould index in central Canada cities: Calgary, Saskatoon and Winnipeg were lower than other cities regardless the type of moisture load. Noticeable changes in the mould index during projected time periods were found only in Winnipeg. Moderate uncertainties were identified in cases using water entry functions. When the moisture load was considered as 1% of the WDR load the eastern inland cities: Toronto, Ottawa, and Montreal, had similar average mould index as those located in central Canada. However, when the water entry function was considered for the moisture load estimation, the average mould index increased drastically compared to cases using 1% of WDR for moisture load. The average mould index for Toronto was expected to reduce during the projected time periods, whereas the one for Ottawa and Montreal were predicted to increase in the future. Also, the extended bars in Fig. 5.6 a), show that the greatest uncertainties of the average mould index were recognized for cases using the water entry function in these 3 cities. For east coast cities, the mould index for Moncton and Charlottetown were similar to each other, as well as that for Halifax and St. John's. Higher levels of mould index were expected during the projected time periods in all these 4 cities. Relatively greater uncertainties were observed for Moncton and Charlottetown.

The mould index at the exterior surface of the OSB for the brick veneer wall (Figure 5.6 b) for all cities would increase during the projected time periods. Lower mould index was observed for cases using less moisture load derived from the water entry functions. The greatest uncertainties of the mould index were found in central Canada cities. West coast city Vancouver, eastern inland cities, Toronto, Ottawa, Montreal, and two east coast cities, Moncton and Halifax, had comparable levels of mould index. The average mould index in central Canada cities were lower than other cities located in other regions of Canada.

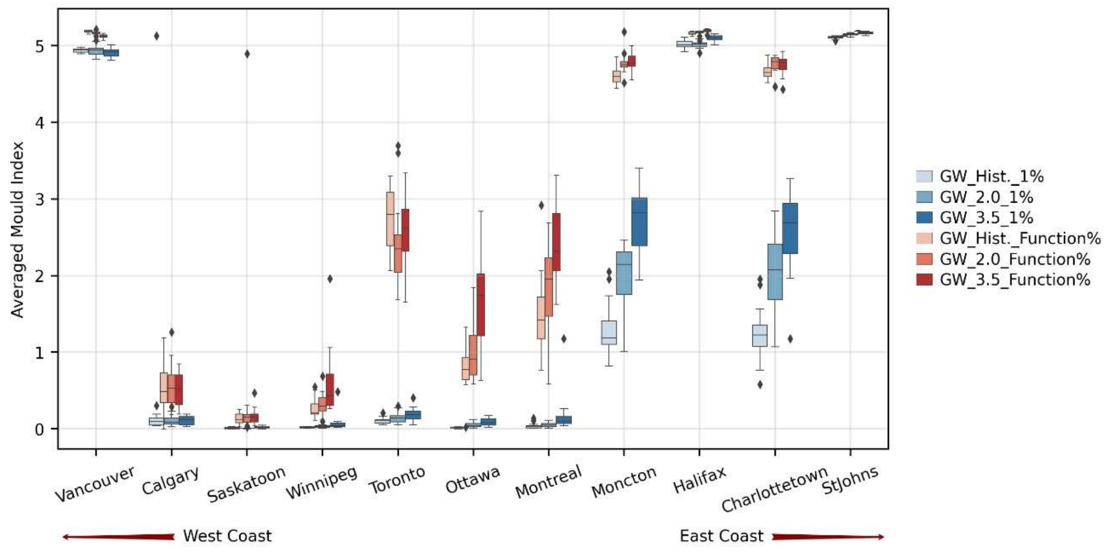

(a)

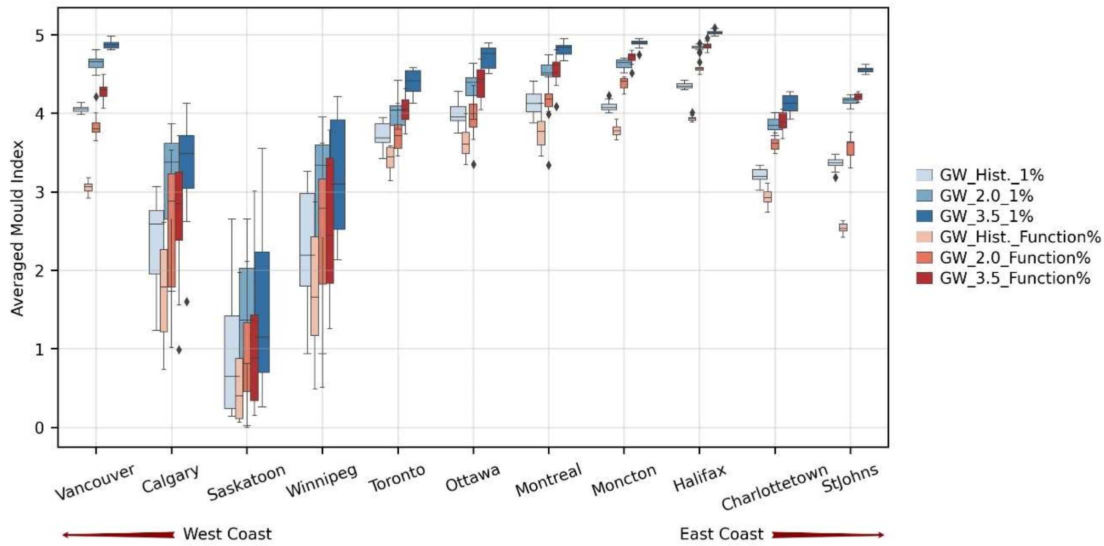

(b)

Figure 5.6 31-year average mould index at the exterior surface of the OSB for (a) vinyl-clad wall assembly and (b) brick veneer wall assembly.

Correlations between the 31-year average moisture load and the 31-year average mould index are shown in Figure 5.7. The R-squared value of these two parameters was 0.45 for the vinyl-clad wall assembly and was only 0.21 for the brick veneer wall assembly. Thus, the level of moisture load didn't reflect the level of mould index.

Nevertheless, the increase in moisture load resulted in the increase in the mould index as shown in Figure 5.6.

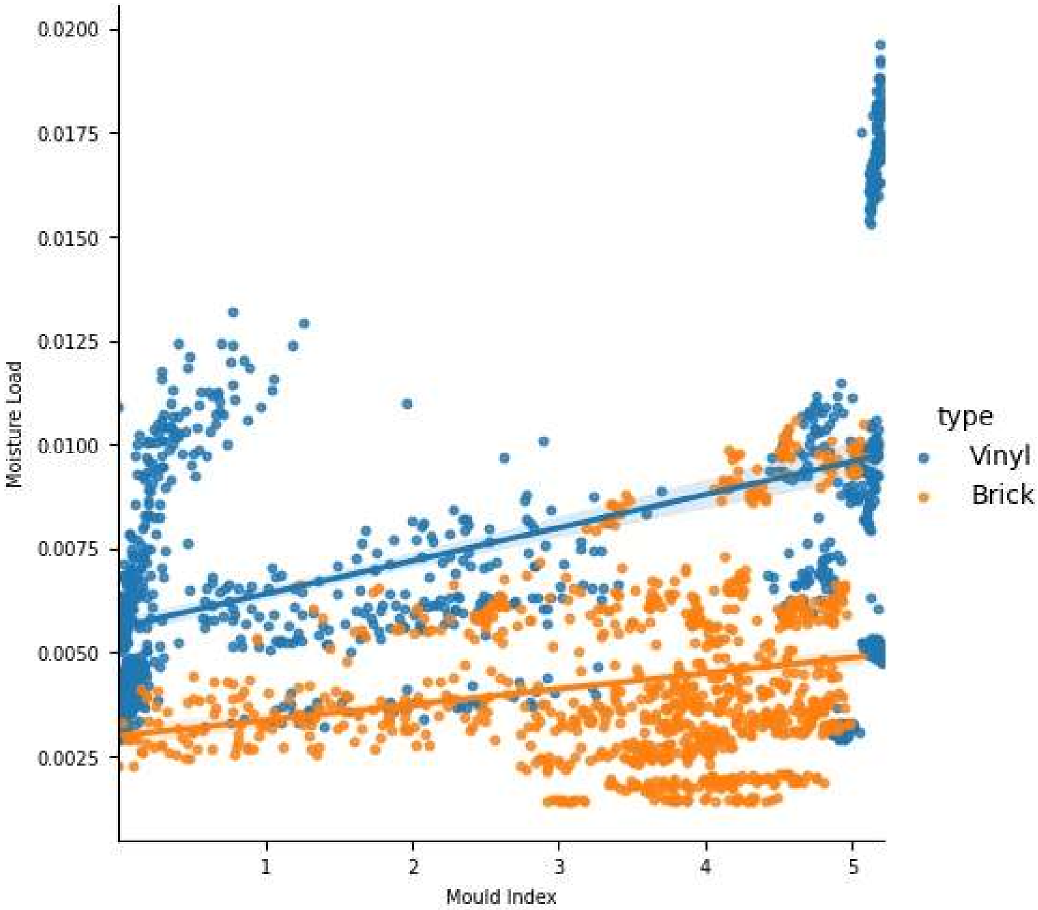

Figure 5.7 Correlations between the 31-year average moisture load and 31-year average mould index.

5.1.4.2.2 Duration and frequency of different levels of mould index

The main object of the mould growth model was developed "to give tools for better prediction and evaluation of the risks for biological growth on structure surface" (Ojanen et al., 2010). Such tools have classified the mould index into 6 levels. For the mould index between 0 and 2, the mould can only be detected using a microscope, and when the index is above 2, the mould can be visually detected. The higher the value of mould index the greater the amount of mould growth rate. It is evident that, depending on the species of the mould, the illness could be related to the mould exposure (Kuhn & Ghannoum, 2003). With a higher mould growth rate and higher durations of such a rate, higher risks could be expected to compromise one's health. Thus, the frequency, duration for different levels of mould index for wall assemblies in different cities were also investigated.

For analyzing the frequency and duration for different levels of mould index, an event was first defined as a period of time for which the mould index was within a designated range. The adjacent hours for which the mould index exceed or was lower than this range were considered for a different event (Figure 5.8). The duration of each event was obtained and sorted into several categories and the frequencies of events with different categories of durations and different levels of mould index were counted. An event with a longer duration and higher mould index level is considered as a more severe event.

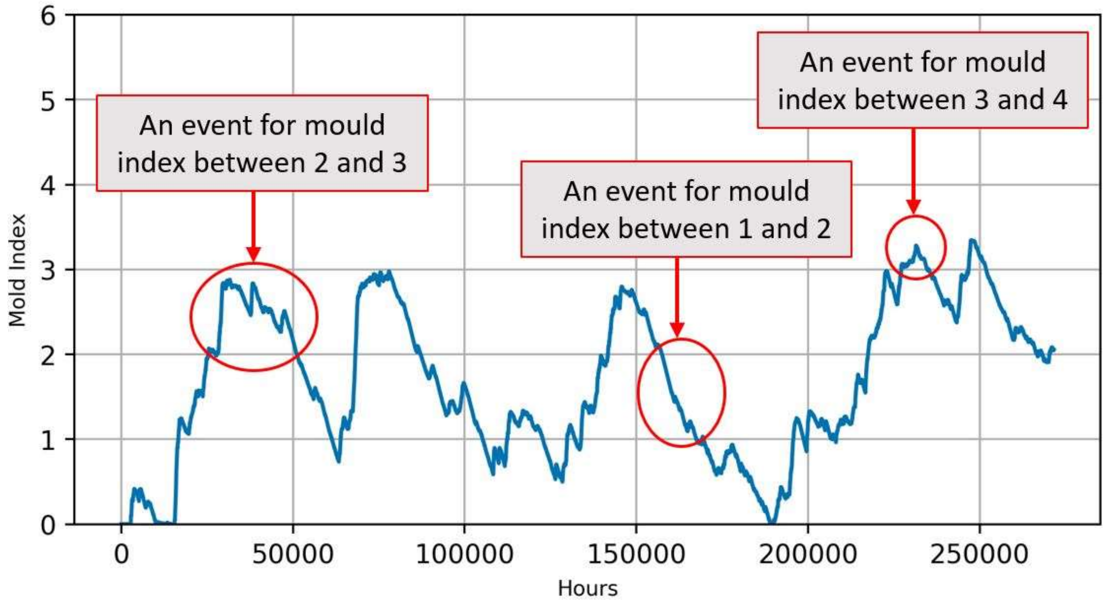

Figure 5.8 An example of the distribution in values of mould index for a 31-year time period and definition of an 'event'.

The distributions of events for each city during different time periods for the vinyl and for the brick veneer wall assemblies are represented in Figure 5.9 and Figure 5.10. The mould index was classified into 6 categories, which were the same as those used for the mould growth model. The duration of events was arranged into 7 classes: 0 to 7 days, 7 to 30 days, 30 to 90 days, 90 to 180 days, 180 to 365 days, 1 to 10 years, and 10 to 31 years. The number in each bubble in Figs. 5.9 and 5.10 represented the events' frequencies corresponding to one duration level and one mould index level, as collected from 15 realizations of climate data. The colours and sizes of the bubbles also reflected the frequencies. The plots from left to right represent the results for different time periods. An overview of the results is provided below by cities.

Calgary – During the historical time period considered, 21 events with a mould index above 3 were observed in the vinyl-clad wall assembly using 1% of the WDR load as moisture load, whereas, during the two future projected time periods, the mould index values, for all events, were below 3. When the moisture load was obtained from the water entry function, for the historical time, 20 events had a mould index above 3, and 7 events lasted over a year but less than 10 years. During the future projected time periods, both the severity and the frequencies of events having mould index above 3 decreased. For the brick veneer wall, 231 events with a mould index above 3 were observed during the historical time period and 26 of them lasted over a year. More severe events occurred more frequently during the future projected time periods for cases using both the 1% of WDR load and the moisture loads derived from the water entry function. Using the water entry function as moisture load generated slightly less severe events than using the 1% WDR as moisture load.

Charlottetown – The vinyl-clad wall assembly evaluated as per the climatic conditions of this east coast city was exposed to more events with a mould index above 3 during the future projected time periods as compared to that occurring over the historical time period. These events with a mould index above 3 would also become more severe during future projected time periods. If the moisture load was considered as 1% of the WDR load, only a few events occurred having the mould index above 4. Whereas, when using the moisture load derived from the water entry function, most of events during all 3 time periods were above 4. With an increase of temperature during the future projected time period, the frequency of occurrence of longer duration events increased. For the brick veneer wall assembly, most events had a mould index between 2 and 5 and durations were between a month and 10 years. With temperature increasing during projected time periods, the frequency of events with higher values of mould index and of longer duration increased. Simulations using moisture load derived from the water entry function generated less severe events than those using the 1% of WDR load as the moisture load.

Halifax – As shown in Figure 5.6, the vinyl-clad wall assembly investigated for Halifax climatic conditions, had one of the highest average mould indices among the 11 cities analyzed. Comparably, during each time period, over 10 events experienced mould index levels of 5 to 6 (i.e. highest values) and were of the longest duration category of 10 to 31 years regardless of the moisture load implemented to the simulation model. The distribution of these events during different time periods did not demonstrate any obvious tendencies for change, as it was observed for the average mould index. When the 1% moisture load was considered, the brick veneer wall assembly during the historical time period experienced 10 events of mould index values ranging between 4 and 5 that lasted over 10 years. Whereas during future projected time periods, the durations of high mould index events decreased although the frequencies of these events significantly increased. Regarding the brick veneer wall assembly and for the moisture load based on the water entry function, the long duration (10-31 years) high mould index events occurred during the 2034 – 2064 time period when the temperature increased 2°C. During the subsequent time period 2062 – 2092, events with higher mould indices took place more often than that for the historical time period.

Moncton – Most events during the historical time period for the vinyl-clad wall assembly had mould index values of less than 3 when the 1% moisture load was considered. Frequencies of higher mould index events increased along with the increases in temperature during future projected time periods. When using the moisture load derived from the water entry functions, the mould index level for most events was greater than 4. The frequencies of events having longer durations and higher mould index levels increased during the projected time periods. The situation in the brick veneer wall assembly was similar to that for the vinyl-clad wall assembly; frequencies of events with higher mould index levels and of longer duration would increase during the future projected time period regardless of the type of moisture load. When using the moisture load derived from the water entry function, the frequency of events with higher values of mould index, and of longer duration, were less than those using the 1% of moisture load, with the exception of 7 events observed during the future time period of 2034 – 2064 for which mould index values ranging between 4 and 5 that lasted over 10 years.

Montreal – Considering the moisture load as 1% of the WDR, no event for the vinyl-clad wall assembly evaluated for Montreal during the time periods of 1986 – 2016 and 2034 – 2064 had a mould index value above 2. During the 2062 – 2092 time period, only 4 events had a mould index above 3. For the moisture load derived from the water entry function, more events with a mould index above 3 were obtained during the three time periods analyzed. Events with higher mould indices levels, and of longer duration, are expected during future projected time periods having increased annual temperature. The brick veneer wall assembly in Montreal experienced more severe circumstances than that of the vinyl-clad wall assembly. Most of the events, regardless of the type of moisture load, produced a mould index value of above 3. More severe events were expected during the future projected time periods than as occurred for the historical time period. The brick veneer wall assembly that was subjected to the moisture load derived from the water entry had fewer events with a mould index above 4, than when subjected to a 1% moisture load.

Ottawa – The mould index for all the events for the vinyl-clad wall assembly evaluated for Ottawa climate conditions, during the historical time period were lower than 1 when the 1% moisture load was used. As such, no event was given in the bubble plot in these circumstances. With the increase in temperatures during the future projected time periods, mould index levels of events had increased although the mould indices for all events were still less than 2. When the moisture load derived from the water entry function was considered, 21 events had mould indices greater than 3 during the historical time period. Number of occurrence of such events increased to 30 during 2034 – 2064, and 108 during 2062 – 2092. As for the brick veneer wall assembly, during the periods of 1986 – 2016 and 2034 – 2064, mould index values of most events ranged between 3 and 5. The future time period 2034 – 2064 had more severe events than the historic time period of 1986 – 2016, whereas, during the 2062 – 2092 time period, values of mould indices for most events fluctuated between 4 and 6. These observations were evident to both simulation scenarios that used different moisture loads.

Saskatoon – The vinyl-clad wall assembly investigated for Saskatoon did not have any events with a mould index greater than 3 during the 1986 – 2016 and 2062 – 2092 time periods when a 1 % moisture load was considered. During the 2034 – 2064 time period, it was noticed that 28 events had a mould index level between 5 and 6 that lasted over half a year. The reason for this substantial discrepancy resulted from climate data of one of the realizations, as generated by the climate model, being significant different from the average climate as compared to that of the other 14 realizations. If the climate of this realization had been ignored, the observations during the 2034 – 2064 time period would have been similar to those during the 1986 – 2016 and 2062 – 2092 time periods. When the moisture load was derived from the water entry functions, only one event was found to have a mould index above 3 for the vinyl-clad wall assembly. The increase in temperatures during the future projected time periods did not worsen the performance of the vinyl-clad wall assembly. In respect to the brick veneer wall assembly during the historical time period, there were 60 and 18 events had mould indices above 3, respectively, for simulation scenarios including the 1% moisture load and the moisture load derived from the water entry function. With increases in temperature during future projected time periods, frequencies of events having mould index above 3 increased. The 1% moisture load scenario had more severe events than the scenario with the moisture load derived from the water entry function.

St. John's – The situation for the vinyl-clad wall assembly for St. John's conditions, was very similar to that in Halifax. For both moisture loads considered, during the future projected time periods of 2034 – 2064 and 2062 – 2092, 15 events with mould index levels between 5 and 6 that lasted over 10 years were evident. During the historical time period, more fluctuations in the mould index values were observed as compared to the future projected time periods as there were shorter event durations for the same mould index level. For the brick veneer wall assembly, in general, more severe events were observed during the projected time periods than that of the historical time period. As to the 1% moisture load simulation scenario, the mould indices of most events were distributed between 2 and 5 during the historical time period. During the future projected time periods of 2034 – 2064 and 2062 – 2092, the mould indices ranged between 3 and 5 and 4 and 6 respectively, for the most frequently occurring events. For the simulation scenario for a moisture load derived from the water entry function, the mould index level for the most frequently occurring events were 1 level lower than those that occurred for the 1% moisture load scenario.

Toronto – During the time periods of 1986 – 2016 and 2034 – 2064, no event had a mould index above 3 for the vinyl-clad wall assembly, when the simulation scenario for a 1% moisture load was considered. During the 2062 – 2092 time period, only 1 such event occurred. Given the simulation scenario for a moisture load derived from the water entry function, events with all levels of mould index occurred for the vinyl-clad wall assembly. With increases in temperature during future projected time periods, more severe events were observed. As to the brick veneer wall assembly, mould indices for most events were above 3 during all three time periods and the frequency of events having higher values of mould index and longer durations would increase during the future projected time periods regardless the moisture load scenario. The performance of the brick veneer wall assembly using the moisture load scenario derived from the water entry function was slighter better than that using the 1% moisture load scenario.

Vancouver – The vinyl-clad wall assembly in Vancouver experienced numerous severe events and of long duration for all 3 time periods analyzed. When the 1% moisture load was considered, the mould index values for most events were greater than 4. The frequency of events with durations between 1 and 10 years were significantly reduced during the future projected time periods whereas more events of shorter duration occurred. For the moisture load simulation scenario derived from the water entry function, 15 events of 10 – 31 years duration and having a 5 – 6 mould index level were observed during the historical time period. The number of these types of events were drastically reduced for the future projected time periods whereas the frequency of events of shorter duration increased. The maximum mould index level of events for the brick veneer wall assembly during historical time periods was less than 5 for both moisture load scenarios. The durations and frequencies for events with higher mould index levels increased during the future projected time periods. The brick veneer wall assembly for the 1% moisture load scenario had more events of higher mould index level than for the moisture load scenario derived from the water entry function.

Winnipeg – There was only 1 event which had mould index above 3 for the vinyl-clad wall assembly using the 1% moisture load during the 3 analyzed time periods. More events with mould index above 3 were observed for the function moisture load scenario. During the projected time periods, frequencies of events with higher mould indices increased for the same duration category in the vinyl-clad wall assembly. For the brick veneer wall assembly, no event lasted over 10 years during all analyzed time periods. Durations of most events extended between 30 days to 10 years. Events with higher mould index levels and of longer duration occurred more frequently during future projected time periods for both types of moisture load scenarios. For the brick veneer wall, the 1% moisture load scenario generated more severe events than that of the scenario derived from the water entry function.

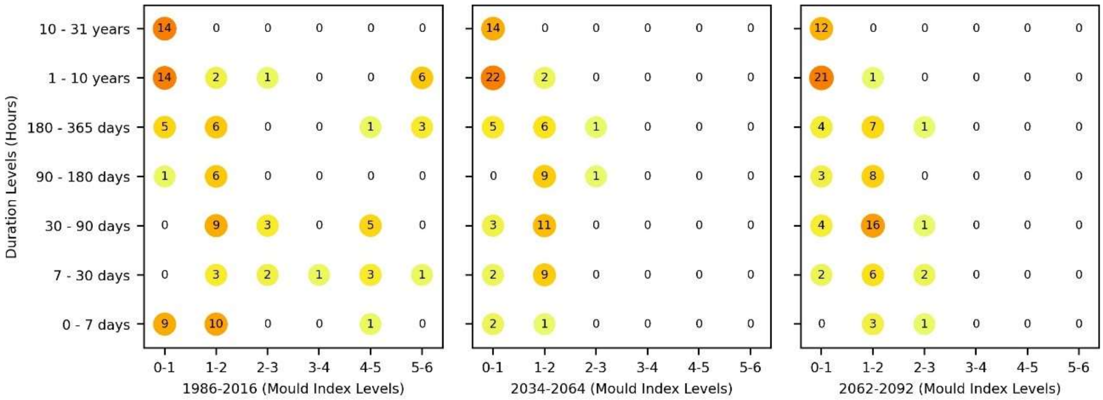

Calgary_1% Moisture Load

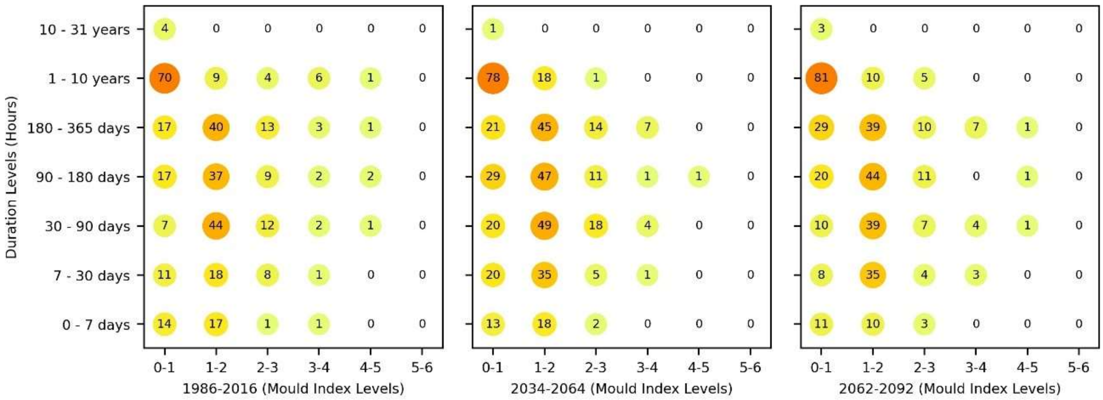

Calgary_Function% Moisture Load

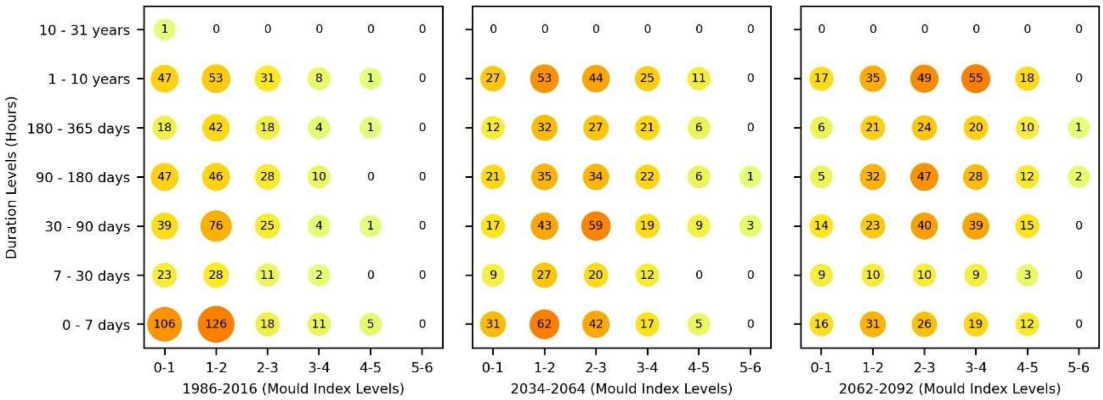

Charlottetown_1% Moisture Load

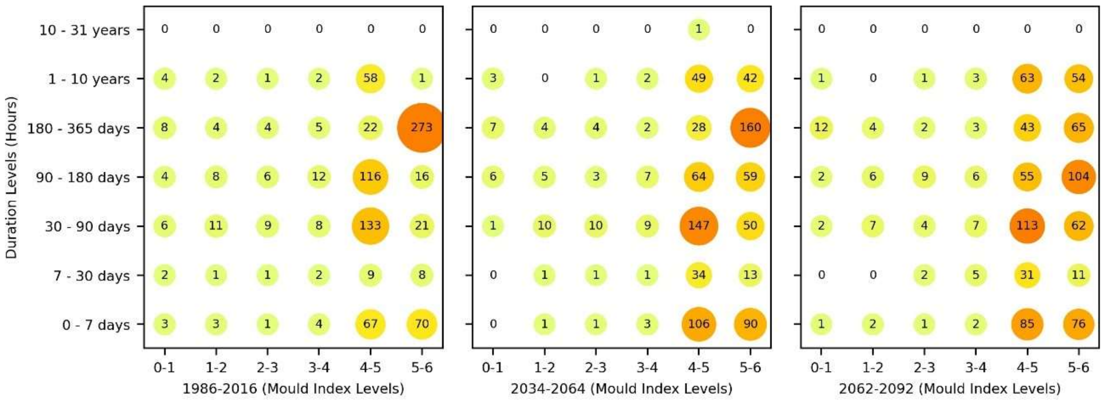

Charlottetown_Function% Moisture Load

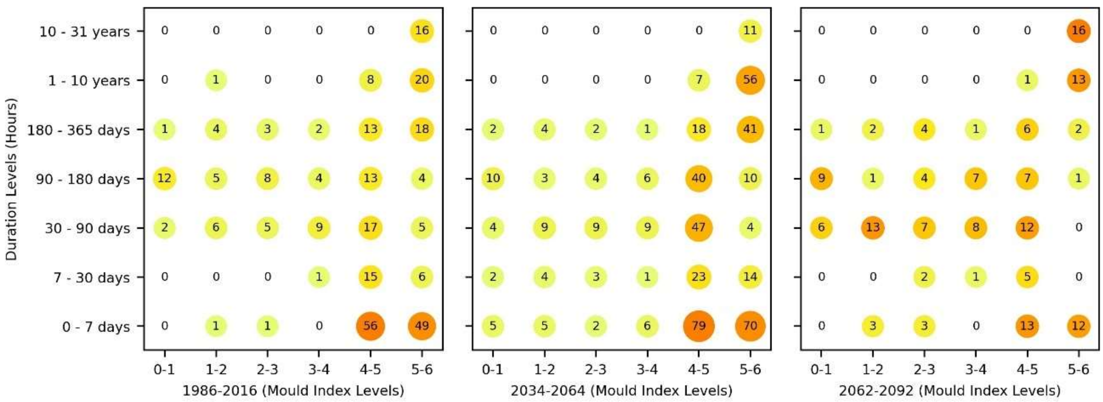

Halifax_1% Moisture Load

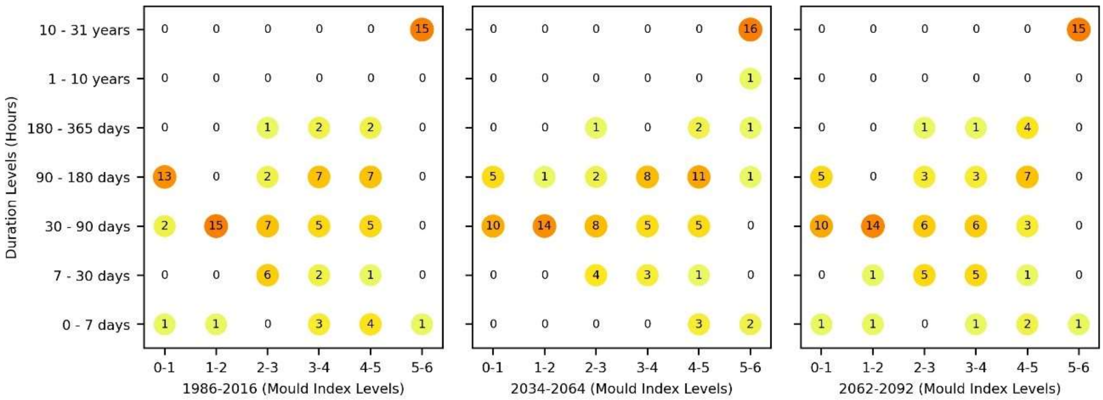

Halifax_Function% Moisture Load

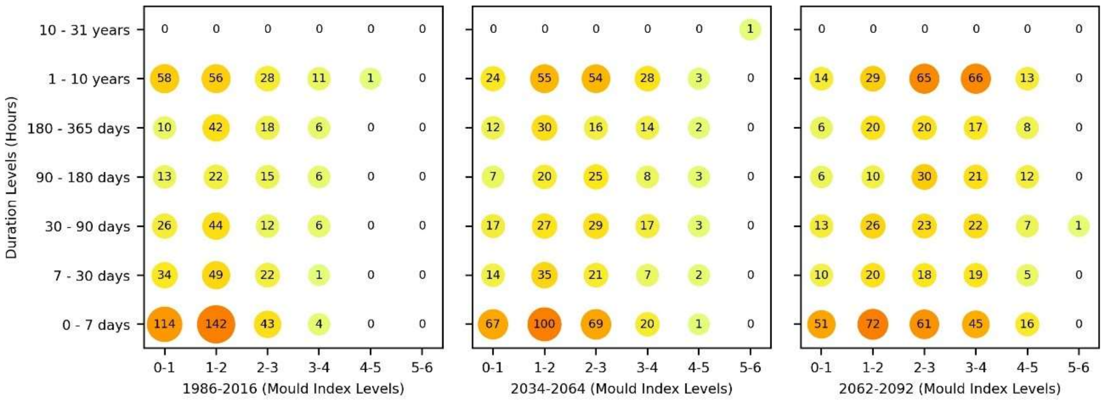

Moncton_1% Moisture Load

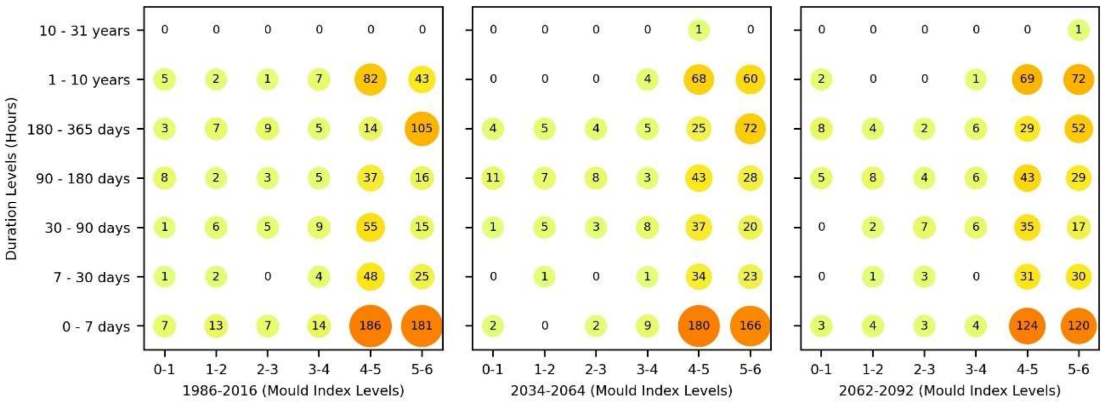

Moncton_Function% Moisture Load

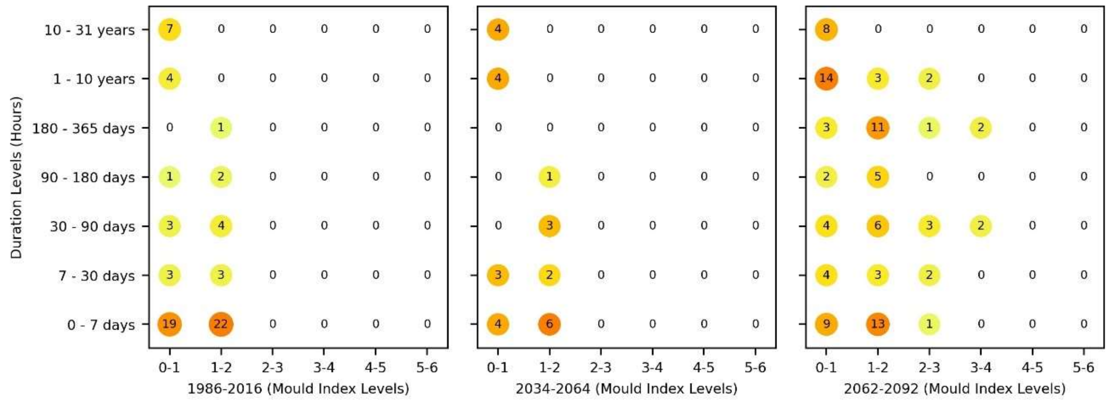

Montreal_1% Moisture Load

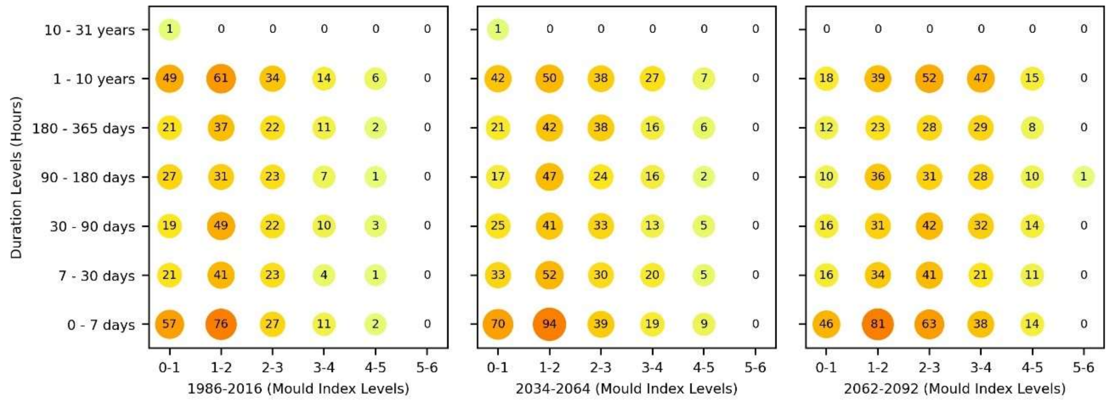

Montreal_Function% Moisture Load

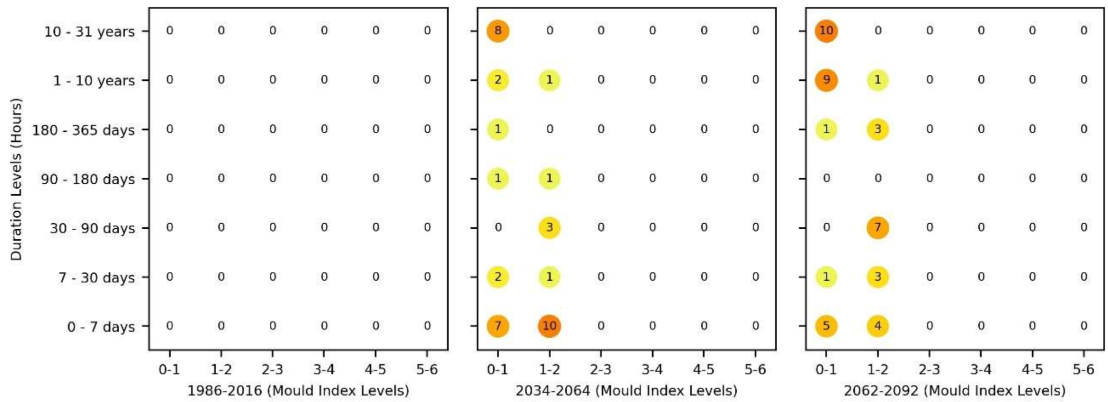

Ottawa_1% Moisture Load

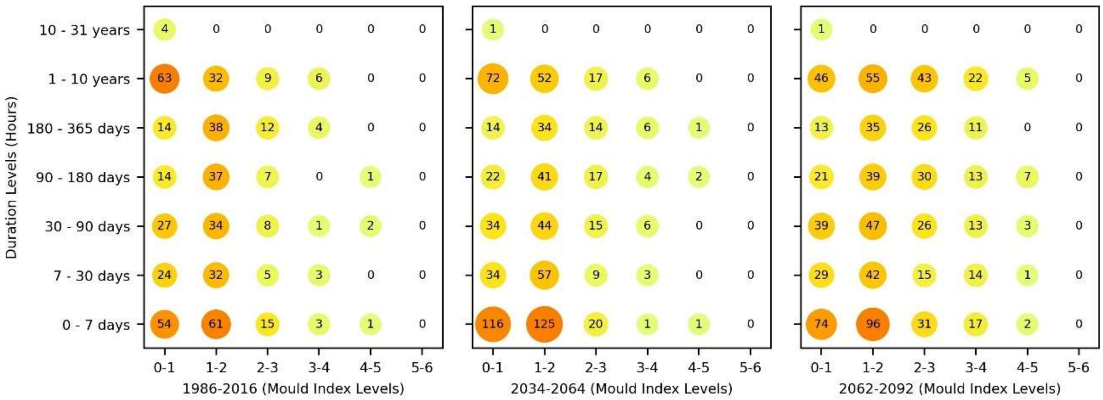

Ottawa_Function% Moisture Load

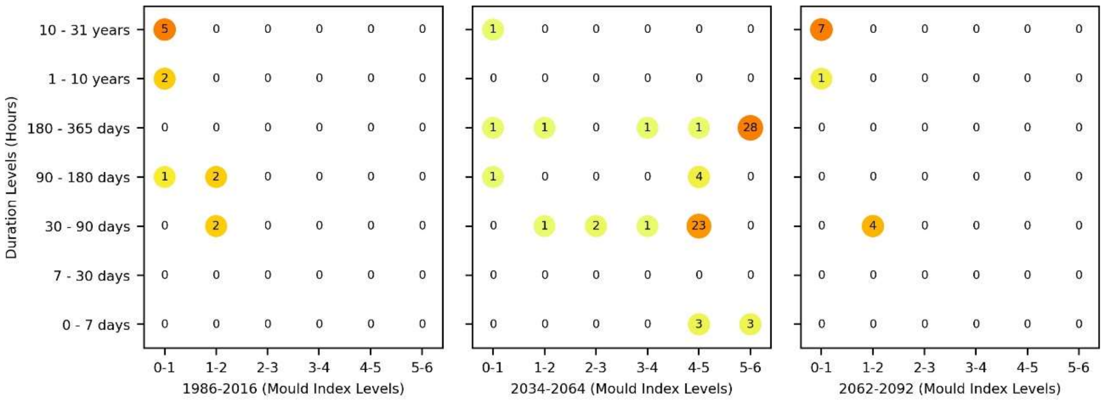

Saskatoon_1% Moisture Load

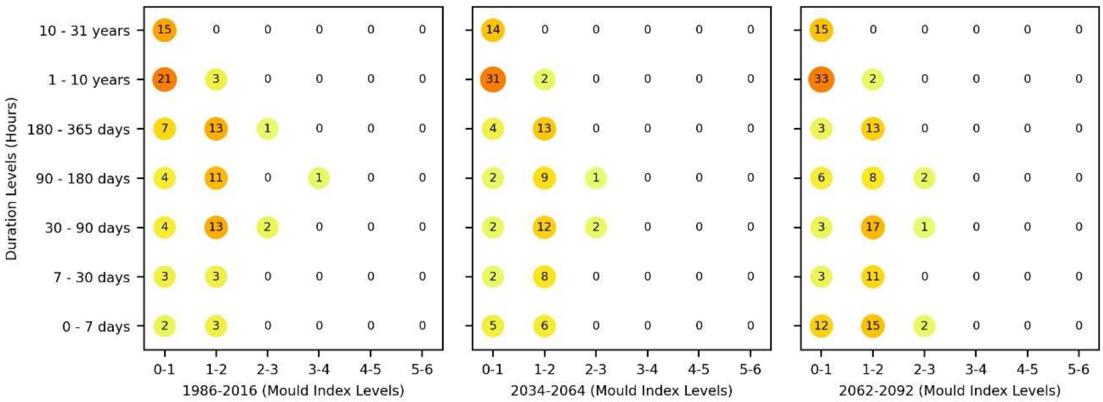

Saskatoon_Function% Moisture Load

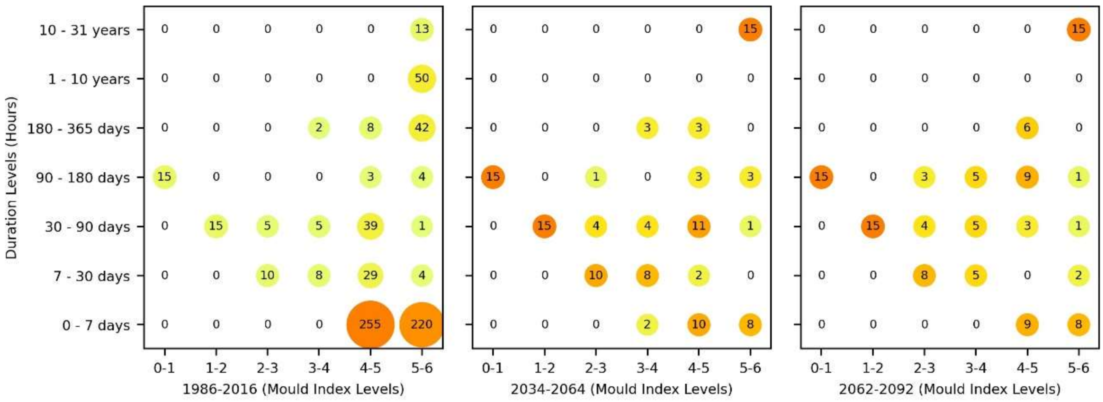

St. John's_1% Moisture Load

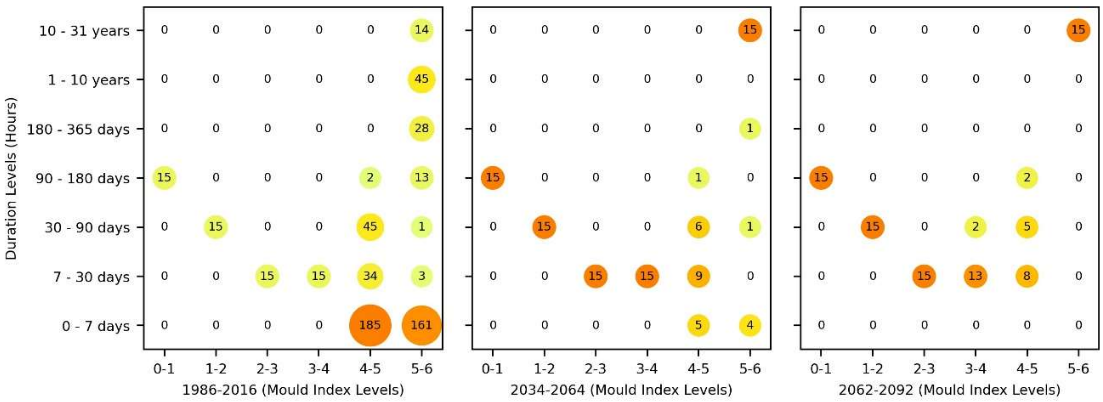

St. John's_Function% Moisture Load

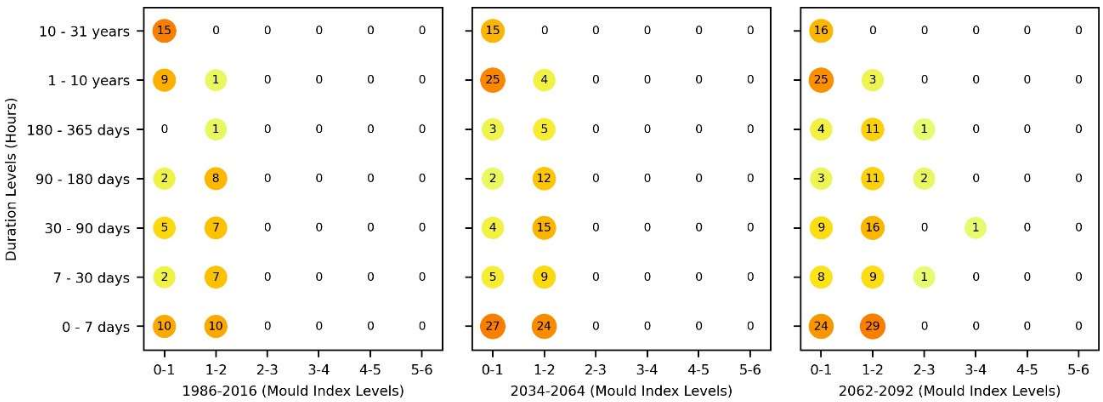

Toronto_1% Moisture Load

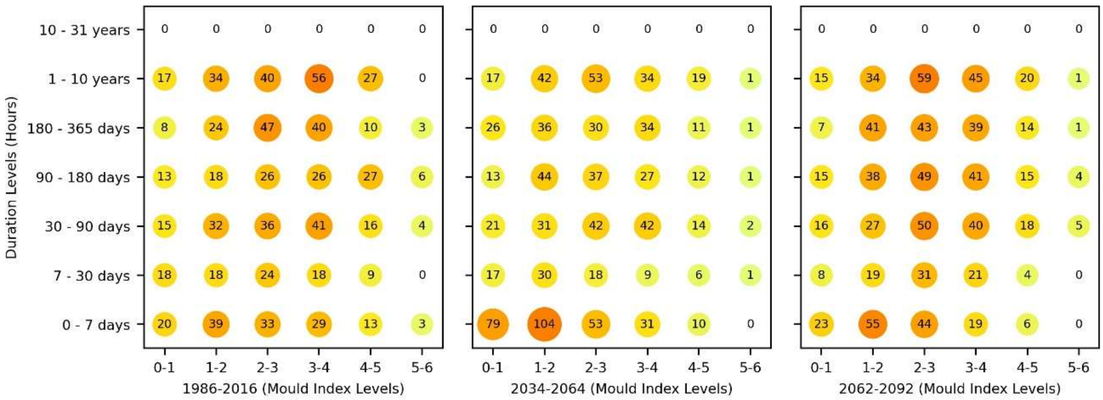

Toronto_Function% Moisture Load

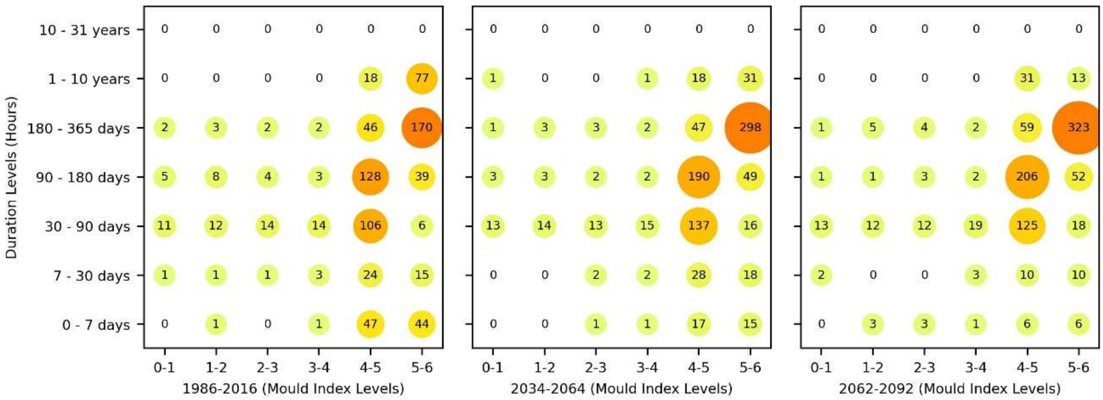

Vancouver_1% Moisture Load

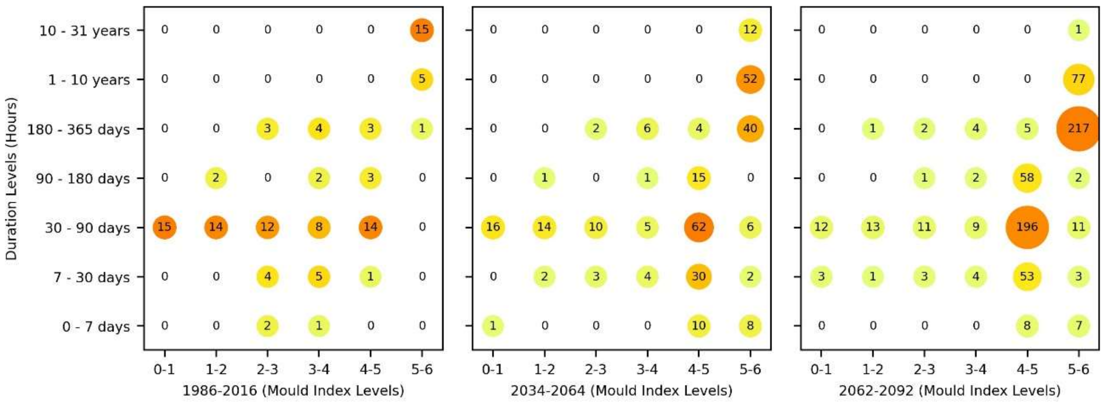

Vancouver_Function% Moisture Load

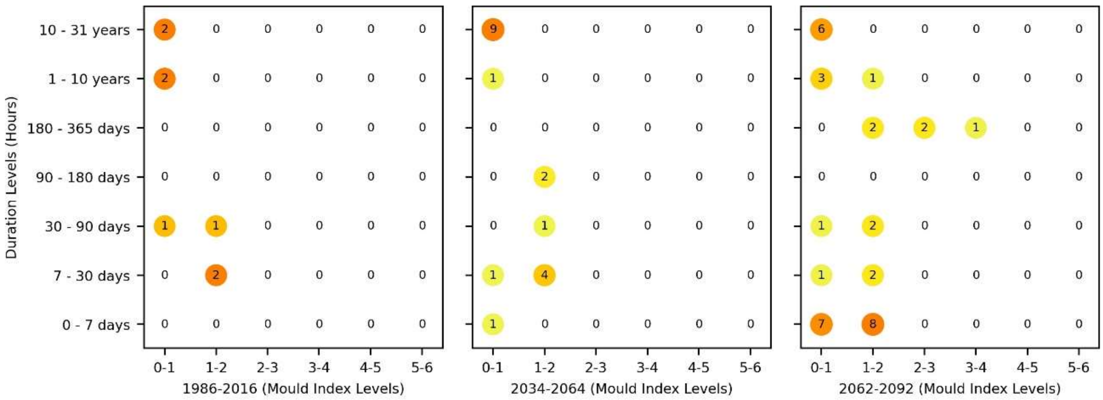

Winnipeg_1% Moisture Load

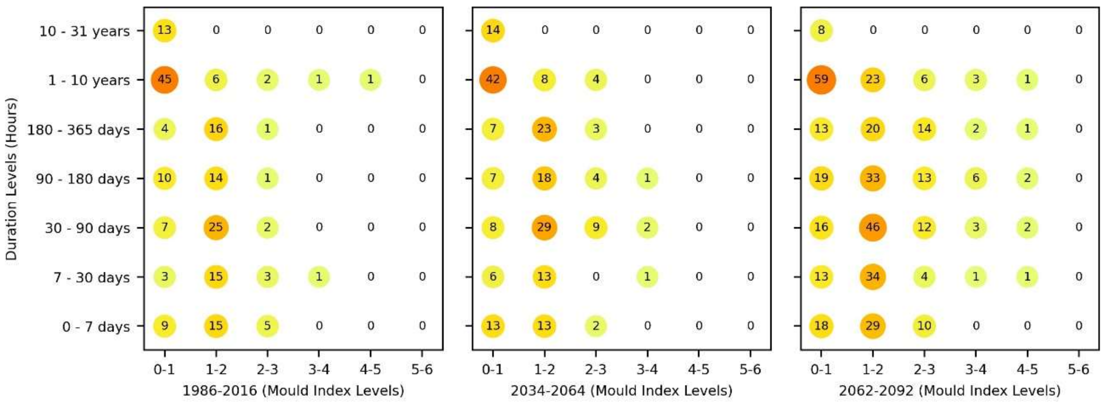

Winnipeg_Function% Moisture Load

Figure 5.9 Frequencies of events with different durations and mould index levels for the vinyl-clad wall assembly in each city.

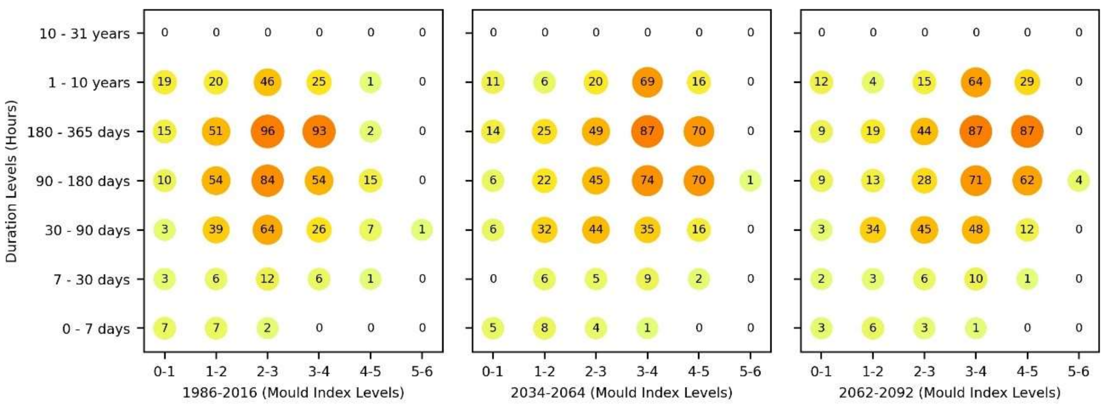

Calgary_1% Moisture Load

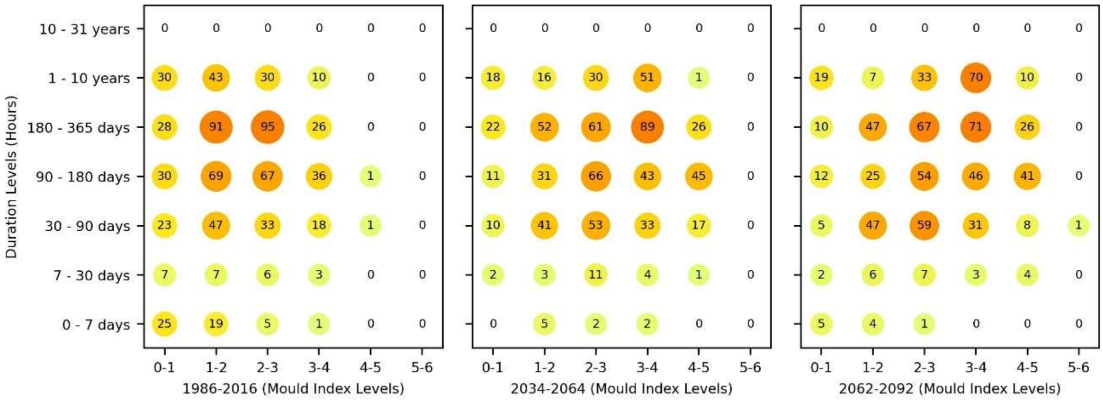

Calgary_Function% Moisture Load

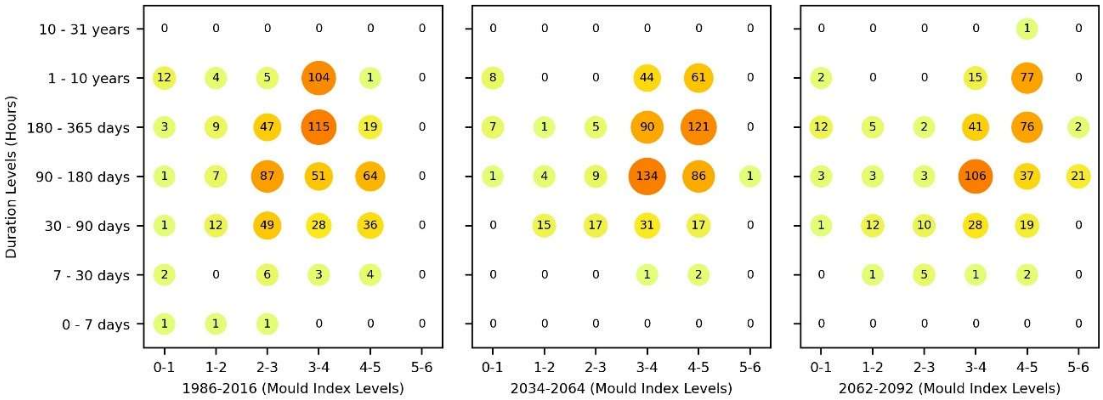

Charlottetown_1% Moisture Load

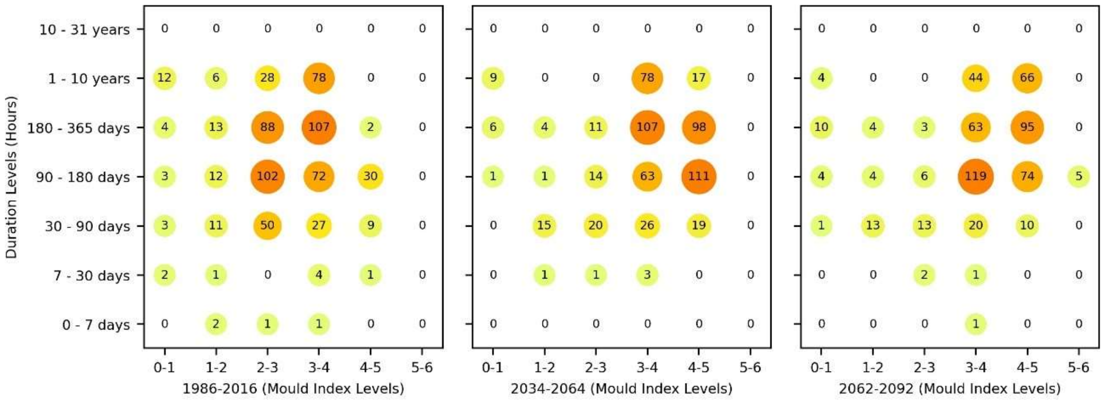

Charlottetown_Function% Moisture Load

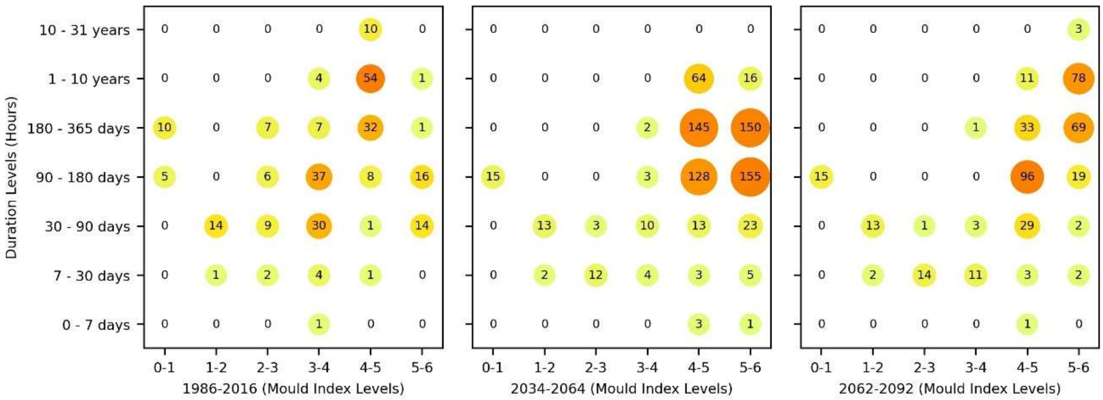

Halifax_1% Moisture Load

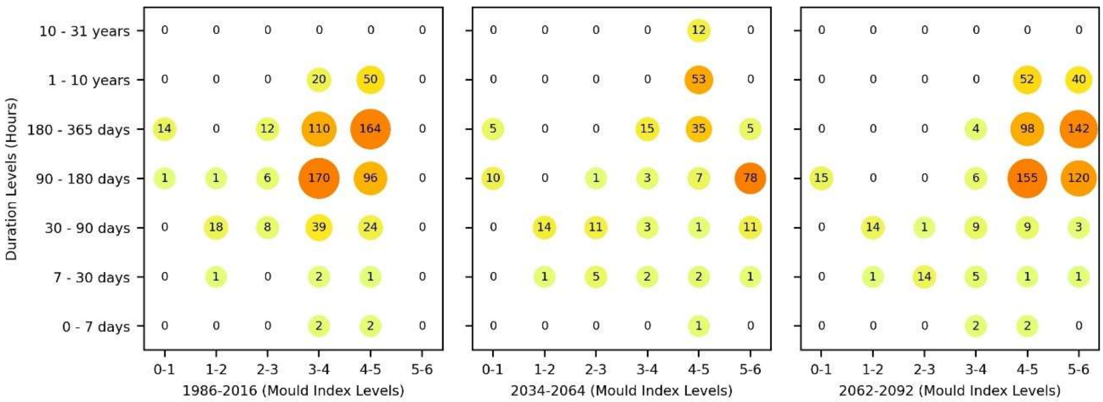

Halifax_Function% Moisture Load

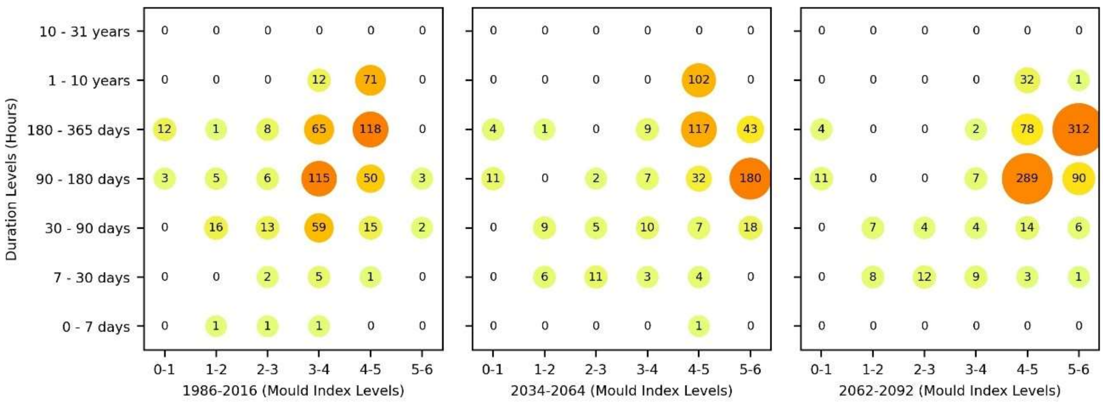

Moncton_1% Moisture Load

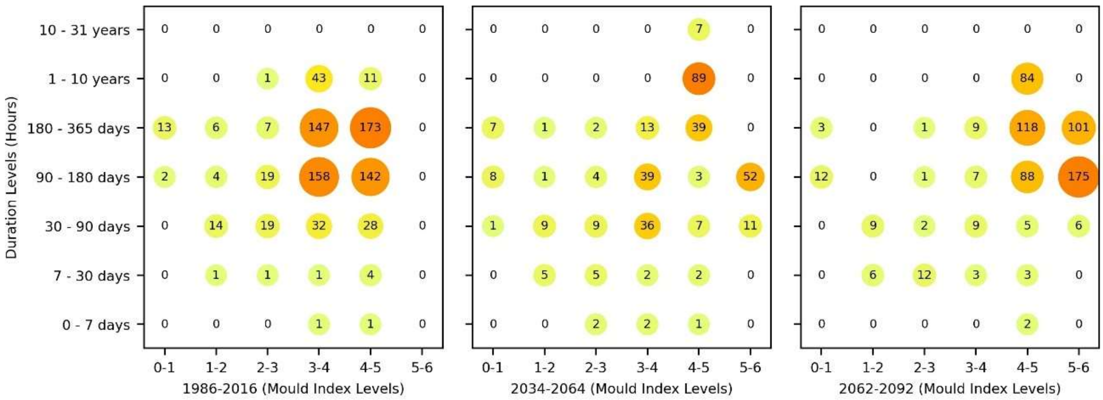

Moncton_Function% Moisture Load

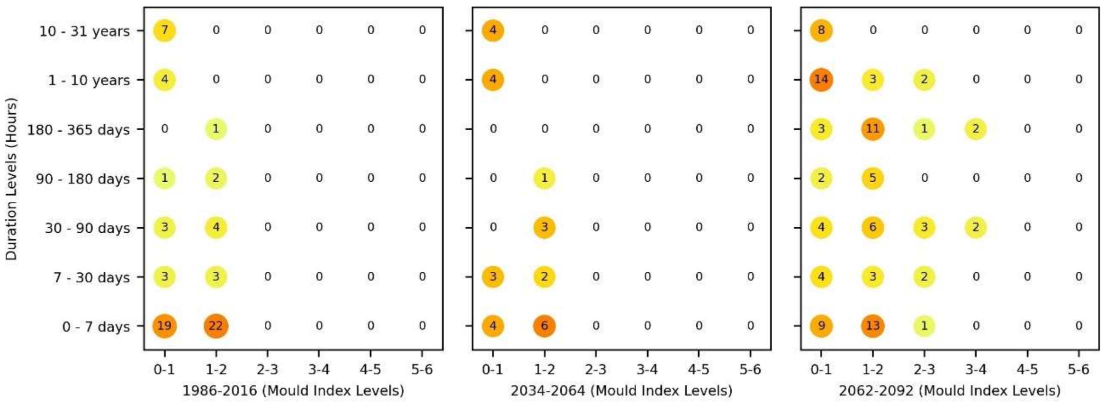

Montreal_1% Moisture Load

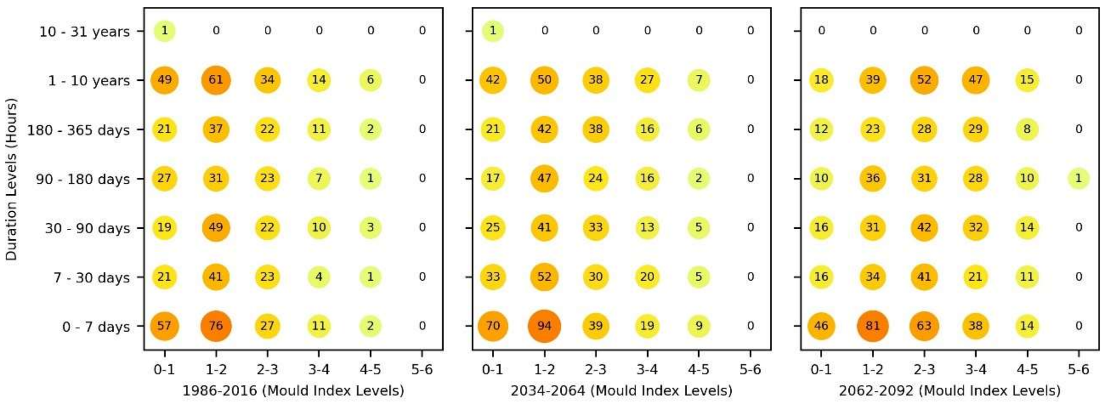

Montreal_Function% Moisture Load

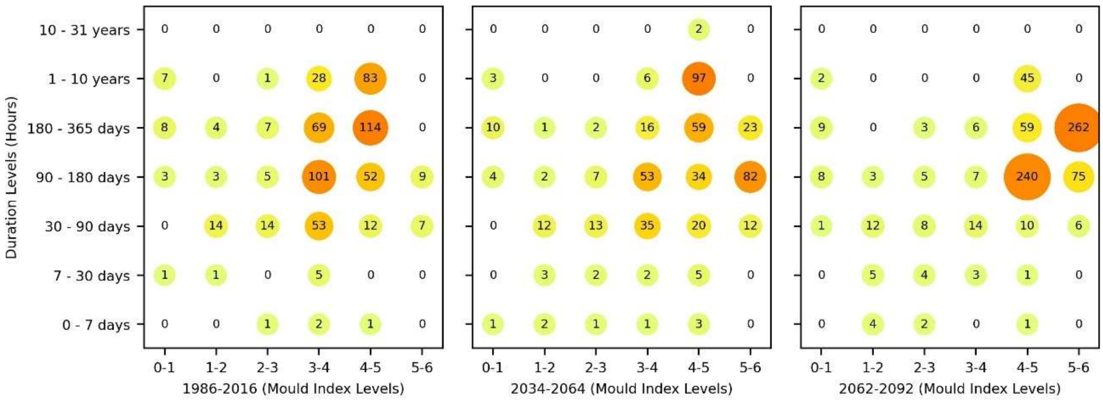

Ottawa_1% Moisture Load

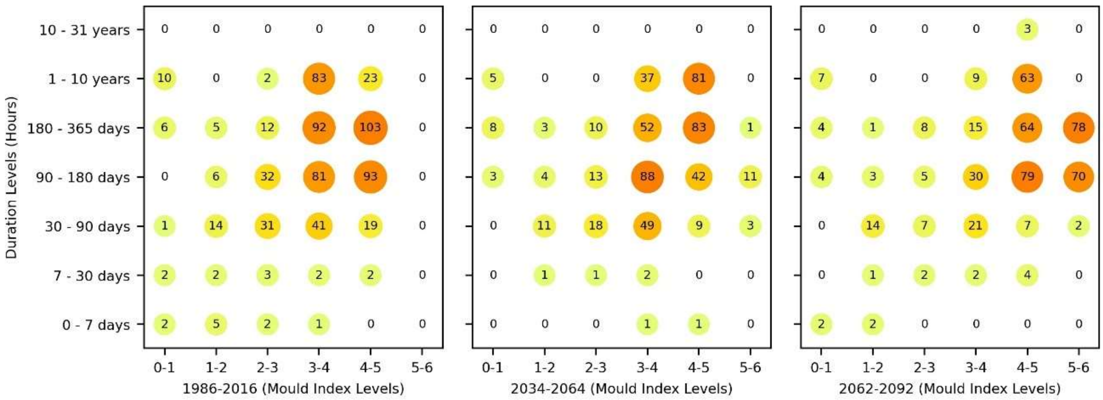

Ottawa_Function% Moisture Load

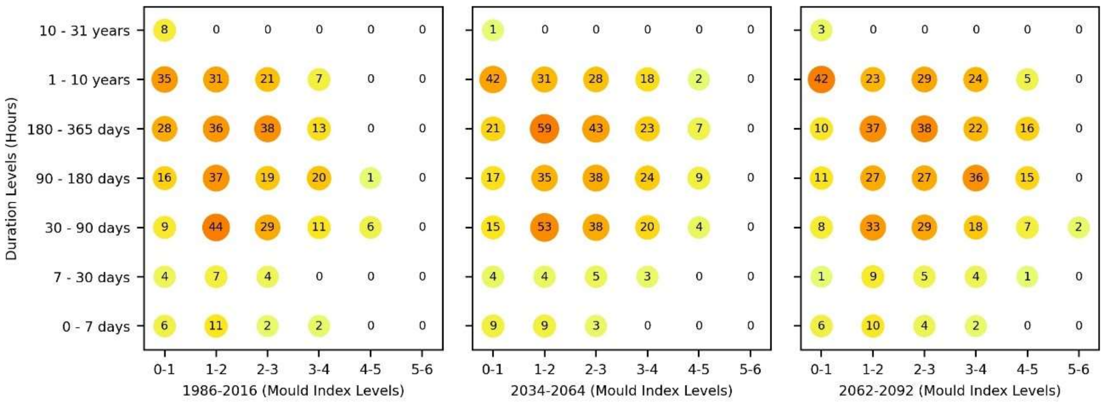

Saskatoon_1% Moisture Load

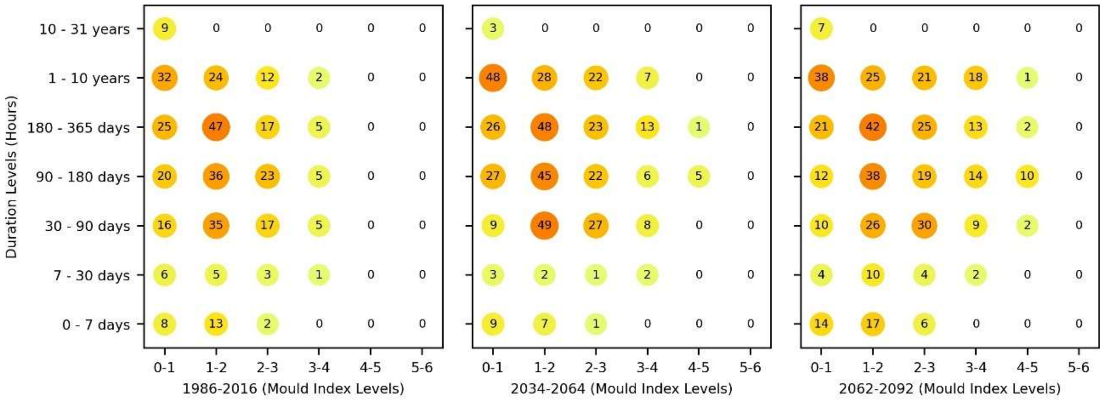

Saskatoon_Function% Moisture Load

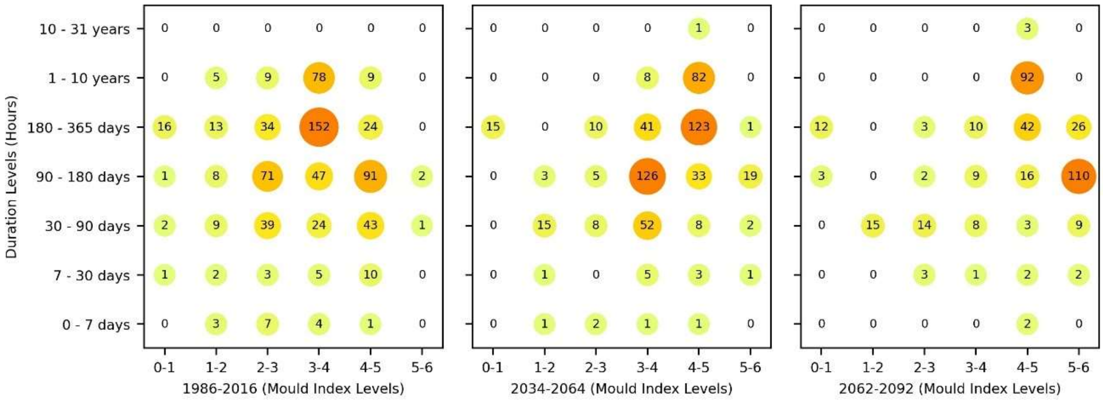

St. John's_1% Moisture Load

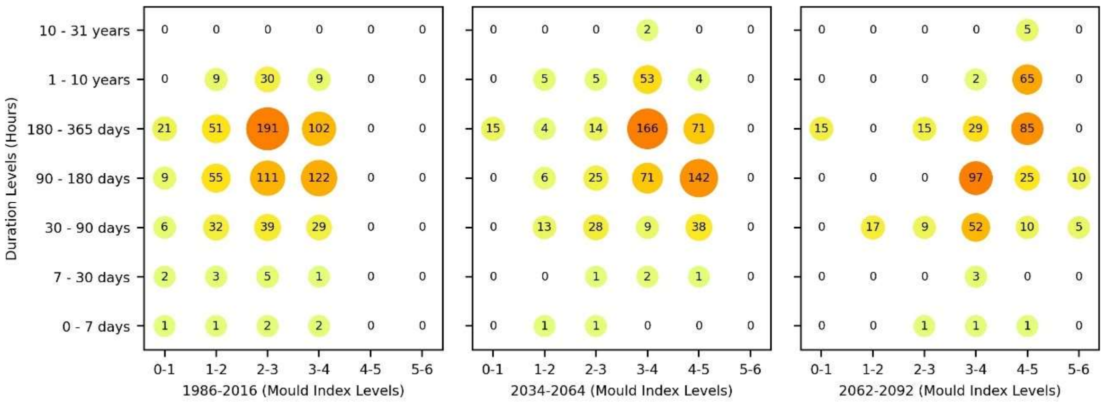

St. John's_Function% Moisture Load

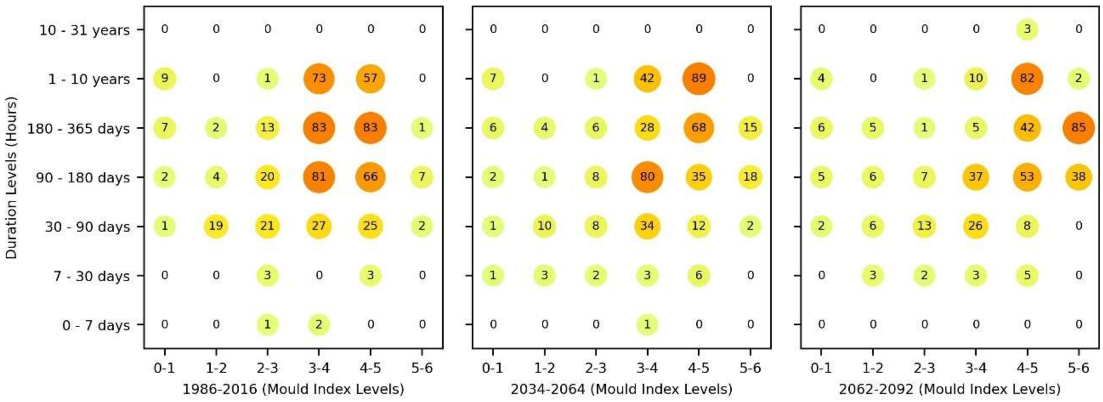

Toronto_1% Moisture Load

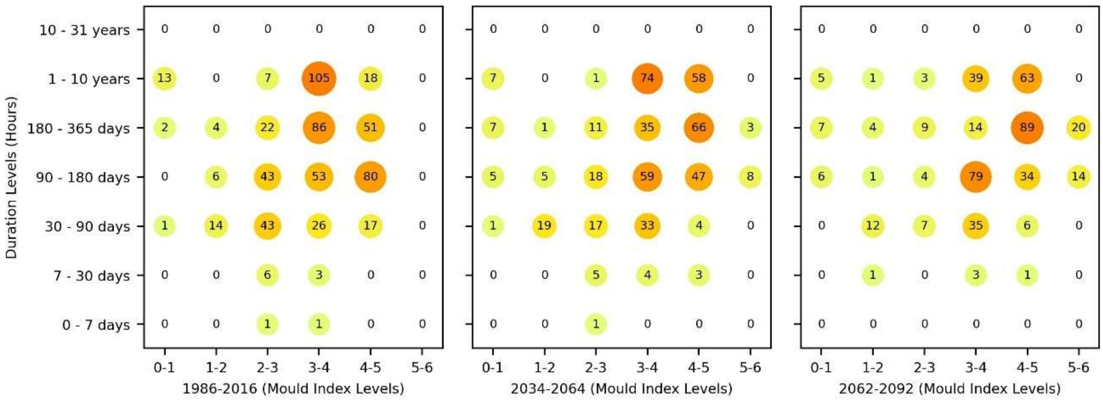

Toronto_Function% Moisture Load

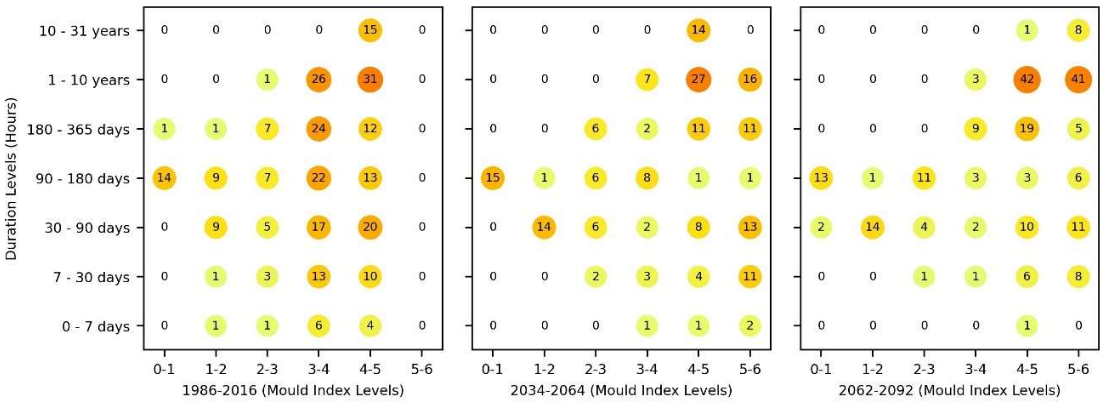

Vancouver_1% Moisture Load

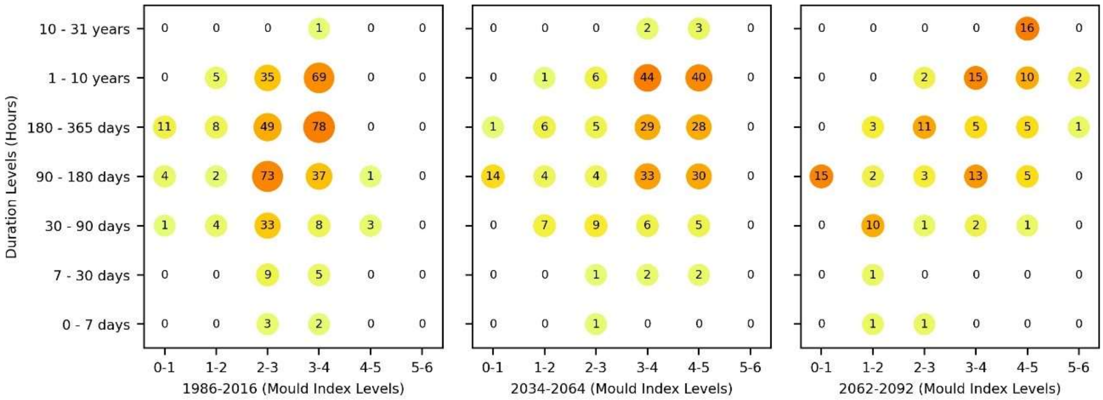

Vancouver_Function% Moisture Load

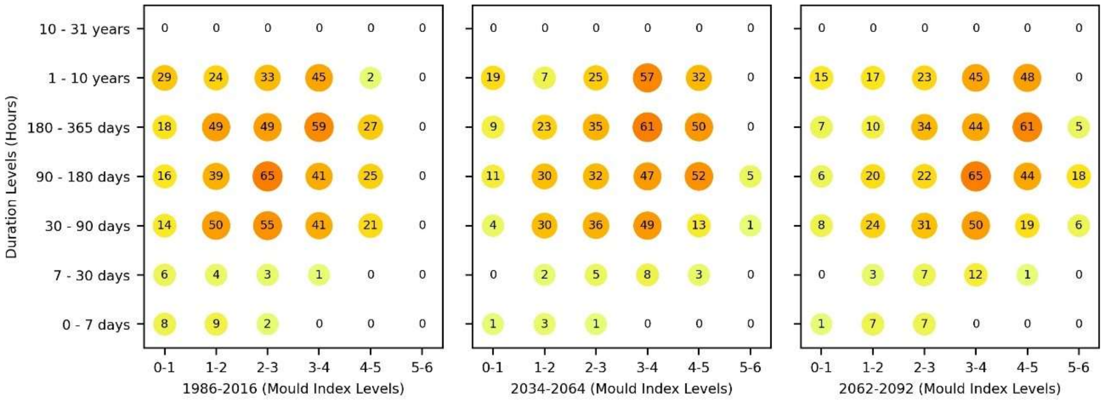

Winnipeg_1% Moisture Load

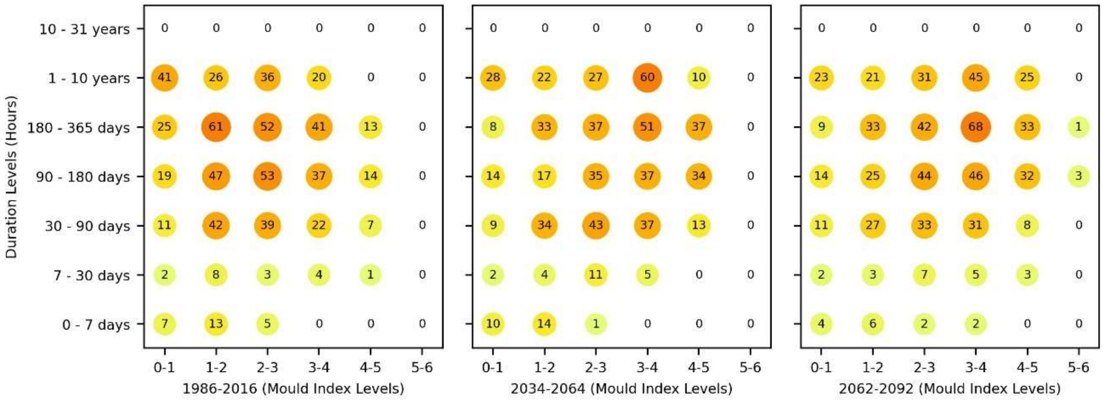

Winnipeg_Function% Moisture Load

Figure 5.10 Frequencies of events with different durations and mould index levels for the brick veneer-clad wall assembly in each city.

5.1.5 Conclusions

In this study the moisture performance of a brick veneer and of a vinyl-clad brick veneer wall assembly were investigated through the use of HAM simulations in which the walls had been subjected to a moisture load equivalent to 1% of the WDR load, as well as, a moisture load derived from the water entry functions established from the results of the watertightness tests performed. The simulations were conducted for 11 major Canadian cities using historical (1986 – 2016) as well as two future projected time periods (2034 – 2064, 2062 – 2092). The temperature during the two projected time periods was predicted to increase by 2.0°C and by 3.5°C, respectively. Moreover, each time period had 15 realizations of climate data generated by the climate model. The two types of wall assemblies were modelled and the moisture loads as well as other necessary climatic parameters were implemented in the hygrothermal simulations to obtain hygrothermal parameters for the different layers of the wall assembly. The values for relative humidity and the temperature at the exterior surface of the OSB were used to generate values for the mould growth index which was selected as the criterion for the performance assessment of both wall assemblies. Discussions in this study were made for 31-year average values of temperature, relative humidity, and mould growth index. In addition, the frequencies and durations for different levels of mould index for each city during the different time periods were also investigated.

It has been found that the average temperature over 31-years at the exterior surface of the OSB increased with the temperature increase predicted for the projected time periods investigated. It was also noted that during the same time period, the temperature in the brick veneer wall assembly was higher than the one for the vinyl-clad wall assembly located on the west coast (Vancouver) and for the centrally located cities of: Calgary, Saskatoon, and Winnipeg. Whereas, the average temperature in the brick veneer wall assembly was similar to, or slightly higher than, that of the vinyl-clad wall assembly for the remaining locations analyzed eastern inland (i.e. Toronto, Ottawa, Montreal), as well as, for cities located on the east coast (i.e. Moncton, Halifax, Charlottetown and St. John's). The temperature variation between different realizations of climate data were very small, which indicated a low level of uncertainty in temperature for the future projected time periods.

The results further showed that the average relative humidity in the vinyl-clad wall assembly decreased for all the analyzed cities during future projected time periods whereas the relative humidity for the brick veneer wall assembly increased. The relative humidity for the vinyl-clad wall assembly in cities located on the west (i.e. Vancouver) and on the east coast of Canada (i.e. Moncton, Halifax, Charlottetown and St. John's) was higher than that obtained for cites in other regions of Canada. For the brick veneer wall assembly, the relative humidity for inland cities in the east (i.e. Toronto, Ottawa and Montreal) was at the same level as that of the coastal cities. Great uncertainties in the relative humidity were observed between climate data of different realizations for cities located in the central region of Canada (i.e. Calgary, Saskatoon, and Winnipeg). The moisture load in the wall assemblies had direct impact on the level of average relative humidity. However, the correlations between the magnitude of the average moisture load and the magnitude of the average relative humidity were moderate for the vinyl-clad wall assembly, and were weak for the brick veneer wall assembly.

The mould growth index was calculated from the hourly temperature and hourly relative humidity. The average mould index in both the vinyl-clad wall assembly and brick veneer wall assembly increased for all the cities during the future projected time periods. For the vinyl-clad wall assembly, the extent of changes for various regions were entirely different. The greatest changes were found for the eastern inland cities (i.e. Toronto, Ottawa and Montreal) and two east coast cities. As for the brick veneer wall assembly, the extent of changes in the average mould index were uniform for all the cities. The input of the moisture load significantly affected the levels of average mould indices. The greatest uncertainties between climate data of different realizations were also observed for the cities located in central Canadian regions (i.e. Calgary, Saskatoon and Winnipeg). The correlations between the average moisture load and the average mould index were similar to those determined between the average moisture load and the average relative humidity, in which the correlation was moderate for the vinyl-clad wall assembly and weak for the brick veneer wall assembly.

The time history of the mould index during a 31- year period was divided into individual events. The frequencies of these events with designated mould index levels and durations were counted and summarized in a bubble matrix. The mould index was categorized in 6 levels by the amount of mould on the surface of materials, however by the duration this was classified into 7 levels from 0 to 7 days to 10 to 31 years. For most of the cities investigated, frequencies of events with higher mould index levels and longer durations in both the vinyl-clad and brick veneer wall assemblies increased during the future projected time periods, except for those in Calgary. The type of input of moisture load as used in this study (i.e. 1 % of WDR and value derived from water entry function), significantly affected the resulting level of mould index, durations and frequencies of the events. Thus, it is crucial to provide a reliable input for moisture load to help ensure reasonably accurate performance assessment of wall assemblies.

Limitations and future applications – based on the information obtained from this study, performance or changes of performance of wall assemblies evaluated for climate conditions in different regions of Canada were evaluated. The assessment of hygrothermal parameters in wall assemblies may not be sufficiently accurate to be representative of the real hygrothermal conditions in actual wall assemblies. However, from the attempts carried out in this study, the tendency of changes regarding the moisture performance of wall assemblies, as determined using a mould growth index, during the projected time periods could be estimated. Consequently, control measures that target improving or maintaining the long-term performance of wall assemblies, as well as mitigating the effects induced by climate change in the future, could be developed or quantified. The subsequent work of this study may include investigating performance of other elements in wall assemblies, as well as other types of wall assemblies, during the future projected time periods. Also, other performance criteria will be explored to describe more comprehensively the effects of the predicted climate change to the moisture performance of wall assembly over the long-term and the risk to a reduced service life.

5.1.6 References

Abdul Hamid, A., & Wallentén, P. (2017). Hygrothermal assessment of internally added thermal insulation on external brick walls in Swedish multifamily buildings. *Building and Environment*, *123*, 351–362. https://doi.org/10.1016/j.buildenv.2017.05.019

Abuku, M., Janssen, H., & Roels, S. (2009). Impact of wind-driven rain on historic brick wall buildings in a moderately cold and humid climate: Numerical analyses of mould growth risk, indoor climate and energy consumption. *Energy and Buildings*, *41*(1), 101–110. https://doi.org/10.1016/j.enbuild.2008.07.011

ASHRAE. (2016). ASHRAE standard 160P-criteria for moisture control design analysis in buildings. In *ASHRAE Transactions*.

Burch, D. M., Thomas, W. C., Mathena, L. R., Licitra, B. A., & Ward, D. B. (1989). Transient Heat and Moisture Transfer in Multi- Layer, Non-Isothermal Walls—

Comparison of Predicted and Measured Results. *Proceedings of Thermal Performance of the Exterior Envelopes of Buildings IV*, 513–531.

Charola, A. E., & Lazzarini, L. (1986). Deterioration of Brick Masonry Caused by Acid Rain. In *ACS Symposium Series* (pp. 250–258). https://doi.org/10.1021/bk-1986-0318.ch017

Chouinard, K. L., & Lawton, M. D. (2001). Rotting wood framed apartments-Not just a Vancouver problem. *Proc of the 8th Canadian Conference on Building Science and Technology*, 304–318.

Cunningham, M. J. (1990a). Modelling of moisture transfer in structures—I. A description of a finite-difference nodal model. *Building and Environment*, *25*(1), 55–61. https://doi.org/10.1016/0360-1323(90)90041-O

Cunningham, M. J. (1990b). Modelling of moisture transfer in structures—II. A comparison of a numerical model, an analytical model and some experimental results. *Building and Environment*, *25*(2), 85–94. https://doi.org/10.1016/0360-1323(90)90019-N

Defo, M., Lacasse, M., & Laouadi, A. (2021). A comparison of hygrothermal simulation results derived from four simulation tools. *Journal of Building Physics*, 174425912098876. https://doi.org/10.1177/1744259120988760

Delgado, J. M. P. Q., Barreira, E., Ramos, N. M. M., & de Freitas, V. P. (2013). *Hygrothermal Numerical Simulation Tools Applied to Building Physics*. Springer Berlin Heidelberg. https://doi.org/10.1007/978-3-642-35003-0

Delgado, J. M. P. Q., Ramos, N. M. M., Barreira, E., & De Freitas, V. P. (2010). A critical review of hygrothermal models used in porous building materials. *Journal of Porous Media*, *13*(3), 221–234. https://doi.org/10.1615/JPorMedia.v13.i3.30

Finch, G., & Straube, J. (2007). Ventilated wall claddings: Review, field performance, and hygrothermal modeling. *Thermal Performance of the Exterior Envelopes of Whole Buildings*.

Franke, L., Schumann, I., van Hees, R. P. J., van der Klugt, L., Naldini, S., Binda, L., Baronio, G., Van Balen, K., & Mateus, J. (1998). Damage Atlas: Classification and Analyses of Damage Patterns Found in Brick Masonry. In *Protection and Conservation of European Cultural Heritage, Research Report No. 8, Volume 2*. Fraunhofer IRB Verlag.

Frasca, F., Verticchio, E., Cornaro, C., & Siani, A. M. (2021). Performance assessment of hygrothermal modelling for diagnostics and conservation in an Italian historical church. *Building and Environment*, *193*, 107672. https://doi.org/10.1016/j.buildenv.2021.107672

Hens, H. (1996). *Final report task 1: Modelling common exercises. Summary reports. Annex 24, heat and moisture transfer in insulated envelope parts*. International Energy Agency.

Jensen, N. F., Bjarløv, S. P., Rode, C., & Møller, E. B. (2020). Hygrothermal assessment of four insulation systems for interior retrofitting of solid masonry walls through calibrated numerical simulations. *Building and Environment*, *180*, 107031. https://doi.org/10.1016/j.buildenv.2020.107031

Karagiozis, A., & Solonvaara, M. (1994). Moisture Transport in Building Envelopes Using an Approximate Factorization Solution Method. *CFD Society of Canada Meeting*.

Kerestecioglu, A., Swami, M., Fairey, P., Gu, L., & Chandra, S. (1989). Modelling Heat Moisture and Contaminant Transport in Buildings: Toward a New Generation Software. *Professional Paper FSEC-PF-165-89, Florida Solar Energy Center*.
Kohonen, R. (1984). Transient analysis of the thermal and moisture physical behaviour of building constructions. *Building and Environment*, *19*(1), 1–11. https://doi.org/10.1016/0360-1323(84)90008-8
Kuhn, D. M., & Ghannoum, M. A. (2003). Indoor Mould, Toxigenic Fungi, and Stachybotrys chartarum : Infectious Disease Perspective. *Clinical Microbiology Reviews*, *16*(1), 144–172. https://doi.org/10.1128/CMR.16.1.144-172.2003
Kumaran, K., Lackey, J., Normandin, N., Van Reenen, D., & Tariku, F. (2002). *Summary report from task 3 of MEWS project at the Institute for Research in Construction - Hygrothermal properties of several building materials. Report IRC-RR-110*.
Kumaran, M. (2006). A thermal and moisture property database for common building and insulation materials. *Ashrae Transactions*, 485–497.
Langmans, J., Desta, T. Z., Alderweireldt, L., & Roels, S. (2016). Field study on the air change rate behind residential rainscreen cladding systems: A parameter analysis. *Building and Environment*, *95*, 1–12. https://doi.org/10.1016/j.buildenv.2015.09.012
National Standard of Canada. (2019). *CSA S478:19 Durability in buildings*. CSA Group.
Nicolai, A., Grunewald, J., & Zhang, J. J. (2007). Recent improvements in HAM simulation tools: Delphin 5 / CHAMPS-BES. *Conference Proceedings of 12th Symposium of Building Physics*.
Ojanen, T., & Kohonen, R. (1989). Hygrothermal Influence of Air Convection in Wall Structures. *Proceedings of Thermal Performance of the Exterior Envelopes of Buildings IV*, 234–242.
Ojanen, T., Viitanen, H., Peuhkuri, R., Lähdesmäki, K., Vinha, J., & Salminen, K. (2010). Mould growth modeling of building structures using sensitivity classes of materials. *Thermal Performance of the Exterior Envelopes of Whole Buildings - 11th International Conference*.
Pedersen, C. R. (1989). MATCH—A Computer Program for Transient Calculation of Combined Heat and Moisture Transfer. *Contribution to CIB-40 Meeting*.
Pedersen, C. R. (1992). Prediction of moisture transfer in building constructions. *Building and Environment*, *27*(3), 387–397. https://doi.org/10.1016/0360-1323(92)90038-Q
Shi, X., & Burnett, E. (2007). Ventilation drying in enclosure walls with vinyl cladding. *Thermal Performance of the Exterior Envelopes of Whole Buildings*.
Simpson, Y. (2010). *Field evaluation of ventilation wetting and drying of rainscreen walls in coastal British Columbia*. Concordia University. Montreal, Canada.
Straube, J., & Burnett, E. F. P. (2001). Overview of hygrothermal (HAM) analysis methods. *ASTM Moisture Control Manual*, 81–89.
Tang, W., Davidson, C. I., Finger, S., & Vance, K. (2004). Erosion of limestone building surfaces caused by wind-driven rain: 1. Field measurements. *Atmospheric Environment*, *38*(33), 5589–5599. https://doi.org/10.1016/j.atmosenv.2004.06.030
Van Balen, K. (1996). Expert system for evaluation of deterioration of ancient brick masonry structures. *Science of The Total Environment*, *189–190*, 247–254. https://doi.org/10.1016/0048-9697(96)05215-1
Van Straaten, R. (2004). *Measurement of ventilation and drying of vinyl siding and brick clad wall assemblies*. Master's Thesis. University of Waterloo. Waterloo, Canada.

Vandemeulebroucke, I., Defo, M., Lacasse, M. A., Caluwaerts, S., & Van Den Bossche, N. (2021). Canadian initial-condition climate ensemble: Hygrothermal simulation on wood-stud and retrofitted historical masonry. *Building and Environment*, *187*, 107318. https://doi.org/10.1016/j.buildenv.2020.107318

Wang, L., & Ge, H. (2017). Effect of air leakage on the hygrothermal performance of highly insulated wood frame walls: Comparison of air leakage modelling methods. *Building and Environment*, *123*, 363–377. https://doi.org/10.1016/j.buildenv.2017.07.012

Wang, R., Ge, H., & Baril, D. (2020). Moisture-safe attic design in extremely cold climate: Hygrothermal simulations. *Building and Environment*, *182*, 107166. https://doi.org/10.1016/j.buildenv.2020.107166

5.2 Decay of wood components

Abstract: The performance of wall assemblies is closely related to the water entry and WDR which create internal moisture. The extended exposure to moisture will determine different degrees of decay for the wood components of wall assemblies. The current study investigated the mass loss during the decay of various wood components, and decay intensity indexes were determined for one historical climatic data set (1986-2016) and two predicted climatic data time periods (2034-2064 and 2062-2092), using the VTT wood decay model. A severity index ratio was proposed based on the relative humidity severity index and temperature severity index; these were quantified as the accumulative above threshold values of relative humidity and temperature, respectively, which would trigger the wood decay. Thereafter, this study investigated the averaged annual decay intensity and annual decay durations for each time period analyzed. The severity of the decay, which was the product of the annual decay intensity and the annual decay duration, for different wall assemblies located in different cities analyzed, were discussed and concluded in this section.

The integrity of wood members is a prerequisite to ensure complete functionality, as well as, performance of a wall assembly. The wood members provide structural support to resist loads applied to the wall assembly, and backing for the functional elements, such as the water resistive barrier and drainage components. When wood materials are exposed for prolonged period of time to persistent moisture and a temperate favorable to the growth of wood decaying fungi, mass loss to wood members can occur. This could become a significant issue, given that the loss in strength of wood materials is positively correlated with mass loss (Wilcox, 1978). Such phenomenon may not be very intense, nor produce noticeable consequence over a relatively short period of time. However, over the long term, the presence of decay would definitely compromise the durability of the wood structure and consequently undermine the overall performance of the wall assembly. Moreover, poor moisture performance could also result in a greater degree of exposure to an environment conductive to the decay of wood elements and thereby initiate a continuous cycle of degradation.

The extent of decay in wood materials can be estimated using numerical models developed based on a comprehensive set of experimental data (Saito, 2017; H. Viitanen et al., 2010; H. A. Viitanen, 1997; Hannu Viitanen, 1996). Temperature and relative humidity, as well as time, are the parameters of importance for these numerical models. The VTT wood decay model (H. Viitanen et al., 2010) considers wood decay in 2 stages: the initial stage of decay and, thereafter, the mass loss stage. During the initial decay stage, the wood material would be exposed to different levels of relative humidity and temperature for sufficient duration to favour the onset of the stage 2. An indicator to determine this stage is coefficient α (Eq. 5.7 – 5.9), which ranges in value from 0 to 1. When the value of α is less than 1, the decay process is in stage 1; otherwise, the decay process is in stage 2. When the ambient environment has changed from a favourable to an unfavorable condition, the value of coefficient α would gradually decrease. The rate of hourly mass loss in stage 2 is described by Eq. (5.10).

$$\alpha(t) = \int_0^t d\alpha = \sum_0^t (\Delta\alpha) \tag{5.7}$$

$$\Delta\alpha = \begin{cases} \dfrac{\Delta t}{t_{crit}(RH,T)}, if\ T > 0°C\ and\ RH > 95\% \\ \dfrac{\Delta t}{17520}, otherwise \end{cases} \tag{5.8}$$

$$t_{crit}(RH,T) = (\frac{2.3T + 0.035RH - 0.024T \cdot RH}{-42.9 + 0.14T + 0.45RH})[h] \tag{5.9}$$

$$\frac{ML(RH,T)}{dt} = -5.96 \cdot 10^{-2} + 1.96 \cdot 10^{-4}T + 6.25 \cdot 10^{-4}RH[\%/h] \tag{5.10}$$

Where RH is the relative humidity and T is the temperature.

The Japanese wood decay model (Saito, 2017) has been developed using the same strategy as that used to develop the VTT model. Temperature, relative humidity and exposure time are factors that determine the mass loss of wood materials. However, the Japanese decay model neglects the initial stage of decay and the temperature is considered as the only factor to determine the severity of decay.

In this study, only stage 2 of the VTT model has been used to determine the level of decay of OSB in assessing the moisture performance of wall assemblies in consideration of the following: (i) It is difficult to estimate the degree of exposure of wood materials to temperature and relative humidity conditions favourable to the onset of decay prior to construction. Stage 1 of the decay may already have occurred before the materials are placed in service; (ii) the current numerical model employed for estimating the initial stage of decay has not been validated. Hypothetical parameters were used to derive the value of coefficient α, which is the indicator to determine the decay stage; (iii) if estimating the time for the onset of the initial stage becomes valid in the future, it can be easily incorporated to any subsequent analyses. The values for relative humidity and temperature were obtained from the hygrothermal simulation described in previous sections of this chapter.

5.2.1 Decay severity index

According to Eq. 10, the mass loss of wood materials, due to decay, is positively correlated with the values of temperature and relative humidity when they are both above threshold values. To permit assessing the relative importance of temperature and relative humidity to mass loss of wood elements in wall assemblies for different locations in Canada, a temperature severity index, a relative humidity severity index, as well as an integrated severity index were proposed in this study, where the integrated severity index is equal to the root sum square of these two former severity indices (Eq. 5.11). The temperature and relative humidity severity indices were defined as the areas beneath a time series plots above the threshold values when both parameters attained favourable conditions for wood decay, as shown in Figure 5.11.

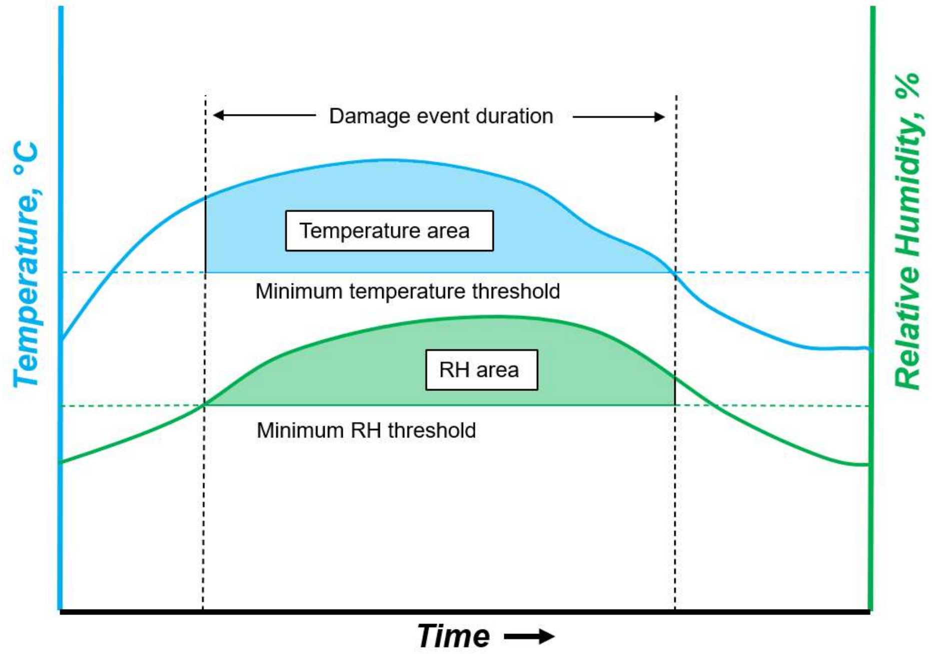

Figure 5.11 The value of the severity index for each parameter is the area of the time series plot above the threshold.

$$Severity\ Index = \sqrt[2]{Temperature\ Severity\ Index^2 + RH\ Severity\ Index^2} \qquad (5.11)$$

The magnitudes of temperature and relative humidity usually have different values ranges. Therefore, the area obtained from the plot for each parameter must be normalized to become comparable. According to CSA standard (CSA S478:19, 2019) on the Durability in buildings, the service life for a typical wall assembly in Canada is 50 years. If 100% mass loss within 50 years is considered as a benchmark criterion, then for each year, such a criterion is a 2% mass loss. Thereafter, the dimensionless parameter to normalize the temperature parameter was considered as the value of area for temperature that could cause 2% mass loss each year, while the relative humidity had a constant threshold value of 95%. Similarly, the dimensionless parameter to normalize the area for relative humidity was the value of area for relative humidity that could cause 2% mass loss each year with a constant temperature threshold value of 0°C. Hence, the parameter to normalize the relative humidity was 6,351 and the parameter to normalize the temperature had a value of 20,260.

The 31-year summation of relative humidity severity indices and their ratios to the temperature severity indices of the vinyl wall assembly using 1% of WDR as the moisture load, in selected cities for different time periods are shown in Figure 5.12, Figure 5.13, and Figure 5.14. The horizontal axis of each plot represents the relative humidity severity index (RH severity index) in log scale and the vertical axis of the plots represents the ratio between the relative humidity severity index and the temperature severity index. Markers with different colors represent corresponding indices for different cities. Each city has 15 realizations of 31-year data; thus, each color has 15 markers. When the ratio of the relative humidity severity index to the temperature severity index is above 1, the decay process is more affected by the relative humidity severity index and vice versa. For all three analyzed time periods, most realizations for the cities of: Vancouver, Halifax, Charlottetown, and St. John's, had a ratio of the two indices greater than 1. These four cities are located in the coastal region of Canada and their relative humidity severity indices were also greater than those of all other cities. Moncton, as another coastal city, had greater relative humidity severity indices than other inland cities. The relative humidity indices for inland cities had a similar range of values. The broad variation in values of severity index ratio for inland cities indicated a large uncertainty within the temperature and relative humidity for the projected time periods. With a temperature increase for the projected time periods, the ratios of the relative humidity to the temperature severity indices decreased for the projected time periods for all cities. Whereas, the relative humidity severity indices increased for the same projected time periods. The decrease in the ratio and the increase in the relative humidity severity index suggested a greater increase in the temperature severity index for future time periods.

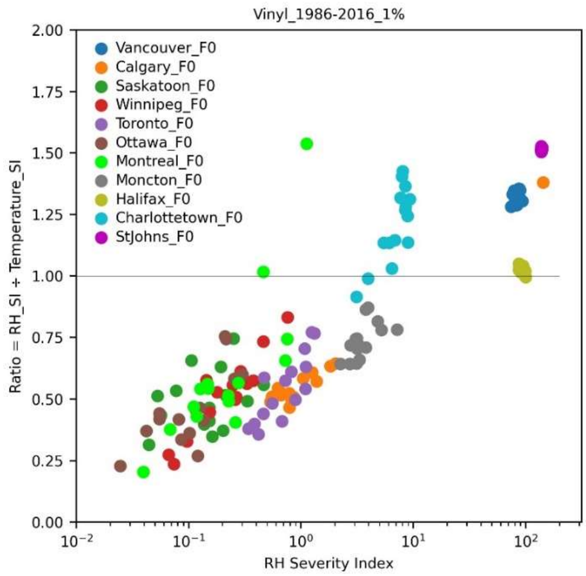

Figure 5.12 Relative humidity severity indices and ratios of relative humidity severity indices to temperature severity indices of vinyl wall assembly using 1% of WDR as moisture load for the historic time period 1986-2016.

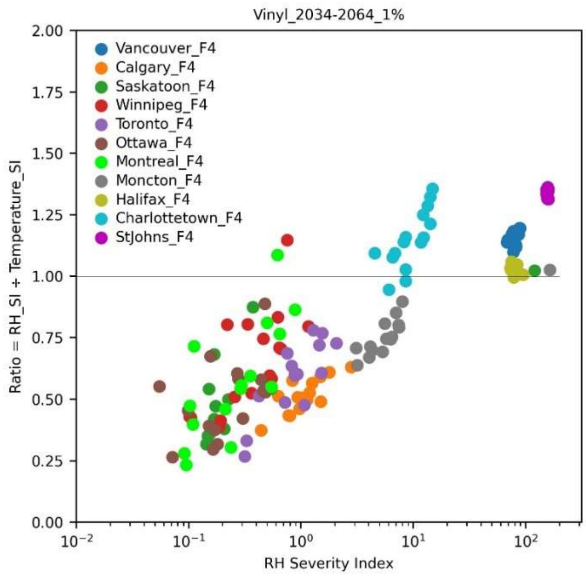

Figure 5.13 Relative humidity severity indices and ratios of relative humidity severity indices to temperature severity indices of vinyl wall assembly using 1% of WDR as moisture load for the projected time period 2034-2064.

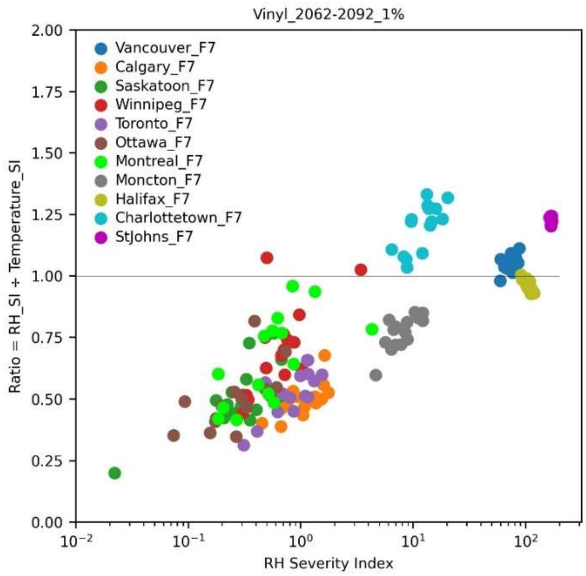

Figure 5.14 Relative humidity severity indices and ratios of relative humidity severity indices to temperature severity indices of vinyl wall assembly using 1% of WDR as moisture load for the projected time period 2062-2092.

The severity indices for vinyl wall assemblies using the moisture load calculated from the water entry functions (section 4.4.2) are shown in Figure 5.15, Figure 5.16, and Figure 5.17. When comparing these results to those cases using 1% of WDR load as the moisture load, the relative humidity severity indices and the ratio of the two indices increased for all cities, due to a greater moisture load obtained from the water entry functions. The relative humidity severity indices for the projected future time periods had not changed much from the historical time periods. The ratios of the two indices decreased slightly for all cities except for Charlottetown due to an increase in temperature for projected future time periods. The range of values for the relative humidity severity indices and the ratios of indices obtained from different realizations for each city were more concentrated that those observed in cases using 1% of WDR load as the moisture load. A reduction in uncertainty within the data would necessarily be beneficial to any subsequent quantitative analysis.

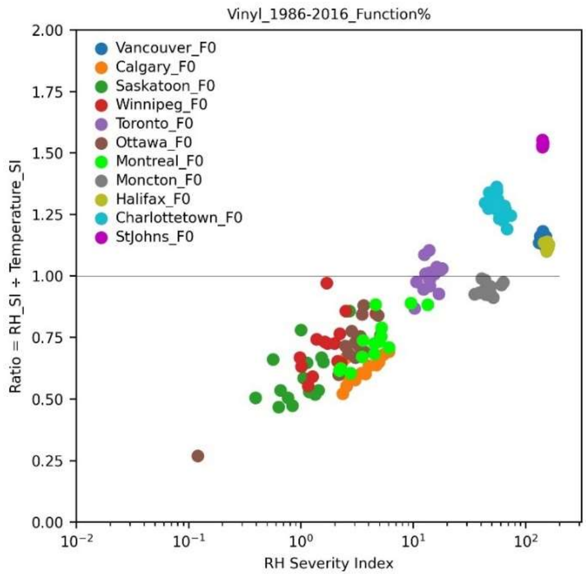

Figure 5.15 Relative humidity severity indices and ratios of relative humidity severity indices to temperature severity indices of vinyl wall assembly using moisture load calculated from water entry functions for the historic time period 1986-2016.

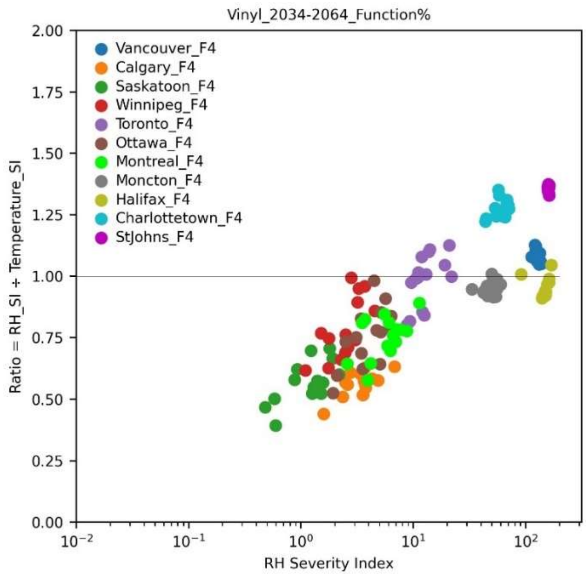

Figure 5.16 Relative humidity severity indices and ratios of relative humidity severity indices to temperature severity indices of vinyl wall assembly using moisture load calculated from water entry functions for the projected time period 2034-2064.

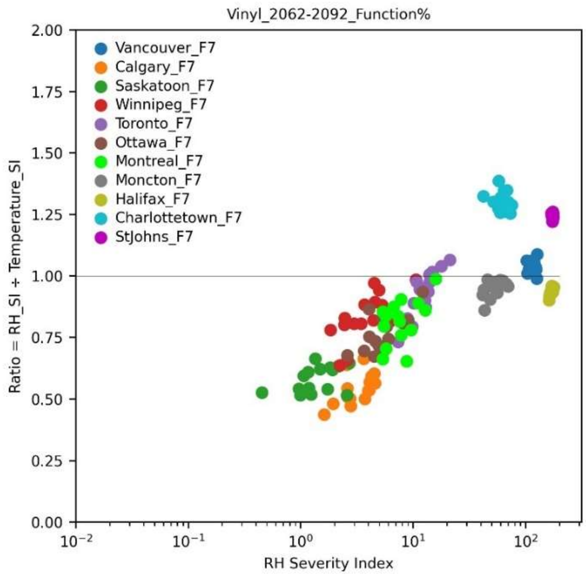

Figure 5.17 Relative humidity severity indices and ratios of relative humidity severity indices to temperature severity indices of vinyl wall assembly using moisture load calculated from water entry functions for the projected time period 2062-2092.

The severity indices for the brick wall assemblies that were analyzed, are shown in Figure 5.18 – Figure 5.23. It is obvious that the temperature was the dominant factor in determining the level of decay in brick wall assemblies regardless of the type of moisture load applied, given that most of the ratios for the relative humidity to the temperature severity indices were less than 0.5 in all cities for all time periods that were analyzed. The relative humidity severity index had increased for projected future time periods in all cities. The ratios of indices for the projected future time periods had decreased in the cities of Calgary, Saskatoon, Vancouver, and St. John's and increased in the other cities. As compared to the results obtained for the vinyl wall assembly, the relatively large values for the relative humidity severity indices were not only evident in coastal cities, but were also observed in Toronto and Montreal for the brick wall assembly. The uncertainties in the ratios of the two indices decreased with an increase in temperature for the projected future time periods. Using the 1% WDR load as the moisture load for the brick wall assembly resulted in greater values for severity indices for relative humidity than using the moisture load obtained from water entry functions.

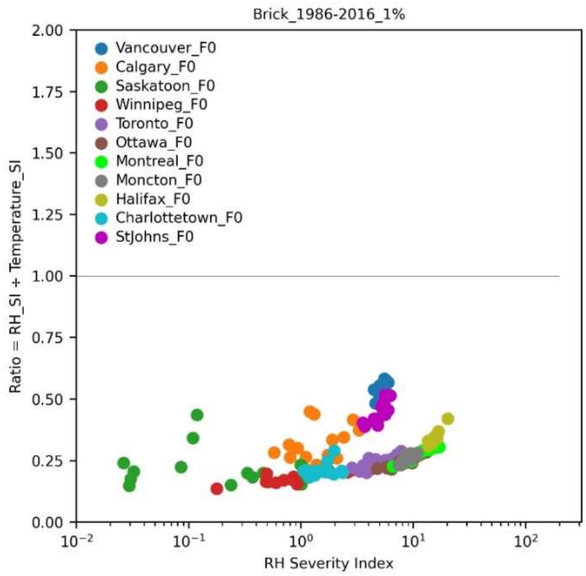

Figure 5.18 Relative humidity severity indices and ratios of relative humidity severity indices to temperature severity indices of brick wall assembly using 1% of WDR as moisture load for time period 1986-2016.

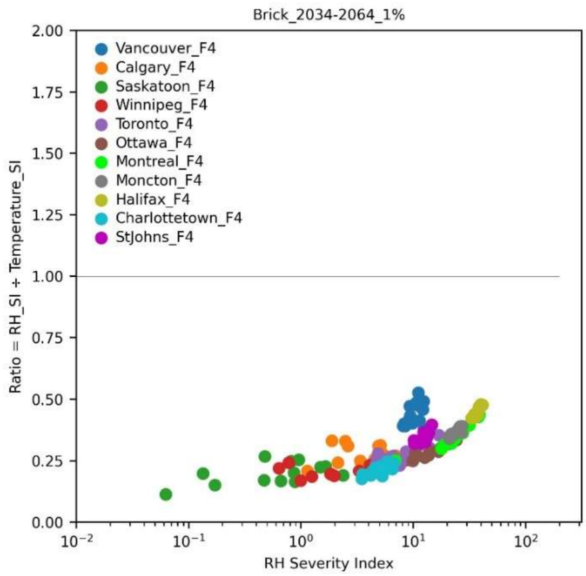

Figure 5.19 Relative humidity severity indices and ratios of relative humidity severity indices to temperature severity indices of brick wall assembly using 1% of WDR as moisture load for time period 2034-2064.

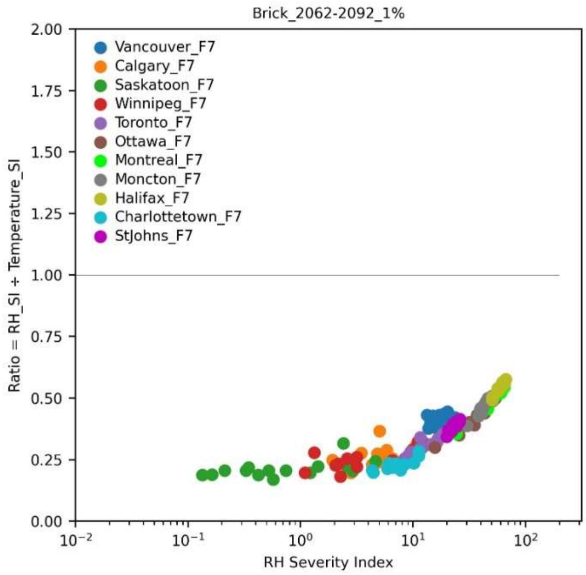

Figure 5.20 Relative humidity severity indices and ratios of relative humidity severity indices to temperature severity indices of brick wall assembly using 1% of WDR as moisture load for time period 2062-2092.

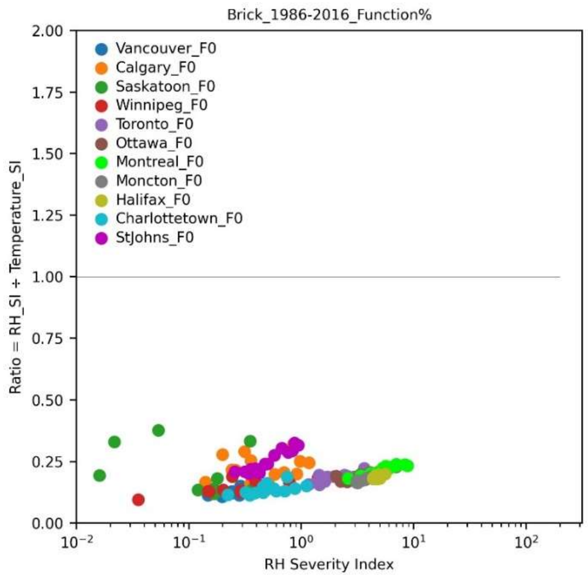

Figure 5.21 Relative humidity severity indices and ratios of relative humidity severity indices to temperature severity indices of brick wall assembly using 1% of WDR as moisture load for time period 1986-2016.

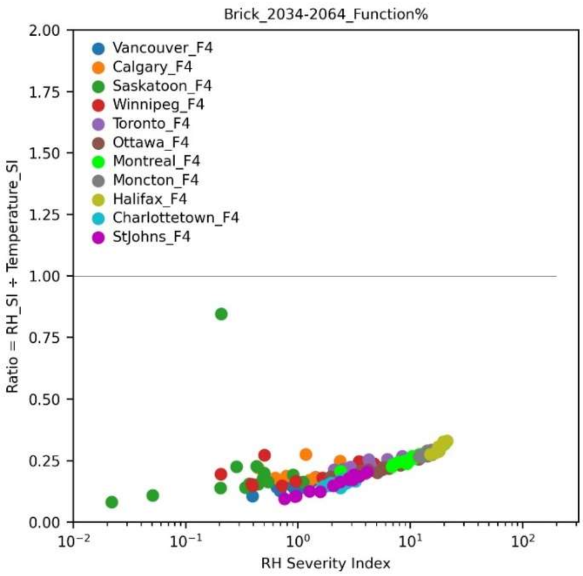

Figure 5.22 Relative humidity severity indices and ratios of relative humidity severity indices to temperature severity indices of brick wall assembly using 1% of WDR as moisture load for time period 2034-2064.

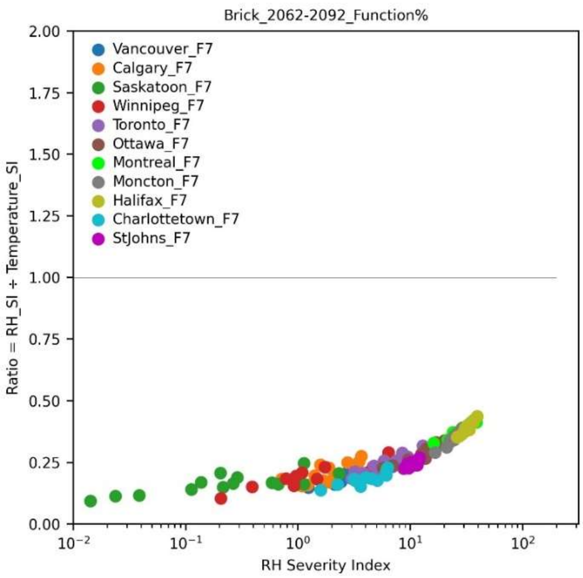

Figure 5.23 Relative humidity severity indices and ratios of relative humidity severity indices to temperature severity indices of brick wall assembly using 1% of WDR as moisture load for time period 2062-2092.

The R-squared coefficients between the mass loss (%) and the integrated severity index (Figure 5.24) for the vinyl wall assembly and the brick wall assembly were both 0.999. The very good agreement was mainly due to the linear relationship between the mass loss and the two parameters, e.g., relative humidity and temperature, in Eq. (5.10) The severity index can be used to represent the level of decay in wall assemblies.

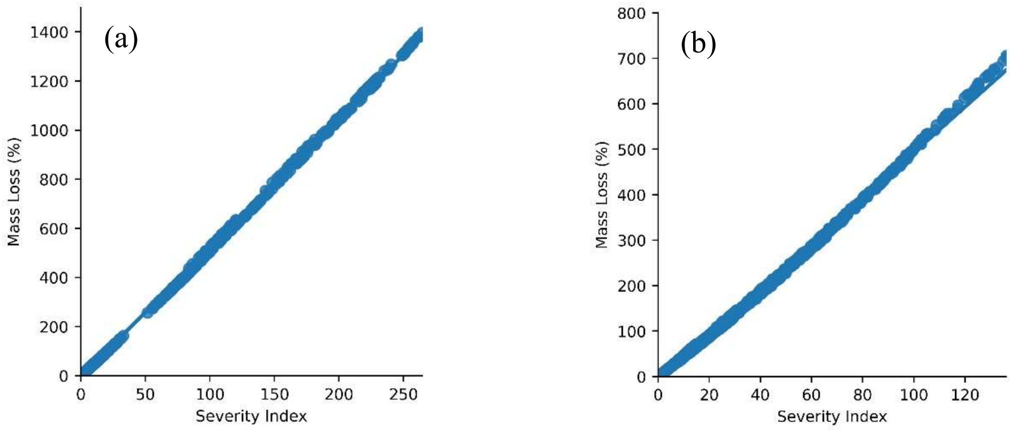

Figure 5.24 (a) Correlations between the mass loss (%) and the severity index for the vinyl wall assembly; (b) Correlations between the mass loss (%) and the severity index for the brick wall assembly.

5.2.2 Intensity and duration of decay

The climate data generated by climate models used in the hygrothermal simulations to assess the ambient relative humidity and temperature at the locations of interest in wall assemblies are inherently uncertain. The output derived from these climate data using a linear analysis is only one of many possibilities. Hence, to permit a broader application of such data, and given its degree of uncertainty, the corresponding parameters need to be analyzed from a probabilistic point of view. In terms of decay, the likelihood of occurrence of a specific decay intensity index value and the likelihood of annual durations of decay events were generated by fitting selected distributions to the histograms of these two parameters.

The decay intensity index was calculated by dividing the mass loss (%) for each hour of a given damage event by 0.000228%, this value being equal to 2% (assumed acceptable annual mass loss) divided by the number of hours in a year (i.e., 8,760 h). The hourly decay intensity index was thereafter used to establish the histogram. The duration of each damage event is illustrated in Figure 5.25. Due to the annual weather cycle, the duration of damage events for each year should be similar. Thus, the total duration of all damage events within a year was considered as one element for the histogram. Each histogram had 465 elements as it included all the data from 15 realizations, each with 31 years of data. The distributions of the decay intensity index and annual duration of decay events for different cities, had their own characteristics. It was not feasible to use a single type of distribution to fit both types of parameters for all cities and for all analyzed time periods. Thus, during the fitting process, multiple distributions were selected to fit the histograms of the decay intensity index and annual duration of decay. The Residual Sum of Squares (RSS) was used as the selecting criterion. The mean value of the best fitted distribution was considered in the subsequent analysis.

Based on the preliminary observations, the distribution shapes of decay intensity index histograms were bell-shaped and right-skewed. Hence, gamma distribution (Eq. 5.12), exponential modified Gaussian (normal) distribution (Eq. 5.13) and normal distribution (Eq. 5.14) were selected to fit the decay intensity index histograms. In terms of the annual duration of decay, other than bell-shaped and right-skewed histograms, there were also numerous J-shaped histograms. Therefore, the gamma distribution, exponential distribution (Eq. 5.15), exponential modified Gaussian (normal) distribution, Pareto distribution (Eq. 5.16), and normal distribution were selected for the fitting process.

$$f(x) = \frac{1}{\Gamma(\mathrm{k})\theta^k} x^{k-1} e^{-\frac{x}{\theta}} \tag{5.12}$$

$$f(x) = \frac{\lambda}{2} e^{\frac{\lambda}{2}(2\mu+\lambda\sigma^2-2x)} erfc(\frac{\mu + \lambda\sigma^2 - x}{\sqrt{2}\sigma}) \tag{5.13}$$

$$f(x) = \frac{1}{\sigma\sqrt{2\pi}} e^{-\frac{1}{2}\left(\frac{x-\mu}{\sigma}\right)^2} \tag{5.14}$$

$$f(x) = \lambda e^{-\lambda x} \tag{5.15}$$

$$f(x) = \frac{\alpha x_m^\alpha}{x^{\alpha+1}} \tag{5.16}$$

For the OSB in the brick wall assembly in Vancouver using 1% of the WDR as the moisture load, the histograms and the fitted distributions for the decay intensity index and annual decay duration, are illustrated in Figure 5.25. Different colors of histograms and distributions represent the data for different time periods. The best fitted distribution for each histogram and its mean values are also shown in the plot. For the hourly decay intensity index (Figure 5.25a), the Gamma distribution was the best fit distribution to the histogram of hourly decay intensity index for the historical time period 1986-2016. The histogram included all the data from 15 realizations, each with 31-year data. For the two projected future time periods, the Normal distribution was the best choice to fit the histograms. The mean values of the hourly decay intensity index were predicted to increase in the future for the brick wall in Vancouver. The histograms of durations of decay events (Figure 5.25b) had different shapes than those of hourly decay intensity index. Thus, the selected fitting distributions were also different. The Exponential Modified Gaussian (normal) distribution was fitted to the data for the historical time period and Gamma distribution was selected to fit with the data for the projected future time periods. The increment in durations of decay events in the future was much greater than the increment in decay intensity index. It almost increased 200% by the end of 21st century as compared to the historical time period 1986-2016.

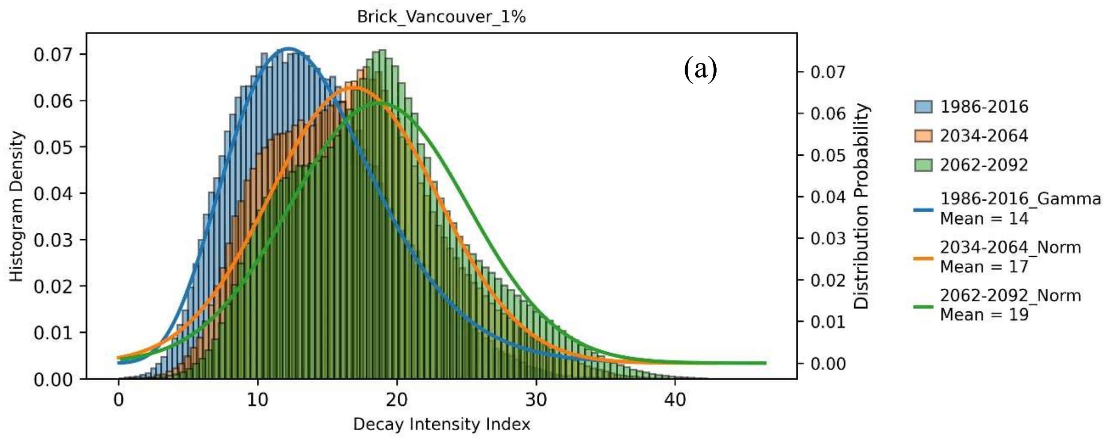

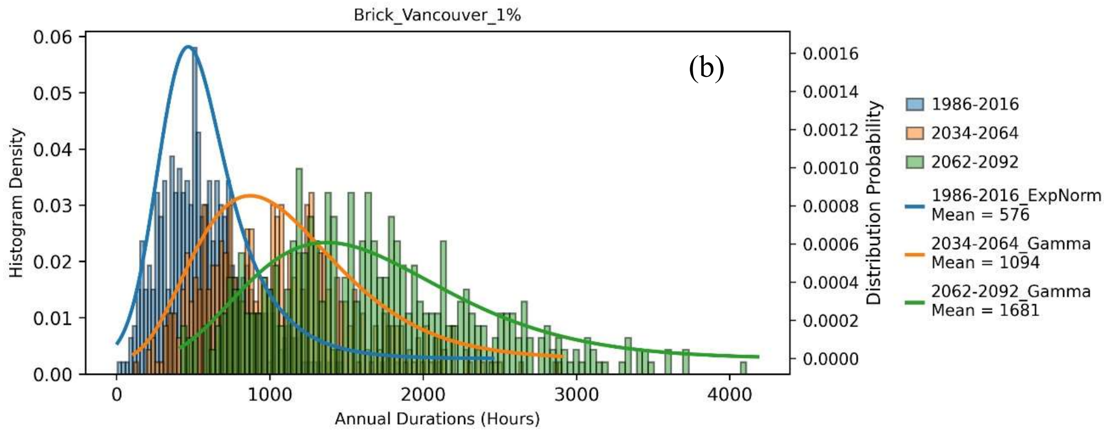

Figure 5.25 (a) Histograms and fitted distributions of hourly decay intensity index for the OSB in a brick wall in Vancouver considered 1% of the WDR as the moisture load; (b) Histograms and fitted distributions of annual decay duration for the OSB in a brick wall in Vancouver considered 1% of the WDR as the moisture load.

The histograms and fitted distributions for the wall assembly in other cities are listed in Appendix B. The mean values of hourly decay intensity index for both the brick and vinyl wall assembly in each city for different time periods are shown in Table 5-5. For the brick wall assembly, the decay intensity indices were predicted to increase for the projected future time periods regardless of the source of moisture load. The highest mean value for the decay intensity index was observed in Montreal, followed by Ottawa and thereafter, Moncton. The lowest mean value for the decay intensity index was found in Vancouver. In regards to the vinyl wall assembly, the decay intensity indices were relatively lower than those in the brick wall assembly. On the other hand, similar to the brick wall assembly, when the moisture load was derived from water entry functions, the value for the decay intensity index was greater than those obtained using 1% of the WDR as the moisture load. The decay intensity indices for the vinyl wall assembly in most cities were predicted to increase in the future. However, the level of increase was very small compared to those obtained for the brick wall assembly. The maximum increase was only ca. 10%. Higher values for the decay intensity indices were found in the coastal cities of: Halifax, St. John’s, Moncton, and Vancouver. Whereas the lowest index value was observed in Ottawa for the vinyl wall assembly. Such observations are totally different from those obtained for the brick wall assembly. Hence, different wall assemblies in different cities may be subjected to diverse decay conditions.

Table 5-5 Mean value of decay intensity index

Cities	Time Periods	Brick		Vinyl	
		1% WDR	Functions	1% WDR	Functions
Calgary (Central)	1986-2016	18.2	19.5	14.7	16.0
	2034-2064	21.1	21.9	15.5	17.2
	2062-2092	22.8	23.3	16.4	18.0
Charlottetown (East Coast)	1986-2016	17.9	19.6	10.0	16.8
	2034-2064	20.6	21.6	11.0	17.0
	2062-2092	22.7	23.3	10.9	16.7
Halifax (East Coast)	1986-2016	18.9	19.5	20.1	23.6
	2034-2064	22.4	22.7	19.8	23.7
	2062-2092	25.1	25.4	21.9	25.2
Moncton (East Coast)	1986-2016	20.6	20.9	11.0	17.3
	2034-2064	23.9	23.7	17.9	17.5
	2062-2092	26.8	26.3	12.4	18.0
Montreal (East Inland)	1986-2016	23.2	23.4	9.40	12.0
	2034-2064	26.1	25.5	9.32	11.9
	2062-2092	29.1	27.8	10.3	12.1
Ottawa (East Inland)	1986-2016	22.8	23.2	8.50	11.2
	2034-2064	25.1	24.9	9.82	11.5
	2062-2092	27.9	26.9	8.80	11.8
Saskatoon (Central)	1986-2016	20.2	21.2	12.7	14.4
	2034-2064	23.1	23.6	12.9	15.3
	2062-2092	23.9	24.5	13.9	15.3
St. John’s (East Coast)	1986-2016	15.5	15.4	21.3	21.4
	2034-2064	18.2	18.5	22.4	22.5
	2062-2092	20.3	20.8	23.2	23.4
Toronto (East Inland)	1986-2016	21.9	21	10.3	13.1
	2034-2064	23.9	24.1	10.7	13.0
	2062-2092	25.5	24.9	11.1	12.8
Vancouver (West Coast)	1986-2016	14	21	18.6	21.5
	2034-2064	16.9	23.4	19.6	22.2
	2062-2092	18.7	24	20.3	22.7
Winnipeg (Central)	1986-2016	22	23	9.77	12.6
	2034-2064	24.2	24.9	9.85	12.6
	2062-2092	25.6	25.8	10.8	13.0

The mean values for the annual duration of decay events for both wall assemblies are given in Table 5-6. For both wall assemblies, the mean values for the annual duration of decay events increased for the projected future time periods. In general, a climate scenario having higher temperatures would result in a longer annual duration, except for the cities of Calgary, Toronto and Vancouver. In Calgary, the longest duration of decay for the brick wall assembly was observed for the time period 2034-2064, when a 2.0°C temperature increase is expected. For the vinyl wall assembly, depending on the type of moisture load, the longest duration of decay events was found in time 1986-2016 and 2034-2064 periods for the cities Calgary, Toronto and Vancouver. The changes in durations of decay events for the brick wall assembly were much greater than those for the vinyl wall assembly. The types of water source would thus make an important difference in the annual duration of decay events. The longest annual duration of decay for the brick wall assembly was observed in Halifax, and the shortest annual duration of decay for that occurred in Vancouver. Meanwhile, the vinyl wall assembly in Vancouver would experience the longest decay each year compared to other cities, and the vinyl wall assembly in Saskatoon would experience the shortest decay events. It was noticed that the annual duration of decay events for the brick wall assembly and the vinyl wall assembly were quite different although they were exposed to the same environmental conditions. For instance, the brick wall assembly in Montreal would experience much longer decay events than in Vancouver, whereas, the annual duration of decay events for the vinyl wall assembly in Vancouver was roughly 20 times longer than that in Montreal considering 1% of WDR as the moisture load, and 10 times longer if the moisture load was derived from the water entry function.

Table 5-6 Mean value of annual durations (hours) of decay events

Cities	Time Periods	Brick		Vinyl	
		1% WDR	Functions	1% WDR	Functions
Calgary (Central)	1986-2016	301	167	180	447
	2034-2064	743	454	181	358
	2062-2092	690	445	179	320
Charlottetown (East Coast)	1986-2016	318	184	711	3277
	2034-2064	792	599	913	3458
	2062-2092	1004	644	1104	3583
Halifax (East Coast)	1986-2016	1725	858	4928	6848
	2034-2064	2877	1890	4371	6967
	2062-2092	3650	2465	5302	7612
Moncton (East Coast)	1986-2016	1180	711	451	3023
	2034-2064	2041	1475	596	3112
	2062-2092	2734	2048	821	3326
Montreal	1986-2016	1302	760	131	686

(East Inland)	2034-2064	1940	1125	146	640
	2062-2092	2946	2006	237	816
Ottawa (East Inland)	1986-2016	1041	743	116	507
	2034-2064	1513	824	116	477
	2062-2092	2381	1433	150	637
Saskatoon (Central)	1986-2016	190	150	99	196
	2034-2064	306	248	103	244
	2062-2092	357	280	116	268
St. John's (East Coast)	1986-2016	573	106	5897	5966
	2034-2064	1413	511	6616	6690
	2062-2092	2232	1410	7139	7247
Toronto (East Inland)	1986-2016	847	434	223	1178
	2034-2064	1077	549	248	1102
	2062-2092	1360	761	243	1101
Vancouver (West Coast)	1986-2016	576	90	4243	6787
	2034-2064	1094	251	4021	5947
	2062-2092	1681	373	3807	5420
Winnipeg (Central)	1986-2016	363	276	131	327
	2034-2064	757	442	139	382
	2062-2092	902	628	211	536

The extent of decay is to be determined using the decay intensity and the duration of decay events; the annual mass loss due to decay is calculated by Eq. 17. The decay intensity index and the annual durations were the mean values obtained from the fitted distributions listed in Table 5-5 and Table 5-6. In this study, 100% mass loss within 50 years was considered as the criterion to derive relevant parameters. Hence, the number of years required to reach the 100% mass loss in each wall assembly in different cities was calculated by dividing 100% by the annual mass loss (%), as obtained from Eq. 17.

$$Annual\ Mass\ Loss\ (\%) = Decay\ Intensity\ Index \times Annual\ Durations \times 0.000228 \quad (17)$$

The number of years required to reach 100% mass loss for the vinyl wall assembly in different cities are shown in Figure 5.26. The vinyl wall assembly having 1% of the WDR load as the moisture load would take longer to reach the 100% mass loss criterion than that using the moisture load derived from water entry functions. The wood frame wall assemblies located in the coastal cities of Vancouver, Moncton, Halifax, Charlottetown and St. John's would decay at a faster rate than other cities considered in this study. In most cities, the required year to reach the 100% mass loss would diminish over the projected future time periods except for those located in Vancouver, Calgary and Toronto should the moisture load be derived from water entry functions. In Vancouver for the vinyl wall assemblies, 3 to 3.5 years were required to reach a 100% mass loss considering a moisture load derived from water entry functions. These periods in years determined in the current study, will be discussed in consideration of a previously completed field investigation of homes located in British Columbia.

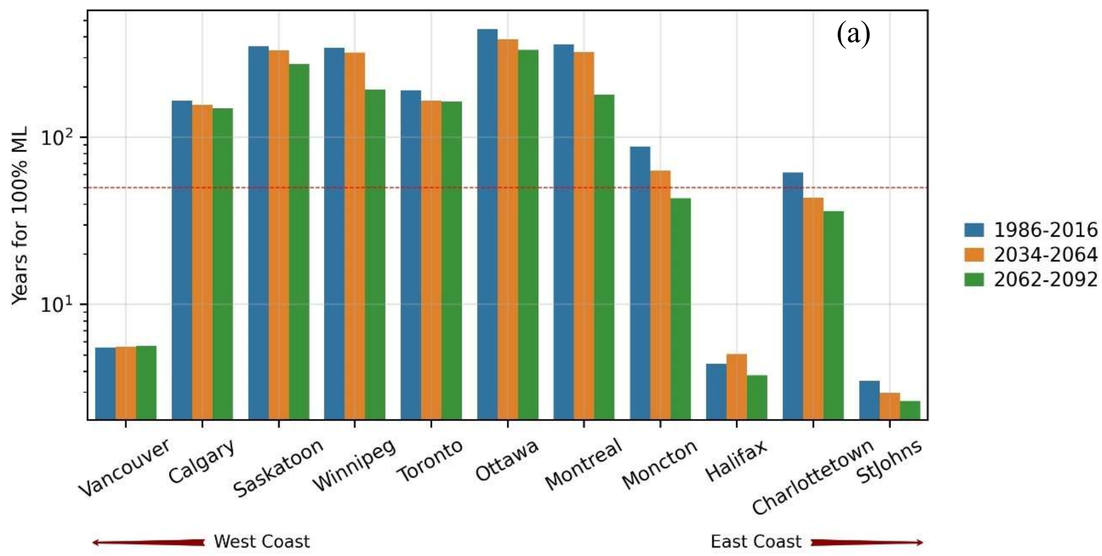

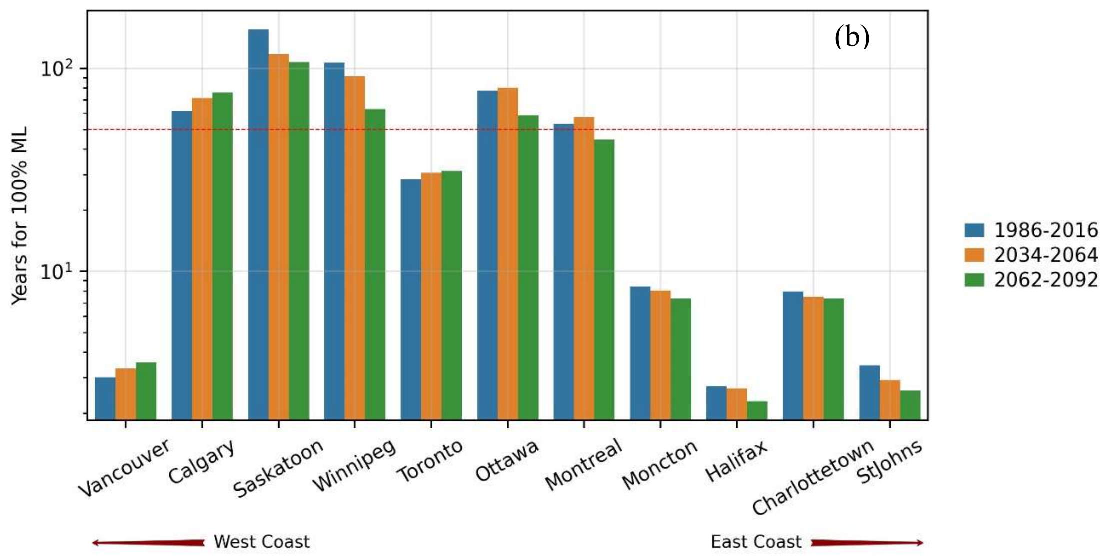

Figure 5.26 (a) Required years to reach the 100% mass loss in the vinyl wall assembly using 1% of the WDR as the moisture load; (b) Required year to reach the 100% mass

loss in the vinyl wall assembly using moisture load derived from water entry functions. The red dotted line is the 50-year threshold.

For the brick wall assembly, the number of years required to reach 100% mass loss would significantly diminish, for the projected future time periods in all cities (Figure 5.27). The extent of decay for the brick wall assembly for the cities of Toronto, Ottawa, Montreal, Moncton, and Halifax would bring about 100% mass loss within 50 years for all analyzed time periods, regardless of the type of moisture load. Saskatoon was the only city for all time periods for which the time required to reach 100% mass loss was over 50 years. In the other cities of Vancouver, Calgary, Winnipeg, Charlottetown, and St. John's, the required years were greater than 50, for the historical time period 1986-2016, and this value decreased to less than 50 years for the two projected future time periods. The distribution of the required years for the brick wall assembly in different cities was different from that for the vinyl wall assembly although both wall assemblies were subjected to the same environmental conditions in the hygrothermal simulations. According to previous investigations, the WDR load in coastal cities were greater than that in other inland cities analyzed. Correspondingly, the decay for the vinyl wall assembly in coastal cities was also more severe than for other inland cities. Thus, compared to the brick wall assemblies, the decay in the vinyl wall assembly was more sensitive to the WDR load. Moreover, it is evident that the decay in the brick wall assembly was much more sensitive to temperature than that of the vinyl wall assembly as the required number of years to reach 100% mass loss was substantially reduced for both projected future time periods, when the temperature is expected to increase by 2°C and 3.5°C respectively. Whereas for the vinyl wall assembly, such changes in the required number of years for 100% mass loss were much smaller.

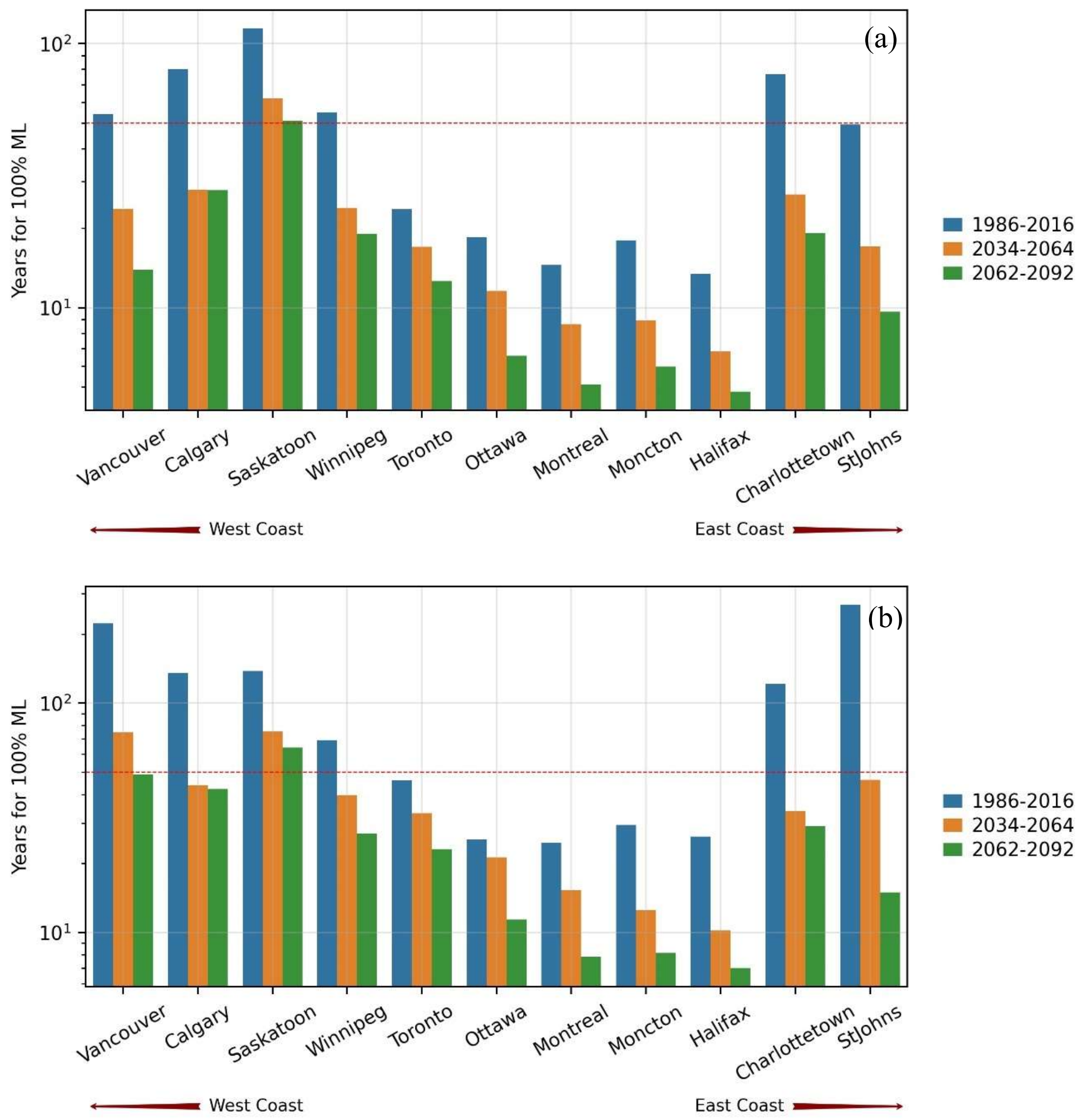

Figure 5.27 (a) Required years to reach the 100% mass loss in the brick wall assembly using 1% of the WDR as the moisture load; (b) Required year to reach the 100% mass loss in the brick wall assembly using moisture load derived from water entry functions. The red dotted line is the 50-year threshold.

5.2.3 Discussion and Limitations

The mass loss for the decay study was evaluated by weighing the wood pieces over the course of the decay experiment. However, wood materials that were tested had small dimensions that may not be representative of the development of decay for an OSB panel as is typically used in a full-scale wall assembly. For instance, the mass loss due to decay may only occur within a certain depth from the surface of a thicker or greater volume of wood. To date, any of the studies on wood decay have yet to provide relevant information in this regard. Thus, additional efforts are still needed to permit evaluating the actual consequences caused by mass loss in wood components used in wall assemblies. Field studies would be ideal to validate the damage caused by mass loss due to decay, given that the specimens are exposed to the actual in-service climatic conditions, although such an investigation would require the assistance of building practitioners capable of and having access to installed specimens. Fortunately, a survey completed in British Columbia 30 years ago (Canada Mortgage and Housing Corporation, 1996; Rousseau, 1999) has provided some insights on the damage caused by the deterioration in building envelope, due to the moisture load from a cost point of view. More important, the survey collected information regarding the time to observe the degradation, which may be taken as evidence of stage 2 decay for wood materials. In this survey, 46 buildings located in, or near Vancouver, and built within 8 years, provided the basis for the study. Problems were defined as damage in walls, decks and exterior frames that required over $10,000 of repair (equivalent to $16,574 today). Wood frame wall assemblies with stucco, vinyl siding and wood sidings were investigated. As discussed in the survey report, of particular importance were those moisture problems which were evidently affecting the OSB-sheathed walls. The mean time to observe moisture problems in these OSB-sheathed walls was 3.2 years, which is very similar to the time required for the vinyl wall assembly to reach 100% mass loss in Vancouver using the moisture load derived from the water entry functions as shown in Figure 5.26b. Since the moisture problems as observed were considered to be caused by decay of the wood elements, the same or similar detrimental effects could be expected to occur for OSB-sheathed wall assemblies in other cities, when they reach 100% mass loss.

By incorporating the results from mathematical models and observations from a field survey, the assessment of the actual damage, as it occurred in the wall assemblies and the corresponding risks, offer a more realistic and accurate account of degradation due to wood decay in walls. Nevertheless, additional observations from field studies are required to further validate the model results, or experimental tests should be conducted to further validate the conclusions obtained from the mathematical models derived in this study. Additionally in this study, the initial stage of decay was ignored, which would render a more conservative estimation for the decay rate. Once information regarding the initial stage for wood decay is validated, it can then be readily incorporated into the current analysis by considering a reduction in the duration of decay events.

5.2.4 References

Canada Mortgage and Housing Corporation. (1996). *Survey of Building Envelope Failures in the Coastal Climate of British Columbia*.

CSA S478:19. (2019). *Durability in buildings*. National Standard of Canada.

Rousseau, M. (1999). Overview of the survey of building envelope failures in the coastal climate of British Columbia, performed by Morrisson-Hershfield Limited for CMHC (1996). *Journal of Thermal Envelope and Building Science*. https://doi.org/10.1177/109719639902200411

Saito, H. (2017). Application of the Wood Degradation Model to an Actual Roof Assembly subjected to Rain Penetration. *Energy Procedia*, *132*, 399–404. https://doi.org/10.1016/j.egypro.2017.09.644

Viitanen, H. A. (1997). Modelling the Time Factor in the Development of Brown Rot Decay in Pine and Spruce Sapwood - The Effect of Critical Humidity and Temperature Conditions. *Holzforschung*, *51*(2), 99–106. https://doi.org/10.1515/hfsg.1997.51.2.99

Viitanen, H., Toratti, T., Makkonen, L., Peuhkuri, R., Ojanen, T., Ruokolainen, L., & Räisänen, J. (2010). Towards modelling of decay risk of wooden materials. *European Journal of Wood and Wood Products*, *68*(3), 303–313. https://doi.org/10.1007/s00107-010-0450-x

Viitanen, Hannu. (1996). *Factors affecting the development of mould and brown rot decay in wooden material and wooden structures. Effect of humidity, temperature and exposure time*.

Wilcox, W. (1978). Review of literature on the effects of early stages of decay on wood strength. *Wood Fiber*, *9*(4), 352–357.

5.2.5 Appendix C

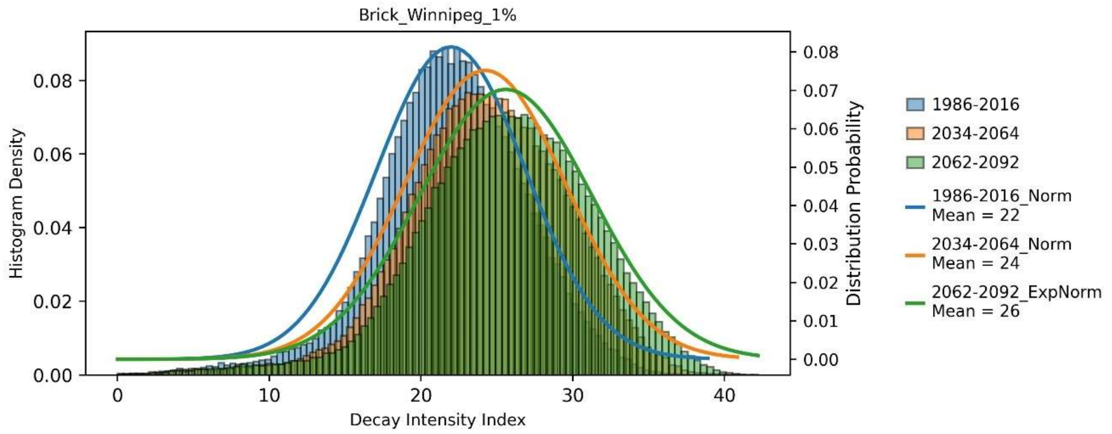

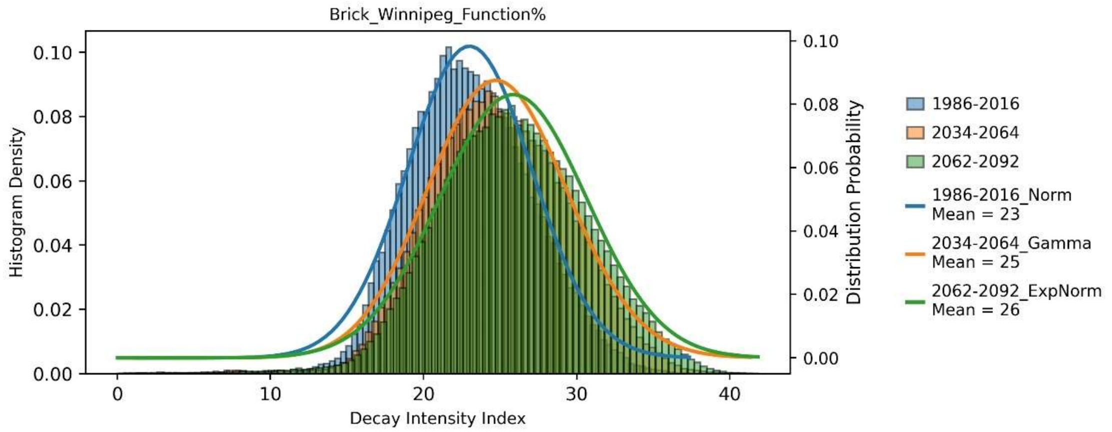

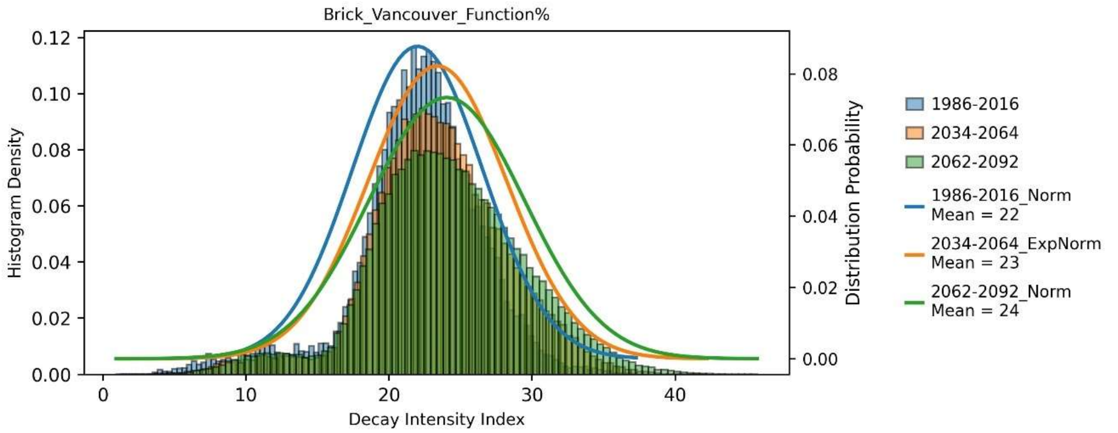

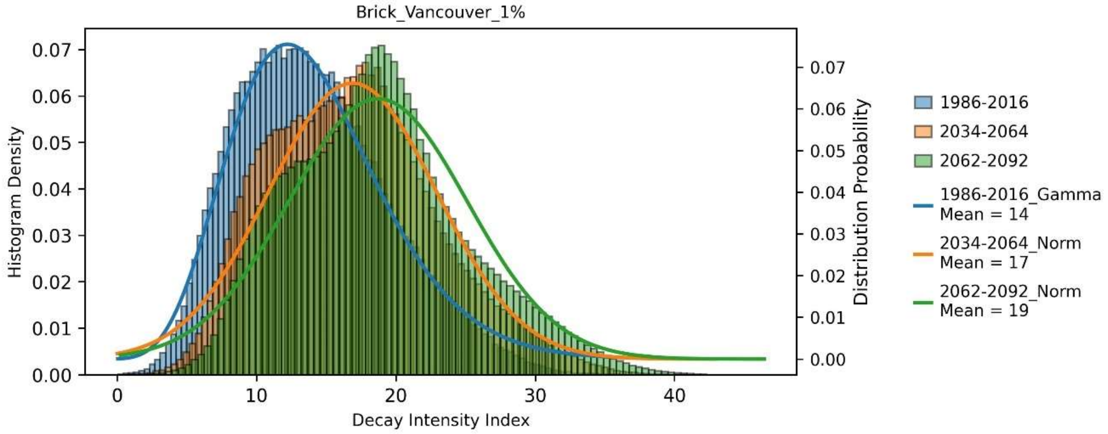
Brick_Vancouver_1%
Histogram Density
Distribution Probability
Decay Intensity Index
1986-2016
2034-2064
2062-2092
1986-2016_Gamma
Mean = 14
2034-2064_Norm
Mean = 17
2062-2092_Norm
Mean = 19

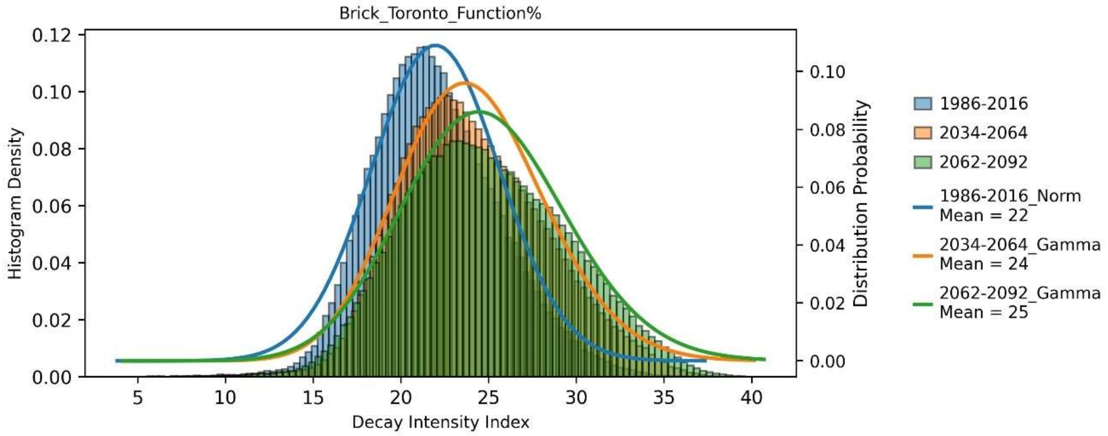
Brick_Toronto_Function%
Histogram Density
Distribution Probability
Decay Intensity Index
1986-2016
2034-2064
2062-2092
1986-2016_Norm
Mean = 22
2034-2064_Gamma
Mean = 24
2062-2092_Gamma
Mean = 25

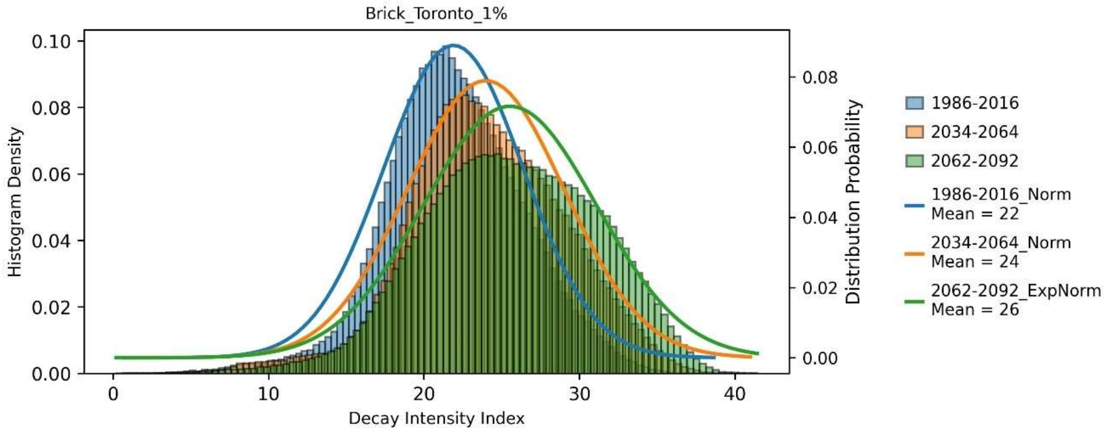
Brick_Toronto_1%
Histogram Density
Distribution Probability
Decay Intensity Index
1986-2016
2034-2064
2062-2092
1986-2016_Norm
Mean = 22
2034-2064_Norm
Mean = 24
2062-2092_ExpNorm
Mean = 26

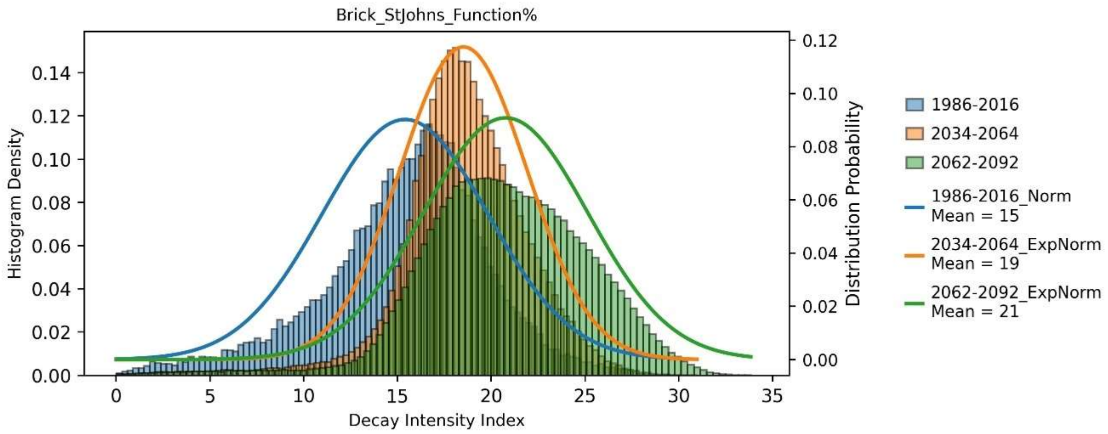
Brick_StJohns_Function%
Histogram Density
Distribution Probability
Decay Intensity Index
1986-2016
2034-2064
2062-2092
1986-2016_Norm
Mean = 15
2034-2064_ExpNorm
Mean = 19
2062-2092_ExpNorm
Mean = 21

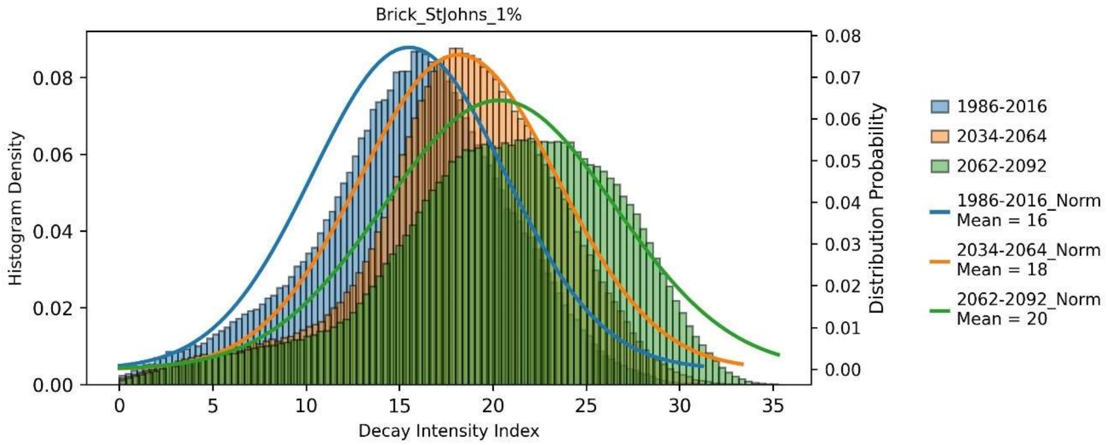
Brick_StJohns_1%
Histogram Density
Distribution Probability
Decay Intensity Index
1986-2016
2034-2064
2062-2092
1986-2016_Norm
Mean = 16
2034-2064_Norm
Mean = 18
2062-2092_Norm
Mean = 20

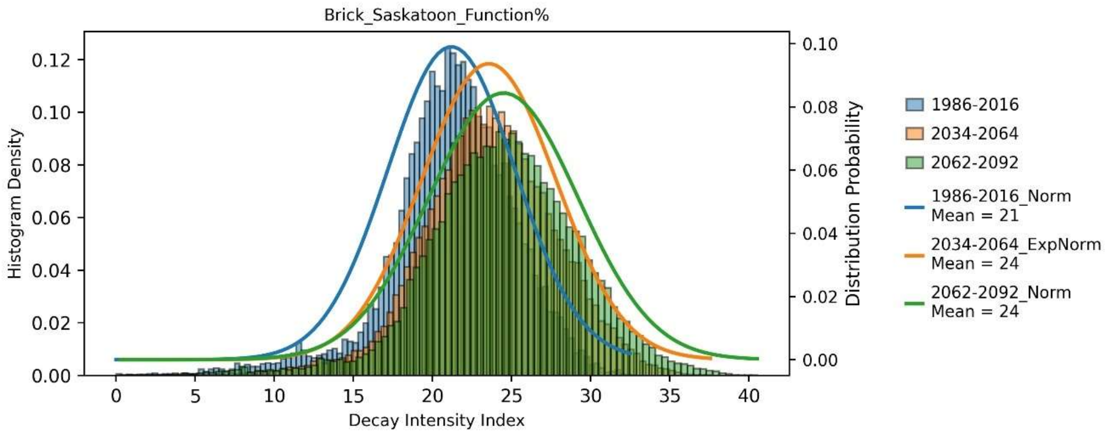
Brick_Saskatoon_Function%
Histogram Density
Distribution Probability
Decay Intensity Index
1986-2016
2034-2064
2062-2092
1986-2016_Norm
Mean = 21
2034-2064_ExpNorm
Mean = 24
2062-2092_Norm
Mean = 24

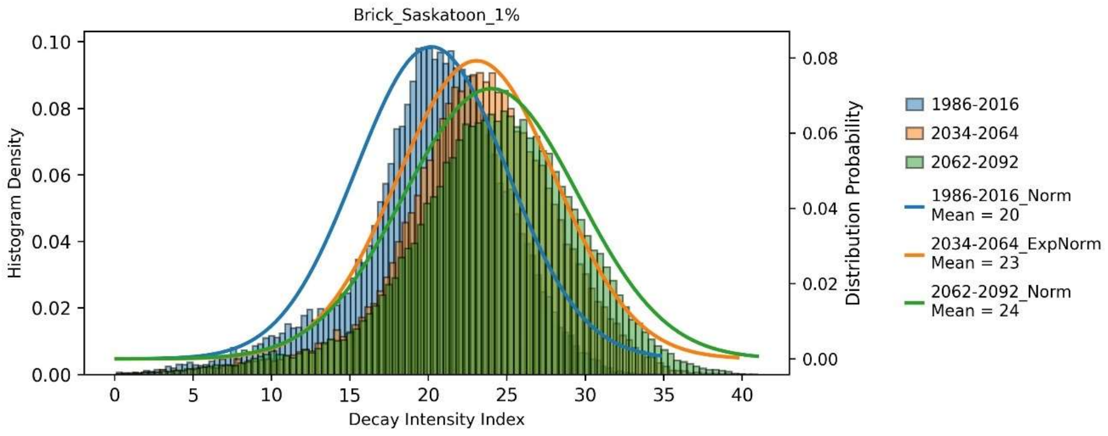
Brick_Saskatoon_1%
Histogram Density
Distribution Probability
Decay Intensity Index
1986-2016
2034-2064
2062-2092
1986-2016_Norm
Mean = 20
2034-2064_ExpNorm
Mean = 23
2062-2092_Norm
Mean = 24

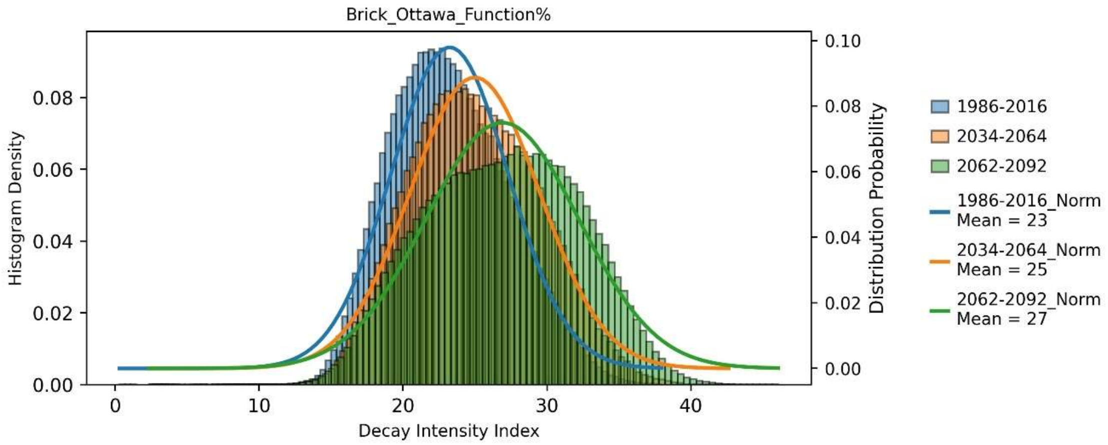
Brick_Ottawa_Function%
Histogram Density
Distribution Probability
Decay Intensity Index
1986-2016
2034-2064
2062-2092
1986-2016_Norm
Mean = 23
2034-2064_Norm
Mean = 25
2062-2092_Norm
Mean = 27

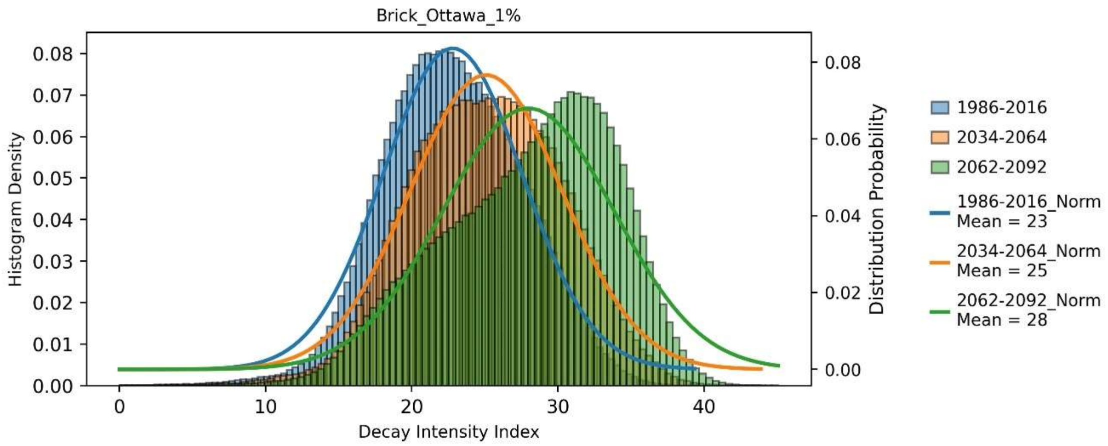
Brick_Ottawa_1%
Histogram Density
Distribution Probability
Decay Intensity Index
1986-2016
2034-2064
2062-2092
1986-2016_Norm
Mean = 23
2034-2064_Norm
Mean = 25
2062-2092_Norm
Mean = 28

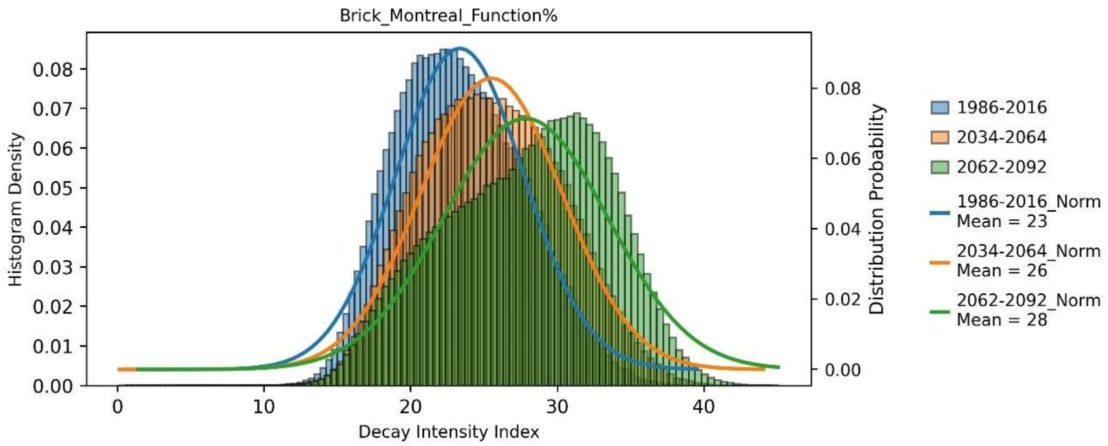
Brick_Montreal_Function%
Histogram Density
Distribution Probability
Decay Intensity Index
1986-2016
2034-2064
2062-2092
1986-2016_Norm
Mean = 23
2034-2064_Norm
Mean = 26
2062-2092_Norm
Mean = 28

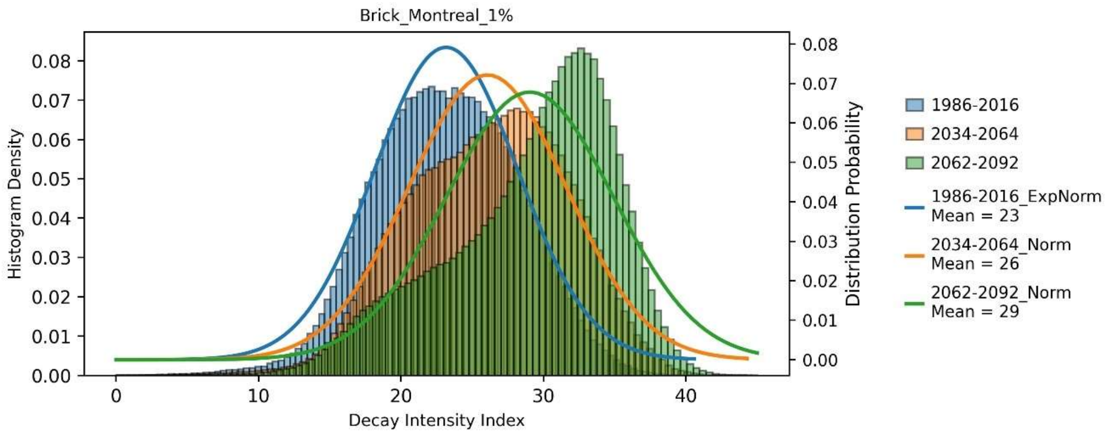
Brick_Montreal_1%
Histogram Density
Distribution Probability
Decay Intensity Index
1986-2016
2034-2064
2062-2092
1986-2016_ExpNorm
Mean = 23
2034-2064_Norm
Mean = 26
2062-2092_Norm
Mean = 29

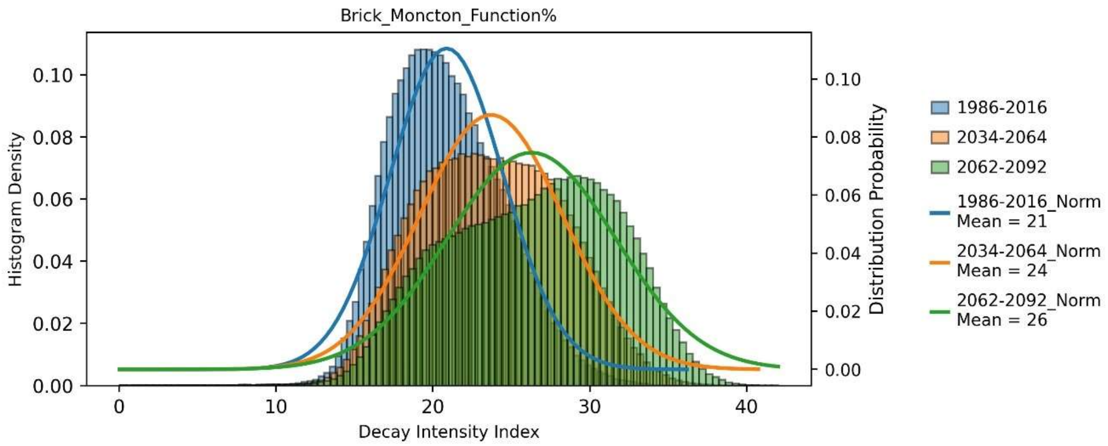
Brick_Moncton_Function%
Histogram Density
Distribution Probability
Decay Intensity Index
1986-2016
2034-2064
2062-2092
1986-2016_Norm
Mean = 21
2034-2064_Norm
Mean = 24
2062-2092_Norm
Mean = 26

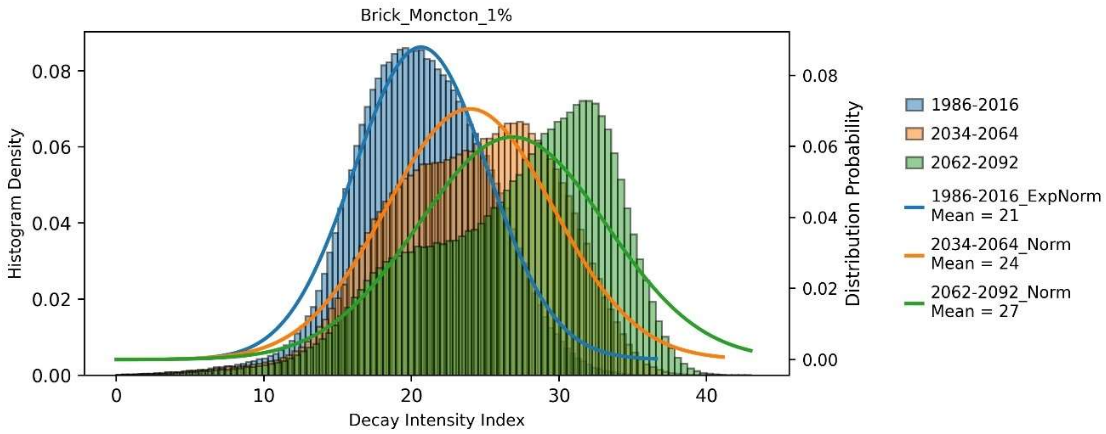
Brick_Moncton_1%
Histogram Density
Distribution Probability
Decay Intensity Index
1986-2016
2034-2064
2062-2092
1986-2016_ExpNorm
Mean = 21
2034-2064_Norm
Mean = 24
2062-2092_Norm
Mean = 27

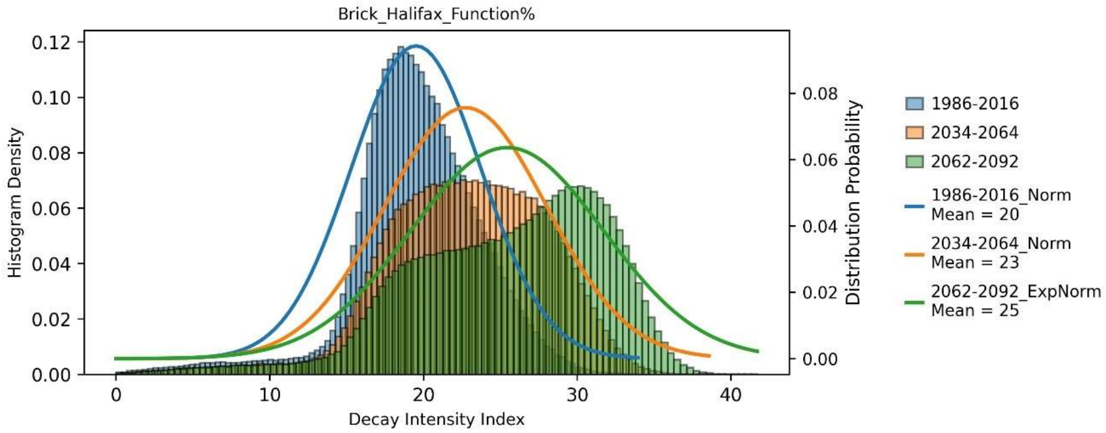
Brick_Halifax_Function%
Histogram Density
Distribution Probability
Decay Intensity Index
1986-2016
2034-2064
2062-2092
1986-2016_Norm
Mean = 20
2034-2064_Norm
Mean = 23
2062-2092_ExpNorm
Mean = 25

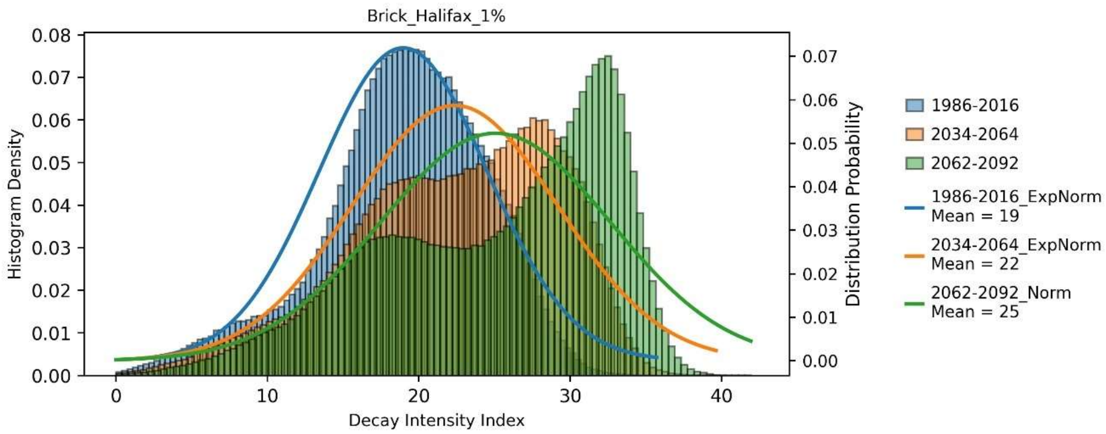
Brick_Halifax_1%
Histogram Density
Distribution Probability
Decay Intensity Index
1986-2016
2034-2064
2062-2092
1986-2016_ExpNorm
Mean = 19
2034-2064_ExpNorm
Mean = 22
2062-2092_Norm
Mean = 25

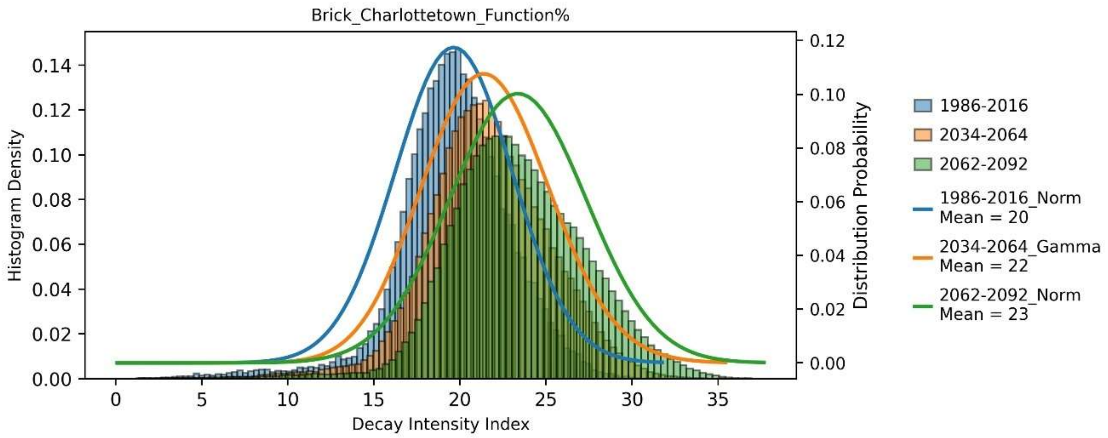

Brick_Charlottetown_Function%
Histogram Density
Distribution Probability
Decay Intensity Index
1986-2016
2034-2064
2062-2092
1986-2016_Norm
Mean = 20
2034-2064_Gamma
Mean = 22
2062-2092_Norm
Mean = 23

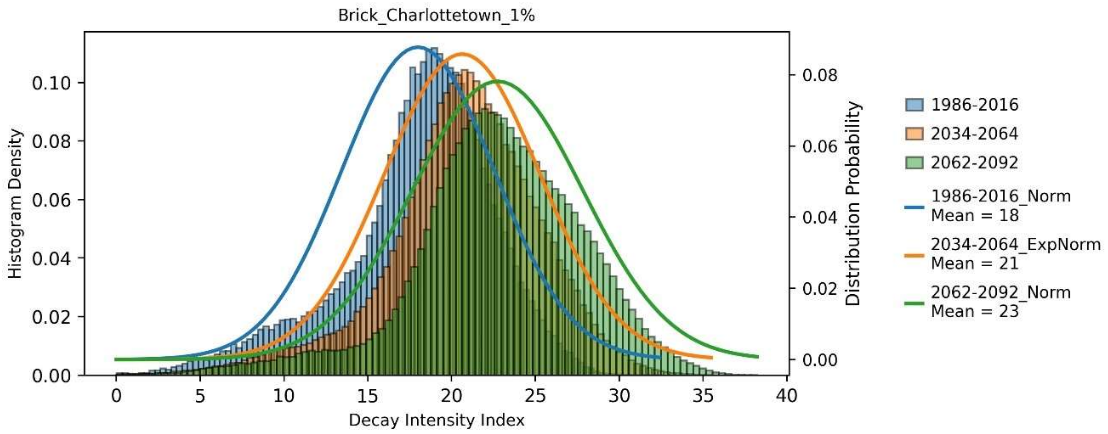

Brick_Charlottetown_1%
Histogram Density
Distribution Probability
Decay Intensity Index
1986-2016
2034-2064
2062-2092
1986-2016_Norm
Mean = 18
2034-2064_ExpNorm
Mean = 21
2062-2092_Norm
Mean = 23

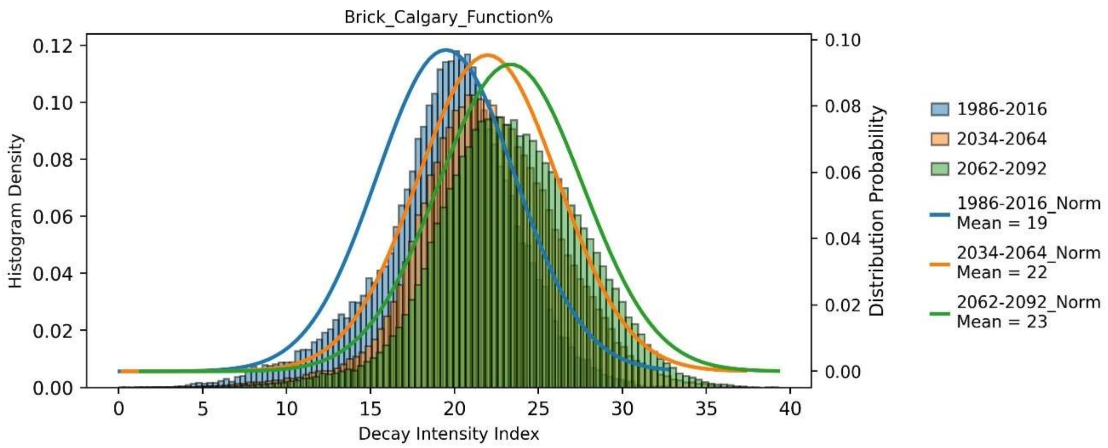

Brick_Calgary_Function%
Histogram Density
Distribution Probability
Decay Intensity Index
1986-2016
2034-2064
2062-2092
1986-2016_Norm
Mean = 19
2034-2064_Norm
Mean = 22
2062-2092_Norm
Mean = 23

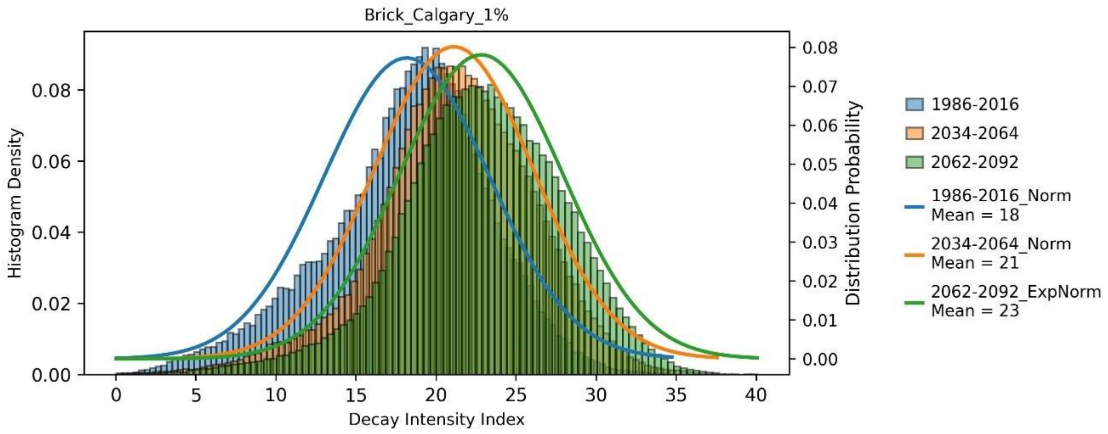
Brick_Calgary_1%
Histogram Density
Distribution Probability
Decay Intensity Index
1986-2016
2034-2064
2062-2092
1986-2016_Norm
Mean = 18
2034-2064_Norm
Mean = 21
2062-2092_ExpNorm
Mean = 23

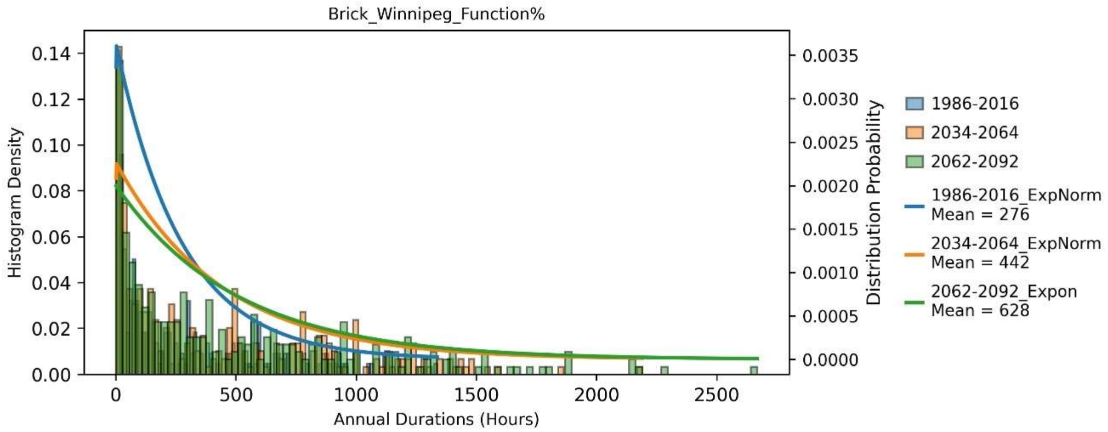
Brick_Winnipeg_Function%
Histogram Density
Distribution Probability
Annual Durations (Hours)
1986-2016
2034-2064
2062-2092
1986-2016_ExpNorm
Mean = 276
2034-2064_ExpNorm
Mean = 442
2062-2092_Expon
Mean = 628

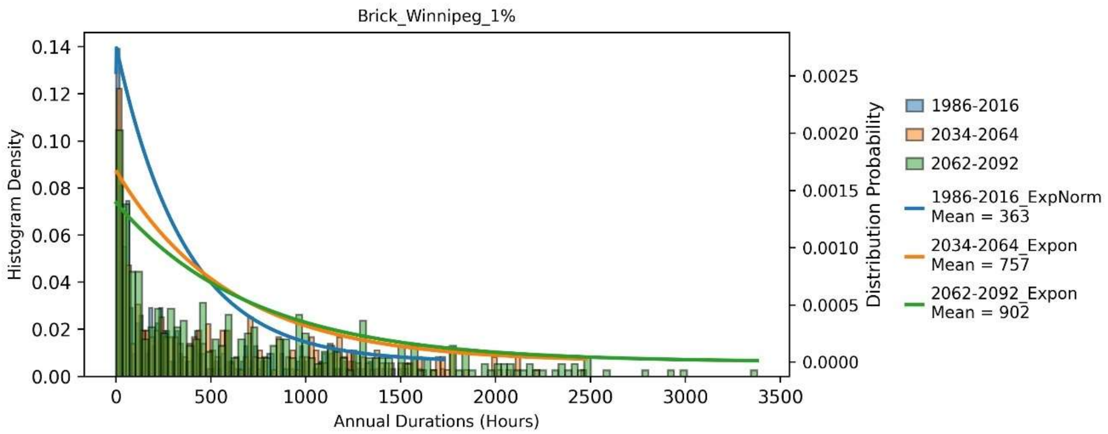
Brick_Winnipeg_1%
Histogram Density
Distribution Probability
Annual Durations (Hours)
1986-2016
2034-2064
2062-2092
1986-2016_ExpNorm
Mean = 363
2034-2064_Expon
Mean = 757
2062-2092_Expon
Mean = 902

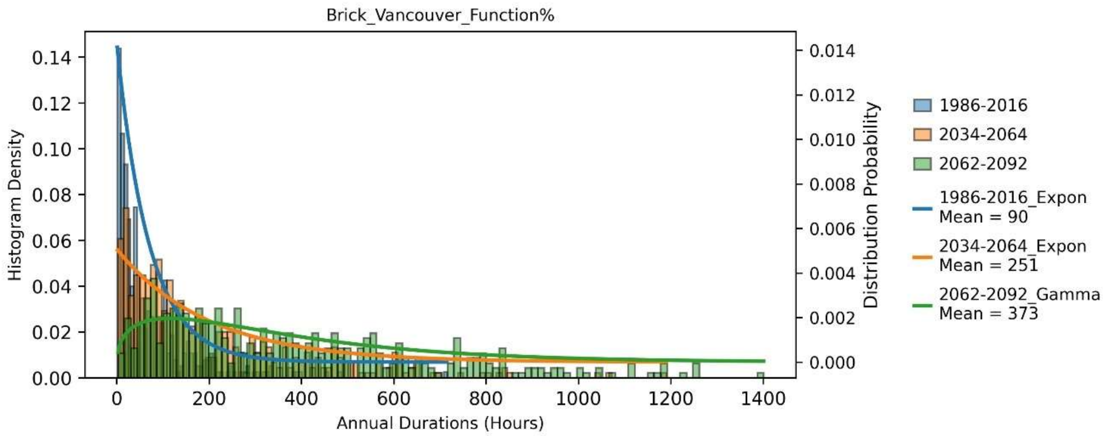
Brick_Vancouver_Function%
Histogram Density
Distribution Probability
Annual Durations (Hours)
1986-2016
2034-2064
2062-2092
1986-2016_Expon
Mean = 90
2034-2064_Expon
Mean = 251
2062-2092_Gamma
Mean = 373

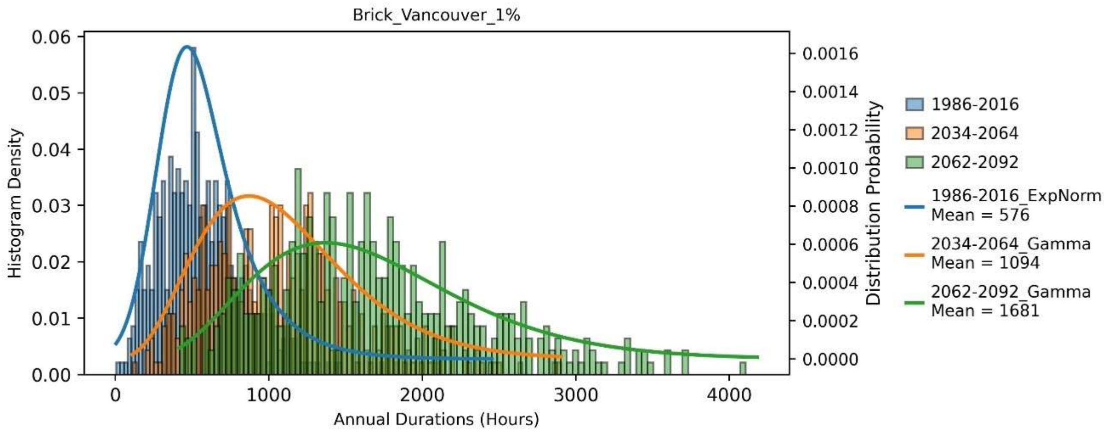
Brick_Vancouver_1%
Histogram Density
Distribution Probability
Annual Durations (Hours)
1986-2016
2034-2064
2062-2092
1986-2016_ExpNorm
Mean = 576
2034-2064_Gamma
Mean = 1094
2062-2092_Gamma
Mean = 1681

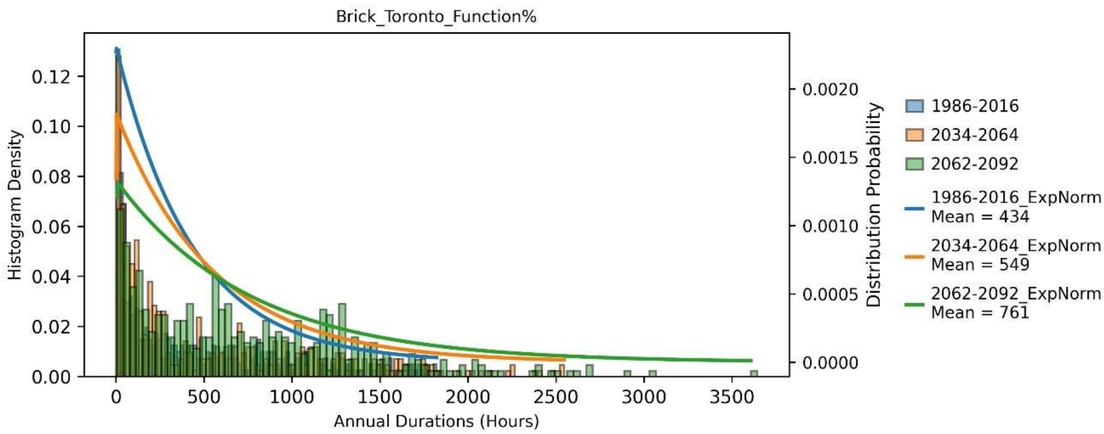
Brick_Toronto_Function%
Histogram Density
Distribution Probability
Annual Durations (Hours)
1986-2016
2034-2064
2062-2092
1986-2016_ExpNorm
Mean = 434
2034-2064_ExpNorm
Mean = 549
2062-2092_ExpNorm
Mean = 761

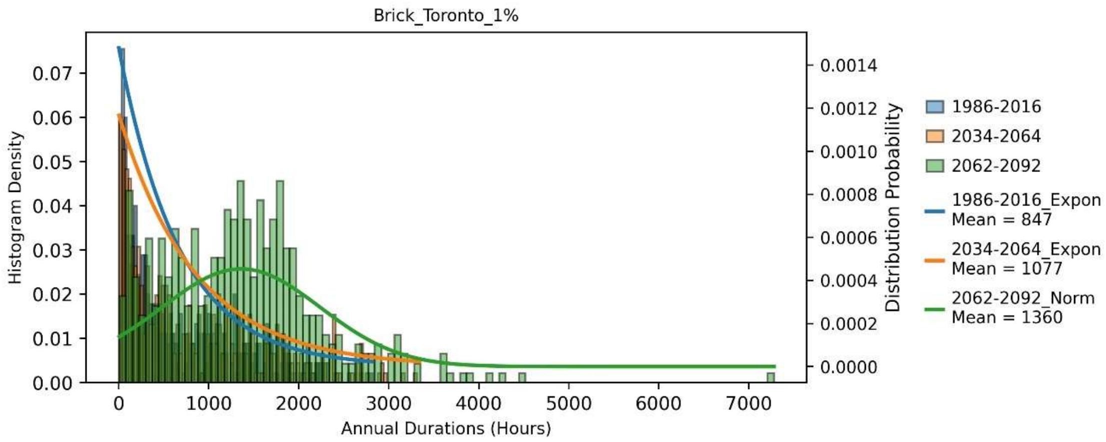

Brick_Toronto_1%
Histogram Density
Distribution Probability
Annual Durations (Hours)
1986-2016
2034-2064
2062-2092
1986-2016_Expon
Mean = 847
2034-2064_Expon
Mean = 1077
2062-2092_Norm
Mean = 1360

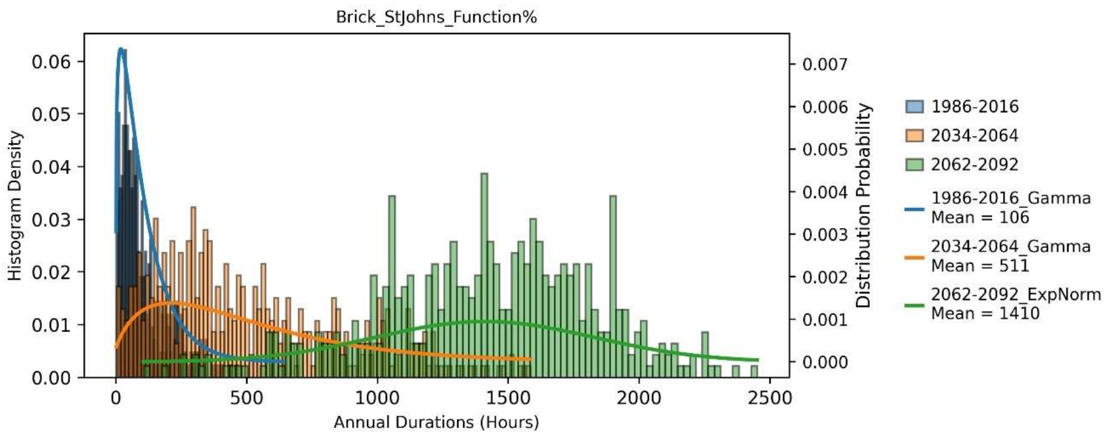

Brick_StJohns_Function%
Histogram Density
Distribution Probability
Annual Durations (Hours)
1986-2016
2034-2064
2062-2092
1986-2016_Gamma
Mean = 106
2034-2064_Gamma
Mean = 511
2062-2092_ExpNorm
Mean = 1410

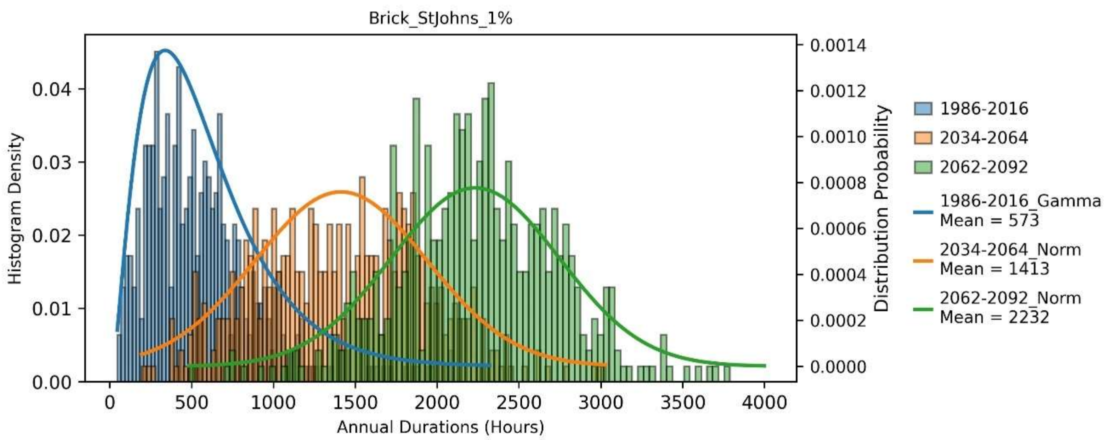

Brick_StJohns_1%
Histogram Density
Distribution Probability
Annual Durations (Hours)
1986-2016
2034-2064
2062-2092
1986-2016_Gamma
Mean = 573
2034-2064_Norm
Mean = 1413
2062-2092_Norm
Mean = 2232

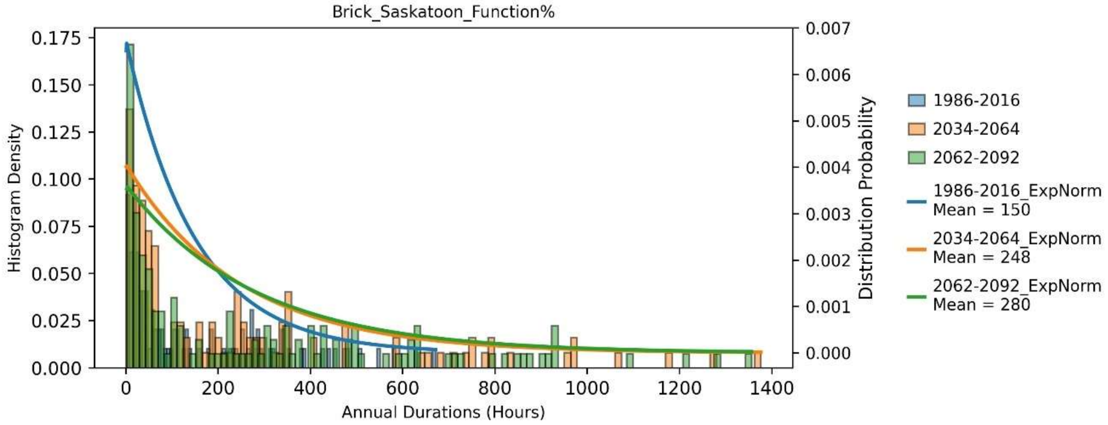
Brick_Saskatoon_Function%
Histogram Density
Distribution Probability
Annual Durations (Hours)
1986-2016
2034-2064
2062-2092
1986-2016_ExpNorm
Mean = 150
2034-2064_ExpNorm
Mean = 248
2062-2092_ExpNorm
Mean = 280

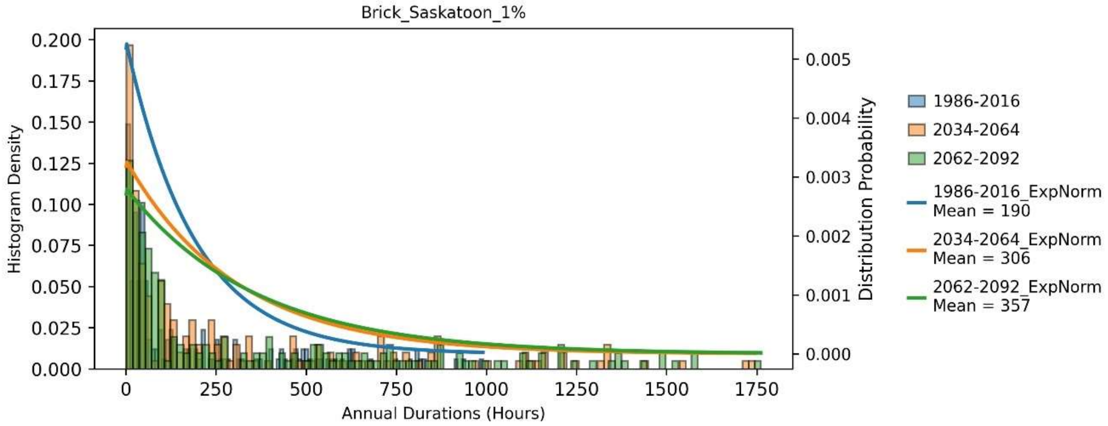
Brick_Saskatoon_1%
Histogram Density
Distribution Probability
Annual Durations (Hours)
1986-2016
2034-2064
2062-2092
1986-2016_ExpNorm
Mean = 190
2034-2064_ExpNorm
Mean = 306
2062-2092_ExpNorm
Mean = 357

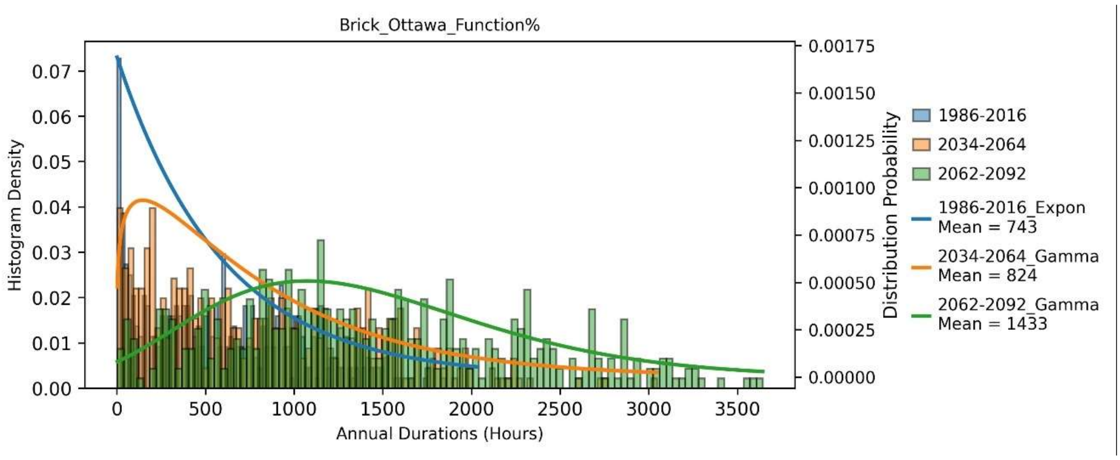
Brick_Ottawa_Function%
Histogram Density
Distribution Probability
Annual Durations (Hours)
1986-2016
2034-2064
2062-2092
1986-2016_Expon
Mean = 743
2034-2064_Gamma
Mean = 824
2062-2092_Gamma
Mean = 1433

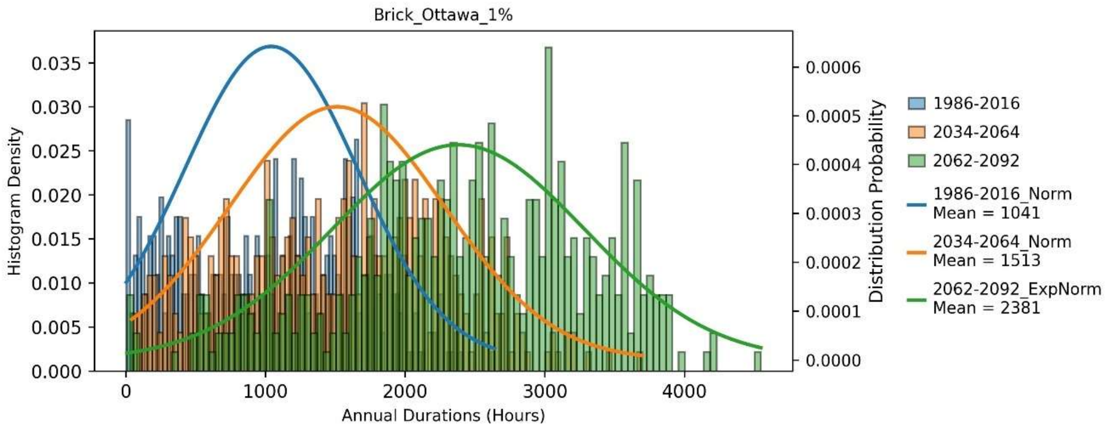
Brick_Ottawa_1%
Histogram Density
Distribution Probability
Annual Durations (Hours)
1986-2016
2034-2064
2062-2092
1986-2016_Norm
Mean = 1041
2034-2064_Norm
Mean = 1513
2062-2092_ExpNorm
Mean = 2381

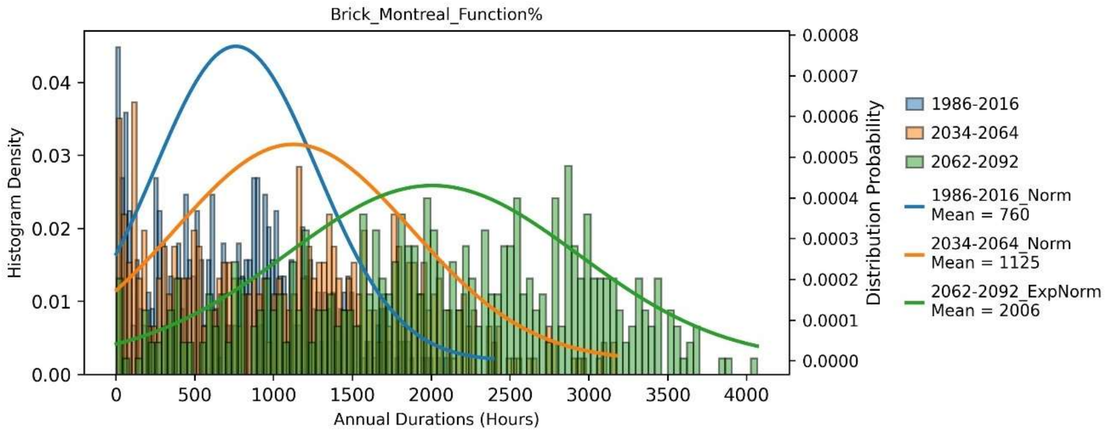
Brick_Montreal_Function%
Histogram Density
Distribution Probability
Annual Durations (Hours)
1986-2016
2034-2064
2062-2092
1986-2016_Norm
Mean = 760
2034-2064_Norm
Mean = 1125
2062-2092_ExpNorm
Mean = 2006

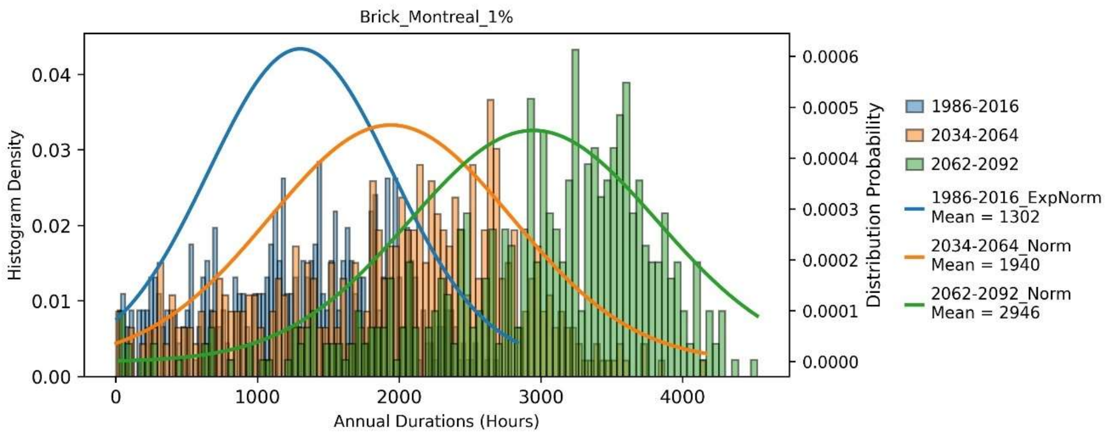
Brick_Montreal_1%
Histogram Density
Distribution Probability
Annual Durations (Hours)
1986-2016
2034-2064
2062-2092
1986-2016_ExpNorm
Mean = 1302
2034-2064_Norm
Mean = 1940
2062-2092_Norm
Mean = 2946

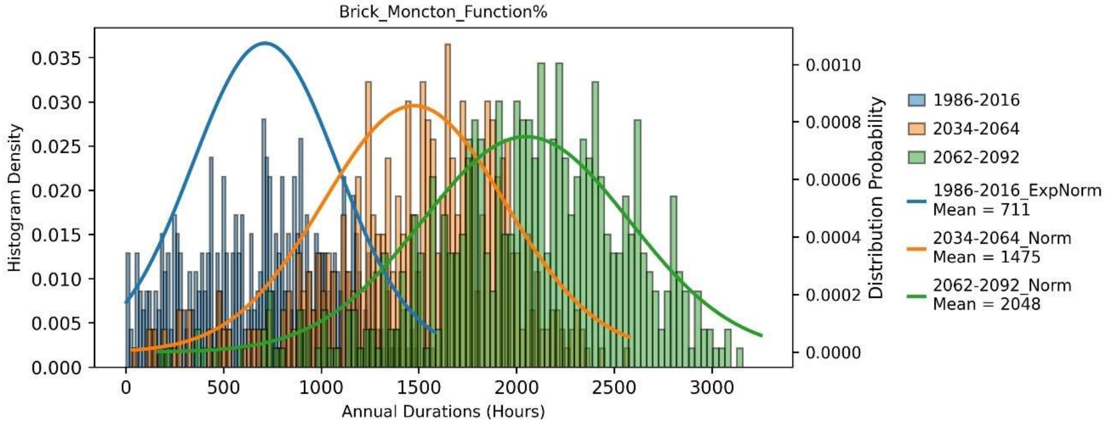
Brick_Moncton_Function%
Histogram Density
Distribution Probability
Annual Durations (Hours)
1986-2016
2034-2064
2062-2092
1986-2016_ExpNorm Mean = 711
2034-2064_Norm Mean = 1475
2062-2092_Norm Mean = 2048

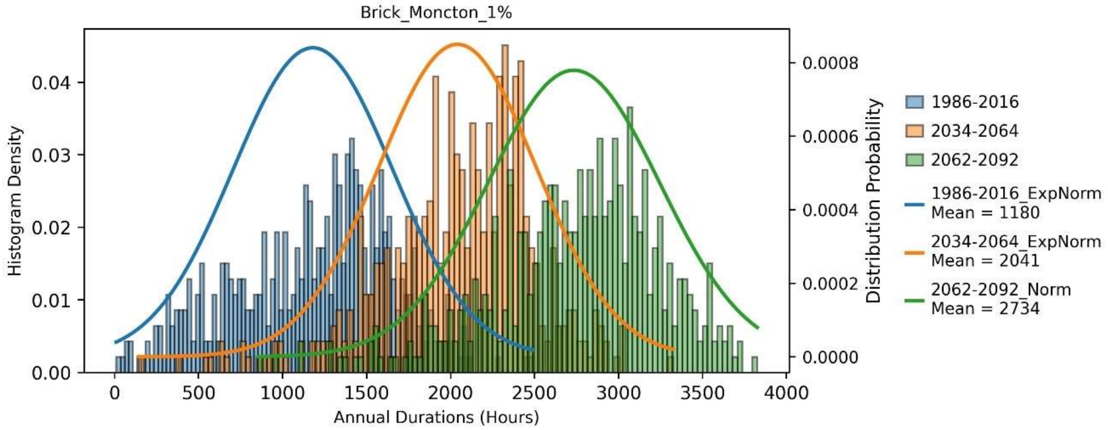
Brick_Moncton_1%
Histogram Density
Distribution Probability
Annual Durations (Hours)
1986-2016
2034-2064
2062-2092
1986-2016_ExpNorm Mean = 1180
2034-2064_ExpNorm Mean = 2041
2062-2092_Norm Mean = 2734

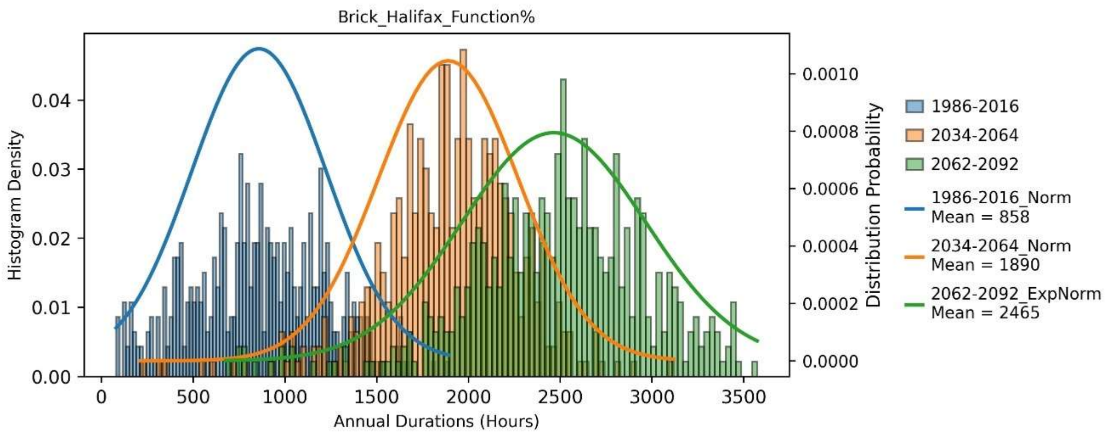
Brick_Halifax_Function%
Histogram Density
Distribution Probability
Annual Durations (Hours)
1986-2016
2034-2064
2062-2092
1986-2016_Norm Mean = 858
2034-2064_Norm Mean = 1890
2062-2092_ExpNorm Mean = 2465

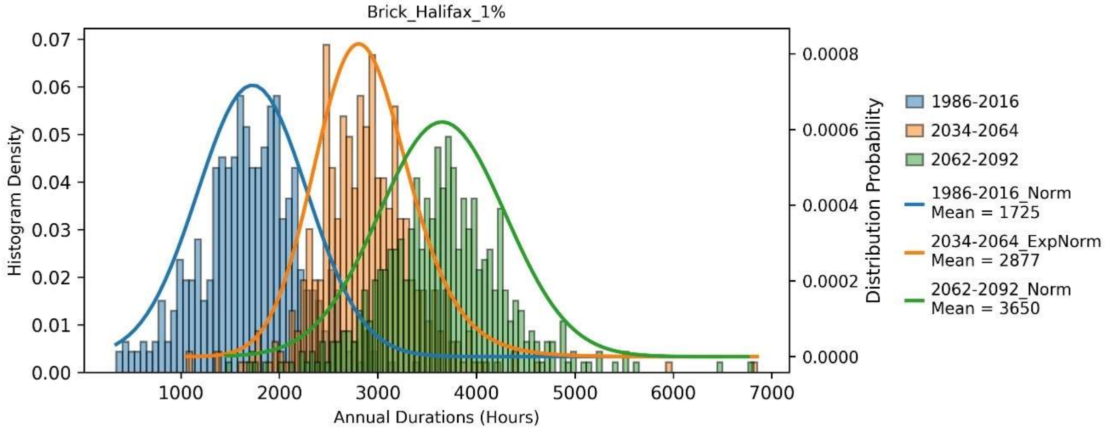
Brick_Halifax_1%
Histogram Density
Distribution Probability
Annual Durations (Hours)
1986-2016
2034-2064
2062-2092
1986-2016_Norm
Mean = 1725
2034-2064_ExpNorm
Mean = 2877
2062-2092_Norm
Mean = 3650

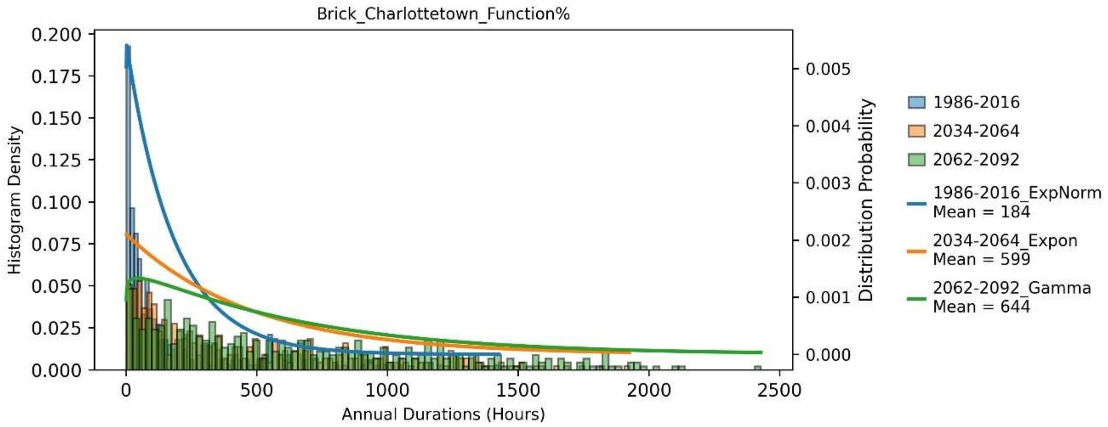
Brick_Charlottetown_Function%
Histogram Density
Distribution Probability
Annual Durations (Hours)
1986-2016
2034-2064
2062-2092
1986-2016_ExpNorm
Mean = 184
2034-2064_Expon
Mean = 599
2062-2092_Gamma
Mean = 644

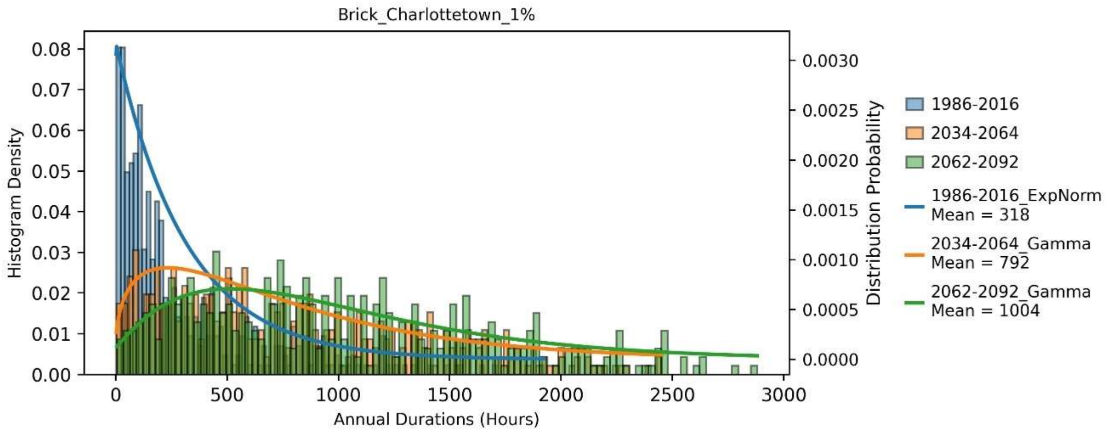
Brick_Charlottetown_1%
Histogram Density
Distribution Probability
Annual Durations (Hours)
1986-2016
2034-2064
2062-2092
1986-2016_ExpNorm
Mean = 318
2034-2064_Gamma
Mean = 792
2062-2092_Gamma
Mean = 1004

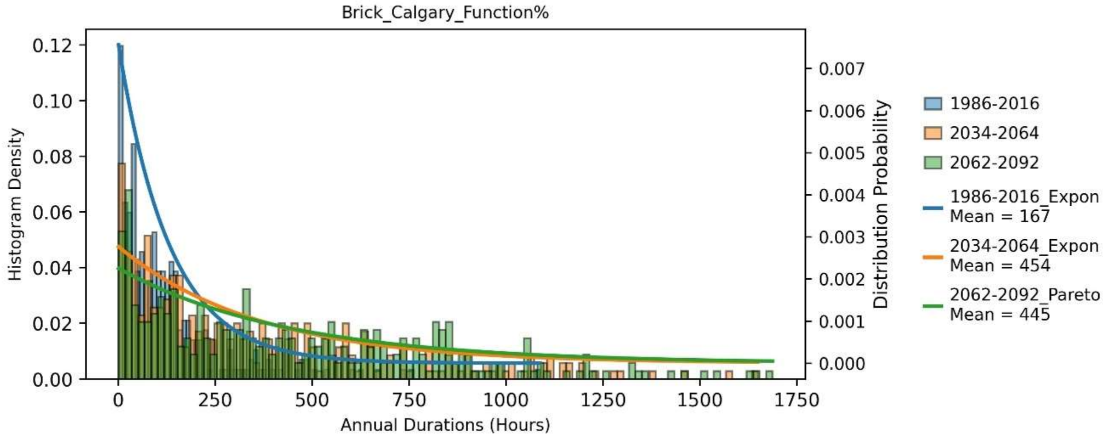
Brick_Calgary_Function%
Histogram Density
Distribution Probability
Annual Durations (Hours)
1986-2016
2034-2064
2062-2092
1986-2016_Expon
Mean = 167
2034-2064_Expon
Mean = 454
2062-2092_Pareto
Mean = 445

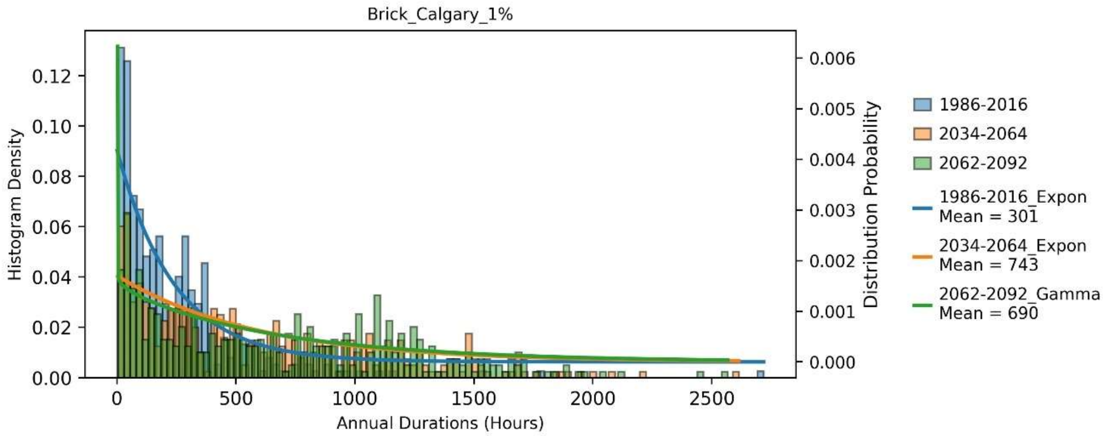
Brick_Calgary_1%
Histogram Density
Distribution Probability
Annual Durations (Hours)
1986-2016
2034-2064
2062-2092
1986-2016_Expon
Mean = 301
2034-2064_Expon
Mean = 743
2062-2092_Gamma
Mean = 690

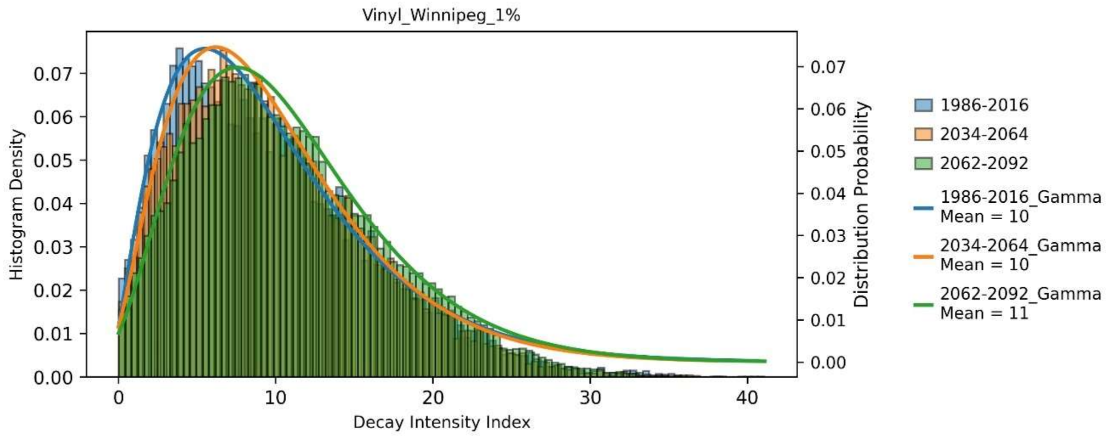
Vinyl_Winnipeg_1%
Histogram Density
Distribution Probability
Decay Intensity Index
1986-2016
2034-2064
2062-2092
1986-2016_Gamma
Mean = 10
2034-2064_Gamma
Mean = 10
2062-2092_Gamma
Mean = 11

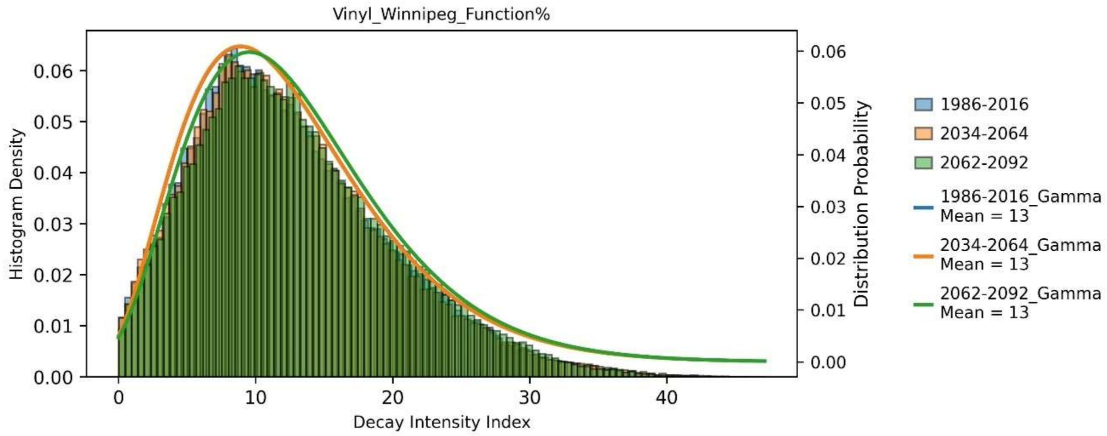
Vinyl_Winnipeg_Function%
Histogram Density
Distribution Probability
Decay Intensity Index
1986-2016
2034-2064
2062-2092
1986-2016_Gamma
Mean = 13
2034-2064_Gamma
Mean = 13
2062-2092_Gamma
Mean = 13

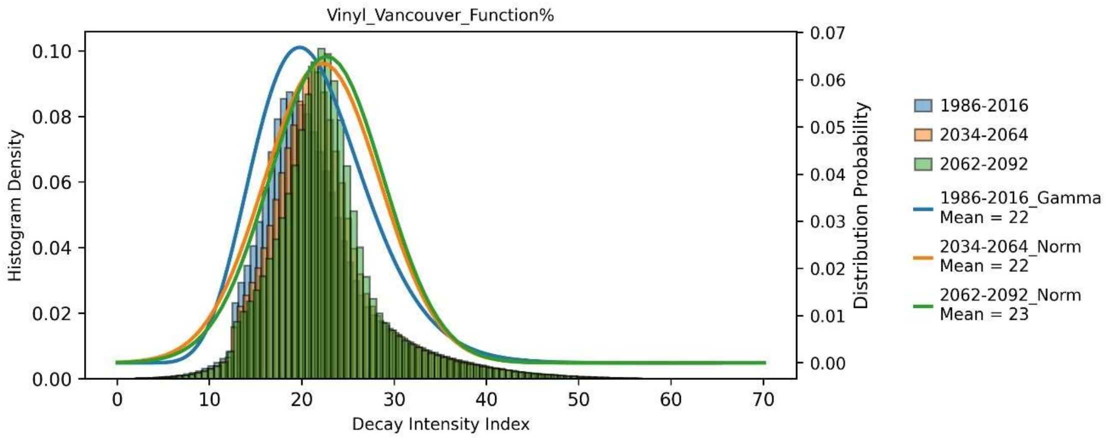
Vinyl_Vancouver_Function%
Histogram Density
Distribution Probability
Decay Intensity Index
1986-2016
2034-2064
2062-2092
1986-2016_Gamma
Mean = 22
2034-2064_Norm
Mean = 22
2062-2092_Norm
Mean = 23

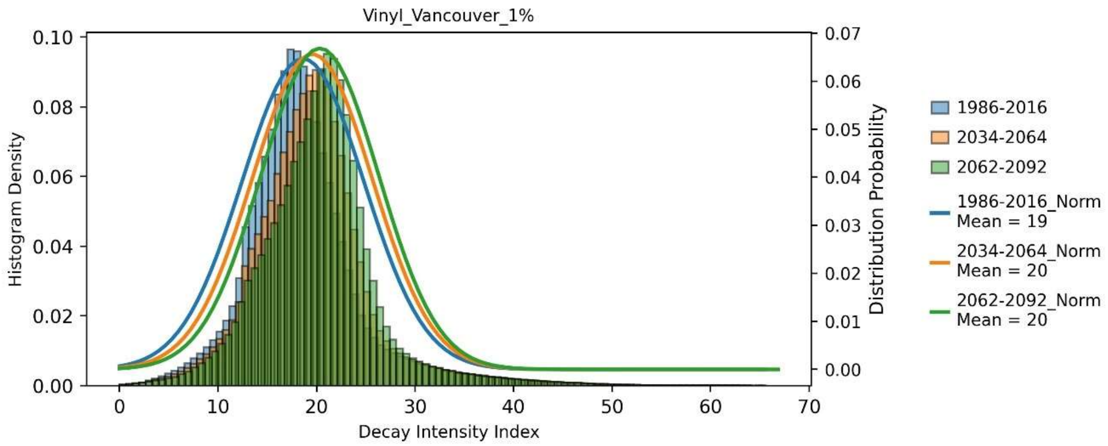
Vinyl_Vancouver_1%
Histogram Density
Distribution Probability
Decay Intensity Index
1986-2016
2034-2064
2062-2092
1986-2016_Norm Mean = 19
2034-2064_Norm Mean = 20
2062-2092_Norm Mean = 20

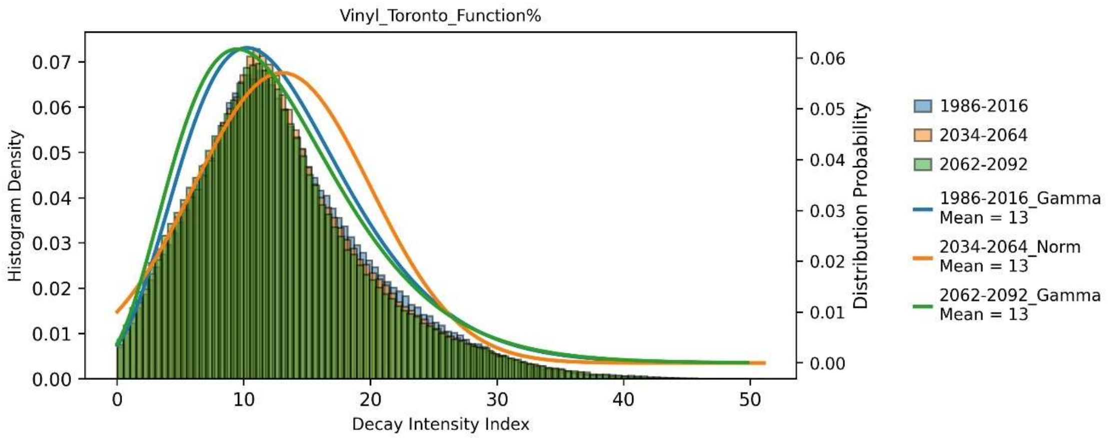
Vinyl_Toronto_Function%
Histogram Density
Distribution Probability
Decay Intensity Index
1986-2016
2034-2064
2062-2092
1986-2016_Gamma Mean = 13
2034-2064_Norm Mean = 13
2062-2092_Gamma Mean = 13

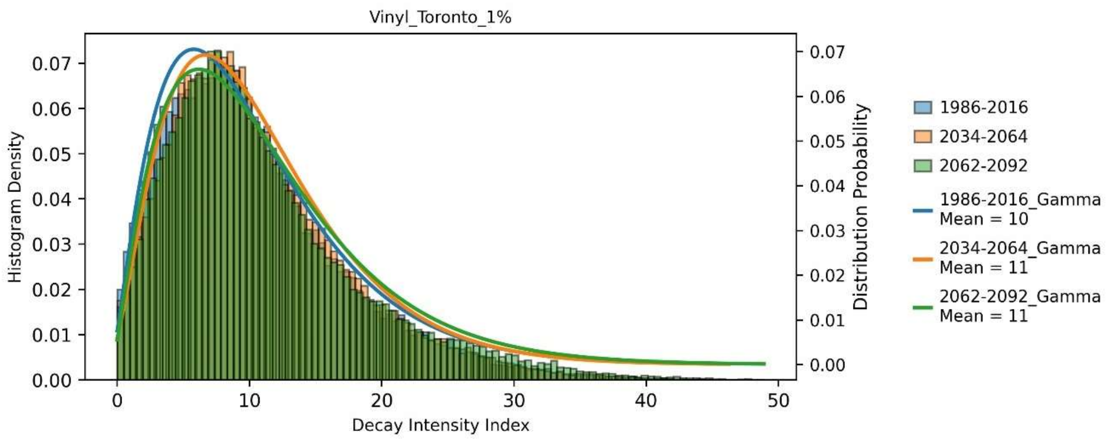
Vinyl_Toronto_1%
Histogram Density
Distribution Probability
Decay Intensity Index
1986-2016
2034-2064
2062-2092
1986-2016_Gamma Mean = 10
2034-2064_Gamma Mean = 11
2062-2092_Gamma Mean = 11

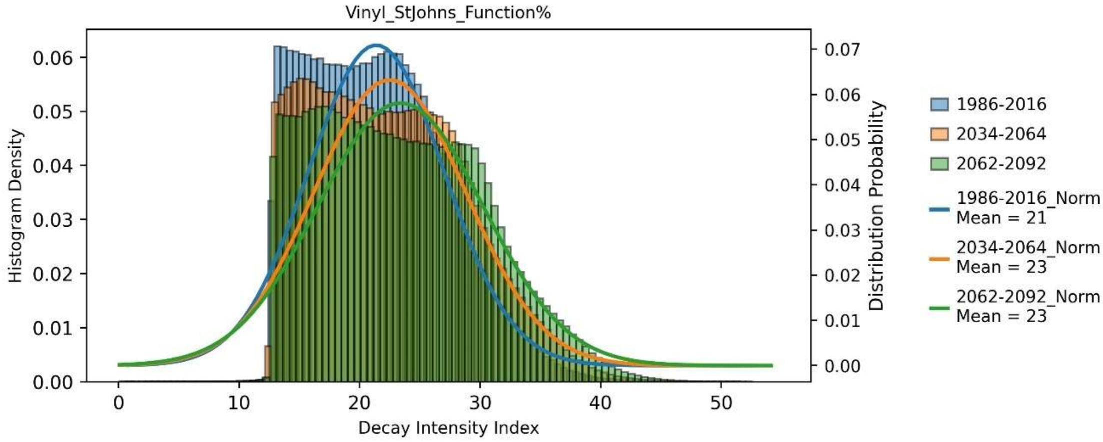
Vinyl_StJohns_Function%
Histogram Density
Distribution Probability
Decay Intensity Index
1986-2016
2034-2064
2062-2092
1986-2016_Norm
Mean = 21
2034-2064_Norm
Mean = 23
2062-2092_Norm
Mean = 23

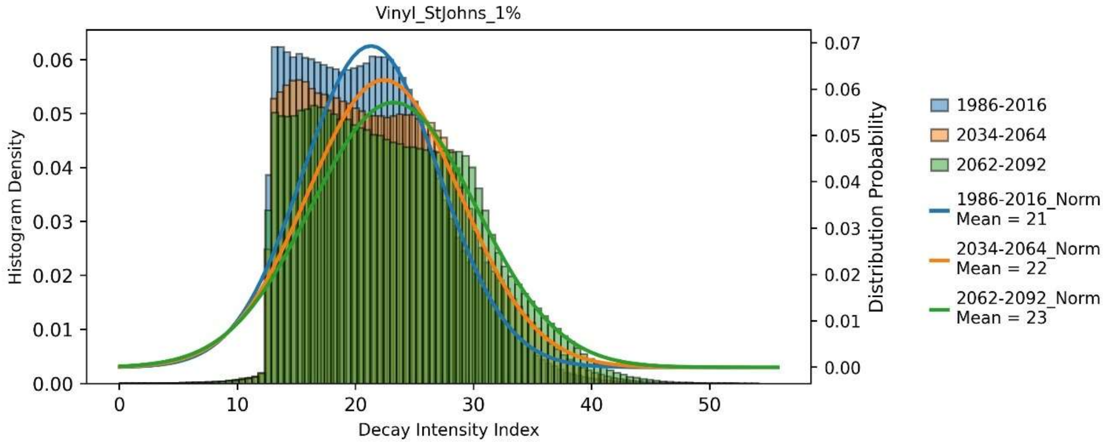
Vinyl_StJohns_1%
Histogram Density
Distribution Probability
Decay Intensity Index
1986-2016
2034-2064
2062-2092
1986-2016_Norm
Mean = 21
2034-2064_Norm
Mean = 22
2062-2092_Norm
Mean = 23

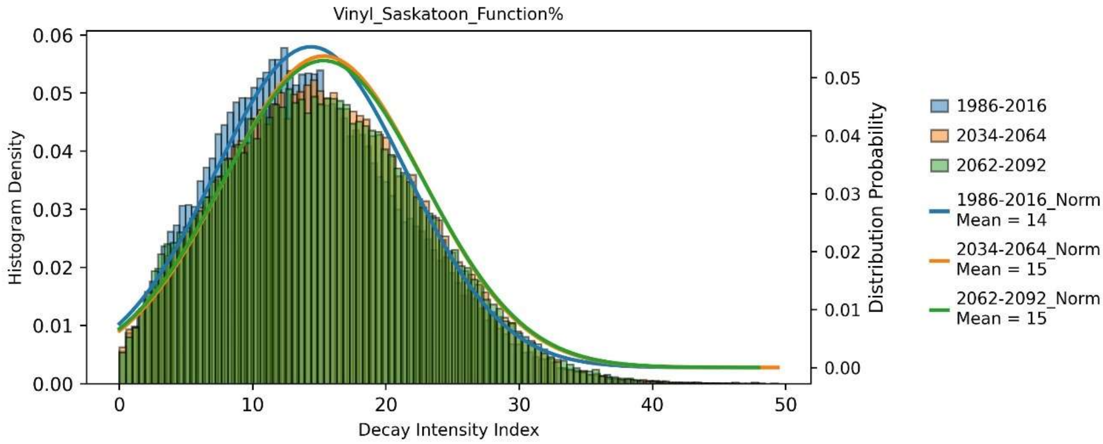
Vinyl_Saskatoon_Function%
Histogram Density
Distribution Probability
Decay Intensity Index
1986-2016
2034-2064
2062-2092
1986-2016_Norm
Mean = 14
2034-2064_Norm
Mean = 15
2062-2092_Norm
Mean = 15

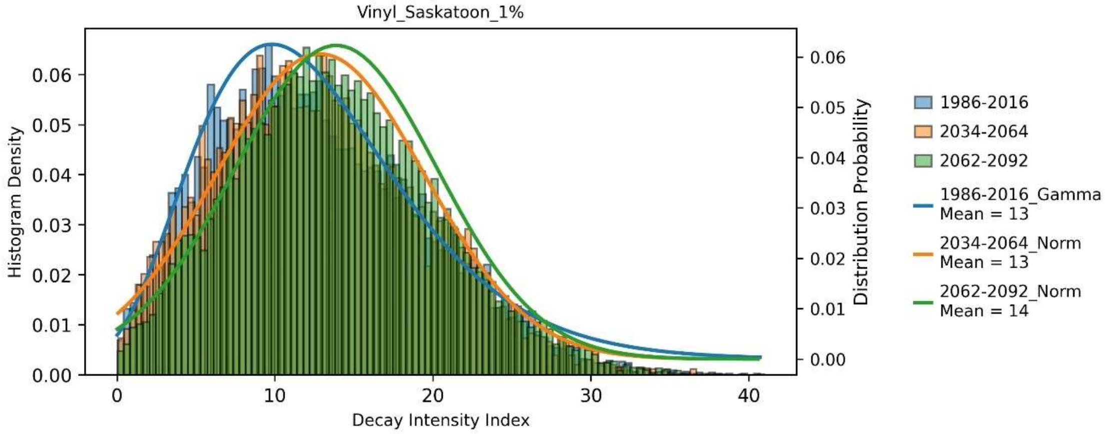
Vinyl_Saskatoon_1%
Histogram Density
Distribution Probability
Decay Intensity Index
1986-2016
2034-2064
2062-2092
1986-2016_Gamma Mean = 13
2034-2064_Norm Mean = 13
2062-2092_Norm Mean = 14

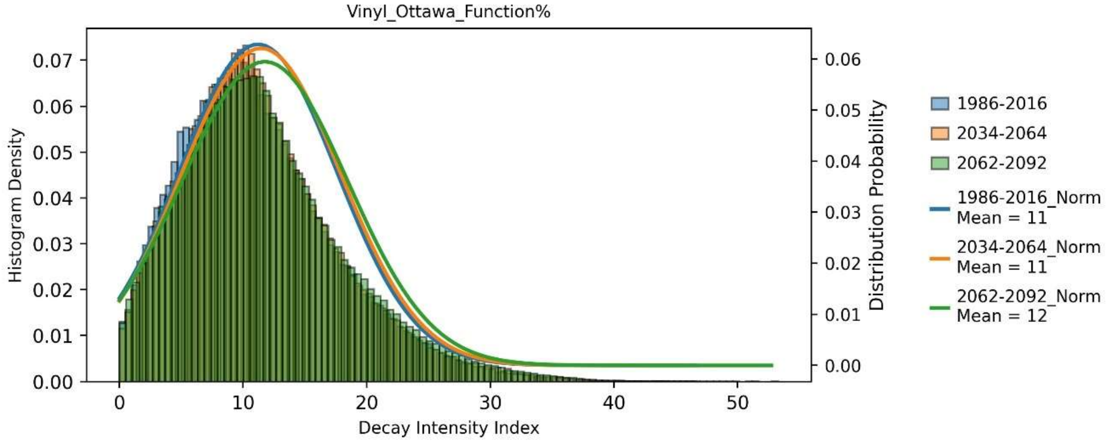
Vinyl_Ottawa_Function%
Histogram Density
Distribution Probability
Decay Intensity Index
1986-2016
2034-2064
2062-2092
1986-2016_Norm Mean = 11
2034-2064_Norm Mean = 11
2062-2092_Norm Mean = 12

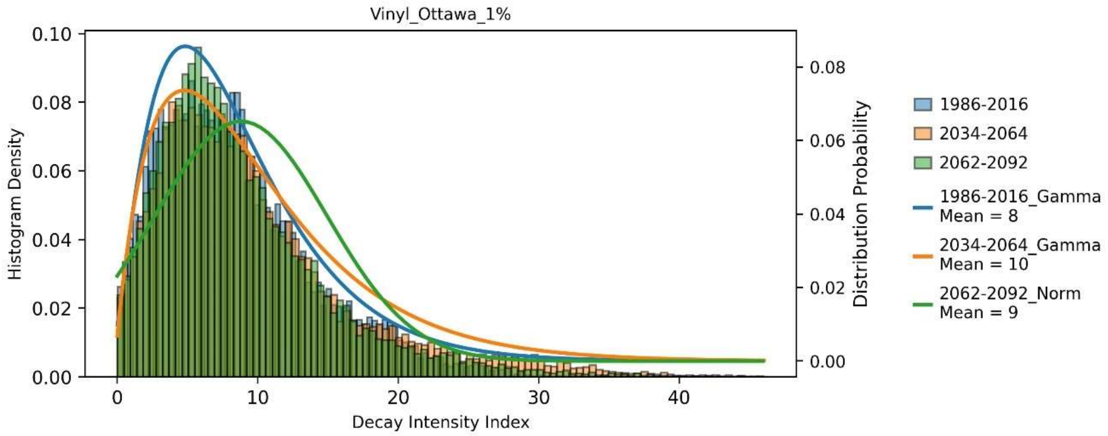
Vinyl_Ottawa_1%
Histogram Density
Distribution Probability
Decay Intensity Index
1986-2016
2034-2064
2062-2092
1986-2016_Gamma Mean = 8
2034-2064_Gamma Mean = 10
2062-2092_Norm Mean = 9

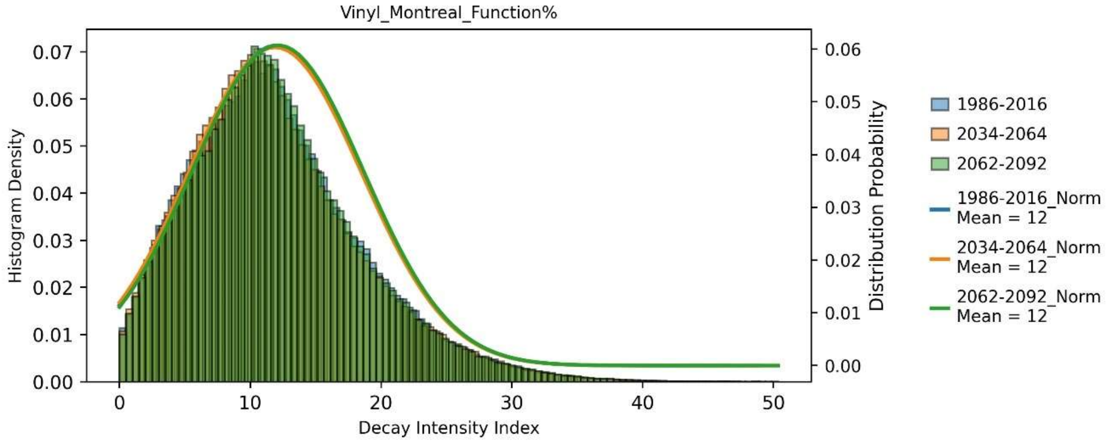
Vinyl_Montreal_Function%
Histogram Density
Distribution Probability
Decay Intensity Index
1986-2016
2034-2064
2062-2092
1986-2016_Norm
Mean = 12
2034-2064_Norm
Mean = 12
2062-2092_Norm
Mean = 12

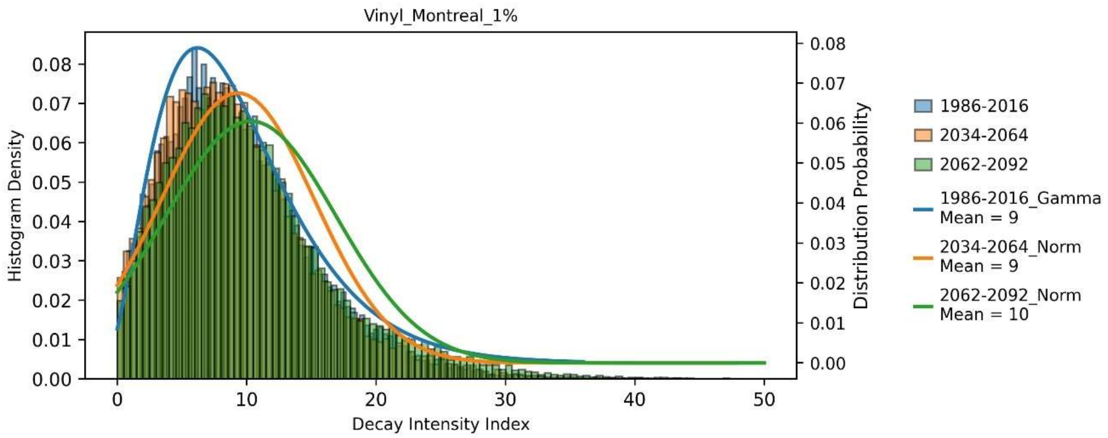
Vinyl_Montreal_1%
Histogram Density
Distribution Probability
Decay Intensity Index
1986-2016
2034-2064
2062-2092
1986-2016_Gamma
Mean = 9
2034-2064_Norm
Mean = 9
2062-2092_Norm
Mean = 10

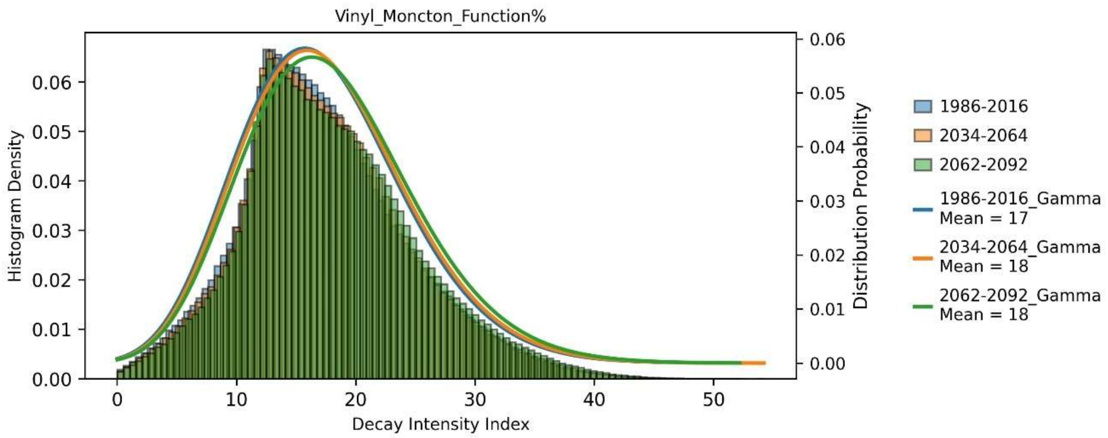
Vinyl_Moncton_Function%
Histogram Density
Distribution Probability
Decay Intensity Index
1986-2016
2034-2064
2062-2092
1986-2016_Gamma
Mean = 17
2034-2064_Gamma
Mean = 18
2062-2092_Gamma
Mean = 18

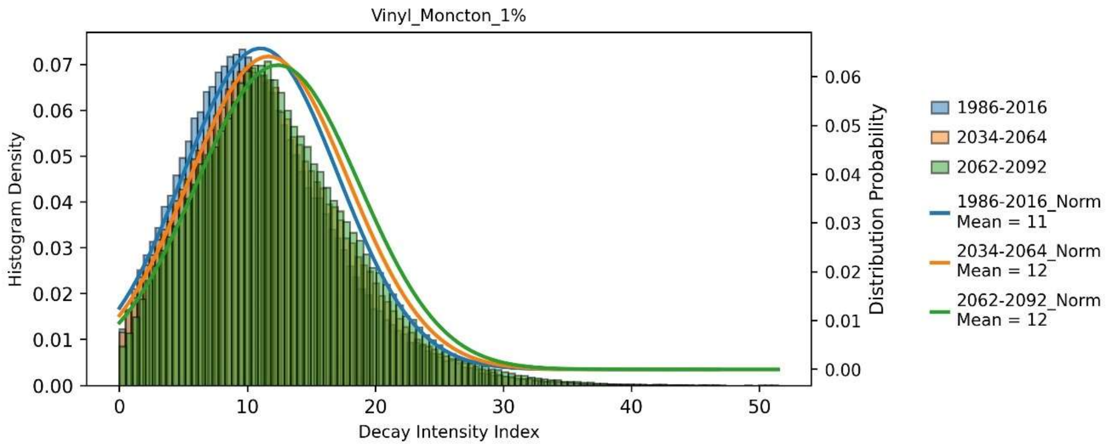
Vinyl_Moncton_1%
Histogram Density
Distribution Probability
Decay Intensity Index
1986-2016
2034-2064
2062-2092
1986-2016_Norm
Mean = 11
2034-2064_Norm
Mean = 12
2062-2092_Norm
Mean = 12

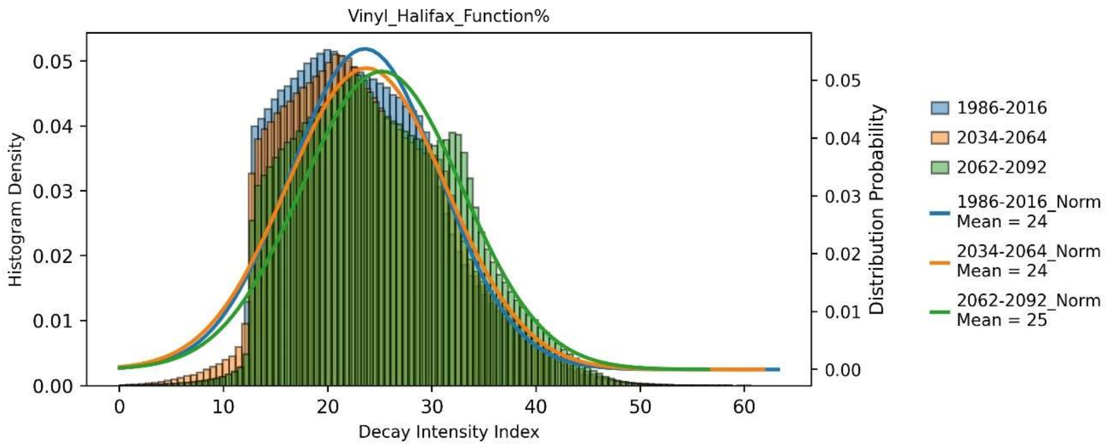
Vinyl_Halifax_Function%
Histogram Density
Distribution Probability
Decay Intensity Index
1986-2016
2034-2064
2062-2092
1986-2016_Norm
Mean = 24
2034-2064_Norm
Mean = 24
2062-2092_Norm
Mean = 25

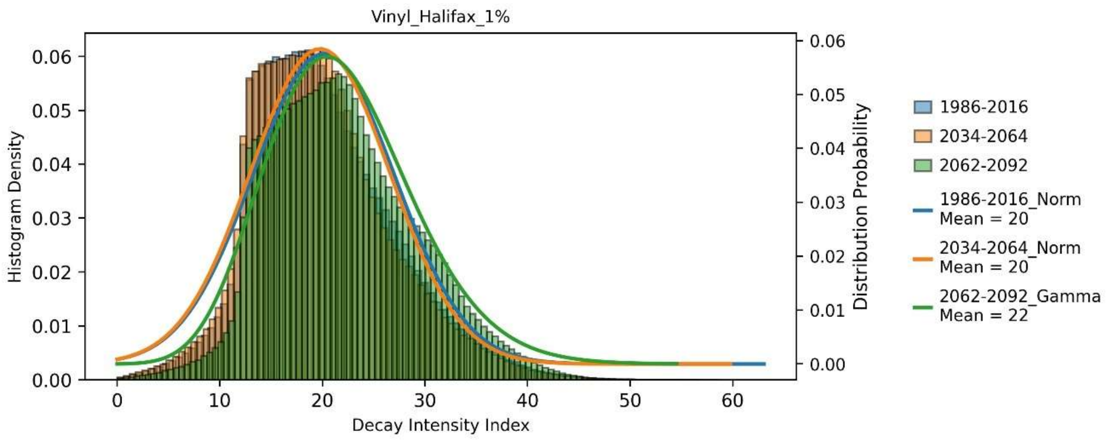
Vinyl_Halifax_1%
Histogram Density
Distribution Probability
Decay Intensity Index
1986-2016
2034-2064
2062-2092
1986-2016_Norm
Mean = 20
2034-2064_Norm
Mean = 20
2062-2092_Gamma
Mean = 22

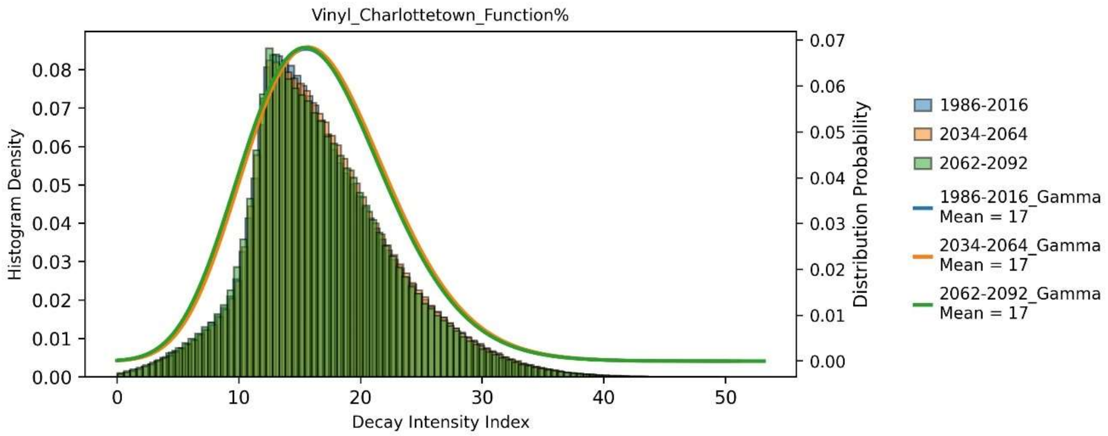
Vinyl_Charlottetown_Function%
Histogram Density
Distribution Probability
Decay Intensity Index
1986-2016
2034-2064
2062-2092
1986-2016_Gamma
Mean = 17
2034-2064_Gamma
Mean = 17
2062-2092_Gamma
Mean = 17

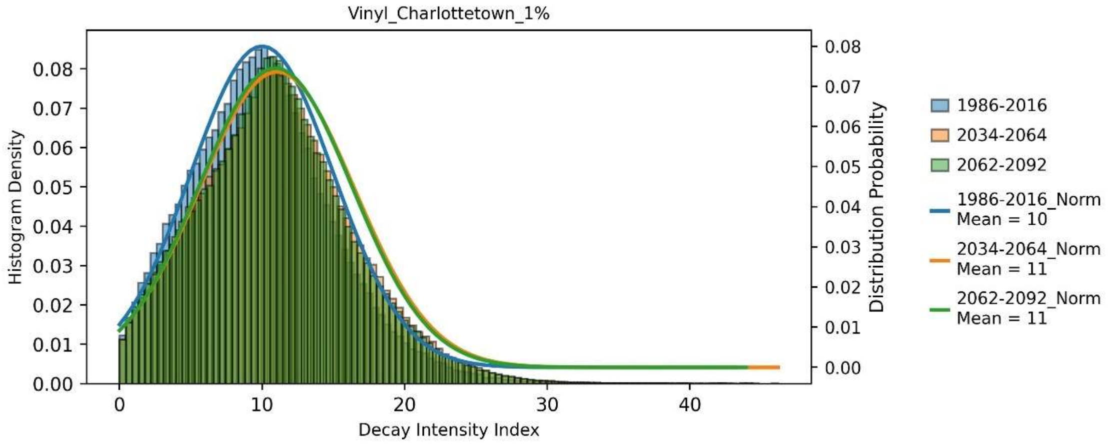
Vinyl_Charlottetown_1%
Histogram Density
Distribution Probability
Decay Intensity Index
1986-2016
2034-2064
2062-2092
1986-2016_Norm
Mean = 10
2034-2064_Norm
Mean = 11
2062-2092_Norm
Mean = 11

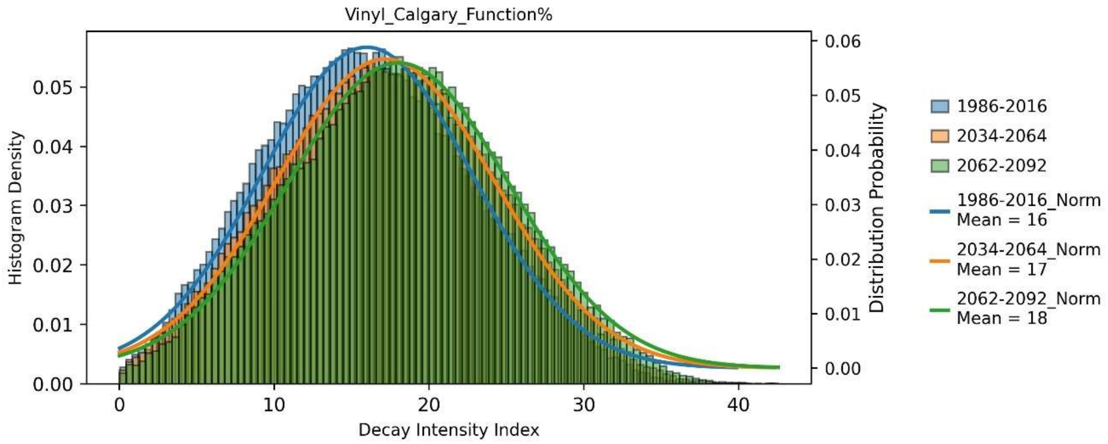
Vinyl_Calgary_Function%
Histogram Density
Distribution Probability
Decay Intensity Index
1986-2016
2034-2064
2062-2092
1986-2016_Norm
Mean = 16
2034-2064_Norm
Mean = 17
2062-2092_Norm
Mean = 18

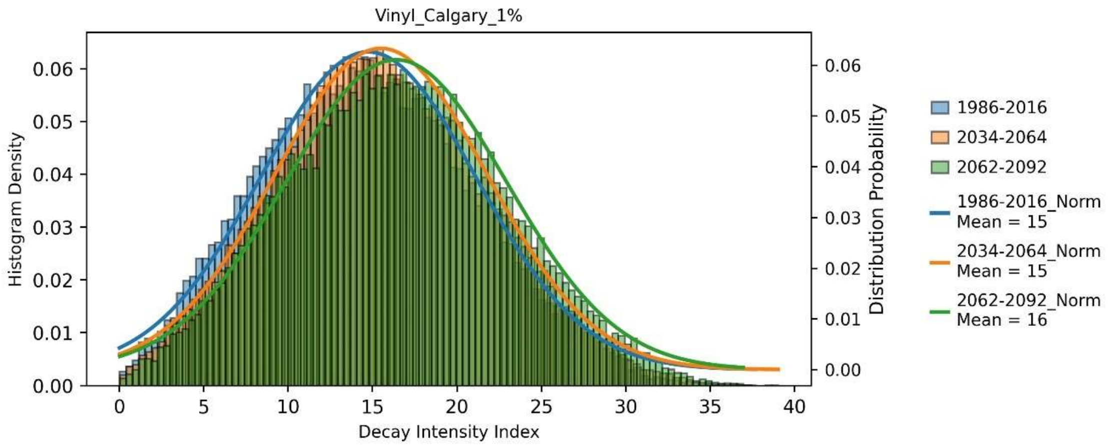
Vinyl_Calgary_1%
Histogram Density
Distribution Probability
Decay Intensity Index
1986-2016
2034-2064
2062-2092
1986-2016_Norm
Mean = 15
2034-2064_Norm
Mean = 15
2062-2092_Norm
Mean = 16

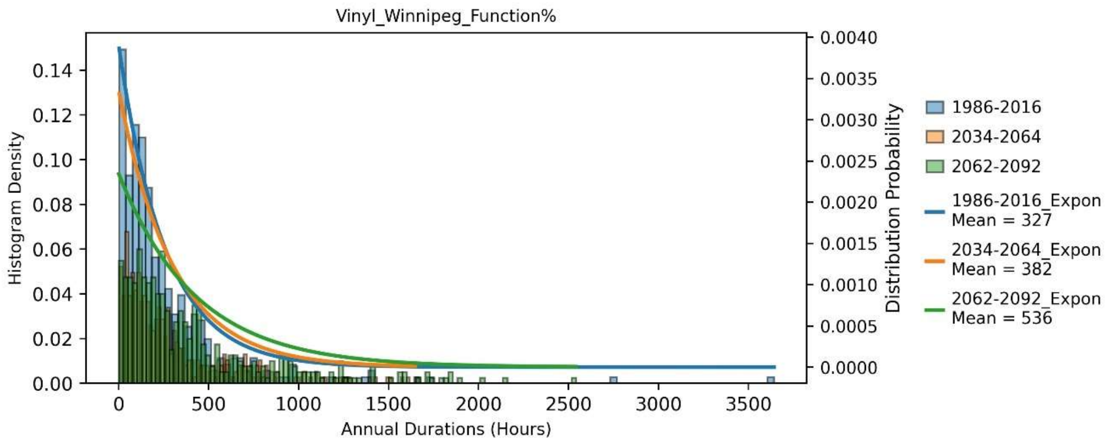
Vinyl_Winnipeg_Function%
Histogram Density
Distribution Probability
Annual Durations (Hours)
1986-2016
2034-2064
2062-2092
1986-2016_Expon
Mean = 327
2034-2064_Expon
Mean = 382
2062-2092_Expon
Mean = 536

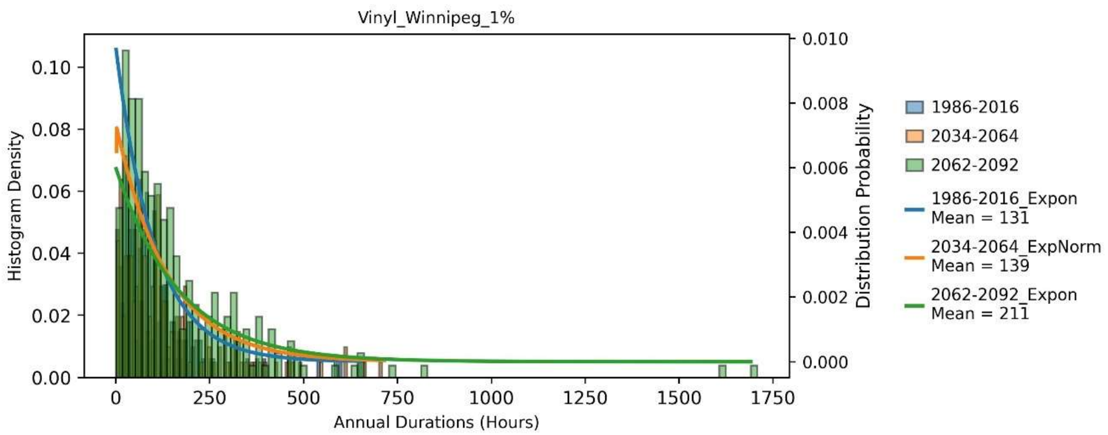
Vinyl_Winnipeg_1%
Histogram Density
Distribution Probability
Annual Durations (Hours)
1986-2016
2034-2064
2062-2092
1986-2016_Expon
Mean = 131
2034-2064_ExpNorm
Mean = 139
2062-2092_Expon
Mean = 211

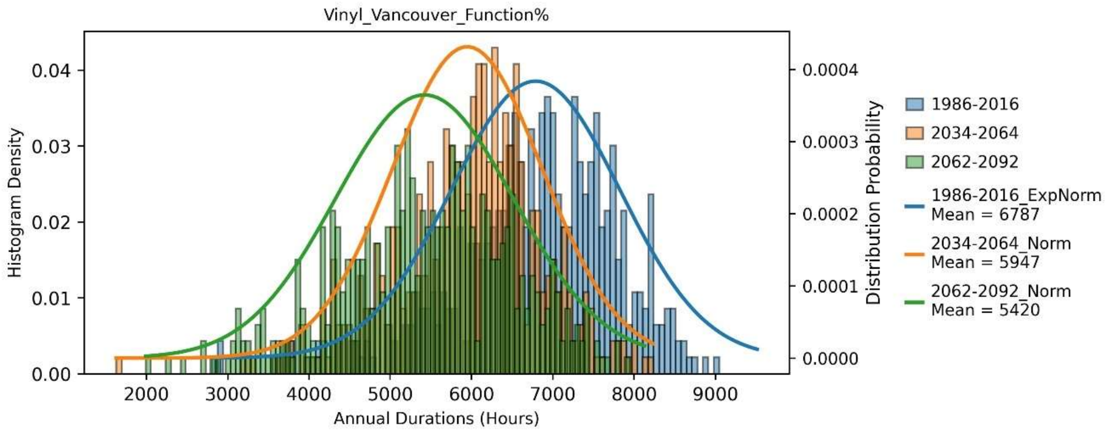
Vinyl_Vancouver_Function%
Histogram Density
Distribution Probability
Annual Durations (Hours)
1986-2016
2034-2064
2062-2092
1986-2016_ExpNorm
Mean = 6787
2034-2064_Norm
Mean = 5947
2062-2092_Norm
Mean = 5420

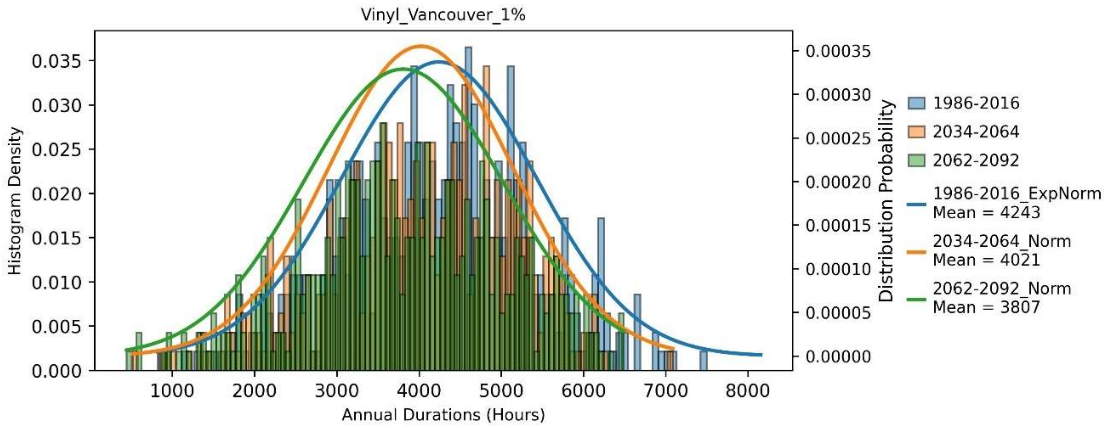
Vinyl_Vancouver_1%
Histogram Density
Distribution Probability
Annual Durations (Hours)
1986-2016
2034-2064
2062-2092
1986-2016_ExpNorm
Mean = 4243
2034-2064_Norm
Mean = 4021
2062-2092_Norm
Mean = 3807

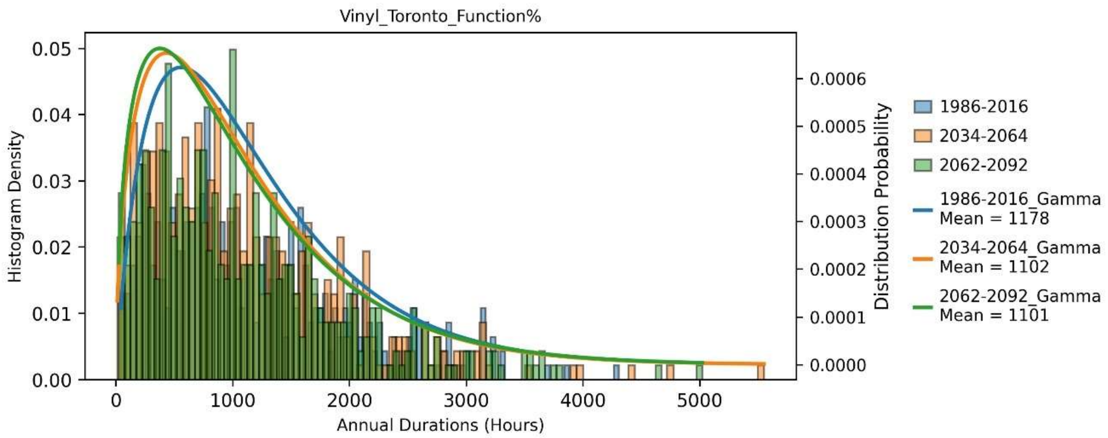
Vinyl_Toronto_Function%
Histogram Density
Distribution Probability
Annual Durations (Hours)
1986-2016
2034-2064
2062-2092
1986-2016_Gamma
Mean = 1178
2034-2064_Gamma
Mean = 1102
2062-2092_Gamma
Mean = 1101

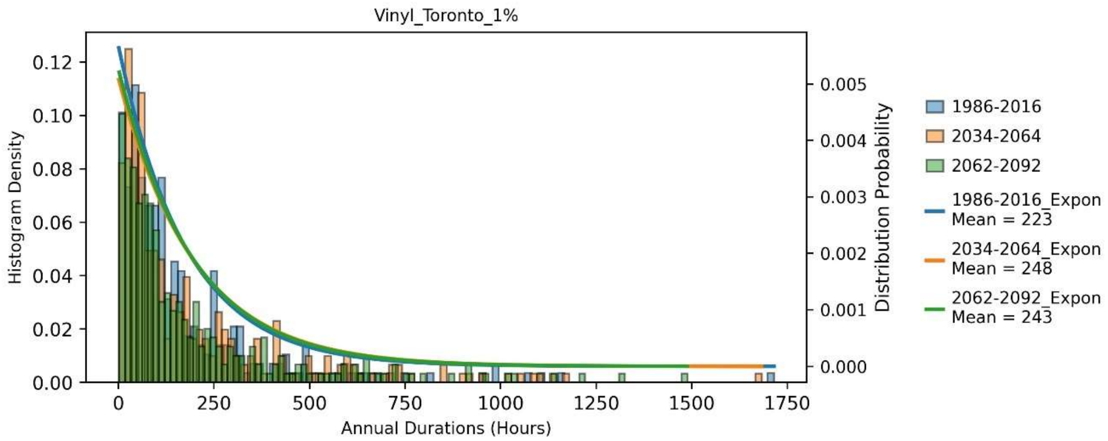
Vinyl_Toronto_1%
Histogram Density
Distribution Probability
Annual Durations (Hours)
1986-2016
2034-2064
2062-2092
1986-2016_Expon
Mean = 223
2034-2064_Expon
Mean = 248
2062-2092_Expon
Mean = 243

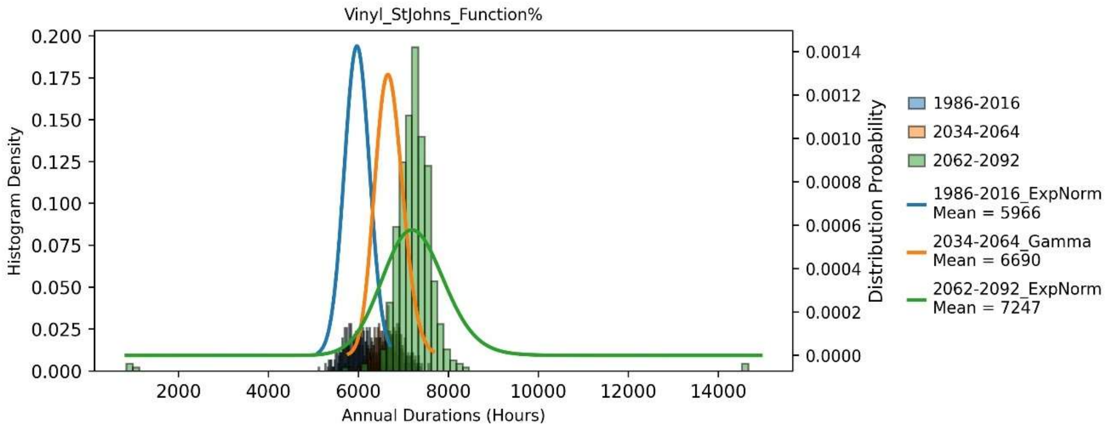
Vinyl_StJohns_Function%
Histogram Density
Distribution Probability
Annual Durations (Hours)
1986-2016
2034-2064
2062-2092
1986-2016_ExpNorm
Mean = 5966
2034-2064_Gamma
Mean = 6690
2062-2092_ExpNorm
Mean = 7247

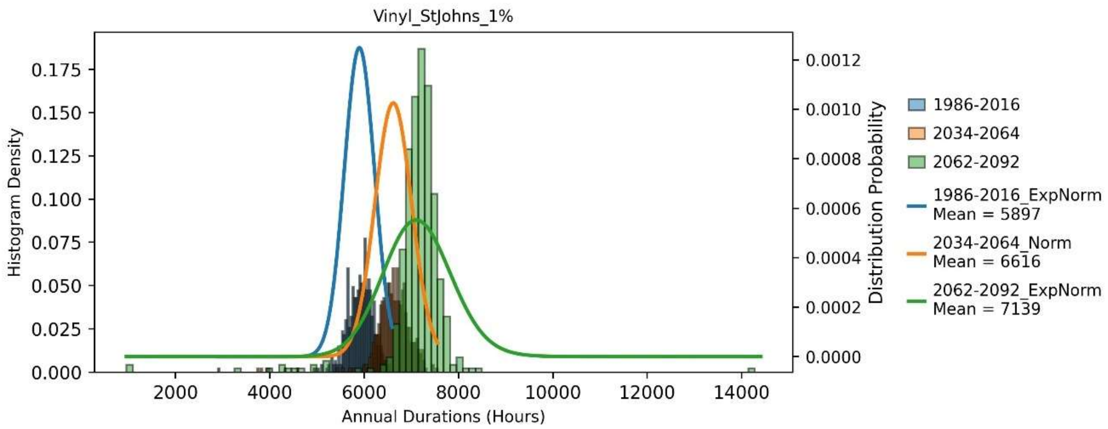
Vinyl_StJohns_1%
Histogram Density
Distribution Probability
Annual Durations (Hours)
1986-2016
2034-2064
2062-2092
1986-2016_ExpNorm
Mean = 5897
2034-2064_Norm
Mean = 6616
2062-2092_ExpNorm
Mean = 7139

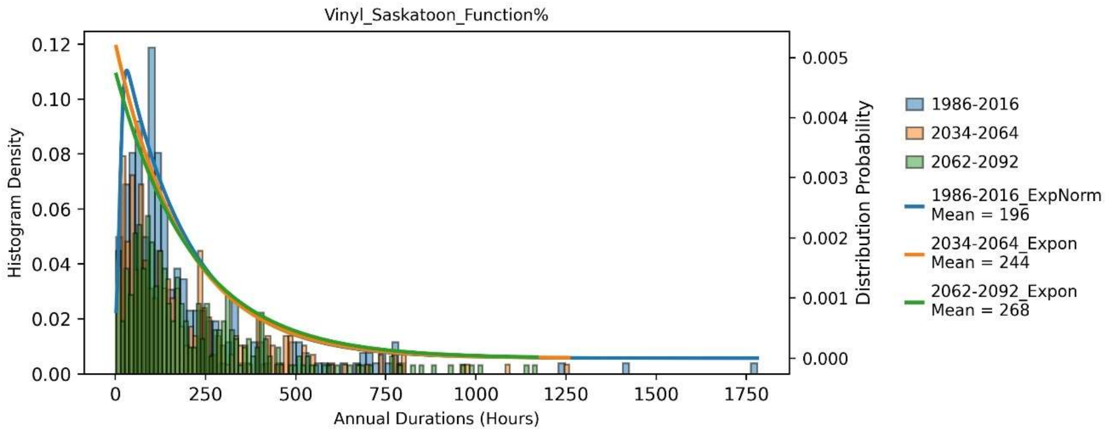
Vinyl_Saskatoon_Function%
Histogram Density
Distribution Probability
Annual Durations (Hours)
1986-2016
2034-2064
2062-2092
1986-2016_ExpNorm
Mean = 196
2034-2064_Expon
Mean = 244
2062-2092_Expon
Mean = 268

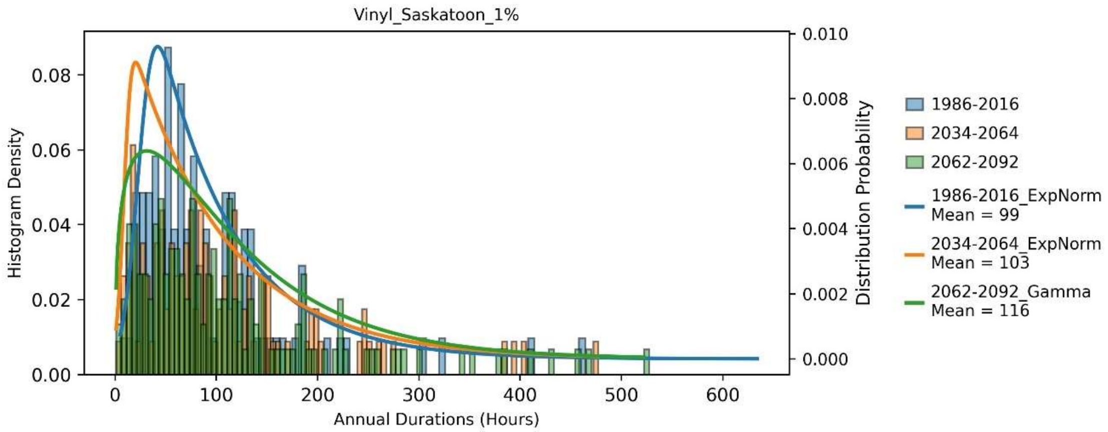
Vinyl_Saskatoon_1%
Histogram Density
Distribution Probability
Annual Durations (Hours)
1986-2016
2034-2064
2062-2092
1986-2016_ExpNorm
Mean = 99
2034-2064_ExpNorm
Mean = 103
2062-2092_Gamma
Mean = 116

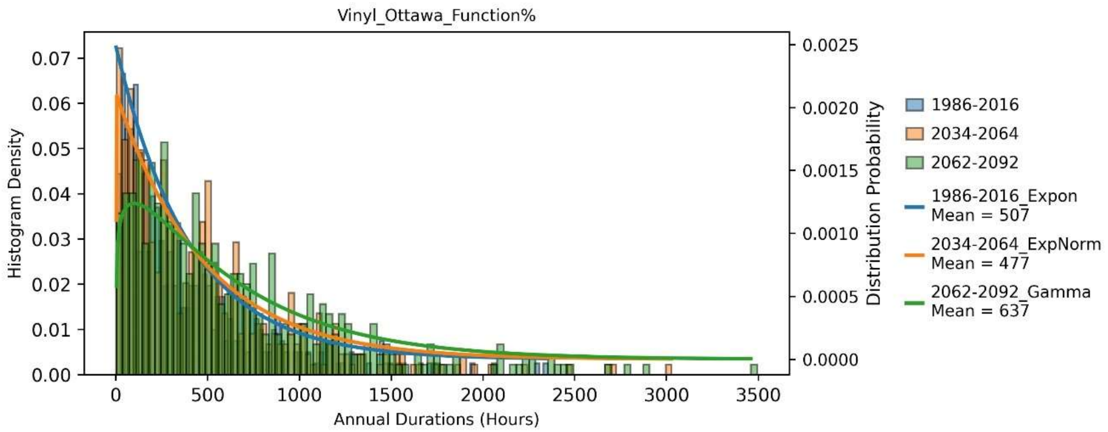
Vinyl_Ottawa_Function%
Histogram Density
Distribution Probability
Annual Durations (Hours)
1986-2016
2034-2064
2062-2092
1986-2016_Expon
Mean = 507
2034-2064_ExpNorm
Mean = 477
2062-2092_Gamma
Mean = 637

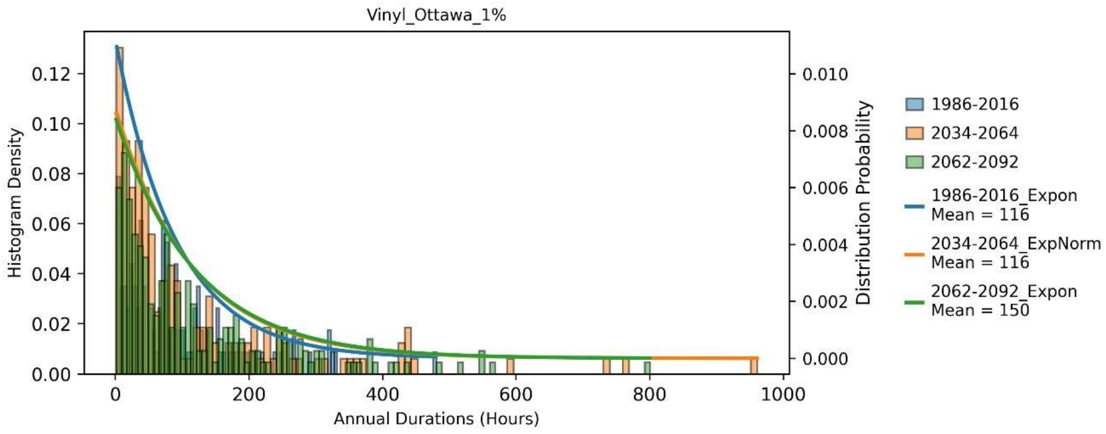
Vinyl_Ottawa_1%
Histogram Density
Distribution Probability
Annual Durations (Hours)
1986-2016
2034-2064
2062-2092
1986-2016_Expon
Mean = 116
2034-2064_ExpNorm
Mean = 116
2062-2092_Expon
Mean = 150

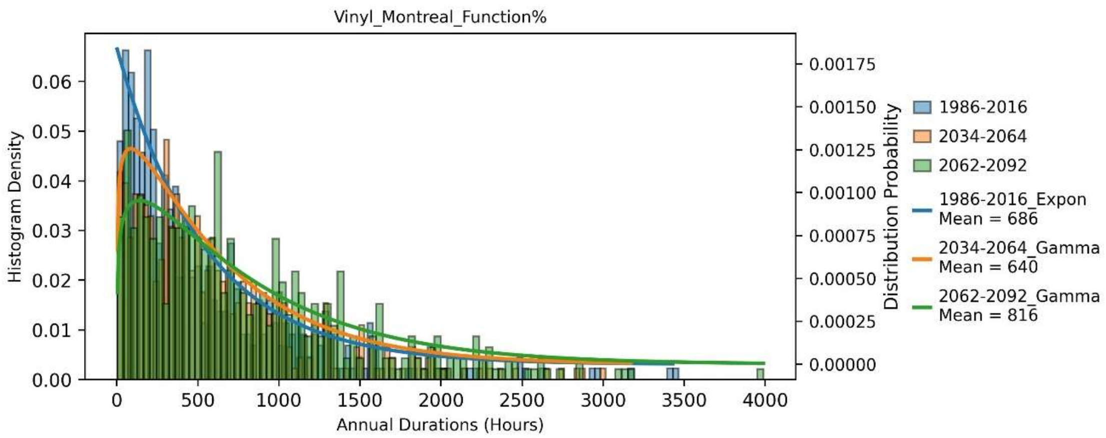
Vinyl_Montreal_Function%
Histogram Density
Distribution Probability
Annual Durations (Hours)
1986-2016
2034-2064
2062-2092
1986-2016_Expon
Mean = 686
2034-2064_Gamma
Mean = 640
2062-2092_Gamma
Mean = 816

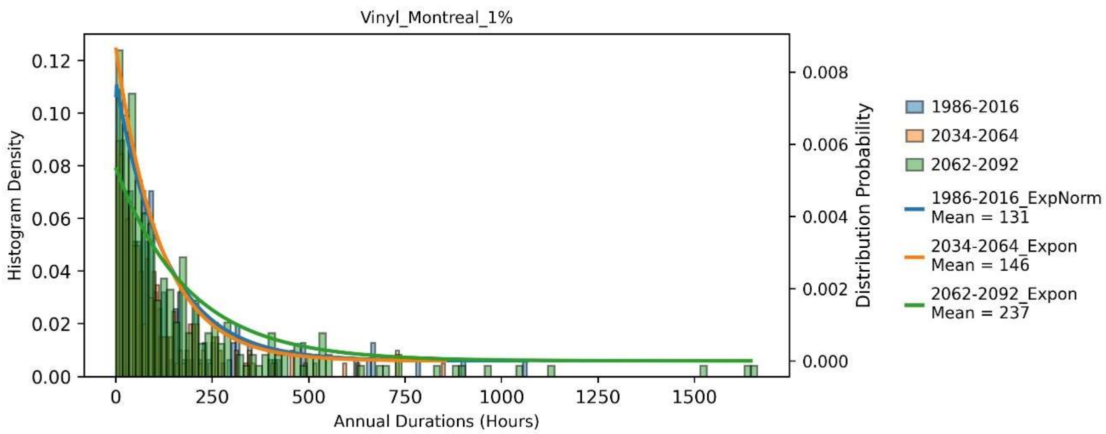
Vinyl_Montreal_1%
Histogram Density
Distribution Probability
Annual Durations (Hours)
1986-2016
2034-2064
2062-2092
1986-2016_ExpNorm
Mean = 131
2034-2064_Expon
Mean = 146
2062-2092_Expon
Mean = 237

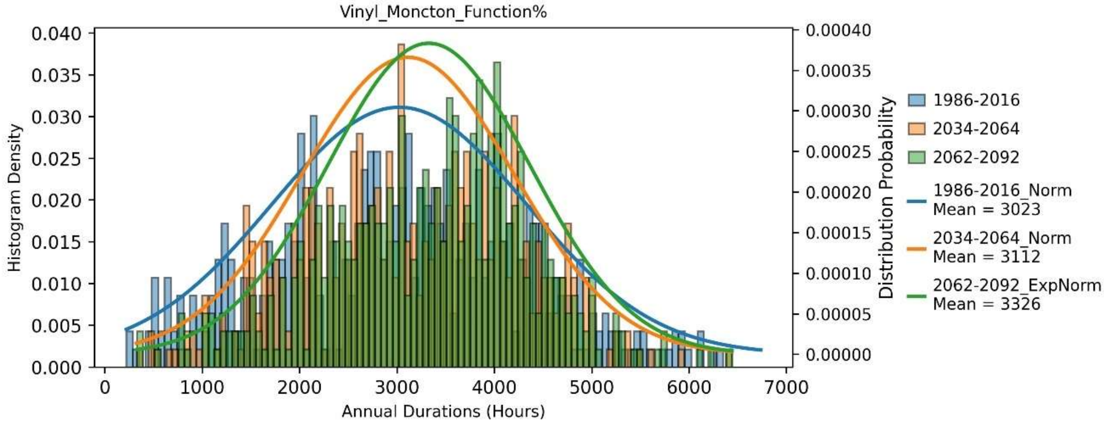
Vinyl_Moncton_Function%
Histogram Density
Distribution Probability
Annual Durations (Hours)
1986-2016
2034-2064
2062-2092
1986-2016_Norm
Mean = 3023
2034-2064_Norm
Mean = 3112
2062-2092_ExpNorm
Mean = 3326

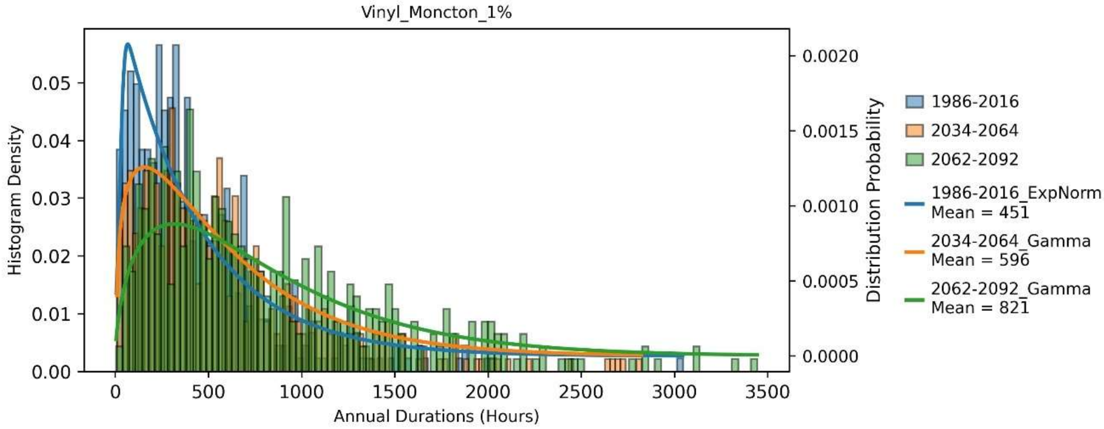
Vinyl_Moncton_1%
Histogram Density
Distribution Probability
Annual Durations (Hours)
1986-2016
2034-2064
2062-2092
1986-2016_ExpNorm
Mean = 451
2034-2064_Gamma
Mean = 596
2062-2092_Gamma
Mean = 821

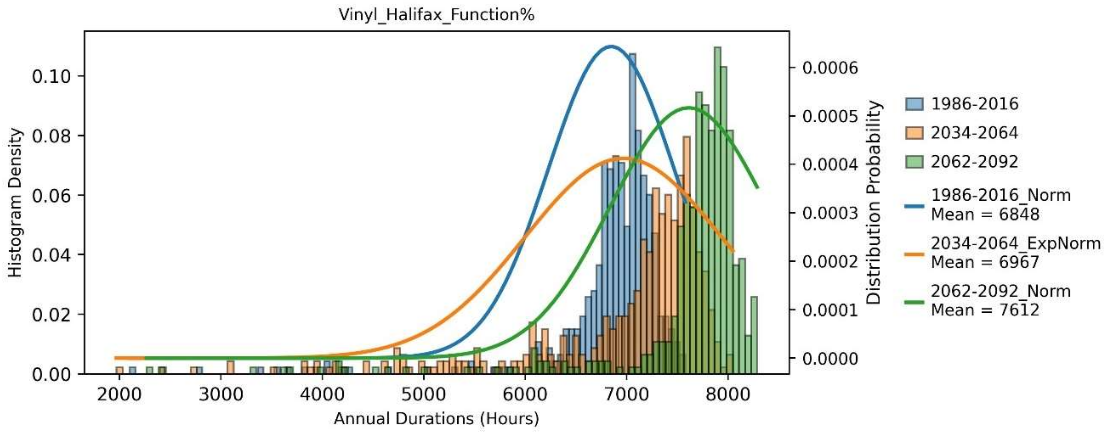
Vinyl_Halifax_Function%
Histogram Density
Distribution Probability
Annual Durations (Hours)
1986-2016
2034-2064
2062-2092
1986-2016_Norm
Mean = 6848
2034-2064_ExpNorm
Mean = 6967
2062-2092_Norm
Mean = 7612

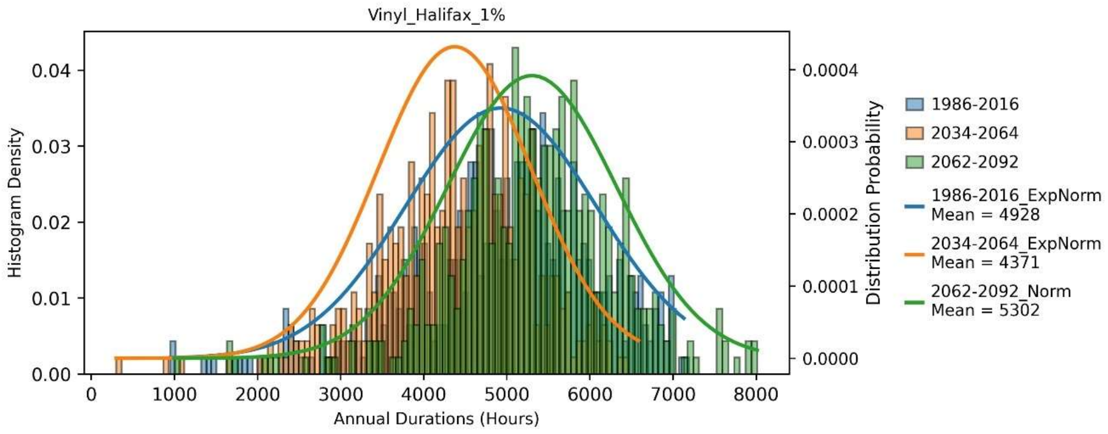
Vinyl_Halifax_1%
Histogram Density
Distribution Probability
Annual Durations (Hours)
1986-2016
2034-2064
2062-2092
1986-2016_ExpNorm
Mean = 4928
2034-2064_ExpNorm
Mean = 4371
2062-2092_Norm
Mean = 5302

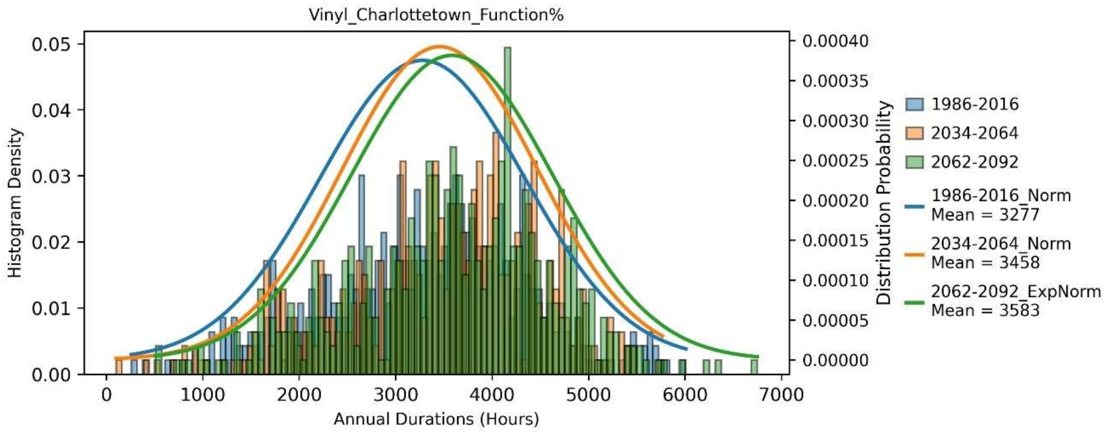
Vinyl_Charlottetown_Function%
Histogram Density
Distribution Probability
Annual Durations (Hours)
1986-2016
2034-2064
2062-2092
1986-2016_Norm
Mean = 3277
2034-2064_Norm
Mean = 3458
2062-2092_ExpNorm
Mean = 3583

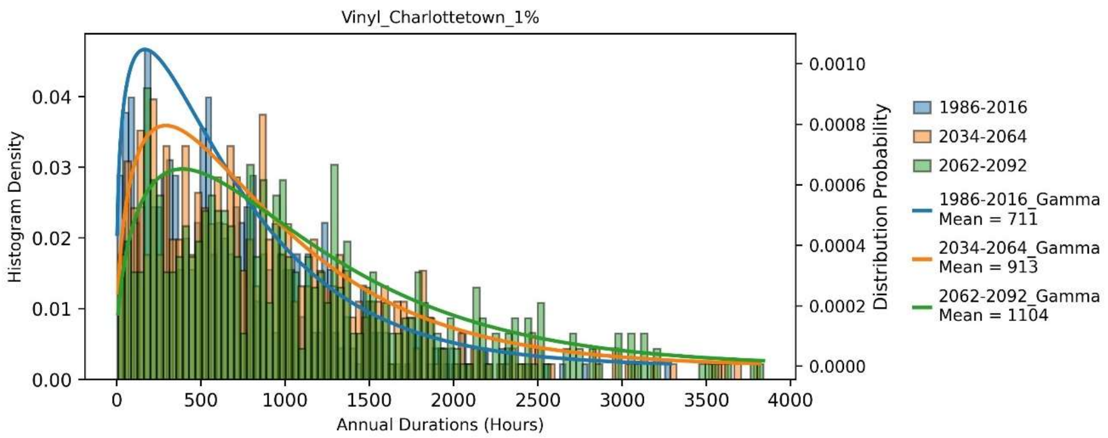
Vinyl_Charlottetown_1%
Histogram Density
Distribution Probability
Annual Durations (Hours)
1986-2016
2034-2064
2062-2092
1986-2016_Gamma
Mean = 711
2034-2064_Gamma
Mean = 913
2062-2092_Gamma
Mean = 1104

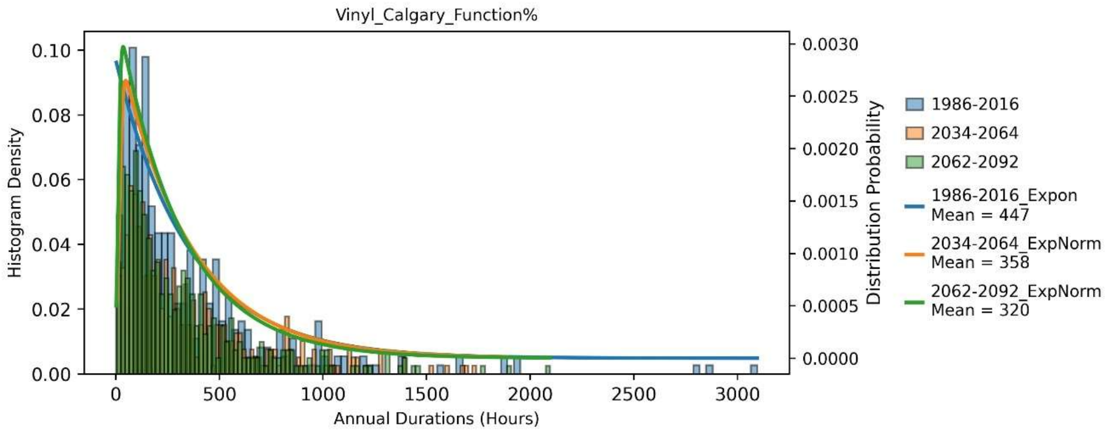

Vinyl_Calgary_Function%
Histogram Density
Distribution Probability
Annual Durations (Hours)
1986-2016
2034-2064
2062-2092
1986-2016_Expon
Mean = 447
2034-2064_ExpNorm
Mean = 358
2062-2092_ExpNorm
Mean = 320

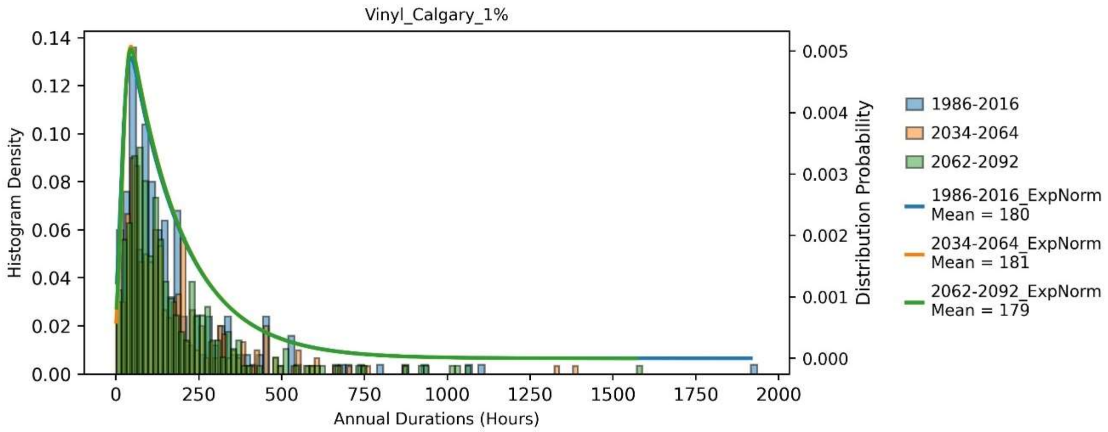

Vinyl_Calgary_1%
Histogram Density
Distribution Probability
Annual Durations (Hours)
1986-2016
2034-2064
2062-2092
1986-2016_ExpNorm
Mean = 180
2034-2064_ExpNorm
Mean = 181
2062-2092_ExpNorm
Mean = 179

Chapter 6 Conclusions

The primary contribution derived from this research project was the development of a performance evaluation framework to properly estimate the effects of a changing climate on the moisture performance of different types of wood frame wall assemblies subjected to Wind-Driven-Rain (WDR) events. The use of this evaluation framework can help determine the moisture resilience of wall assemblies, can assess risks of degradation and performance loss and can provide design guidance on wood frame wall assemblies, for projected future climate scenarios. The performance evaluation framework developed, implied several research milestones as follows: conducting an analysis of historical and future projected climate loads to identify possible changes of WDR conditions on wall assemblies; performing watertightness tests to correlate the WDR and moisture loads in wall assemblies, and executing hygrothermal simulations to permit assessing the risks to the occurrence of damaging effects to wall elements. The main findings of each research stage are summarized below.

6.1 Conclusions and discussion

Based on numerous previous studies and observations of watertightness tests, water deposited on the building façades is the primary source of moisture loads to the wall assembly. Rain water is always driven by the constant movement and flow of air in the atmosphere, and this water reaches the building façade at different deposition rates, depending on the rainfall intensity, wind velocity, wind direction, as well as the surrounding environment. By analyzing WDR conditions for one historical time period (1986-2016) and two future projected time periods (2034-2064, 2062-2092), possible changes in the severity of WDR events for eleven selected Canadian cities were identified. In addition, a novel Wind Driven Rain Pressure Index (WDRPI) was proposed to describe the concurrent effect of WDR and Driving Rain Wind Pressure (DRWP) acting on the exterior surface of a wall given that the amount of water penetration into a wall assembly is positively correlated with these two parameters. It has been demonstrated that for most of the analyzed cities, the WDR events would become more frequent and the severity of extreme events would increase for future projected time periods. The goodness of fit test showed that the Gumbel distribution was the best choice for conducting the extreme value analysis of WDR. The WDR and DRWP extremes obtained from the analysis, laid the foundation for developing a watertightness test protocol in a subsequent phase of this research.

The climate data analysis for different time periods provided information regarding WDR to which wall assemblies may be exposed to. To permit estimating the moisture load in wall assemblies for all possible weather conditions, testing parameters specified in the test protocol covered WDR and DRWP extremes for a 50-year return period. Thereafter, a two-step approach was proposed to correlate watertightness test results with experimental inputs, including water spray rates and dynamic pressure that represent the WDR load and DRWP in the atmosphere, respectively. Using this approach, the moisture load acting on the wall assembly can be calculated from the hourly WDR loads and hourly DRWPs, collected from weather stations or generated by climate models. Full-scale brick veneer and vinyl-clad wall assemblies installed with common components, such as a window, electric outlet and ventilation duct, were tested using the watertightness test protocol. Water entry functions using hourly WDR loads and hourly DRWPs were developed to calculate the moisture load acting on these two types of wall assemblies. The use of these functions was implemented in the subsequent research phase as input to hygrothermal simulation models. The test results demonstrated that the moisture load derived from watertightness tests using water entry functions was different from the moisture load in the ASHRAE 160 standard, which is equivalent to 1% of the WDR load, a standard that is widely used by building practitioners.

Based on the results of watertightness tests, the next step was to explore the hygrothermal performance of tested wall assemblies when subjected to different moisture loads using hygrothermal simulation tools. The mould index and development of wood decay for oriented strand boards (OSB) used in the wall assembly were calculated from the outputs of hygrothermal simulations; these were selected as indicators to evaluate the moisture performance of the wall assemblies. The time history of the mould index during the time periods over which the moisture performance was analyzed was divided into individual events. The frequencies of the events having a designated level of mould index and durations of such events were counted and summarized in a bubble matrix. It was found that, for most of the investigated cities, frequencies of events with higher levels of mould index and of longer duration, for both the brick and vinyl-clad wall assemblies, would increase during projected time periods except for those located in Calgary. Also, was shown that by considering the moisture load derived from water entry equations, the mould growth for the vinyl-clad wall assembly would be more severe than that using 1% of the WDR load as the moisture load. This observation was opposite to that of the brick wall assembly. These differences demonstrated the importance of deriving moisture loads from watertightness tests when evaluating the performance of wall assemblies. In terms of the decay, a severity index which was calculated from normalized values of relative humidity and temperature, was proposed to represent the extent of decay for wood elements in wall assemblies subjected to moisture loads. The mass loss caused by wood elements decay in different cities for different time periods was assessed by considering both the intensity and duration of decay separately, given that the inherent uncertainty of climate data generated by the climate models. The output derived from one set of climate data was only one of many possibilities. Hence, to permit a broader application of such data, and given its degree of uncertainty, the corresponding parameters were then analyzed from a probabilistic standpoint. More specifically, the likelihood of occurrence of a specific decay intensity and the likelihood of annual durations of decay events were generated by fitting selected distributions to the histograms of these two parameters. The findings suggested that the mass loss rate of wood elements for different wall assemblies, and for each city location, needed to be characterised separately as they were significantly different under the same local environmental conditions. Moreover, the mass loss rates for future time periods would increase in most cities, although the degree of response to the changing climate was substantially different.

Overall, this research has established the investigative framework for correlating future climate conditions to the performance of wall assemblies, by conducting watertightness tests and thereafter, on the basis of test results, performing hygrothermal simulations. The climate analysis provided basic input parameters for the analysis whereas the moisture load in wall assemblies arising from WDR was identified through the use of watertightness tests. The hygrothermal simulations generated parameters to permit estimating the occurrence and severity of detrimental effects caused by the changing climate to wall components in wall assemblies.

6.2 Future Research

Continuing this research is of critical importance to the development of new guidelines or to update the building design codes, in the light of the imminent impacts of climate change on the moisture performance of wall assemblies.

Based on these new methodologies and findings, future work, that had been considered, but was judged to be beyond the scope of the current research, can be further developed from the following proposals:

- Evaluate the performance of other types of wood frame wall assemblies, such as wall assemblies clad with hardboard siding, stucco, wood fibre, for future projected time periods using the same moisture performance evaluation framework.
- Evaluate the moisture performance of other wood components in the wall assembly, including the vertical wood studs and wood plates at the top and bottom of the wall.
- Explore the initial stage of wood decay by finding the survival time for wood decay fungi.
- Validate the damage due to wood decay through the use of laboratory experiments or field tests.
- Validate by field investigations the WDR loads to which wall assemblies are subjected to, in respect to the local WDR events as may occur and the building and climate parameters that affect WDR loads.
- Validate the extent of water entry and uptake in building elements from field investigations of wall assemblies subjected to WDR events as they may arise from actual local conditions.
- Evaluate the moisture performance of the wall assembly in respect to the corrosion of metal fasteners in the wall; identify the instances for the corrosion of metal fasteners and thus the prevalent damage mode as compared to wood decay.
- Identify the wall design mitigation measures to offset the impact of a changing climate on the moisture performance of wall assemblies.
- Investigate the WDR conditions for high-rise buildings and incorporate relevant information into a revised watertightness test protocol that could be used to assess façade systems typically applied to the exterior of such buildings.